dortmund university

UNIVERSITÉ Clermont Auvergne

A document submitted for the degree of
Doktor der Naturwissenschaften/
Docteur d'université en physique

Electroweak heavy flavour precision observables: connecting open dots with the FCC-ee

Lars Röhrig
born in Wuppertal

2024

AG Kröninger
Technische Universität Dortmund

and

École Doctorale des Sciences Fondamentales
Université Clermont Auvergne

This dissertation was submitted to the Department of Physics at the Technical University of Dortmund and the Graduate School of Fundamental Sciences at the University of Clermont Auvergne for the award of the academic degree of Doctor of Natural Sciences.

First examiner:	Prof. Dr. Kevin Kröninger
Second examiner:	Prof. Dr. Frank Simon
Third examiner:	Dr. Emmanuel Perez
Chair of the examination board:	Prof. Dr. Gudrun Hiller
Further members of the examination board:	Prof. Dr. Stéphane Monteil
	Dr. Romain Madar
Submission date:	15 August 2024
Defence date:	30 October 2024

Diese Arbeit wurde von der Deutsch-Französischen Hochschule finanziell gefördert.
Cette thèse a fait l'objet d'un soutien financier de l'Université franco-allemande.
This work was financially supported by the Franco-German University.

Abstract

The heaviest third-generation fermions are expected to be most sensitive to effects from Beyond the Standard Model (BSM) physics, which will be probed with very high precision at a possible FCC-ee. In this thesis, a novel approach to measuring Electroweak Precision Observables in the beauty-quark sector is pioneered using exclusively reconstructed beauty-hadrons as hemisphere-flavour taggers for the partial decay-width ratio R_b and the forward-backward asymmetry A^b_{FB}, which receive virtual contributions from the heaviest states of the Standard Model (SM): top quarks, Higgs, and $W^{\pm}$ boson. This approach effectively eliminates the contamination from light-quark physics events and reduces leading systematic uncertainties; arising from background contamination, tagging-efficiency correlations, and radiated gluon corrections by exploiting the geometric and kinematic properties of beauty hadrons. This results in a total relative uncertainty of the order of 0.01 % for both observables. From A^b_{FB}, the weak mixing angle can be determined with a relative precision of 0.002 %. Building on this innovative methodology, the thesis is extended to the top-quark sector by extracting the sensitivity of top-quark observables to SM Effective Field Theory operators, which describe the effects of BSM physics by extending the SM with higher-dimensional operators on energy scales that are currently inaccessible. In a FCC-ee environment, top-quark pairs are reconstructed, and the expected observational precision is used to derive constraints on the Wilson coefficients that are up to a factor of five and three more stringent than those derived from top-quark measurements at LHC and HL-LHC, respectively.

Kurzfassung

Die schwersten Fermionen der dritten Generation werden voraussichtlich am sensitivsten auf Effekte der Physik jenseits des Standardmodells (BSM) reagieren, die mit hoher Präzision an einem möglichen FCC-ee untersucht werden sollen. In dieser Dissertation wird ein neuartiger Ansatz zur Messung elektroschwacher Präzisionsobservablen im Beauty-Quark-Sektor entwickelt, bei dem ausschließlich rekonstruierte Beauty-Hadronen als Hemisphären-Flavour-Tagger für das partielle Zerfallsverhältnis R_b und die Vorwärts-Rückwärts-Asymmetrie A_{FB}^b verwendet werden, welche Beiträge von Prozessen mit den schwersten Teilchen des Standardmodells (SMs) erhalten: Top-Quarks, Higgs- und $W^{\pm}$-Bosonen. Dieser Ansatz eliminiert effektiv die Kontamination durch Ereignisse der leichtesten Quarks und reduziert führende systematische Unsicherheiten, die durch Hintergrundereignisse, Korrelationen der Tagging-Effizienz und Korrekturen durch emittierte Gluonen entstehen, indem die geometrischen und kinematischen Eigenschaften von Beauty-Hadronen genutzt werden. Dies führt zu einer relativen Gesamtunsicherheit in der Größenordnung von 0,01 % für beide Observablen. Aus A_{FB}^b kann der schwache Mischungswinkel mit einer relativen Präzision von 0,002 % bestimmt werden. Darauf aufbauend wird die Dissertation auf den Top-Quark-Sektor erweitert, indem die Sensitivität von Top-Quark-Observablen auf Operatoren der Effektiven Feldtheorie des SMs extrahiert wird, welche Effekte der BSM-Physik durch die Erweiterung des SMs mit höherdimensionalen Operatoren auf derzeit unzugänglichen Energieskalen beschreiben. In einer FCC-ee-Umgebung werden Top-Quark-Paare rekonstruiert, und die erwartete experimentelle Präzision wird genutzt, um Grenzen für die Wilson-Koeffizienten abzuleiten, die bis zu fünfmal bzw. dreimal strenger sind als die aus Top-Quark-Messungen am LHC und HL-LHC abgeleiteten.

Résumé

Les fermions de la troisième génération, qui sont les plus lourds, sont censés être les plus sensibles aux effets de la physique au-delà du Modèle Standard (BSM), qui seront étudiés avec une très grande précision dans le cadre d'un éventuel FCC-ee. Dans cette thèse, une approche novatrice pour mesurer les observables de précision électrofaible dans le secteur des quarks beaux est proposée en utilisant exclusivement des hadrons beaux reconstruits comme étiqueteurs de saveur des hémisphères pour le rapport de désintégration partielle R_b et l'asymétrie avant-arrière A_{FB}^b, qui reçoivent des contributions de processus incluant des particules virtuelles lourdes : quarks top, Higgs et $W^{\pm}$ dans le Modèle Standard (SM). Cette approche élimine efficacement la contamination provenant des événements de physique des quarks légers et réduit les principales incertitudes systématiques, découlant de la contamination des bruits de fond, des corrélations d'efficacité d'étiquetage et des corrections liées aux gluons rayonnés, en exploitant les propriétés géométriques et cinématiques des hadrons beaux. Cela conduit à une incertitude relative totale de l'ordre de 0.01 % pour les deux observables. À partir de A_{FB}^b, l'angle de mélange électrofaible peut être déterminé avec une précision relative de 0.002 %. En s'appuyant sur cette méthodologie innovante, la thèse est étendue au secteur du quark top en déterminant la sensibilité des observables du quark top aux opérateurs de la théorie effective du SM, qui décrivent les effets de la physique BSM en étendant le SM avec des opérateurs de dimension supérieure sur des échelles d'énergie actuellement inaccessibles. Dans un environnement FCC-ee, les paires de quarks top sont reconstruites, et la précision d'observation attendue est utilisée pour dériver des contraintes sur les coefficients de Wilson qui sont jusqu'à cinq et trois fois plus strictes que celles dérivées des mesures des quarks top au LHC et au HL-LHC, respectivement.

Contents

Disclaimer

In this thesis, the physics potential of a possible FCC-ee is presented in the beauty- and top-quark sectors. Among the guidance and assistance of other researchers, the following parts and results of the thesis have been produced by myself.

Chapter 4 The development and application of the hemisphere-flavour tagger, using exclusively reconstructed b-hadrons, was carried out by me, primarily using pregenerated event samples. I was responsible for the entire reconstruction process, performance evaluation, and its application in measuring R_b and A_{FB}^b. All plots and results presented were independently generated by me. Furthermore, I supervised further research work that involved the application of the concept for R_c, R_s, and A_{FB}^s in the context of master's theses and internships.

Chapter 5 I generated my own event samples using `MadGraph_aMC@NLO` to investigate the sensitivity of various observables to modifications induced by dimension-six operators. For reconstruction and precision studies of these observables within an FCC-ee environment, I used pregenerated samples. Furthermore, I produced and analysed additional simulated event samples with varied input parameters to investigate systematic effects.

Chapter 6 The determination of limits on the Wilson coefficients, involving the setup of `EFTfitter.jl` and the development of suitable parameterisations, was carried out by me. These results were influenced by previous publications by colleagues, which provided essential input for my analysis.

1 Introduction

Since the beginning of human curiosity, people have aimed to understand and explain the phenomena in nature, from the largest scales in astronomy to the tiniest particles that constitute visible matter. The ultimate goal is to derive comprehensive mathematical models that describe observations while being predictive at the same time. The most successful model, developed during the 20^{th} century, is the Standard Model of Particle Physics (SM), which unifies three of the four fundamental forces in nature. The SM's success in predicting and explaining measurements of fundamental parameters has been validated through successive generations of experimental setups, with the largest constructed colliders at Fermilab in the Chicago region and at the European Organisation for Nuclear Research (CERN) in the Geneva region over the last 35 years.

A crucial aspect of probing the SM involves precision measurements, particularly of Electroweak Precision Observables (EWPOs). The Large Electron-Positron Collider (LEP), which was operated at CERN from 1989 to 2000 at centre-of-mass (COM) energies up to 209 GeV, and the Large Hadron Collider (LHC) currently running at a COM energy of 13.6 TeV, which is operational since 2008, have been crucial in this quest. LEP provided an exceptionally clean environment for precision measurements of the properties of the Z^0 boson, such as its mass, width, and decay rates into various fermions, which have been in remarkable agreement with the SM predictions [1]. The LHC, designed to explore higher energy-scales to search for new heavy particles, enabled the discovery of the Higgs boson in 2012 [2, 3] by the dedicated efforts of the scientific community. It has also facilitated numerous measurements of SM processes involving the Higgs boson and the heaviest particle of the SM, the top quark. However, it has not found conclusive evidence for BSM physics, despite extensive searches for supersymmetry, extra dimensions, and other exotic particles [4–9].

In light of these findings and the presence of effects like dark matter that cannot be explained by the SM, the particle-physics community is looking toward future experiments that can provide even greater precision and reach higher energies. One of the most promising proposed projects is the Future Circular Collider (FCC), enabling unprecedented precision in the measurement of electroweak (EW) and heavy-flavour observables as an electron-positron collider (FCC-ee) in the first stage [10]. In a second, upgraded phase, the FCC tunnel would host a proton-proton collider (FCC-hh) operating at the highest achievable collision energies of up to 100 TeV [11] until the end of the century. The FCC-ee will enable a deep exploration of processes

involving Z^0-, $W^{\pm}$-, and the Higgs-boson, in addition to the top quark, with a particular focus on third-generation quarks. Given their significant mass among fermions, these particles are expected to have an increased sensitivity to BSM effects, which could reveal in subtle deviations from SM predictions.

A global approach to describe and interpret these potential deviations is the Standard Model Effective Field Theory (SMEFT), allowing to also combine effects across different energy scales and sectors in the SM. The SMEFT framework extends the SM by including higher-dimensional operators, allowing to explore BSM physics effects at energy scales beyond the reach of current collider experiments. For the sake of this thesis, this allows to consistently combine precision measurements in the beauty- and top-quark sectors through a common set of operators. Beauty EWPOs, specifically the forward-backward asymmetry and the ratio of Z^0-boson decay rates into beauty quarks to its total hadronic decay-rate, still show the highest tension of up to $2.9\,\sigma$ with the SM prediction among all EWPOs [12]. With a significant reduction of experimental uncertainties, tight indirect constraints on operators affecting the coupling of gauge bosons to the top quark are expected. For this, a new synergy between flavour physics and EWPOs for measuring beauty EWPOs is envisaged at the potential FCC-ee, which allows enhancing the precision by about two orders of magnitude. Furthermore, the sensitivity of selected top-quark observables and their expected precision are presented, enabling the combination of the measurements in a Bayesian fit to limit the effective coupling strength.

The structure of this thesis is organised as follows:
In Chap. 2, the SM is described with a focus on beauty- and top-quark observables followed by a description of the basic concept of SMEFT. The landscape of future Higgs factories highlighting the FCC with its physics motivation and programme of FCC-ee, together with the simulated event samples, is presented in Chap. 3. In Chap. 4, a new synergy is introduced between flavour physics and beauty EWPOs, providing a detailed discussion of the measurement principle and uncertainties associated with the observables. Novel approaches to make use of the sheer amount of Z^0-boson decays at FCC-ee are validated before concluding on the expected precision of the weak mixing angle, a fundamental SM parameter. Top-quark observables and their sensitivity to a selection of SMEFT operators are investigated in Chap. 5. The expected precision of these observables in a FCC-ee environment including the reconstruction of top-quark pairs concludes the chapter. In Chap. 6, the expected uncertainties on the top-quark observables are used to derive limits on the SMEFT operator strength and to compare the limits with the ones currently achievable at LHC and its upgrade. The thesis concludes in Chap. 7.

2 Theoretical background

An accurate understanding of the world around us on the smallest scale requires a robust description of the underlying dynamics and the most fundamental interactions. This description is summarised in the SM, the–to-date–world's most accurate theory of elementary particles. It has survived dozens of tests in collider and fixed-target experiments over the past decades without significant deviations from the measurements. In the following, its theoretical framework is briefly described in Sec. 2.1, before the observables of interest in this thesis are introduced to measure fundamental parameters of the SM in Sec. 2.2. The extension of the SM with higher-dimensional operators within an Effective Field Theory (EFT) approach is introduced in Sec. 2.3.

2.1 Fundamentals of the Standard Model

The SM is the theoretical framework that describes the fundamental particles and their interaction, excluding gravity. Developed throughout the 20^{th} century, the SM has been remarkably successful in explaining a wide range of experimental results and also in predicting new phenomena that were later confirmed experimentally. One of the first breakthroughs was the discovery of the electron by J. J. Thomson in 1897 [13], followed by the identification of the proton and neutron in the early 20^{th} century [14, 15]. Follow-up discoveries of various particles in cosmic rays and particle accelerators led to the realisation that there were more fundamental particles and interactions to be understood.

2.1.1 Symmetry groups

Mathematically expressed, the SM is a renormalisable quantum field theory (QFT) that operates under the principle of local gauge invariance, dictated by the symmetry group $\mathrm{SU(3)_C} \otimes \mathrm{SU(2)_L} \otimes \mathrm{U(1)_Y}$. This framework, based on the QFT approach that was pioneered with the formulation of the quantum electrodynamics (QED) in the 1940s [16–18], provides a unified description of the electromagnetic (EM), weak, and strong interactions. QED describes the EM force with remarkable precision, making it one of the most successful theories in physics. The unification of EM and weak interactions by S. Glashow [19], A. Salam [20], and S. Weinberg [21], along with

the development of quantum chromodynamics (QCD) [22–24] to describe the strong interaction, resulted in the SM as it is known today.

The $\mathrm{SU(2)_L} \otimes \mathrm{U(1)_Y}$ symmetry group offers a comprehensive theory of the EM and weak forces. The $\mathrm{SU(2)_L}$ component, which governs the weak interaction, is a non-Abelian group that exclusively interacts with left-handed (spin antiparallel to the momentum direction) fermions and uses weak isospin as its associated charge. Meanwhile, the $\mathrm{U(1)_Y}$ component is associated with weak hypercharge $Y = 2T_f + 2Q_f$, with T_f being the third component of the weak isospin and Q_f representing the electric charge of a fermion f.

The weak neutral-current interaction, mediated by the Z^0 boson, involves both vector and axial-vector couplings to fermions. These couplings, denoted by v_f (vector coupling V) and a_f (axial-vector coupling A), can be expressed at tree level as

$$a_f = T_f\,, \tag{2.1}$$

$$v_f = T_f - 2Q_f \sin^2(\theta_\mathrm{W})\,, \tag{2.2}$$

where the Weinberg angle θ_W determines the mixing between the EM and weak interactions. Specifically, $\sin^2(\theta_\mathrm{W})$ quantifies the proportion of the Z^0-boson's coupling that arises from the $\mathrm{U(1)_Y}$ component relative to the total EW interaction. It plays a crucial role in determining the strength of neutral-current interactions and is a key parameter in EW precision tests. The difference between the vector and axial-vector couplings leads to an observable phenomenon known as forward-backward asymmetry in particle collisions.

Ensuring gauge invariance under $\mathrm{SU(2)_L} \otimes \mathrm{U(1)_Y}$ implies that both matter and gauge bosons would initially be massless. However, this apparent paradox is resolved by the introduction of the Higgs mechanism, which spontaneously breaks the EW symmetry. The Higgs mechanism introduces a scalar field that acquires a non-zero vacuum expectation value (vev), breaking the $\mathrm{SU(2)_L} \otimes \mathrm{U(1)_Y}$ symmetry down to $\mathrm{U(1)_{EM}}$, corresponding to electromagnetism. This process, a consequence of the EW symmetry breaking, which has been worked out in the 1960s by P. Higgs [25, 26], R. Brout and F. Englert [27], gives mass to the weak gauge bosons. The Higgs field also provides mass to fermions through Yukawa couplings. The discovery of the Higgs boson at the LHC in 2012 confirmed this vital aspect of the SM.

The strong interaction, on the other hand, is governed by the $\mathrm{SU(3)_C}$ group, with the colour charge serving as the relevant charge. It is characterised by the property of asymptotic freedom, where quarks experience a reduced interaction strength at higher energies (or equivalently, at shorter distances) [24].

After establishing the theoretical foundations of the forces and symmetries within the SM, the following section provides a detailed outline of the particles that mediate these forces and are acted upon by them.

2.1.2 Particle content

At the core of the SM are fundamental particles, grouped by their spin in fermions and bosons with half-integer and integer-one spin values, respectively. The fermions are further categorised into quarks and leptons, which constitute the matter particles, while gauge bosons mediate the fundamental forces. The Higgs boson has a special role in the SM as it is the only spin-zero boson, and the interaction of particles with the Higgs field gives rise to particle masses. The following paragraphs describe the different types of particles and their characteristics.

Quarks Quarks come in six flavours: up (u), down (d), charm (c), strange (s), bottom (b), and top (t). They carry a fractional electric charge, either $+2/3$ (up-type quarks: u, c, t) or $-1/3$ (down-type quarks: d, s, b) and are spin-$1/2$ particles. In addition to electric charge, quarks have colour charge, fundamental to the strong interaction, with three types: red, green, and blue. Each quark has a corresponding antiparticle, the antiquark, with inverted quantum numbers. Due to colour confinement, quarks cannot be isolated; they always form colour-neutral combinations, leading to the formation of baryons (composites of three (anti)quarks) and mesons (composites of a quark and an antiquark).

Leptons Leptons comprise another type of fermions, including three charged particles with an electric charge of -1 and a spin of $1/2$, grouped into three generations: the electron (e), muon (μ), and tau (τ), along with their corresponding, electrically neutral neutrinos (ν_e, ν_μ, ν_τ). In the SM, neutrinos are assumed to be massless. Each lepton has a corresponding antiparticle with opposite quantum numbers. Leptons do not participate in the strong interaction but interact via the weak force and, if charged, via the EM force.

Gauge bosons Gauge bosons are the force carriers of the SM with a spin of one. The photon (γ) mediates the EM force and governs the interaction between charged particles. In particle physics, this force plays a crucial role in processes such as electron-positron annihilation and photon emission during particle collisions.

The weak force, mediated by the $W^\pm$ and Z^0 bosons with masses of $m_{W^\pm} = 80.37\,\text{GeV}$ and $m_{Z^0} = 91.19\,\text{GeV}$ [28–32], is responsible for processes such as the β decay in nuclear reactions in the case of the $W^\pm$. Furthermore, the $W^\pm$ plays the central role in particle interactions that change the flavour of quarks and leptons. The weak force is unique in that it violates parity (P) and charge-parity ($C\!P$) symmetries.

The strong force, mediated by massless gluons, binds quarks together to form colour-neutral hadrons and is described by QCD. However, in contrast to the photon, the

gluons carry themselves the charge of the symmetry group, which allows them to self-interact.

Higgs boson The Higgs boson with a mass of $m_H = 125.20\,\text{GeV}$ [2, 3] and a spin of zero is associated with the Higgs field, which fills the entire space. After the spontaneous symmetry breaking, the vev of the Higgs field becomes non-zero with a value of about 246 GeV. Through the interaction of particles with the Higgs field, they acquire their mass.

Fig. 2.1 provides an overview of the particles in the SM, illustrating the arrangement of fermions into three generations. The gauge bosons, along with the Higgs boson, are displayed on the right side. In the following, no charge is displayed for charged bosons if not stated otherwise.

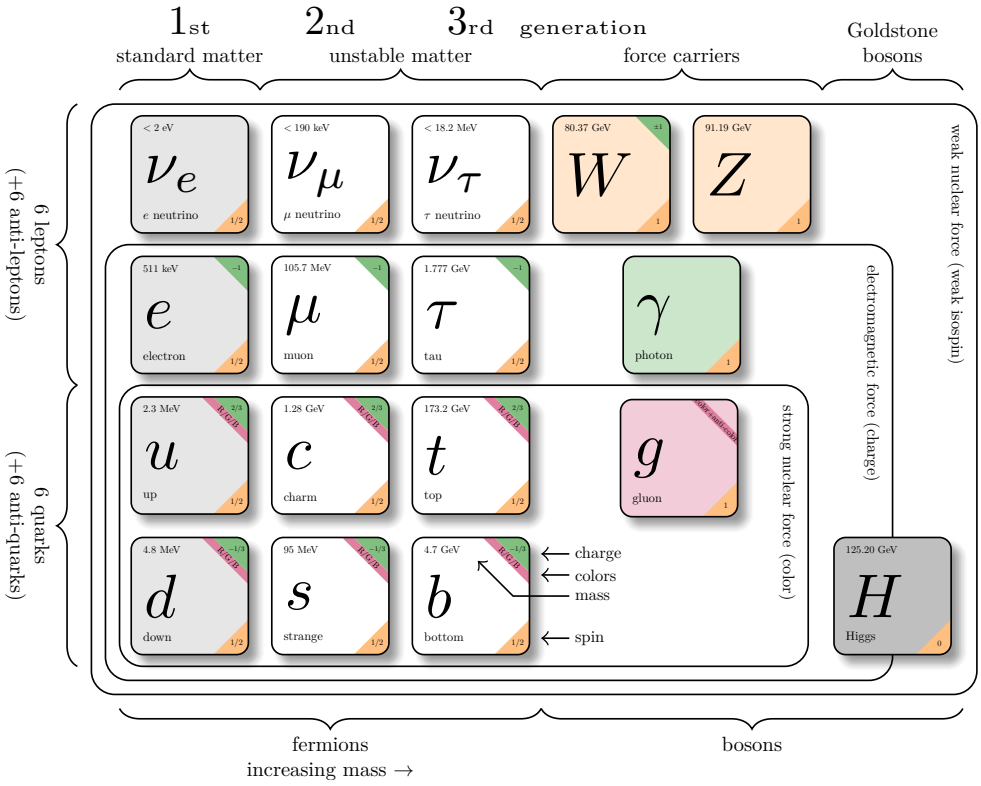

Figure 2.1: The particle content of the SM. The first three columns denote the three generations of fermions. The gauge bosons γ (EM force), $W^{\pm}$ and Z^0 (weak force), and the gluons g (strong force) are presented on the right side, along with the Higgs boson. The figure has been adapted from Ref. [33].

An essential element of the SM is the mixing between quark flavours, which has significant implications for weak interactions and *CP* violation. This mixing not only allows for transitions between beauty and top quarks but also enables the combination of measurements across both sectors, the main motivation of this thesis.

2.1.3 Quark mixing in the Standard Model

The quark mixing is mathematically described by the Cabibbo-Kobayashi-Maskawa (CKM) matrix V_{CKM}, a 3×3 unitary matrix that quantifies the probabilities of transitions between up-type and down-type quarks [34, 35]. The CKM matrix is given by

$$V_{\text{CKM}} = V_{\text{L}}^{u} \left(V_{\text{L}}^{d}\right)^{\dagger} = \begin{pmatrix} |V_{ud}| & |V_{us}| & |V_{ub}| \\ |V_{cd}| & |V_{cs}| & |V_{cb}| \\ |V_{td}| & |V_{ts}| & |V_{tb}| \end{pmatrix} = \begin{pmatrix} 0.97373 & 0.2243 & 0.00382 \\ 0.221 & 0.975 & 0.0408 \\ 0.0086 & 0.0415 & 1.014 \end{pmatrix} . \quad (2.3)$$

The elements are complex numbers, with their magnitudes dictating the strength of flavour-changing weak decays [28]. The CKM matrix can be parameterised by three mixing angles and one *CP*-violating phase. The values in Eq. (2.3) correspond to the measured values, with uncertainties omitted for simplicity. However, it should be noted that $|V_{tb}|$ is consistent with one given the overall uncertainty.

Direct measurements of $|V_{tb}|$ at the LHC by the ATLAS and CMS Collaborations have been obtained from single top-quark cross-section measurements [36]. Additionally, indirect and independent constraints can be derived from EW loop corrections, particularly from the $Z \to b\bar{b}$ process, without assuming the unitary of the CKM matrix. A rather old combination of results from LEP, the Stanford Linear Collider (SLC) Collaboration, Tevatron, and neutrino-scattering experiments yields $|V_{tb}| = 0.77^{+0.18}_{-0.24}$ [37], with large uncertainties. Further refinement of this constraint could potentially reveal deviations from SM predictions, indicating the presence of BSM physics. This is of particular interest, since the interplay between top-quark and beauty-quark observables provides complementary insights into the CKM-matrix elements, either in the modification of top-quark decay observables at the Wtb vertex or in top-quark and W-boson induced vertex corrections in virtual loops in $Zb\bar{b}$ EWPOs.

The interplay with separate focus on both quark sectors is provided in the following section.

2.2 Observables and Standard Model predictions

Experimental validation of the SM has been extensively conducted at facilities like the LEP and the LHC. At LEP, precise measurements of the mass and width of the Z boson, as well as the weak mixing angle, provided stringent tests of the EW sector. At the LHC, the discovery of the Higgs boson and the precise measurement of its mass and decay channels have provided strong validation of the SM, aligning closely with theoretical predictions. Additionally, the data have probed the quark sector by studying the beauty- and top-quark production and decay properties, while also exploring potential extensions to the SM through the search for new particles and interactions.

These experiments have not only confirmed the SM parameters with high precision. Furthermore, they have also provided information on potential areas where the model may be extended or modified, as is the case for A_{FB}^{b} in the process $Z \to b\bar{b}$ being in $2.9\,\sigma$ tension with to the SM prediction. In the following, an introduction of the most important experimental observables in the $Z \to b\bar{b}$ and $Z \to t\bar{t}$ processes is presented, also discussing the interplay between both as a probe for BSM physics.

2.2.1 $Z \to b\bar{b}$ as probe for BSM physics

An important test of the EW sector of the SM is the measurement of the coupling properties of the Z boson to third-generation quarks, which are expected to be the most sensitive to BSM physics contributions due to their high mass. Particularly at a COM energy of $\sqrt{s} = m_Z$, the coupling of the Z boson to the b quark is of interest and has been extensively studied at LEP [1]. This coupling is sensitive to the heaviest degrees of the SM in vertex-corrections including top-quarks, Higgs- and W-bosons in loops at the $Zb\bar{b}$ vertex. Notably, the coupling to the top quark may be particularly sensitive to effects from BSM physics at the Wtb decay and $Zt\bar{t}$ production vertices. The SM vertex-corrections (left panel) and potential modifications by an arbitrary operator (central and right panels), represented as a hashed circle, are illustrated in Fig. 2.2, respectively.

Moreover, the process shown in Fig. 2.2 is sensitive not only to corrections at the Wtb and $Zt\bar{t}$ vertex but also to modifications at the Z propagator, altering the self-energy of the Z boson. The modifications from fermion and boson loops are presented in Fig. 2.3. These effects are referred to as *radiative corrections* and would, in the presence of BSM physics, shift the mass relation between the W and Z boson. In turn, this would affect its coupling to other particles, leading to a modification of the decay width of the Z boson.

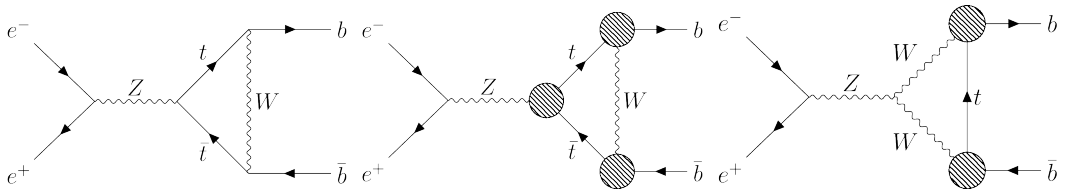

(a) SM vertex-correction. **(b)** Wtb-vertex modification. **(c)** Wtb-vertex modification.

Figure 2.2: Fig. (a) shows the SM vertex-correction from top quarks, while Figs. (b) and (c) include modifications at the $Zt\bar{t}$ and Wtb vertex, which might alter the SM prediction.

Isolating EW loop-corrections To isolate the effect of EW loop-corrections, the ratio of the partial b-quark decay-width to the total hadronic decay-width is defined, thereby cancelling out effects and possible modifications from radiative corrections

$$R_b = \frac{\Gamma_{b\bar{b}}}{\Gamma_{\text{hadr.}}} \,. \tag{2.4}$$

In the SM at tree level, the decay width for any fermion f can be expressed as

$$\Gamma_{f\bar{f}} = 3 \cdot \frac{G_{\text{F}} m_Z^3}{6\sqrt{2}\pi} \left(|a_f|^2 R_{Af} + |v_f|^2 R_{Vf} \right) + \Delta_{\text{EW/QCD}} \,, \tag{2.5}$$

where G_{F} is the Fermi constant [1]. The radiator factors R_{Af} and R_{Vf} account for final-state photon and gluon radiation, as well as non-zero fermion masses. The constant term $\Delta_{\text{EW/QCD}}$ represents the small contributions from non-factorisable EW and QCD corrections. Consequently, the total hadronic decay-width is given by $\Gamma_{\text{hadr.}} = \sum_{q \neq t} \Gamma_{q\bar{q}}$. In the presence of virtual top-quark loops, the coupling constants a_f and v_f are modified. Deviations of R_b from the SM prediction are signs of BSM signatures and can be inferred to originate from, for example, modifications of the Wtb vertex.

Axial-vector and vector interference The differential cross-section for the SM process $e^+e^- \to f\bar{f}$ can be expressed as

$$\frac{\mathrm{d}\sigma}{\mathrm{d}\cos(\theta_f)} \propto 1 + \cos^2(\theta_f) + \frac{8}{3} A_{\text{FB}}^f \cos(\theta_f) \,, \tag{2.6}$$

with the scattering angle $\cos(\theta_f)$ and the forward-backward asymmetry A_{FB}^f. The forward-backward asymmetry quantifies the parity violation of the neutral current, allowing for differentiation between the vector- and axial-vector couplings of the Z boson. In terms of asymmetry parameters of the initial state A_e and the final state

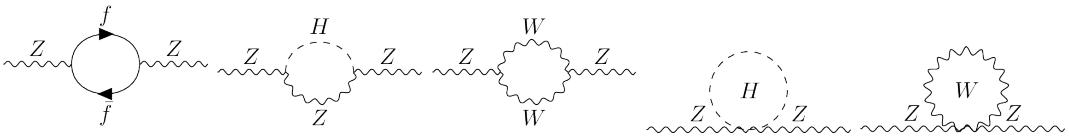

Figure 2.3: Radiative corrections from quantum loop-effects that modify the self energy of the Z boson. Adapted from Ref. [1].

A_f, A_{FB}^f can be written via

$$A_{\mathrm{FB}}^f = \frac{3}{4} A_e A_f \,, \quad \text{with} \quad A_f = \frac{2 v_f a_f}{v_f^2 + a_f^2} \,. \tag{2.7}$$

This relationship allows for the precise determination of $\sin^2(\theta_{\mathrm{W}})$ from Eq. (2.2). Although A_{FB}^{μ} is experimentally well-suited for determining $\sin^2(\theta_{\mathrm{W}})$, its sensitivity is approximately three times lower than that of the b quark due to the fractional charge of the b quark compared to charged leptons [38]. Because effects of modifications to the self-energy of the Z boson do not cancel in the ratio shown in Eq. (2.4), the effective Weinberg angle $\sin^2(\theta_{\mathrm{W}}^{\mathrm{eff}})$ is usually cited. It can be derived from the radiative corrections, where the relation to $\sin^2(\theta_{\mathrm{W}})$ is given by

$$\sin^2(\theta_{\mathrm{W}}^{\mathrm{eff}}) = \xi \sin^2(\theta_{\mathrm{W}}) \,, \tag{2.8}$$

where ξ represents the radiative correction factor. It is derived from loop corrections and has the form $\xi = 1 + \Delta\rho \cdot \mathrm{cotan}^2(\theta_{\mathrm{W}})$ [38]. Since the main contribution arises from fermion loops and the coupling is proportional to the fermion mass, only the dominant contribution from top quarks up to the second order is considered

$$\Delta\rho = 3x_t + 3x_t^2(19 - 2\pi^2) \,, \quad \text{with} \quad x_t = \frac{G_{\mathrm{F}} m_t^2}{8\sqrt{2}\pi^2} \,. \tag{2.9}$$

For a top-quark mass of 173.1 GeV and $\sin^2(\theta_{\mathrm{W}}) = 0.23089$, $\xi = 1.0312$. However, for simplicity, $\sin^2(\theta_{\mathrm{W}})$ is used throughout the thesis, if not otherwise stated.

At a potential next-generation high-luminosity, circular electron-positron collider, $\sin^2(\theta_{\mathrm{W}})$ is expected to be measured with exceptional precision, on the order of 10^{-6}, primarily using the forward-backward asymmetry of the muon [39]. However, with significant advancements in the measurement of A_{FB}^b at such a collider, the precision of determining $\sin^2(\theta_{\mathrm{W}})$ using A_{FB}^b could become comparable to that achieved with A_{FB}^{μ}, thereby providing a critical consistency check of the SM. This potential is explored in this thesis and discussed in Chap. 4.

2.2.2 Implication for top-quark observables

Deviations from the SM prediction in EWPOs such as R_b and A_{FB}^b have direct implications for observables related to the heaviest particle of the SM, the top quark.

This becomes especially relevant for a possible next-generation e^+e^- collider operating from COM energies of $\sqrt{s} = m_Z$ up to the top-quark pair-production threshold. With a mass of $m_t = (172.57 \pm 0.29)\,\text{GeV}$ [28], the top quark exists on a timescale that is shorter than that of the hadronisation process, enabling it to be studied as a quasi-free particle. This is a unique feature of the top quark among all quarks. Precise knowledge of its mass and coupling properties is vital, as these parameters are fundamental to the SM and may be influenced by BSM physics.

Although past and current hadron-collider experiments such as the Tevatron and the LHC have produced a large number of top quarks, the most precise measurements of its mass and decay width Γ_t are expected to come from e^+e^- collisions at the $t\bar{t}$ threshold. Mathematically, the top-quark width at next-to-leading order (NLO) is provided in Ref. [40] and is predicted to be

$$\Gamma_t = \frac{G_\text{F} m_t^3}{8\sqrt{2}\pi} \left(1 - x^2\right)^2 \left(1 + 2x^2\right) \cdot \left(1 - \frac{2\alpha_\text{S}}{3\pi}\left(\frac{2\pi^2}{3} - \frac{5}{2}\right)\right) , \tag{2.10}$$

assuming that $|V_{tb}| \gg |V_{td}|, |V_{ts}|$ and neglecting terms of the order ${}^{m_b^2}/_{m_t^2}$. Here, α_S is the strong coupling constant and $x = {}^{m_W}/_{m_t}$. Since the decay of the top quark is predominantly to a W boson with an associated b quark, there are three main decay channels of a $t\bar{t}$ pair, depending on the decay of the W boson

- Fully hadronic (45.7 %): $t\bar{t} \to W^+ b W^- \bar{b} \to q\bar{q}' b q'' \bar{q}''' \bar{b}$
- Semileptonic (43.8 %): $t\bar{t} \to W^+ b W^- \bar{b} \to q\bar{q}' b \ell \nu_\ell \bar{b}$
- Dileptonic (10.5 %): $t\bar{t} \to W^+ b W^- \bar{b} \to \ell^+ \nu_\ell b \ell'^- \bar{\nu}_{\ell'} \bar{b}$

Here, the quark flavours in the final state can be $[u, d, s, c]$ and ℓ represents all charged lepton flavours.

It might be noted here that several definitions of the top-quark mass exist: the pole mass, which is associated with the mass of a stable heavy-quark, the Monte Carlo (MC) mass, which is used in simulated processes and drives event kinematics, and the renormalisation mass, often referred to as the $\overline{\text{MS}}$ mass, which is a theoretically precise, scale-dependent quantity used in higher-order calculations in QFT [41]. With a $t\bar{t}$ production threshold scan as shown in Fig. 2.4, the pole mass and width could be measured with a precision of $\mathcal{O}(10\,\text{MeV})$ from an interpolation to the cross-section measurement, which is shown in red, and the measured points in black. Variations in these parameters would directly impact the cross section, as depicted in grey and teal curves that represent changes in m_t and Γ_t, respectively. However, in the following and throughout this thesis, no distinction has been made between the different top-quark mass definitions.

Beyond measuring the top-quark mass and decay width, which are fundamental parameters of the SM, extensive studies on various properties of the top quark have been conducted at the Tevatron and LHC. Production- and decay-specific observables,

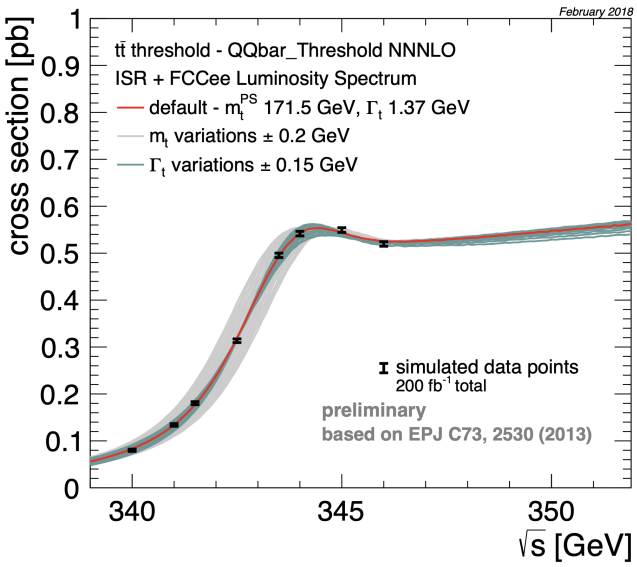

Figure 2.4: The $t\bar{t}$ cross section as a function of the COM energy, where fundamental SM parameters can be derived from a fit (red line) to the measured values (black). Modifications of m_t and Γ_t directly affect the shape of the cross-section curve.

such as the forward-backward asymmetry [42], the correlation of the $t\bar{t}$ spins [43, 44], and Wtb vertex-properties (including the helicity of the W boson [45, 46]) have been measured with high precision.

For the Wtb vertex, the SM predicts a $V-A$ charged-current interaction of the weak force, given by $i\frac{g}{\sqrt{2}}V_{tb}\gamma^{\mu}\frac{1}{2}(1-\gamma_5)$, which requires b quarks[1] to be left-handed. This allows the W boson to be either right-handed (spin parallel to the momentum direction, index R) or longitudinal (index L) at leading order (LO), meaning without any gluon radiation. The fraction of each polarisation is described in Ref. [47] by

$$F_{\mathrm{L}} = \frac{1}{1+2x^2} \approx 0.7\,, \quad F_{\mathrm{R}} = \frac{2x^2}{1+2x^2} \approx 0.3\,, \quad F_0 = 0\,. \tag{2.11}$$

Potential modifications of the $Zt\bar{t}$ and Wtb vertex structures, which would then also manifest in EWPOs, would therefore also influence top-quark observables. However, improving the precision of $t\bar{t}$ measurements is crucial, and this is where the next-generation e^+e^- high-luminosity collider plays a vital role.

In this thesis, recent measurements of top-quark-related observables performed at LHC are reviewed with a focus on the reconstruction of the $t\bar{t}$ system in an e^+e^- collider to derive the expected measurement uncertainties. Furthermore, these uncertainties are used to constrain the free parameters of a higher-dimensional extension of the

[1] In the limit of massless b quarks.

SM. This extension is theoretically described by EFTs, which allows for a global assessment of deviations from SM predictions. The principle of EFTs and their application to this analysis are described in the following section.

2.3 Effective Field Theories

The SM has consistently demonstrated its predictive power and precision across a multitude of observables and energy scales. To date, no substantial discrepancies have been observed between the experimental measurements and SM predictions. However, there are indications that it may be incomplete, as it does not account for all observable phenomena in the universe. In particular, cosmological observations have motivated alternative theories aiming at explaining phenomena not described by the SM, such as dark matter [48, 49] and the dominance of matter compared to antimatter [50], but also other phenomena like neutrino oscillations that require massive neutrinos [51–54].

This inspired scientists to perform direct searches for particles that are currently not described within the SM, and that would show up as resonances in, for example, an invariant-mass spectrum. However, if these new particles are too massive to be produced within the current energy reach of colliders, no resonance would be observable within the accessible energy range. Despite this limitation, their signatures might still be evident as modifications in the tails of the observable spectrum. EFTs enable the comparison of experimentally measured processes with SM predictions, providing a framework to test for BSM physics signatures even within the current energy limits. Fig. 2.5 illustrates this concept. The black curve represents the expected SM behaviour of an observable, such as the invariant mass. A potential resonance due to a new particle not included in the SM is shown in dark blue. Additionally, the effect of heavy BSM physics is indicated by the orange curve, showing a modification in the tail of the observable spectrum, where the resonance peak lies beyond the current energy reach. Both searches for lighter resonances [55–57] and the investigation of altered distribution tails serve as methods to quantify the effects of BSM physics [58, 59].

The following section presents the concept of EFTs and their application in the indirect search for BSM physics effects.

The beta decay The most prominent example of an effective theory is Fermi's theory of the β decay, formulated in the 1930s [60]. Fermi described the neutron decay $n \to p + e^- + \bar{\nu}_e$ as a point-like interaction, with theoretical predictions that matched his observations. Following the development of the weak-interaction theory, this process was understood as the conversion of a down quark in the neutron to an up quark via the exchange of a W boson, followed by the subsequent decay

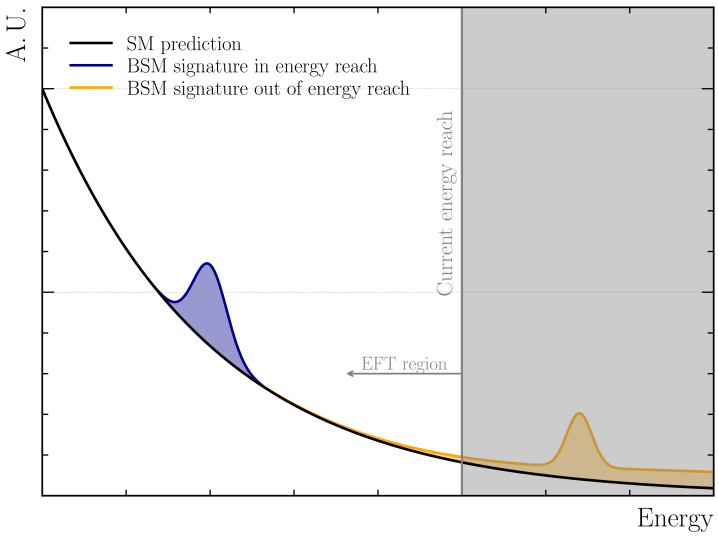

Figure 2.5: A sketched representation of direct resonance production in comparison to a modification of the tail of the distribution from EFT operators in searches for BSM signatures.

into an electron and an electron neutrino. Given that the mass of the W boson is significantly higher than the energy scale of the β decay, the point-like interaction initially described by Fermi was, in fact, an effective description of the underlying process.

Application in collider searches A similar approach can be applied on a larger energy scale than the W mass, specifically for energy scales beyond accessibility in high-energy collider experiments like the LHC and future e^+e^- Higgs factories, which operate from the Z-boson mass-scale up to several TeV. Since no significant deviation from the SM prediction has been found so far, the SM could be considered as a low-energy effective theory of a more general theory, which exists at energy scales Λ currently inaccessible with particle colliders. One popular parameterisation of BSM effects within the SM framework is the SMEFT, described in more detail below.

2.3.1 The Standard Model Effective Field Theory

The energy scale Λ in the SMEFT is expected to be above the Higgs vev with $v = 246\,\text{GeV}$. Consequently, the effective Lagrangian is built up from effective operators O_i that respect the SM gauge symmetries and are formed from SM fields. Since the mass dimension d of the SM Lagrangian is four, higher-dimensional operators with

$d > 4$ are suppressed by the BSM scale $\Lambda^{(4-d)}$. Notably, there is only one dimension-five operator that gives rise to Majorana neutrino-masses and does not conserve lepton number, which is a characteristic of dimension-even operators. Therefore, the leading contributions in SMEFT come from dimension-six operators, which are linearly added to the SM Lagrangian $\mathcal{L}_{\text{SM}}$ to build the SMEFT Lagrangian

$$\mathcal{L}_{\text{SMEFT}} = \mathcal{L}_{\text{SM}} + \Lambda^{-2} \sum_i C_i O_i^{(6)} + \mathcal{O}\left(\Lambda^{-4}\right) , \tag{2.12}$$

with the operator strengths C_i, also referred to as *Wilson coefficient*. Assuming baryon-number conservation, 59 independent operators exist in the so-called Warsaw basis [61]. When including all possible flavour combinations, there are 2499 dimension-six operators, although only a subset has a sizeable impact on observables accessible at collider experiments. Observable predictions can be made by evaluating the matrix element $\mathcal{M}$ from the SMEFT Lagrangian in Eq. (2.12). From $\mathcal{M}$, the cross section σ can be obtained from $|\mathcal{M}|^2$ to

$$\sigma_{\text{SMEFT}} = \sigma_{\text{SM}} + \Lambda^{-2} \sum_i C_i \sigma^{i\text{-int.}} + \Lambda^{-4} \sum_{i \leq j} C_i C_j \sigma^{ij\text{-BSM}} . \tag{2.13}$$

In this equation, σ_{SM} represents the SM part, and the squaring leads to interference terms denoted by $\sigma^{i\text{-int.}}$. The subordinate BSM contribution arises from the pure BSM term $\sigma^{ij\text{-BSM}}$, which is suppressed by Λ^{-4}. In the following, the rescaled Wilson coefficients $\tilde{C}_i$ are used, which are defined as

$$\tilde{C}_i = \frac{v^2}{\Lambda^2} C_i \, . \tag{2.14}$$

As pointed out, BSM effects are expected to occur on an energy scale much higher than v. This makes the heaviest known particle, the top quark, a promising probe for new-physics effects. Many searches at LHC have focused in recent years on BSM effects in the top-quark sector, also utilising the concept of EFTs [62–64]. Since no signs of BSM physics have been found so far, a focus of this thesis is placed on deriving constraints on the Wilson coefficients related to operators sensitive to top-quark observables at a possible future Higgs factory, the FCC-ee. The FCC-ee's physics motivation and further details are given in Chap. 3.

Eight operators in accordance with those from Ref. [65] following the notation from Ref. [66] are considered in top-quark processes at FCC-ee via $e^+e^- \to t\bar{t}$, which are given in the Warsaw basis before spontaneous symmetry breaking. Out of these eight operators, four affect bosonic interactions of the top quark in addition to four

four-fermion operators.

Bosonic operators

$$\begin{aligned} O_{tW} &= (\bar{q}_{\mathrm{L}}\sigma^{\mu\nu}t_{\mathrm{R}})\tau^I\tilde{\varphi}W^I_{\mu\nu} \\ O_{tZ} &= \cos(\theta_{\mathrm{W}})O_{tW} - \sin(\theta_{\mathrm{W}})(\bar{q}_{\mathrm{L}}\sigma^{\mu\nu}t_{\mathrm{R}})\tilde{\varphi}B_{\mu\nu} \\ O^{(-)}_{\varphi Q} &= \left(\varphi^\dagger \mathrm{i}\overleftrightarrow{D}_\mu\varphi\right)(\bar{q}_{\mathrm{L}}\gamma^\mu q_{\mathrm{L}}) - \left(\varphi^\dagger \mathrm{i}\overleftrightarrow{D}_\mu\varphi\right)(\bar{q}_{\mathrm{L}}\tau^I\gamma^\mu q_{\mathrm{L}}) \\ O_{\varphi t} &= \left(\varphi^\dagger \mathrm{i}\overleftrightarrow{D}_\mu\varphi\right)(\bar{t}_{\mathrm{R}}\gamma^\mu t_{\mathrm{R}}) \end{aligned} \tag{2.15}$$

Four-fermion operators

$$\begin{aligned} O^{(1)}_{te} &= (\bar{e}_{\mathrm{R}}\gamma_\mu e_{\mathrm{R}})(\bar{t}_{\mathrm{R}}\gamma^\mu t_{\mathrm{R}}) \\ O^{(1)}_{tl} &= (\bar{l}_{\mathrm{L}}\gamma_\mu l_{\mathrm{L}})(\bar{t}_{\mathrm{R}}\gamma^\mu t_{\mathrm{R}}) \\ O^{(1)}_{Qe} &= (\bar{e}_{\mathrm{R}}\gamma_\mu e_{\mathrm{R}})(\bar{q}_{\mathrm{R}}\gamma^\mu q_{\mathrm{R}}) \\ O^{(-1)}_{Ql} &= (\bar{l}_{\mathrm{L}}\gamma_\mu l_{\mathrm{L}})(\bar{q}_{\mathrm{L}}\gamma^\mu q_{\mathrm{L}}) - (\bar{l}_{\mathrm{L}}\gamma_\mu\tau^I l_{\mathrm{L}})(\bar{q}_{\mathrm{L}}\gamma^\mu\tau^I q_{\mathrm{L}}) \end{aligned} \tag{2.16}$$

In Eqs. (2.15) and (2.16), q_{L} and l_{L} are the $\mathrm{SU}(2)_{\mathrm{L}}$ quark and lepton doublets, while u_{R} and e_{R} are the up-type quarks and charged leptons of the same symmetry group. The Higgs doublet is φ and the field strength tensors of the $\mathrm{U}(1)_{\mathrm{Y}}$ and $\mathrm{SU}(2)_{\mathrm{L}}$ symmetry groups are given as $B_{\mu\nu}$ and $W^I_{\mu\nu}$, respectively. The Pauli matrices are denoted as σ^I and τ^I is defined as $\tau^I = \sigma^I/2$. The gamma matrix is given as γ_μ.

The sensitivities of different top quark observables are derived in Chap. 5 and the fit setup to extract limits on the respective Wilson coefficients is described in detail in Chap. 6.

3 The FCC project at CERN

This chapter provides a comprehensive outline of the FCC project at CERN with a focus on the lepton-collider stage and its physics potential, discussed in Sec. 3.1. An overview of current detector concepts is presented in Sec. 3.2 along with details about the simulated event samples utilised in this thesis, described in Sec. 3.3. The chapter concludes with a description of general objects and experimental methods in Sec. 3.4.

3.1 The landscape of future Higgs factories

Following the discovery of the Higgs boson in 2012, the *European Strategy for Particle Physics* issued an update in 2013 [67], prioritising the development of a high-luminosity phase of the LHC, known as the HL-LHC. However, due to the absence of BSM physics signatures at the LHC thus far, the 2020 update redirected focus towards an electron-positron Higgs factory as the next collider [68]. Current initiatives in various future Higgs factories have been unified under the *European Strategy for Particle Physics*, preparing for the post-LHC era. Looking further ahead, Europe's goals include operating a proton-proton collider in the 100 TeV energy range. Multiple proposals have emerged, and this section explores these projects in detail.

In general, two main concepts for a future Higgs factory are currently under discussion: linear and circular colliders, both aiming for precise measurements of Higgs-boson properties and detecting subtle deviations from SM predictions.

Linear Higgs factories Current discussions on linear-collider designs include the International Linear Collider (ILC) [69–73], the Compact Linear Collider (CLIC) [74], and the latest proposal, the Cool Copper Collider (C^3) [75, 76]. Their designs initially plan to operate at $\sqrt{s} = 250\,\text{GeV}$, with potential upgrades to $\sqrt{s} = 500\,\text{GeV}$ for the ILC and to $\sqrt{s} = 550\,\text{GeV}$ for the C^3. The CLIC concept follows a different strategy, starting at the $t\bar{t}$ energy threshold with $\sqrt{s} = 350\,\text{GeV}$ to $\sqrt{s} = 380\,\text{GeV}$, and extending to higher energies of $\sqrt{s} = 1.5\,\text{TeV}$ and $\sqrt{s} = 3\,\text{TeV}$. These high-energy phases would enable precise measurements of the top-Yukawa coupling via $t\bar{t}H$ production and the Higgs self-coupling with up to 10 % precision. Additionally, a linear electron-positron collider can provide longitudinally polarised electron and

positron beams, with polarisation levels up to $\pm 80\,\%$ and $\mp 30\,\%$ for the electron and positron beams, respectively. This capability allows for the measurement of forward-backward asymmetry, left-right asymmetry, and the disentanglement of several dimension-six operators.

Circular Higgs factories The two circular electron-positron collider designs, the FCC-ee at CERN and the Circular Electron-Positron Collider (CEPC) in China [77], cover a similar energy range and share most of their operational plans and modes. Unlike linear-collider concepts, these designs allow for the study of all SM particles with high precision at a single machine, by running from the $\sqrt{s} = m_Z$ (Z pole) up to the $t\bar{t}$ energy threshold. This capability extends the physics programme far beyond Higgs-boson studies. Additionally, multiple detectors can be hosted at several interaction points (IPs), facilitating the confirmation of findings, similar to the LHC. However, allowing operation at the $t\bar{t}$ threshold requires a collider circumference of $(80 - 100)\,\text{km}$. In the following, the FCC-ee concept, including machine parameters and its physics motivation, is described.

3.1.1 The FCC-ee

Proposed in a 91 km tunnel in the Geneva region that spans the border between Switzerland and France, the FCC project is part of a long-term European vision extending until the end of this century. Its goal is to precisely measure the properties and interactions of all SM particles, initially serving as an e^+e^- Higgs factory, with complementary plans for a second phase as a pp-collider (FCC-hh) within the same tunnel with energy reaches up to 100 TeV.

The concept of such an electron-positron machine, with a circumference ranging from $(80 - 100)\,\text{km}$, was initiated in 2012 [78] and was originally named Tera-LEP (TLEP). However, the first Conceptual Design Report (CDR) under the name FCC was published in 2018 [10, 11, 79]. The current operational plan includes 16 years of FCC-ee activity, followed by a 10-year break to install the hadron collider in the FCC tunnel, concluding with a 25-year period as a pp collider. The ongoing feasibility study is anticipated to conclude in 2025, with a decision expected from the CERN Member States and international partners in 2027. The start of operations is foreseen in the mid-2040s.

FCC-ee: the machine The primary run-plan scenario for FCC-ee initiates an extensive programme of physics research, beginning at the Z pole, progressing through the WW and ZH thresholds, and reaching the $t\bar{t}$ energy frontier, with four IPs planned. The initial estimates of the total expected event statistics and luminosities at the various energy stages are summarised in Tab. 3.1. Commissioning

Table 3.1: Baseline FCC-ee program for 16 years of operation from the Z pole up to the $t\bar{t}$ energy threshold.

	$\boldsymbol{Z}$		$\boldsymbol{WW}$		$\boldsymbol{ZH}$	$\boldsymbol{t\bar{t}}$	
$\sqrt{s}$ / GeV	88, 91	94	157, 163		240	$340-350$	365
Run time / years	2	2	2	tbd.	3	1	4
$\frac{\int \mathcal{L}}{\text{year}} \Big/ \text{ab}^{-1}$	34, 68	4.8	9.6	2.4	0.36	0.58	
Total # events	$6 \cdot 10^{12}$		$2.4 \cdot 10^8$		$1.45 \cdot 10^6$	$1.9 \cdot 10^6$	

phases and limited efficiencies during data collection periods have been considered. Recently, different run plans have been proposed:

1. Z, WW, ZH, $t\bar{t}$, or
2. ZH, WW, Z, $t\bar{t}$.

In both scenarios, the Higgs-boson physics programme is prioritised, which originates from the significant potential for BSM physics discoveries through the study of Higgs-boson interactions, given its coupling to all massive particles within the SM. Nevertheless, runs at the Z pole are essential to accurately calibrate the machine and the tools for higher-energy runs. This also involves accurately determining the COM energy using the concept of resonant depolarisation (RD) [39, 80]. This method is employed to precisely measure the COM energy at the Z pole and the WW threshold and is essential for a potential measurement of the s-channel $e^+e^- \to H$ cross section, which is sensitive to the Yukawa-coupling of the electron [81]. The exploration of this coupling is a distinct feature of a circular lepton collider, however, requiring the COM to be calibrated on the scale of the Higgs decay-width of $\Gamma_H = 3.7^{+1.9}_{-1.4}\,\text{MeV}$ [28]. This is one of the reasons for the need for a large circumference, in which the COM energy is expressed as

$$\sqrt{s} = 2\sqrt{E_{e^+}E_{e^-}}\cos\left(\frac{\alpha}{2}\right) , \tag{3.1}$$

where $E_{e^\pm}$ are the beam energies, and α is the crossing angle of the beams. However, this approach has an inherent limitation due to the beam-energy spread (BES) $\sigma(E_{e^\pm})$, which increases with the beam energy as $\sigma(E_{e^\pm}) \sim {}^{E_{e^\pm}}\!/_{r}$ and decreases with the bending radius r of the accelerator.

RD has already contributed to the success of the LEP programme [82] and enabled precise measurements of the Z-boson mass and decay width up to the 2 MeV level [1]. The principle of RD relies on the Sokolov-Ternov effect [83], which describes the likelihood that the spin of an electron or positron aligns parallel or antiparallel with the direction of an external magnetic field. Through spin-flipping synchrotron radiation emission, the slightly more energetic antiparallel state is preferred, resulting

in a transverse polarisation of approximately $(5-10)\,\%$, as observed at LEP [82]. The electron's spin then precesses around the vertical direction with a precession tune f_s, which itself depends on the electron energy via

$$f_s = E_{e^-} \frac{(g_e - 2)}{2 m_e c^2}\,, \tag{3.2}$$

where $(g_e - 2)/2$ is the gyromagnetic ratio and c is the speed of light [84]. By horizontally exciting the spins at the narrow spin-tune resonance f_s, the polarisation is disrupted, allowing for the precise measurement of the average beam energy by scanning the depolarisation frequency. Since a sufficient level of polarisation can be achieved for a maximum BES of approximately 55 MeV, this method is only applicable up to the WW threshold for beam-energy measurement.

Methods for determining $\sqrt{s}$ beyond the WW threshold rely on radiative fermion pairs from $e^+e^- \to Z\gamma$ with an undetected photon and the subsequent decay of the Z boson to a pair of fermions. At the ZH energy at $\sqrt{s} = 240\,\text{GeV}$, this technique leads to a precision on the COM energy of 1.7 MeV. At the $t\bar{t}$ energy frontier, the COM-energy measurement can be supported by the reconstruction of about two million $e^+e^- \to WW$ events in the fully hadronic and semileptonic decay channel, leading to a precision of approximately 5 MeV [39].

Many EWPOs rely on a highly precise determination of $\sqrt{s}$, which becomes a significant source of systematic uncertainty due to the high statistics of $\mathcal{O}(10^{12})$ Z decays and $\mathcal{O}(10^8)$ WW events. However, it has been shown that with the attainable precision, EWPOs such as m_Z and Γ_Z can be measured with an accuracy of about 30 keV and 22 keV, respectively, considering statistical uncertainties around 4 keV [39].

FCC-ee: the physics case The motivation for the physics case of FCC-ee stems from the discovery of the Higgs boson and the desire for a deeper understanding of its couplings. Numerous unknowns around the Higgs boson remain and are likely to remain unresolved even after HL-LHC concludes its operations, such as the shape of the Higgs potential and the coupling to the first- and second-generation fermions. Furthermore, long-standing discrepancies between EWPO measurements and SM predictions identified by LEP persist, like it is the case for the b-quark forward-backward asymmetry A_{FB}^b with a tension of $2.9\,\sigma$. This necessitates a comprehensive exploration programme in the EW, QCD, and flavour sectors, including studies of the heaviest fermion of the SM, the top quark. A summarised and selected overview of the experimental precision of certain observables is provided in Tab. 3.2 [28, 85]. For the aforementioned observables, uncertainties can be reduced by at least an order of magnitude compared to current levels. The statistical precision will exceed the systematic precision, which, for mass- and decay-width measurements, is constrained by the accuracy of the COM or by QCD calculations, as in the case of m_t and Γ_t.

Table 3.2: Precision for a selection of observables at the Z pole, the WW and $t\bar{t}$ threshold. In most cases, systematic uncertainty is the limiting uncertainty, arising from the knowledge of the COM energy and the order of QCD calculation. The table has been adapted from Ref. [85].

	Observable	Present precision ($\mu \pm \sigma_{\text{tot.}}$)	FCC-ee precision ($\sigma_{\text{stat.}} \pm \sigma_{\text{syst.}}$)
Z pole	m_Z / MeV	91187.6 ± 2.1	0.004 ± 0.03
	Γ_Z / MeV	2495.5 ± 2.3	0.004 ± 0.02
	$\sin^2(\theta_{\text{W}}^{\text{eff}}) \cdot 10^6$	231480 ± 160	2 ± 2.4
	$R_b \cdot 10^5$	21629 ± 66	0.003 ± 0.6
	$A_{\text{FB}}^b \cdot 10^4$	9920 ± 16	0.02 ± 3
WW	m_W / MeV	80377 ± 12	0.25 ± 0.3
	Γ_W / MeV	2085 ± 42	1.2 ± 0.3
$t\bar{t}$	m_t / MeV	172690 ± 300	17 ± $\mathcal{O}(\sigma_{\text{stat.}})$
	Γ_t / MeV	1420 ± 190	45 ± $\mathcal{O}(\sigma_{\text{stat.}})$

However, the clean and well-controlled lepton-collider environment allows to search for subtle deviations from the SM predictions in multiple ways: this begins with EWPO studies at the Z pole, leveraging an extensive number of decays to investigate fundamental SM parameters like the weak mixing angle. It extends to measurements of the Higgs and W properties, the CKM matrix, and continues up to the $t\bar{t}$ threshold.

Moreover, the Z pole offers a comprehensive flavour-physics programme at no additional cost, providing nearly 10 times more $b\bar{b}$, $c\bar{c}$, and $\tau^+\tau^-$ pairs than the final statistics expected from Belle-II [85]. Table 3.3 lists the yields for the different particle species [86]. Compared to B factories, such as Belle-II operating at the J/ψ threshold,

Table 3.3: Number of flavoured particle species in units of 10^9 [86].

Particle species	B^0	B^+	B_s^0	Λ_b	B_c^+	$c\bar{c}$	$\tau^+\tau^-$
Yield / 10^9	370	370	90	80	2	720	200

the particle boost at the Z pole presents new opportunities for modes involving one or more neutrinos in their final state. The extended flight distance allows for an exquisite reconstruction of the visible particles. This advantage is beneficial not only for semileptonic decays, but also for advancing beyond traditional techniques in the field of EWPOs. These advancements will be examined in the context of R_b and A_{FB}^b in Chap. 4.

The operation at the ZH resonance at $\sqrt{s} = 240\,\text{GeV}$, where approximately two million Higgs bosons are produced via Higgsstrahlung, provides a Higgs-boson mass measurement from the recoiling charged leptons ℓ^+ and ℓ^- of the Z-boson decay without exclusively reconstructing the Higgs boson. The mass measurement is based

on the conservation of energy and momentum via

$$m_{\text{rec}} = s + m^2_{\ell^+\ell^-} - 2\sqrt{s}\,(E_{\ell^+} + E_{\ell^-})\ , \tag{3.3}$$

where $m_{\ell^+\ell^-}$ is the invariant dilepton-mass, and E_ℓ is the lepton energy. In the absence of initial-state radiation (ISR), BES, and with a perfect determination of the lepton kinematics, it follows that $m_{\text{rec}} = m_H$. This allows for the determination of m_H and the ZH cross-section σ_{ZH} with a precision of 6 MeV and 1 %, respectively, considering only the $Z \to \mu^+\mu^-$ decay-channel. Including all possible Z and H decay channels, the uncertainty improves to 2 MeV for m_H, compared to the current best value of 110 MeV [28, 87].

Operation at the $t\bar{t}$ threshold and slightly above requires similar detector and reconstruction requirements as at the ZH resonance. Both final states are characterised by numerous hadronic jets, leptons, and neutrinos. The clean experimental environment presents new opportunities for state-of-the-art flavour tagging and missing-energy reconstruction algorithms. Furthermore, knowledge of the initial state imposes stringent constraints on object reconstruction, ultimately enhancing the overall event-reconstruction precision. In the context of this thesis, this is particularly beneficial for reconstructing the dileptonic $t\bar{t}$ decay channel with two neutrinos in the final state. However, inspired by recent top-quark research at and above the threshold, primarily advanced within the linear-collider community for CLIC and ILC [88–91], it is essential to examine collider-specific characteristics such as reduced beamstrahlung (BS) and a lower accessible energy range.

In order to construct suitable detectors, requirements from physics concerning, for example, tracking, vertexing, and calorimetry, have to be identified. To establish a community-wide benchmark, particle-flow objects (PFOs) have been employed to examine, for instance, the performance of jet-clustering and tagging algorithms [92] or to analyse the decay patterns of long-lived particles [93]. However, such a precise machine presents not only experimental challenges but also theoretical calculation milestones, particularly at the $t\bar{t}$ threshold, where $\sigma_{t\bar{t}}$ must be adjusted for contributions from Coulomb-type interactions [94]. Both PFOs and theoretical challenges are briefly outlined and discussed below.

3.1.2 Particle-flow objects

PFOs represent an advanced technique for particle reconstruction and identification in events. Initially developed for the ALEPH experiment at LEP [95], this method has been further refined by the LHC experiments [96]. The approach involves integrating data from all subdetectors, such as the tracker and the calorimeter, to identify and reconstruct individual particles, including photons, leptons, and both charged and neutral hadrons. This method relies heavily on the calorimeter's spatial

granularity to precisely match energy deposits with tracking information. Research conducted at CLIC indicates that the jet-energy resolution achieved with PFOs falls within the $(3-4)\,\%$ range for energies between $\sqrt{s} = 240\,\text{GeV}$ and $365\,\text{GeV}$ [97]. This resolution helps to better distinguish the signal from the background, such as separating hadronic W and Z decays.

PFOs are particularly advantageous for identifying individual components within a hadronic jet. At the Z pole, the emphasis is primarily on particle identification (PID) and the vertex-reconstruction precision, which are crucial for flavour physics and spectroscopy [98]. The success of the flavour programme relies on the ability to effectively discriminate between electrons, pions, and photons, as well as to distinguish between photons from pions [99]. Additionally, the separation of pions and kaons, along with protons and neutral hadrons, is essential for $C\!P$ violation studies in $B_s^0 \to D_s^\pm K^\mp$ decays and for differentiating background events from $B_s^0 \to D_s^\pm \pi^\mp$ [100]. Various detector technologies are under consideration for PID, which has been utilised in a simplified form in Chap. 4.

One such technology is the Ring Imaging Cherenkov (RICH) detector, which differentiates particles by their Cherenkov angle; the angle of light emitted as a charged particle travels through a medium at a velocity greater than the speed of light in that medium. By measuring the Cherenkov angle, particle species can be identified in a momentum range from a few GeV up to around 40 GeV required at FCC-ee. It is currently used in the LHCb experiment [101]. Other options for particle separation, such as measuring the energy loss, $\mathrm{d}E/\mathrm{d}x$, or counting ionisation clusters achieve pion-kaon separations exceeding $3\,\sigma$ across a momentum range from $\mathcal{O}(\text{GeV})$ up to $\mathcal{O}(10\,\text{GeV})$ in the latter case [98, 102].

3.1.3 Theoretical challenges

The large dataset expected at the Z pole offers unparalleled statistical accuracy, necessitating the development of new methods to attain comparable systematic and theoretical precision. To effectively compare these high-precision measurements with SM predictions, where BSM effects might manifest as slight deviations, it is imperative that these predictions reach competitive precisions. Consequently, the theoretical challenges at the Z pole are substantial. It is essential to incorporate higher-order EW corrections up to next-to-next-to-leading order (NNLO) and to enhance the calculation of higher-order radiative corrections, such as those for the Z propagator. This includes complete two-loop corrections in the scattering process and full three-loop corrections in the decay processes.

Near the $t\bar{t}$ production threshold at approximately $2m_t$, the top and antitop quarks primarily interact via EM Coulomb forces due to their non-relativistic behaviour at this energy level. Although this non-relativistic aspect can be described up to NNLO

using an EFT approach, achieving the required accuracy requires extending to N^3LO to properly account for the non-resonant $e^+e^- \to W^+bW^-\bar{b}$ process without actual top quarks. Additionally, QED effects must be included at next-to-next-to-leading log (NNLL) to achieve the statistical precision of 17 MeV for the top-quark mass measurement from the $t\bar{t}$ lineshape [85].

Nevertheless, all measurements face a common challenge: The effectiveness of their physics programme is heavily based on the detectors intended for installation. For the FCC-ee, all detectors must operate within an energy range of about 300 GeV (from Z pole to $t\bar{t}$ energy threshold), although there is a community preference for specific detector designs, such as a flavour-physics detector similar to LHCb at the LHC. The various proposals for the FCC-ee, currently under active discussion, are outlined in the following section.

3.2 Detector concepts

As of now, two well-established detector concepts for the FCC-ee exist: the Innovative Detector for Electron-Positron Accelerators (IDEA) [103] and CLIC Like Detector (CLD) [104]. Recent studies have introduced a third concept, A Lepton Collider Experiment with Granular Calorimeter Read-Out (ALLEGRO) [105]. The following paragraphs discuss the detector models used in the analyses (IDEA and CLD), while the ALLEGRO concept is only briefly summarised. In general, all of these detectors share the typical structure used in collider experiments: a cylindrical barrel with an onion-like structure, closed with endcaps. This onion structure consists of subdetector systems that measure the momentum of charged particles by their bending radius in a magnetic field. Subsequently, EM and hadronic calorimeters stop electrons, photons, and hadrons to measure their energy. A surrounding solenoid generates the magnetic field necessary for the bending of particle trajectories. The outermost part is the muon detection system. The three detector concepts have similar dimensions, with lengths ranging from $(11 - 13)$ m and heights between $(10 - 12)$ m. A sketch of the IDEA and CLD detector concepts is shown in Fig. 3.1.

3.2.1 The IDEA detector concept

The IDEA detector concept is one of the detectors to define, implement, and validate the performance requirements from physics at the FCC-ee. It is described below.

Vertex determination is performed using a silicon vertex detector positioned near the IP in a cylindrical configuration around the beam pipe, as the tracks must be reconstructed before high-density materials measure the particle energy. It detects the ionisation of charged particles across five layers as they pass through, with the closest distance ranging from 1.2 cm to 31.5 cm. The track-resolution requirements for the

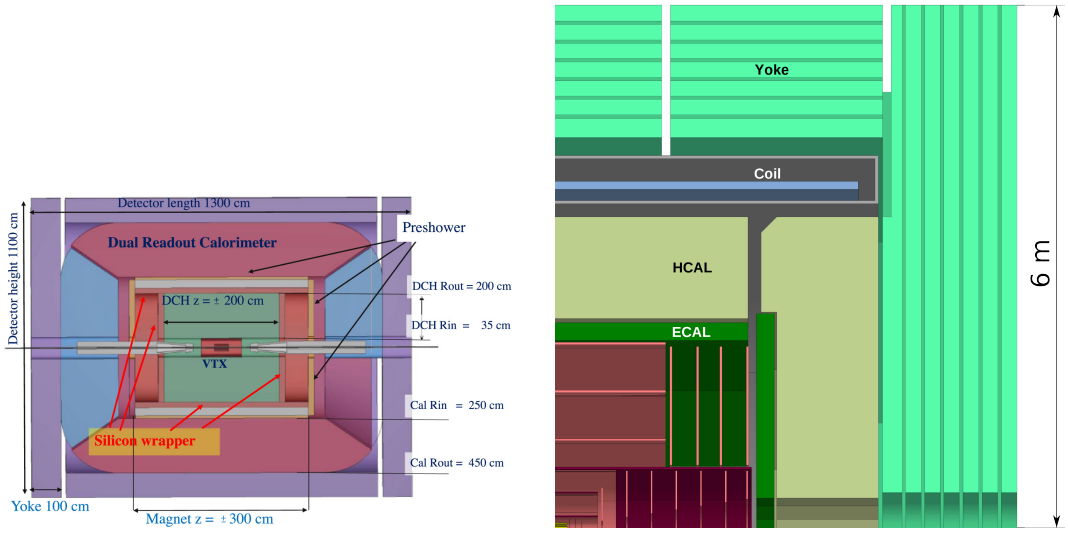

(a) IDEA detector concept [106].

(b) CLD detector concept [104].

Figure 3.1: Both detector concepts are currently under development with distinct studies to derive detector requirements. While the CLD concept has originally been designed with a focus on e^+e^- collisions in the TeV energy, the concept of IDEA is based on reducing the material budget and providing a good energy resolution.

vertex detector are dictated by the flavour-physics programme. Studies investigating the effect of track resolution on rare decays such as $B^0 \to K^*\tau^+\tau^-$ impose stringent and the most rigorous resolution requirements of a transverse vertex-resolution of 5 µm [107]. The drift chamber, composed of 112 wires with radii spanning from 35 cm to 200 cm, facilitates the smooth tracking of charged particles and is utilised for PID via energy loss measurements $^{\mathrm{d}E}/_{\mathrm{d}x}$ as the particles traverse the chamber. At the drift chamber's end, a final layer of silicon detector is placed, aiding in determining the endpoint and flight distance. The tracking system is encased by a superconducting solenoid, generating a 2 T magnetic field aligned with the beam axis.

Particles that interact hadronically and electromagnetically produce showers in the dual-readout calorimeter, which consists of seven layers of lead and fibres, with a total depth of 2 m. The position and energy of these showers are then measured using two sources: scintillation and Cherenkov light, emitted in the active material and collected by photodetectors. This results in a good energy resolution, which is currently being studied in the context of Higgs-boson mass measurements, where the energy resolution is expected to be within the range of the BES. This meets the required energy resolution of 3 % to distinguish between hadronically decaying W, Z, and Higgs bosons. In case of purely electromagnetically interacting particles, such as photons, the resolution, for example in the $H \to \gamma\gamma$ channel, is expected to be within the range of $^{20\,\%}/\sqrt{E}$ [108]. However, the flavour-physics programme at the Z pole

demands a much stricter EM energy-resolution of approximately $2\,\%/\sqrt{E}$, which may be attainable with crystal-based calorimeters using, for instance, high-Z scintillator grains (where Z represents the number of protons in the atom) [108, 109].

Because muons penetrate more deeply than other particles like electrons and hadrons, high-density materials such as iron are required to measure their tracks and infer their energy. To achieve high-precision muon detection, the detection system is positioned outside the tracker and calorimeter structures and comprises micro-Resistive WELL (µ-RWELL) detectors arranged in layers of chambers, which are integrated into the magnet return yoke. The µ-RWELL detector merges features of traditional gaseous detectors with micro-pattern technology, offering both high spatial resolution and high-rate capability.

3.2.2 The CLD detector concept

The primary parameters of the CLD detector are derived from studies intended for operation in a CLIC environment at $\sqrt{s} = 3\,\text{TeV}$, which is significantly beyond the energy reach of the FCC-ee. The initially developed CLICdet [110, 111] model has been modified to suit the different experimental conditions, encompassing COM energies ranging from 91 GeV to 365 GeV.

The tracking data are obtained from a full-silicon tracker system comprising a vertex detector and a tracker system. The vertex detector includes three barrel layers and seven forward discs with radii ranging from 1.75 cm to 5.8 cm. The silicon tracker system consists of an inner and an outer tracker, each with three additional barrel layers, supplemented by seven and four discs, respectively. Compared to the lightweight gaseous detector of IDEA, the track momentum resolution for CLD is slightly inferior, due to the constraints of multiple scattering within the tracker.

Unlike IDEA, which employs a single calorimeter to measure both the EM and hadronic components of, for example, a jet, CLD uses two separate calorimeters, optimised for particle-flow algorithms. This configuration aims to achieve the previously mentioned jet-energy resolution of $(3 - 4)\,\%$. The EM calorimeter spans radii from 215 cm to 235.2 cm in the barrel region and consists of 40 silicon-tungsten layers arranged in a sandwich structure, which has been identified to provide the best photon-energy resolution. The hadronic calorimeter comprises steel absorbers interspersed with 44 polystyrene scintillators. The radius of the barrel ranges from 240 cm to 356.6 cm. The muon detection system is integrated into the iron return yoke and consists of six layers of resistive-plate chambers, similar to those used in the CMS experiment [112]. The solenoid is located between the hadronic calorimeter and the iron yoke, generating a magnetic field limited to 2 T to meet the machine-detector interface requirements.

3.2.3 The ALLEGRO detector concept

The most recent concept on the market is the ALLEGRO detector design, featuring a tracking system composed of a silicon vertex detector and a gaseous drift chamber, encased in an outer layer of silicon for time-of-flight measurement. Various configurations are being considered for the EM calorimeter, including combinations of lead and liquid argon, or tungsten and liquid krypton. A solenoid that generates a magnetic field of 2 T is located between the EM and hadronic calorimeters, closely resembling that of CLD. The muon system is still under discussion.

3.3 Simulated samples

The absence of complete mathematical descriptions to model the theory of the SM up to the reconstruction of particles in a physical detector requires to employ MC simulation. These simulations are essential to mimic the physical phenomena and the dynamics of the particles within an experimental setting. The subsequent description outlines the procedure for event generation and detector-response simulation up to the stage where the final events are prepared for analysis, concluding with the details about the simulated datasets used throughout this thesis.

Centrally generated samples from the FCC community have been produced using the `WHIZARD` event generator [113]. `WHIZARD` models the hard-scattering process, where an electron and positron beam collide and produce other particles through fundamental interactions of, for example, SM. Consequently, the matrix elements using perturbative QFT are calculated, which involves determining Feynman diagrams from contributing processes at various orders. These can be of the lowest order (LO) or can include corrections of higher order in the coupling constant. It also decays the particles according to their branching fractions and probabilities up to the parton level. This implies that no hadronisation to the level of mesons and baryons is performed.

While `WHIZARD` can provide accurate estimates of the hard scattering, parton-shower software such as `PYTHIA` [114] is used to fully account for radiation effects from initial- (ISR) and/or final-state particles (FSR). The amount of radiation is determined by probabilistic distributions, effectively simulating the emission of soft and collinear radiation. `PYTHIA`'s hadronisation model, by default the Lund string model [115], then simulates the hadronisation of coloured partons into colour-neutral hadrons. In addition to the Lund string model, `PYTHIA` offers two additional hadronisation models: the antenna shower model (VINCIA [116]) and the dipole resummation (DIRE) parton shower [117], which includes various higher-order corrections to the parton shower.

The events that have been simulated, showered, and hadronised are subsequently processed to simulate the response of the detector. Detector simulation can be approached in two main ways: fast simulation using DELPHES [118] and full simulation using GEANT4 [119]. Fast simulation focuses on reducing computational demands by using parameterised response functions, whereas full simulation models the interaction of particles with each component of the detector material, making it computationally significantly more intensive but more precise at the same time. Finally, the trajectories and properties of the particles, derived from energy deposits in the calorimeters, are reconstructed. These can be further analysed using FCCAnalyses[1], a software toolkit for defining analysis chains, reading EDM4hep [120] input ROOT [121] files, and plotting, while utilising the RDataFrame format from ROOT as event processor.

As of now, the IDEA detector concept supports fast simulation, whereas fully simulated events can be generated for CLD. The next section provides a brief overview of the simulated events used in the analyses of Chap. 4 and 5.

3.3.1 Event simulation at the *Z* pole

The subsequent paragraphs provide an overview of the simulated events for the EWPOs at the Z pole, where PYTHIA8 has also been used to simulate the hard-scattering process. Various aspects that are particularly relevant to the observables are emphasised in the following.

In general, one sample has been used to evaluate the performance of the hemisphere-flavour tagger, whereas the application for the measurement for R_b and A_{FB}^b has required separate samples. The common sample has been chosen from the centrally generated, inclusive event production of $4 \cdot 10^7$ fast simulated $e^+e^- \to q\bar{q}$ events within IDEA. It is referred to as dataset (1). The different samples used to assess the systematic uncertainty for each EWPO separately are detailed below.

For R_b In case for R_b, the hemisphere-efficiency correlation has been evaluated from about 10^6 fully-simulated samples in CLD to take into account detector acceptance effects. It is referred to as the nominal dataset in this context. For the purpose of the study, double-tagging efficiencies must be evaluated, which involves ensuring that the hadronisation and subsequent decay of the b hadron are known in both hemispheres. For simplicity and to gain statistical precision, the decays in both hemispheres have been forced to be identical up to charge conjugation. The package EvtGen [122] has been used to simulate events with the following decays in the hemispheres:

- Hemisphere 1: $b \to B^+ \to [K^+\pi^-]_{\bar{D}^0}\,\pi^+$
- Hemisphere 2: $\bar{b} \to B^- \to [K^-\pi^+]_{D^0}\,\pi^-$

[1] https://hep-fcc.github.io/FCCAnalyses/

Alongside the nominal sample, simulation input parameters have been independently adjusted to initially evaluate the systematic uncertainty affecting the hemisphere-efficiency calculation. Therefore, the renormalisation scale, which is involved in the infinite absorption appearing in perturbative computations, has been altered from its nominal value of μ_{R} to $\mu_{\mathrm{R}}/\sqrt{2}$ and to $\sqrt{2}\mu_{\mathrm{R}}$. In addition, the b-fragmentation value might influence the exclusive b-hadron reconstruction. This parameter is adjustable in the Bowler modification [123] of the string-fragmentation function within the parton shower. It defines the proportion of energy allocated to the b quark in the fragmentation model. Starting from a nominal value of 0.855, it has been varied to 0.835 and 0.875. The final adjustment has been applied to the selection of the parton-shower model. In this instance, the DIRE parton shower has been used.

For A_{FB}^{b} To study the forward-backward asymmetry of the b quark, a dataset containing approximately $5 \cdot 10^7$ events has been simulated within the IDEA detector. This allows for stringent selection criteria while ensuring high statistical accuracy. The decay structure mirrors that used for the R_b dataset, with enforced decays in both hemispheres. Furthermore, the large number of events in this dataset has been used to validate the results of the hemisphere correlation for R_b from the full-simulation dataset.

3.3.2 Events at the $t\bar{t}$ energy

To interpolate the different $t\bar{t}$ observables as function of the Wilson coefficients, the EFT dependencies have been modelled using the `MadGraph5_aMC@NLO` (MG) [124] event generator in version `2.7.0`, along with the `dim6top_LO` [125] Universal Feyn-Rules Output (UFO) [126] model to simulate the EFT contributions. Further details can be found in Sec. 5.2.

To investigate the experimental precision in a FCC-ee setting, semi and dileptonic events at $\sqrt{s} = 365\,\mathrm{GeV}$ have been used from the centrally available events, which have been generated using `WHIZARD` and then showered with `PYTHIA8`. Alongside the nominal sample, alternative semileptonic $t\bar{t}$ samples have been produced using MG at LO and processed with `PYTHIA8`. Similar to the dataset (2), the renormalisation scale has been adjusted within the interval $[\mu_{\mathrm{R}}/2, 2\mu_{\mathrm{R}}]$, and the `DIRE` parton shower has been used as an alternative shower model. Driven by the accurate knowledge of the top-quark mass m_t from the $t\bar{t}$ threshold scan, the mass has been varied within $\pm 100\,\mathrm{MeV}$ around the pole mass. These samples allow for the study of the impact of different event generators and variations in the generator's input parameters. All detector responses for the $t\bar{t}$ samples have been parameterised using the IDEA card of `DELPHES`. An overview of all datasets is provided in Table 3.4.

Table 3.4: The tabular summary of all samples used throughout this thesis. The naming *semi-exclusive* refers to the exclusive decay of the semi and dileptonic decay of the W bosons.

Dataset and analysis	Simulation type	Exclusive/Inclusive	Sample size
(1) Hemisphere-tagger performance	Fast (IDEA)	Inclusive	$4 \cdot 10^7$
(2) Application for R_b	Full (CLD)	Exclusive	10^6
(3) Application for A_{FB}^b	Fast (IDEA)	Exclusive	$5 \cdot 10^7$
(4) $t\bar{t}$ EFT dependencies	Fast	Semi-exclusive	10^5
(5) $t\bar{t}$ observable precision	Fast (IDEA)	Semi-exclusive	$1.9 \cdot 10^6$

3.4 Excursion: common objects

The thesis places emphasis on two analysis chains, which are outlined at the two energy stages at $\sqrt{s} = 91\,\mathrm{GeV}$ and $\sqrt{s} = 365\,\mathrm{GeV}$. Despite the need for distinct reconstruction techniques for each analysis, both share common definitions of simulation stages, the utilisation of hadronic jets, and mathematical definitions to perform interpolations to, for example, invariant-mass spectra. Consequently, this section provides a concise overview of the object definitions and concludes with the fundamental concepts and clustering methods of hadronic jets.

Parton, particle, and object level A key feature of simulated events is to be able to identify their origins and identify their species. This allows the calculation of metrics such as reconstruction efficiencies and enables the comparison and isolation of detector effects. Here, various stages of the hadronisation and reconstruction process are used. Starting with the hard-scattering and parton-showering processes, particles prior to hadronisation are described at the *parton level*. At this stage, leptons, for instance, from leptonically decaying W bosons, have not yet emitted photons. However, photon emission of the initial-beam particles and gluon radiation from quarks have taken place at this stage.

The kinematics and interactions of both stable and unstable particles, such as hadrons (including pions, kaons, and protons), are described at the *particle level*. At this point, leptons have emitted photons.

The detection signatures of hadrons and leptons within the calorimetry system, along with their identification using additional data from the tracking system, are described at the *object level*. This stage is designed to replicate the detector response and simulate measurements within a real detector. Nonetheless, it is feasible to trace the particle's origin and conduct a truth-matching process. Furthermore, and as mentioned earlier, this has been used to identify the type of final-state particles. An

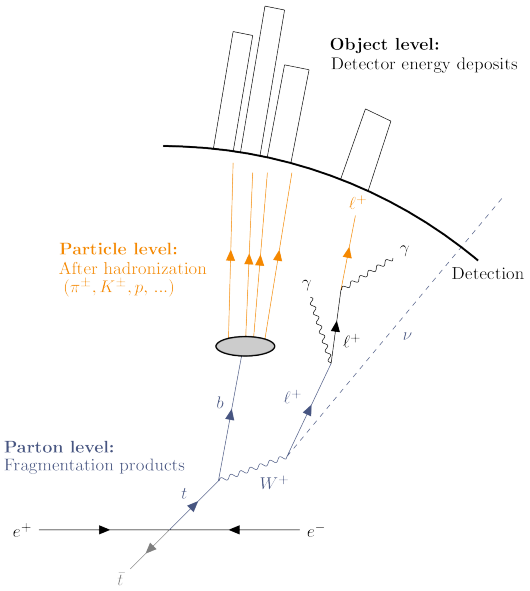

Figure 3.2: Definitions of the parton, particle, and object level using a top-quark decay as example. At parton level, the kinematics of particles from the hard-scattering process are described, and particle level refers to stable and unstable particles after the hadronisation process. At the object level, energy deposits and tracks from the tracking system are used to reconstruct the particles and quantities of interest. However, the PID has been taken from the link between the object and particle level.

illustration showing the various stages and their definitions used throughout this thesis is shown in Fig. 3.2.

Isolated leptons and photons In DELPHES, charged leptons are referred to as electrons and muons, since the tau-lepton decays before detection. The detection probability of charged leptons has been simulated to be 99 % over the tracker-acceptance range and a minimum transverse momentum p_{T}^{ℓ} of 0.5 GeV. In the case of photons, their reconstruction is only based on the information of the EM calorimeter, with reconstruction efficiencies of 99 % for candidates with $p_{\mathrm{T}}^{\gamma} \geq 0.5\,\mathrm{GeV}$. The isolation of leptons and photons is based on the activity in its vicinity, where the ratio of the summed p_{T} of particles that lie within a cone of radius 0.5 around the particle of interest and the p_{T} of that particle must be less than 0.5 [118].

Hadronic jets Hadronic jets (hereafter referred to as *jets*) are sequences of particles generated when quarks or gluons are emitted and are then hadronised to hadrons. These hadrons form a cascade that moves roughly in the same direction as the originating quark or gluon, resulting in a jet-like formation.

To study the reconstruction of top quarks or additional jets originating from high-energy gluons emitted by quarks, it is necessary to understand the underlying quark kinematics. Clustering algorithms are employed for this reconstruction. The anti-k_t algorithm [127] is a widely used clustering method in current experiments, such as those at the LHC which involve pp collisions. This algorithm generates cone-shaped jets that are less affected by the complex underlying environment with numerous particles in an event. These particles also result from multiple simultaneous collisions within the same event window, introducing extra particles that are not related to the primary collision of interest (pile-up). Due to the unpredictable number of these additional particles, jets are clustered into an indefinite number of jets per event, a process known as *inclusive* clustering. The anti-k_t algorithm is tailored for high-multiplicity settings in pp collisions and uses a distance measure d_{ij}, which is a quantitative measure to decide which particles should be grouped into jets. The distance metric depends on the transverse momentum p_T and a cone-radius parameter R, as follows

$$d_{ij} = \min\left(p_{\mathrm{T},i}^{-2}, p_{\mathrm{T},j}^{-2}\right) \frac{(y_i - y_j)^2 + (\phi_i - \phi_j)^2}{R^2} \,. \tag{3.4}$$

In Eq. (3.4), y_i and ϕ_i represent the rapidity and azimuth of particle i and j, respectively, with $i \neq j$. This definition is provided here as it has been used in the analysis of the b-quark forward-backward asymmetry.

Unlike the busy pp environment, the clean e^+e^- collision essentially generates no pile-up events and exhibits minimal hadronic background noise. In addition, the energy of the colliding particles is precisely known, enabling the application of energy and momentum conservation in the jet-clustering process. Consequently, the number of jets is more predictable, allowing the use of *exclusive* clustering with algorithms that also use the geometric properties of the jet constituents. The algorithm typically employed in e^+e^- collider experiments, such as LEP, is the Durham k_t algorithm [128], with a distance measure d_{ij} defined as

$$d_{ij} = \frac{2\min\left(E_i^2, E_j^2\right) \cdot \left(1 - \cos(\theta_{ij})\right)}{s} \,, \tag{3.5}$$

with $\cos(\theta_{ij})$ being the angle between particle i and j. Hadronic jets are defined both at the particle and object level, where the particle-level jet is built from all stable particles of the event, while the object-level jet is clustered from information of the detector response. The tools are provided in the `FastJet` software [129, 130].

Ultimately, it is essential not only to estimate the direction and energy of quarks and gluons using jets, but also to extract information about the underlying quark flavour. This process is known as *jet-flavour tagging* and typically employs multivariate methods to consider various aspects of the jet's constituents, such as secondary vertices, soft leptons within the jet, or the number of tracks associated with the jet. Nevertheless, flavour tagging must be tailored and calibrated to the specific

experimental conditions at different energy levels. This aspect has not been further explored; instead, within the reconstruction of the $t\bar{t}$ system, a constant efficiency has been applied to determine the true flavour of the jet.

Primary vertex (fitting) The primary vertex (PV) represents the location of the initial collision, leading to the creation of primary particles. It serves as a crucial reference point in an event, separating the particles and their trajectories from the collision from those arising from later decays, such as those of heavy hadrons. The method employed to identify the PV involves using a PV fitting algorithm, which is described in the following.

Initially, all event tracks are fitted to a common vertex, with each track assigned a unique quality χ^2-measure relative to the determined position. Through an iterative process, the track with the highest χ^2 value is excluded from the list, and the fit of the vertex is repeated until the highest χ^2 value of any track falls below a certain threshold. Using knowledge of the beam sizes to seed the initial vertex position can enhance the precision of the PV position, and this method has been employed throughout this thesis wherever a PV has been reconstructed. The PV distribution in $(x, y, z, t)^\top$ coordinates is modelled using a four-dimensional Gaussian distribution, derived from the beam's bunch sizes $(\delta_x, \delta_y, \delta_z)$. The bunch sizes and standard deviations of the Gaussian distribution for the two energy stages used in this thesis are provided in Tab. 3.5. The values listed below correspond to the so-called *winter2023* sample campaign, instead of the ones provided in the CDR report from 2019.

Table 3.5: Beam-spot parameters of the interaction region, separately for the Z pole and the $t\bar{t}$ energy threshold.

Component	$\sqrt{s} = 91\,\text{GeV}$	$\sqrt{s} = 365\,\text{GeV}$
(δ_x, σ_x) / µm	(8.4, 5.96)	(38.6, 27.3)
(δ_y, σ_y) / nm	(33.7, 23.8)	(69.1, 48.8)
(δ_z, σ_z) / mm	(15.4, 0.397)	(2.74, 1.33)

Fitting distributions In the analyses presented in the subsequent chapters, various distributions of invariant masses or resolutions have been interpolated with probability density functions. The mathematical expressions for these functions are provided in the next paragraph. Unless specified otherwise, the distributions have been fitted using an unbinned maximum likelihood method, which has been technically realised using the `zfit` package [131].

Gaussian The Gaussian distribution in its simplest form is given as

$$f(x;\mu,\sigma) = \frac{1}{\sqrt{2\pi\sigma^2}} \cdot \mathrm{e}^{-\frac{(x-\mu)^2}{2\sigma^2}} \,. \tag{3.6}$$

Eq. (3.6) can be generalised by adding multiple Gaussian distributions, each with its own standard deviation σ and either a common mean μ or distinct means. In this thesis, the summations of Gaussian distributions have used only common mean values.

(Double-sided) Crystal-Ball The Crystal-Ball probability density function is used to model distributions with a Gaussian core but also has a non-Gaussian tail, expressed with a power law. The tail can be either on one side (One-sided Crystal-Ball) or on both sides (Double-sided Crystal-Ball). It is particularly useful to model asymmetric deviations from the Gaussian shape in the tail regions. Its functional form is given via

$$f(x;\mu,\sigma,\alpha_{\mathrm{L}},n_{\mathrm{L}},\alpha_{\mathrm{R}},n_{\mathrm{R}}) = \begin{cases} A_{\mathrm{L}} \cdot (B_{\mathrm{L}} - \frac{x-\mu}{\sigma})^{-n_{\mathrm{L}}}\,, & \text{for } \frac{x-\mu}{\sigma} < -\alpha_{\mathrm{L}} \\ \mathrm{e}^{-\frac{(x-\mu)^2}{2\sigma^2}}, & \text{for } -\alpha_{\mathrm{L}} \leq \frac{x-\mu}{\sigma} \leq \alpha_{\mathrm{R}} \\ A_{\mathrm{R}} \cdot (B_{\mathrm{R}} - \frac{x-\mu}{\sigma})^{-n_{\mathrm{R}}}\,, & \text{for } \alpha_{\mathrm{R}} > \frac{x-\mu}{\sigma} \end{cases} \tag{3.7}$$

with

$$\begin{aligned} A_{\mathrm{L/R}} &= \left(\frac{n_{\mathrm{L/R}}}{\left|\alpha_{\mathrm{L/R}}\right|}\right)^{n} \cdot \mathrm{e}^{-\frac{\left|\alpha_{\mathrm{L/R}}\right|^2}{2}}\,, \\ B_{\mathrm{L/R}} &= \frac{n_{\mathrm{L/R}}}{\left|\alpha_{\mathrm{L/R}}\right|} - \left|\alpha_{\mathrm{L/R}}\right| \,. \end{aligned} \tag{3.8}$$

4 Ultra-pure EWPO measurements

The operation around and at the Z-boson mass, covering COM energies from 88 GeV, over 91 GeV up to 94 GeV, aims to precisely measure the Z lineshape to extract the width of the Z boson with a statistical precision of 4 keV. In 4 years of the foreseen operation, data that correspond to an integrated luminosity of $150\,\mathrm{ab}^{-1}$ are expected to be collected that reflect in approximately $6 \cdot 10^{12}$ Z decays. Beyond its role in precision EW measurements, the immense dataset provided by the FCC-ee at the Z pole offers the potential for discovery, including the identification of new long-lived [93] or axion-like [132] particles, as well as the detection of subtle deviations from SM predictions in EWPOs, whose precision benchmark is still set by measurements obtained from LEP. The couplings of the Z boson to quarks and leptons are therefore useful to directly probe BSM physics, but the abundant production of heavy flavours at the Z pole makes FCC-ee a multiple heavy-flavour factory as well: it is simultaneously a tau, a charm, and a beauty factory. Measurements of rare c- and b-hadron decays, as well as τ decays, will complement the EWPO constraints, offering a coherent picture of New Physics.

Fundamental SM parameters will be measured with exquisite statistical precision, such as $\sin^2(\theta_\mathrm{W})$, which can be inferred from the measurement of forward-backward asymmetries, arising from the vectorial-axial P-violating coupling of the Z boson to fermions. As described in Sec. 2.2.1, for the measurement of $\sin^2(\theta_\mathrm{W})$, the forward-backward asymmetry of the muon, as well as that of the b quark, have been used in measurements at LEP [133, 134]. The most precise projection for A^{μ}_{FB} at FCC-ee has been estimated to be $\sigma_{\mathrm{stat.}} \approx \sigma_{\mathrm{syst.}} = 2 \cdot 10^{-6}$ [39]. Although this leads to an exceptional precision in the determination of $\sin^2(\theta_\mathrm{W})$, however, it would require a precise validation in the case of a potential deviation from the SM prediction. This could be brought about by the forward-backward asymmetry of the b quark A^{b}_{FB}, which, among any other forward-backward asymmetry, shows the highest sensitivity to $\sin^2(\theta_\mathrm{W})$, as described in Sec. 2.2.1. Nevertheless, its precision at the Z pole is constrained by the systematic uncertainty.

Furthermore, the partial b-quark decay width with respect to all hadronic Z decays, R_b [28], provides direct access to vertex corrections at the $Zb\bar{b}$ vertex from top-quark and W-boson loops, since higher-order radiative corrections to the Z propagator cancel out in

$$R_b = \frac{\Gamma_{b\bar{b}}}{\Gamma_{Z\to\mathrm{had.}}} = 0.216\,29 \pm 0.000\,66\,. \tag{4.1}$$

This allows for unique tests of modifications to the Wtb coupling (as well as the indirect $Zt\bar{t}$ coupling), potentially offering a higher precision than any direct top-quark measurement. Although both observables will be measured with outstanding statistical precision, the limitations are given by the control over systematic uncertainties. In this chapter, a new measurement philosophy will be presented and discussed in detail. If not stated otherwise, the index $Z \rightarrow$ had as in Eq. (4.1) is replaced by simply stating Z as the index, which accounts for the hadronic fraction of Z-boson decays.

The chapter is organised as follows: first, the R_b and A_{FB}^b measurements are presented in their historical context, concluding with implications for the Tera-Z programme at FCC-ee in Sec. 4.1. Second, the need for a new identification technique of the hemisphere flavour (and charge) is motivated by introducing exclusive b-hadron reconstructions as b-hemisphere tagger in Sec. 4.2. Its performance is evaluated in Sec. 4.3. The specific use cases for the measurement of R_b and A_{FB}^b are described in Secs. 4.4 and 4.5, respectively. The chapter is closed in Sec. 4.6 with an outlook in Sec. 4.7.

4.1 Measurement principle and lessons learnt from history

Both b-quark observables, R_b and A_{FB}^b, share the need for an unambiguous identification of the quark flavour, also called *tag*. Although this is sufficient for R_b, for A_{FB}^b it is necessary to identify the charge of the quark and its direction. Since the most precise measurements have been made at LEP and SLAC Large Detector (SLD), it is worth looking back at the tagging techniques used at the time. Principally, two main methods of flavour identification have been used in decays of the Z boson, whose event topology is briefly highlighted before going into further detail of the tagging techniques used by the time.

4.1.1 Event topology and equations

A schematic view of a hadronic Z-boson decay is shown in Fig. 4.1. The initial quarks produced by the Z-boson decay can radiate high-energetic gluons before they hadronise and form at least two sprays of particles, which are indicated as cones in the figure. The hadronic decay products therefore emerge back-to-back from the IP (the reconstructed IP is called the PV).

The plane perpendicular to the direction of the thrust $\boldsymbol{T}$ defines the two hemispheres of the event, where the thrust vector is the vector that maximises the expression

$$\tilde{T} = \max_{\boldsymbol{T}} \left(\frac{\sum_i |\boldsymbol{p}_i \cdot \boldsymbol{T}|}{\sum_i |\boldsymbol{p}_i|} \right) , \tag{4.2}$$

with i running over all particles in the event with their momentum vector $\boldsymbol{p}$. The thrust axis in the first approximation models the direction of the initial quark and is shown as a green vector in Fig. 4.1. It has often been used at LEP in analyses of A_{FB}^{b} [134–137] or the strong coupling constant α_{S} [138].

For the measurement of R_b, the b-flavour identification of the hemispheres is required and is based on a *double-tag method*. This allows for the simultaneous determination of R_b as well as the b-tagging efficiency ε_b directly from the data. The number of single- and double-tagged events N_b and $N_{b\bar{b}}$ is given by

$$\begin{aligned} N_b &= 2N_Z \cdot (R_b \varepsilon_{b_{1,2}} + R_c \varepsilon_{c_{1,2}} + (1 - R_b - R_c)\varepsilon_{uds_{1,2}}) \,, \\ N_{b\bar{b}} &= \; N_Z \cdot (R_b \varepsilon_{b_1} \varepsilon_{b_2} C_b + R_c \varepsilon_{c_1} \varepsilon_{c_2} C_c + (1 - R_b - R_c)\varepsilon_{uds_1} \varepsilon_{uds_2} C_{uds}) \,. \end{aligned} \tag{4.3}$$

In Eq. (4.3), $\varepsilon_{i_{1,2}}$ and $\varepsilon_{i_1}\varepsilon_{i_2}$ are the single- and double-tagging efficiencies to identify the flavour of the quark i and C_i is the *hemisphere efficiency correlation* (further simply referred to as *hemisphere correlation*). The correlation term accounts for a biased tagging efficiency of the other hemisphere, if the first hemisphere has been identified to originate from a quark of flavour i. Its mathematical expression can be derived from Eq. (4.3)

$$C_i = \frac{\varepsilon_{i_1}\varepsilon_{i_2}}{\varepsilon^2_{i_{1,2}}} \,. \tag{4.4}$$

The efficiencies ε_{c_j} and ε_{uds_j} account for the mis-identification (ID) of a c- or light quark as b quark. Their size depends on the technique for tagging b quarks, where state-of-the-art methods are presented below. However, the impact of actual b quarks in the hemisphere from gluon radiations is discussed in Sec. 4.4 in the case of the novel approach introduced below.

While ε_{b_j} and R_b are determined from data, ε_{c_j} and ε_{uds_j} must be estimated from MC simulations. The same is true for C_b. Due to the small values of ε_{c_j} and ε_{uds_j}, C_c and C_{uds} have been assumed to be unity in the former measurements.

In addition to the simple knowledge of the flavour of the hemisphere, the charge information as well as the direction of the inital b quark have to be known with high precision for a measurement of the b-quark forward-backward asymmetry A_{FB}^{b}.

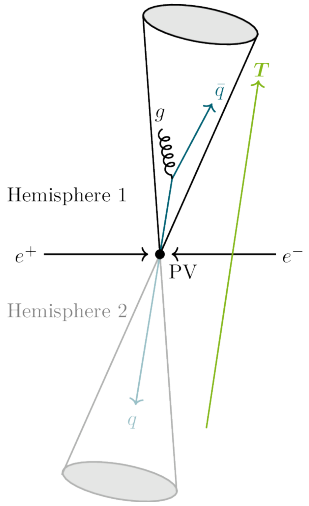

Figure 4.1: Sketch of a $Z \to q\bar{q}$ event.

For both observables, an effective reduction of systematic uncertainties to the scale of the statistical one for R_b and A_{FB}^{b} requires a more accurate b-hemisphere tagging. Therefore, the latest b-flavour

tagging techniques that have been used in measurements at LEP are discussed in the following paragraphs, and their limitations in an application at the Tera-Z programme at FCC-ee will be described afterwards. However, it must be stated that the main goal and challenge of tagging the flavour and charge of the hemisphere is to use flavour-specific properties of the hemispheres, such as longer lifetimes of b hadrons or higher masses, to reduce misidentification from $udsc$ physics as much as possible. Due to the similar physics properties of c quarks compared to b quarks (lifetime, semileptonic decays, etc.), the main challenge is therefore the suppression of the contribution of c -quarks compared to b quarks.

Lifetime-mass tag (hemisphere-flavour tag) The lifetime-mass tag combines two tags into a single one. The sole lifetime tag is based on the large displacement of the b hadron from the PV due to its comparatively long lifetime of about 1.6 ps and the boost at the Z pole. The displacement is calculated via

$$\langle L \rangle = \langle \beta\gamma \rangle c\tau, \tag{4.5}$$

with the mean $\beta\gamma$-factor of

$$\langle \beta\gamma \rangle = \frac{\langle p \rangle}{m_{\text{had.}}} = \frac{\sqrt{\langle 0.72\, E_{b\text{-quark}} \rangle^2 - m_{\text{had.}}^2}}{m_{\text{had.}}}\,. \tag{4.6}$$

In Eq. (4.6), $E_{b\text{-quark}} = 45.2\,\text{GeV}$, the mass of the hadron is $m_{\text{had.}}$ and the speed of light is $c = 299\,792\,458\,\text{m}\,\text{s}^{-1}$. In the following, the D^+ and B^+ meson have been taken to compare typical decay lengths at the Z pole

$$\begin{aligned} m_{D^+} &= 1869.66\,\text{MeV} \quad \Rightarrow \quad \langle L_{D^+} \rangle \approx 5.4\,\text{mm}\,, \\ m_{B^+} &= 5279.34\,\text{MeV} \quad \Rightarrow \quad \langle L_{B^+} \rangle \approx 3.0\,\text{mm}\,. \end{aligned} \tag{4.7}$$

Therefore, due to the similar decay lengths of b and c hadrons, additional information is required to purify the event selection. This information is taken from the invariant mass of the particles that form secondary vertices, since b hadrons have a significantly larger mass than c hadrons. The highest b-tagging purity following this flavour technique has been achieved by the OPAL Collaboration with 98.6 % with an efficiency of 29.6 % [139].

Lepton tagging (hemisphere-flavour and charge tag) The decay signatures of the heavy b- and c-hadrons can provide (additional) identification and separation power. The identification of high-momentum leptons produced in semileptonic decays is an example of such a tagging property. Although both quark flavours produce high-momentum leptons, the transverse momentum p_{T} is larger for b hadrons, since it is kinematically limited to $m_{\text{hadr.}}/2$. Nevertheless, a flavour identification using only

the lepton tag on its own is not competitive with the lifetime-mass tag, but is used to identify the quark charge. Actually, the charge of the lepton corresponds to the flavour of the decaying b hadron. It must be noticed that the correspondence to the initial quark charge is diluted in the presence of neutral b-meson $B^0-\bar{B}^0$ mixing or secondary semileptonic $b \to c \to \ell^+$ cascades.

Jet charge (hemisphere-charge tag) From the average charge of particles in a jet or hemisphere, the initial quark charge can be inferred via

$$\bar{Q} = \frac{\sum_i q_i p_{\parallel,i}^{\alpha}}{\sum_i p_{\parallel,i}^{\alpha}} \,. \tag{4.8}$$

In Eq. (4.8), q_i and $p_{\parallel,i}^{\alpha}$ are the charge and the longitudinal momentum of particle i with respect to the thrust axis. The parameter α is adjustable and is set between 0.3 and 1. In combination with other taggers, such as the vertex charge, very high purities have been reached for the measurement of A_{FB}^{b} [134].

Although the tags using techniques such as the lifetime, mass, high-energetic leptons, or the vertex charge have made the most of the statistics available at the former lepton collider generation, their application at a Tera-Z programme becomes challenging: the estimation of the quantities ε_{c_j} and ε_{uds_j} would simultaneously require enormous amounts of simulated events and much more accurate control of the physics details of the simulation to achieve a precision comparable to that obtainable with data on ε_b.

4.1.2 Limitations

In the following, a new hemisphere-flavour tagger is motivated in the context of the Tera-Z programme at FCC-ee with $\mathcal{O}(10^{12})$ $Z \to b\bar{b}$ events. Although with this amount of data at hand, statistical precision is no longer a limiting factor, efficient control over the (sources of) systematic uncertainties becomes inevitable to improve the measurement uncertainty for R_b and A_{FB}^{b} to actually reach $\mathcal{O}(\sigma_{\mathrm{syst.}}) = \mathcal{O}(\sigma_{\mathrm{stat.}})$.

The breakdown of systematic uncertainties from the ALEPH measurement of R_b points to the region in the measurement, which can bring the largest improvement to shrink the respective source of systematic uncertainty. The three main sources of systematic uncertainties are briefly summarised below, indicating their percentage weight in parentheses [140].

Monte-Carlo statistics (16 %) The finite number of MC events leads to a small uncertainty in determining ε_{c_j} and ε_{uds_j}. Studying systematic effects from c and light-quark physics modelling would require unfeasible amounts of simulated events. This is directly linked to the next point.

***udsc* physics (62 %)** Systematic uncertainties on ε_{c_j} and ε_{uds_j} arise from two main sources: in the simulation of tracking and in the physics modelling of charm- and light-quark events. Momentum and angular dependencies on the impact-parameter resolution affect the tagging efficiency, and have been treated as systematic uncertainty. Furthermore, uncertainties on the physics inputs to model *udsc* events have been propagated to estimate the impact on R_b. The modelling of hadronisation fractions, which control the production of different charm states, is particularly important due to the hierarchy in lifetimes and, therefore, influence ε_{c_j}. The main uncertainty in ε_{uds_j} originates from the modelling of gluon-splitting events, where ε_c and ε_{uds_j} depend on the $g \to b\bar{b}$ rate.

Hemisphere correlation (22 %) The departure of the hemisphere correlation value C_b from unity is a source of systematic uncertainty, which contributes to the total uncertainty budget. A detailed study of C_b discussing its sources and how to overcome its implications for R_b is given in Sec. 4.4.

For R_b, it can be concluded that approximately 80 % of the systematic uncertainty arises from the contamination of *udsc*-physics events and the estimation of their respective tagging uncertainties in b-quark events. This leads to the two main ingredients in order to measure R_b at FCC-ee with a comparable systematic uncertainty to the statistical one:

1. b-quark events need to be identified with a purity of 100 %, which in turn results in $\varepsilon_{c_j} = \varepsilon_{uds_j} = 0\,\%$.
2. The hemisphere correlation C_b must be controlled to the per-mille level around one.

For A_{FB}^b, the systematic uncertainty budget consists of about 50 % referred to corrections that have to be applied to account for gluon radiations from the b quark (QCD corrections). Further uncertainties arise from the knowledge on hadronisation and modelling parameters, contamination from *udsc*-physics events, and detector-related uncertainties. Similarly to R_b, two main conclusions can be drawn for the measurement of A_{FB}^b at FCC-ee:

1. The charge and the flavour of the b-quark events need to be identified with a purity of 100 %.
2. The QCD corrections need an effective reduction up to a level such that the systematic uncertainty is competitive with the statistical one.

All of the aforementioned lessons from the LEP measurements are addressed with a new hemisphere-flavour tagger, which is based on the exclusive reconstruction of b-hadrons in the hemispheres. This leads to a background-free, up to a charge-unambiguous tag when using only non-mixing b hadrons, which reduces the systematic

uncertainty budget for both measurements by about 70 %. In the following section, the exclusive reconstruction and its implications for R_b and A_{FB}^b are detailed.

4.2 Exclusive *b*-hadron reconstruction

The following section describes the fundamental principle of tagging hemispheres with exclusively reconstructed b-hadrons. The basic principle lies in the reconstruction of a list of b-hadron decay modes that, if one of them has been reconstructed in an event, gives an unambiguous tag of the b-quark flavour in $Z \to q\bar{q}$ events with no contribution from light quarks. Furthermore, the charge ambiguity in the application for A_{FB}^b can be removed by considering only charged b-mesons and -baryons as a flavour and charge tagger, namely $B^{\pm}$ and Λ_b^0.

In turn, this means for R_b, that $\varepsilon_{c_j} = \varepsilon_{uds_j} = 0$ and Eq. (4.3) simply reduces to[1]

$$N_b = 2N_Z R_b \varepsilon_{b_{1,2}} \tag{4.9}$$

$$N_{b\bar{b}} = \; N_Z R_b \varepsilon_{b_1} \varepsilon_{b_2} C_b \,. \tag{4.10}$$

With these updated equations at hand, the statistical uncertainty can be calculated to serve as a benchmark for the systematic uncertainty.

Statistical uncertainty of R_b Since charge information is not required for R_b, the list of b hadrons to be used can be extended to neutral b mesons so that it covers the decays of B^0, B_s^0, $B^{\pm}$ and Λ_b^0. Due to the limited branching ratio (Br), only decay modes with sufficiently large probabilities (typically greater than 10^{-3}) are considered. In addition, a maximum number of two neutral pions in the final state and no leptonic modes have been selected. The complete list of the decay modes included is presented in App. A.1.1. In conclusion, an overall tagging efficiency of $\varepsilon_{b_{1,2}} = 1\,\%$ is within reach. From this, the statistical precision is calculated from the known Gaussian uncertainty propagation

$$\sigma_{\mathrm{stat.}}(R_b) = \sqrt{\sum_{i \in [Z,b,b\bar{b}]} \left(\frac{\partial R_b}{\partial N_i} \cdot \sqrt{N_i} \right)^2 + \sum_{i,j,i \neq j} \kappa_{N_i,N_j}(R_b)} \,, \tag{4.11}$$

with the correlation expressions

$$\kappa_{N_i,N_j}(R_b) = 2\,\mathrm{cov}(N_i, N_j) \frac{\partial R_b}{\partial N_i} \frac{\partial R_b}{\partial N_j} \,. \tag{4.12}$$

[1] Here, gluon radiations and splitting into a $b\bar{b}$ pair has been neglected in this first, simplified approach

Taking into account the correlations between N_b, N_{bb} and N_Z (assuming the foreseen number of Z-boson decays listed in Tab. 3.4), $\sigma_{\text{stat.}}(R_b)$ is derived numerically with the `ForwardDiff` package [141] and results to

$$\sigma_{\text{stat.}}(R_b) = 2.22 \cdot 10^{-5}\,, \tag{4.13}$$

which is an improvement of a factor of 30 with respect to the most precise measurement [142].

Statistical uncertainty of A_{FB}^b In case of A_{FB}^b the list of b-hadrons is reduced, which results in a lowered b-tagging efficiency of $\varepsilon_{b_{1,2}} \approx 0.45\,\%$. However, for A_{FB}^b, only single-tagged *forward* and *backward* events N_{F} and N_{B} are needed, and $\varepsilon_{b_{1,2}}$ does not scale to the square as for R_b. In this context, forward and backward refer to the angle between the incoming electron and the outgoing b quark. The statistical uncertainty follows from the definition of A_{FB}^b expressed in terms of N_{F} and N_{B}

$$A_{\text{FB}}^b = \frac{N_{\text{F}} - N_{\text{B}}}{N_{\text{F}} + N_{\text{B}}}\,. \tag{4.14}$$

Again, the statistical uncertainty is derived numerically and gives

$$\sigma_{\text{stat.}}(A_{\text{FB}}^b) = 1.56 \cdot 10^{-5}\,. \tag{4.15}$$

This bare statistical precision translates into an improvement of about a factor 60 compared to the statistically most precise measurement [134].

In the following section, the new tagger method is applied to simulated events in order to test the purity assumptions in an FCC-ee environment. In the next step, the remaining systematic uncertainties are investigated in the application of the tagger for the measurement of R_b and A_{FB}^b.

4.2.1 Representative decays: one of the six

Out of the 200 decay modes considered, a comprehensive selection of six has been made to serve as representative modes for the rest. These six modes are characterised by the number of tracks and the number of neutral pions in their respective final state and have been exclusively reconstructed from a sample of $4 \cdot 10^7$ $Z \to q\bar{q}$ events (dataset ① from Tab. 3.4). They are grouped into three classes.

Including one *c* meson $B^+ \to \bar{D}^0\pi^+$ with Br $= 4.61 \cdot 10^{-3}$, considering different $\bar{D}^0$ decays:

Fully charged: $\bar{D}^0 \to K^+\pi^-$, with Br $= 3.947\,\%$

One neutral pion: $\bar{D}^0 \to K^+\pi^-\pi^0$, with Br $= 14.4\,\%$

Two neutral pions: $\bar{D}^0 \to K^+\pi^-\pi^0\pi^0$, with Br $= 8.86\,\%$

Four charged tracks at the decay vertex: $\bar{D}^0 \to K^+\pi^-\pi^-\pi^+$, with Br $= 8.22\,\%$

Including two *c* mesons $B^+ \to \bar{D}^0 D_s^+$ with Br $= 9 \cdot 10^{-3}$ and the fully charged decay of $\bar{D}^0 \to K^+\pi^-$ and $D_s^+ \to K^+K^-\pi^+$, which has a Br of $5.37\,\%$

Including a *c*$\bar{c}$ meson $B^+ \to J/\psi\, K^+$ with Br $= 1.02 \cdot 10^{-3}$ and fully leptonic decay of $J/\psi \to \ell^+\ell^-$ with Br $= 11.932\,\%$ for $\ell \in [e, \mu]$

In the following, the mode $B^+ \to \bar{D}^0\pi^+ \to [K^+\pi^-\pi^0]_{\bar{D}^0}\pi^+$ has been chosen to exemplary present the reconstruction process and to quantify its tagging performance. The reconstruction is divided into two main steps:

1. Reconstruction of the intermediate neutral $\bar{D}^0$
2. Full reconstruction of the B^+ meson

If not stated otherwise, the charge conjugated decay is considered likewise. The results of the remaining five decay modes are presented in App. A.1.2.

$\bar{D}^0$ decay with one π^0 In the following reconstruction steps, a perfect particle-ID has been assumed by matching the reconstructed particles with their simulated MC particles. At first, a neutral pion π^0 has been reconstructed from two photons. An angular cut on the opening angle of the two photons has been applied to reduce the combinatorial background and to remove candidates where photons from opposite hemispheres have been combined. In Fig. 4.2a, the distribution of the opening angle of the two photons is presented for the two cases where both photons originate from the same π^0 in orange (signal) and the rest in black (background). The signal photons receive a significant boost from the π^0 decay, resulting in a narrower opening angle. A broad and almost uniform distribution can be observed for photon combinations that do not stem from the π^0. An approach to find the best cut in the opening-angle distribution which leads to the best separation of signal and background consists in evaluating the ROC curve to assess the discrimination performance as its discrimination threshold is varied. In Fig. 4.2b, the true positive rate (correct pairing rate) against the false positive rate (wrong pairing rejection rate) is shown and the maximum diagonal distance has been used to evaluate the optimal cut of $\angle(\gamma_1, \gamma_2) < 0.27\pi\,\text{rad}$. It is indicated as a black dot and leads to a correct pairing rate of about $80\,\%$ while correctly rejecting falsely paired photons in about $70\,\%$ of the cases. However, for simplicity, the cutoff has been set to $\pi/4\,\text{rad}$.

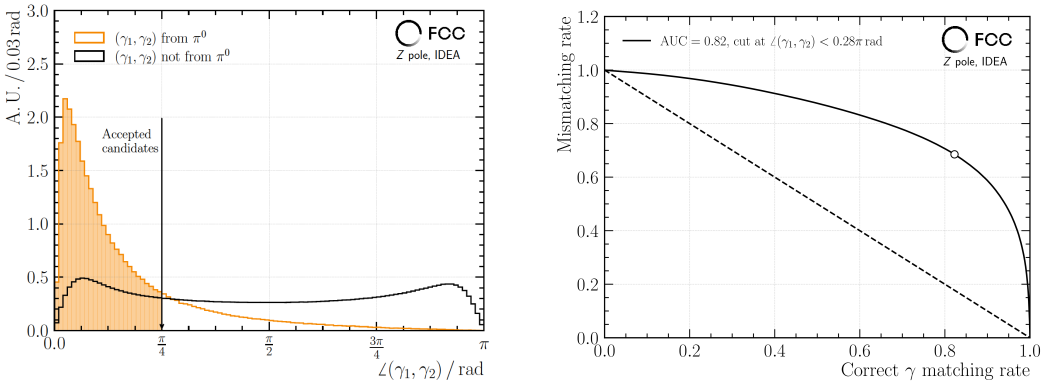

(a) Opening-angle distribution of the two photons for the $\pi^0 \to \gamma_1\gamma_2$ reconstruction.

(b) ROC curve to find the optimal cut in the opening-angle distribution from the point furthest away from the diagonal.

Figure 4.2: The π^0 reconstruction plays a central role for the $\bar{D}^0$ reconstruction. An optimal cut for the opening angle of the two photons has been found to be $\angle(\gamma_1, \gamma_2) < \pi/4$ rad.

The π^0 invariant-mass distribution is shown in Fig. 4.3 for different cuts on the diphoton-opening angle, where cutting at $\angle(\gamma_1, \gamma_2) < \pi/4$ rad removes about 20 % of the events. In addition, the right panel of Fig. 4.3 shows the π^0 mass-distribution without combinatorial background, together with an unbinned maximum likelihood fit. The distribution has been found to fit best with the sum of three Gaussian distributions. The combined resolution is calculated to be $\sigma_{\pi^0} = 6.65$ MeV, while the mean value is $\mu_{\pi^0} = (134.51 \pm 0.01)$ MeV. An additional cut on the π^0 mass has been chosen to be within $5\sigma_{\pi^0}$ around μ_{π^0} and the accepted regions are shown as shaded areas in Fig. 4.3. At $\pm 5\sigma_{\pi^0}$, only 3 % of the actual π^0 candidates are removed.

To conclude on the $\bar{D}^0$ reconstruction, the pair of oppositely charged kaons and pions (again matched to their corresponding MC particles to extract their type) is required to have a common vertex. In order to emulate vertex-resolution effects, the true production vertex of the particle-level kaon and pion tracks is used and the candidate is accepted in case their three-dimensional distance is below 50 µm. At this early stage of the analysis, vertex-fitting tools for neutral pseudotracks were not available yet in the `DELPHES` tool [118, 143]. Hence, the sole four-vectors of the reconstructed particles have been used. The invariant mass of the $\bar{D}^0$ candidates has been modelled with the sum of three Gaussian distributions from which the mass window of $(1790 \leq m(\bar{D}^0) < 1940)$ MeV has been chosen to accept the candidates for the B^+ reconstruction.

***B^+* reconstruction** In the second step an additional charge-matching pion has been added to the $\bar{D}^0$ to form B^+ candidates. Similarly to the $\bar{D}^0$ reconstruction, a vertex

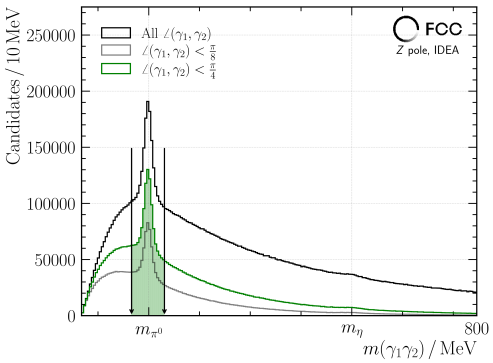

(a) Invariant-mass distribution of the two photons for different allowed opening angles. The green distribution shows the one from the optimal cut analysis, and the shaded area presents the region for the accepted candidates.

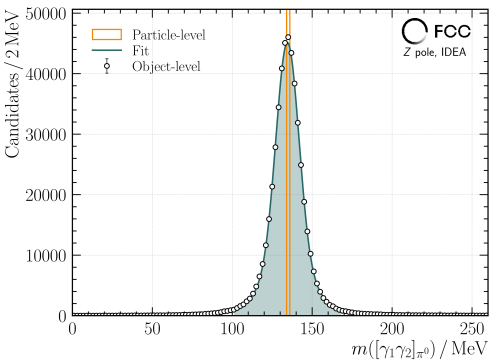

(b) Invariant-mass distribution of the truth-matched π^0 candidates. An unbinned maximum likelihood fit has been performed to find the region of accepted candidates $\pm 5\sigma_{\pi^0}$ around the pole mass.

Figure 4.3: Mass distributions for π^0 candidates. To be accepted, candidates have to lie in the mass window $(101 \leq m_{\pi^0} \leq 168)\,\text{MeV}$.

resolution of 50 µm has been emulated. To further remove the contribution from background events and to make use of the boost at the Z pole, a cut on the B^+ flight distance of 300 µm with respect to the PV has been applied. In Fig. 4.4, the left panel shows the invariant-mass distribution at the particle and object level of the truth-matched B^+ signal candidates, including an unbinned maximum likelihood fit to the object-level distribution. Further exclusion of contamination from background events in the signal region, which enter only from gluon splitting through $q \to q + [b\bar{b}]_g$ with $q \in [u, d, s, c]$, has been achieved by inspecting the energy spectrum of the background candidates, which is expected to be softer than from the signal, as shown in the right panel of Fig. 4.4. The limited amount of data at hand does not allow for a proper statistical evaluation of a suitable energy cut; therefore, an opportunistic one has been set at $E_{B^+} > 20\,\text{GeV}$, which removes most of the background B^+ candidates.

In the following section, the performance of the tagger in terms of purity and reconstruction efficiency is evaluated from the invariant mass spectrum of the reconstructed B^+ candidates.

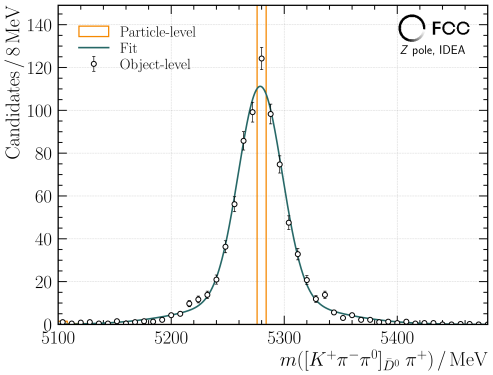

(a) Truth-matched B^+ candidates with an unbinned maximum likelihood fit, showing the distributions at the particle- and object level in orange and black dots, respectively.

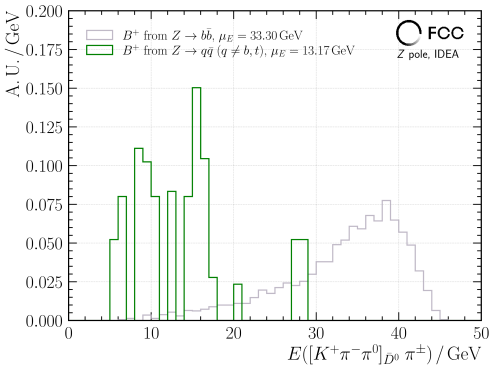

(b) The energy distribution of the B^+ candidates, for the signal (grey) and background (green) candidates. The background events originate only from gluon-splitting events and have much less energy.

Figure 4.4: Fit to the invariant-mass distribution around the signal peak in Fig. (a) and the B^+-energy distribution in Fig. (b). An opportunistic cut on the energy is set to $E_B \geq 20\,\text{GeV}$.

4.3 Performance of the tagger

So far, neither the direction of the hemisphere has been considered nor has the question of whether events have one or two tagged hemispheres been considered. However, the bare reconstruction and tagger performance can be evaluated from the invariant B^+-mass spectrum, which serves as observable to quantify the purity of the hemisphere-flavour tagger. The spectrum is presented in the range from $(2000 \leq m([K^+\pi^-\pi^0]\pi^+) \leq 5500)\,\text{MeV}$ in Fig. 4.5, distinguishing between different contributions: the grey peak shows the candidates from the signal B^+ mesons, while the partially reconstructed[2] and combinatorial background candidates from $Z \to b\bar{b}$ events are coloured red and black, respectively. The overall background contribution from $Z \to q\bar{q}$ events with $q \in [u, d, s, c]$ is shown in green, while each contribution is weighted with their respective fraction R_q.

For the purpose of flavour (and charge) tagging the event, candidates within the mass-peak region of $(5100 \leq m_{B^+} \leq 5500)\,\text{MeV}$ have been selected, also to first assess systematic uncertainties in this region. The purity P, where every contribution except

[2]Partially reconstructed particles refer to the (intermediate) particles where not all decay products are fully reconstructed. In case of $B^+ \to \bar{D}^0\pi^+$, this can include $B^+ \to \bar{D}^0\pi^+\pi^+\pi^-$ with a Br of $5.5 \cdot 10^{-3}$ and two missing charged pions.

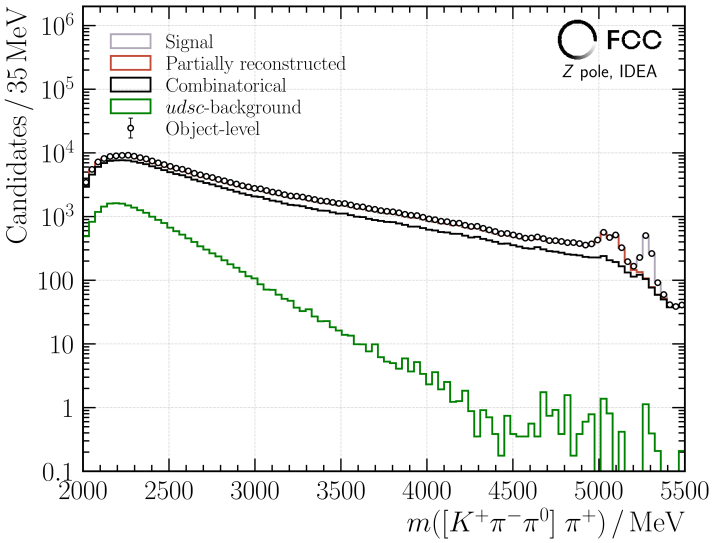

Figure 4.5: Invariant mass-spectrum for the $B^+ \to [K^+\pi^-\pi^0]_{\bar{D}^0}\pi^+$ decay mode. The different contributions from the signal, partially reconstructed, and combinatorial background, as well as from the *udsc*-physics background events are shown in grey, red, black, and green, respectively. The purity in the mass region of $(5150 \leq m_{B^+} \leq 5400)\,\text{MeV}$ has been evaluated to be $(99.89 \pm 0.09)\,\%$ with $E_{B^+} \geq 20\,\text{GeV}$. Lowering the mass constraint to also include partially reconstructed events greatly increases the efficiency of the exclusive tagger.

the *udsc*-physics background is taken as signal N_S, results in

$$P = \frac{N_\text{S}}{N_\text{S} + N_\text{B}} = (99.89 \pm 0.09)\,\%\,, \tag{4.16}$$

where the uncertainty given is statistical and N_B refers to the number of background events. Here, it can already be concluded that the exclusive reconstruction as a tagger achieves ultra-high purities, which are only contaminated from the physical, non-reducible background arising from gluon splitting. Their impact on the systematic uncertainty, also in comparison to the hemisphere correlation, is studied in further detail in Sec. 4.4.

The performance of the other representative decay modes is summarised in Tab. 4.1. As can be seen, for all decay modes a purity above 99.7 % has been reached, where the uncertainty stated in the table refers to the finite statistical precision of the dataset. For the decay $B^+ \to D_s^+\bar{D}^0$, no energy cut has been applied, since no background events have been found, also due to the smallest Br among all modes. However, the energy cut will probably be required with the full event statistics in place.

The reconstruction efficiencies ε_reco are calculated as the ratio of reconstructed candidates with respect to the generated ones. Therefore, the efficiency includes

Table 4.1: Reconstruction efficiencies and purities for the six representative decay modes in the mass-peak region. In total, purities above 99.7 % are in reach for all considered B^+ decay modes.

B^+ decay-mode	$\varepsilon_{\text{reco}}$ / %	Purity / %
$\bar{D}^0\pi^+ \to [K^+\pi^-]_{\bar{D}^0}\pi^+$	77.17 ± 2.99	99.93 ± 0.11
$\bar{D}^0\pi^+ \to [K^+\pi^-\pi^0]_{\bar{D}^0}\pi^+$	64.89 ± 1.41	99.89 ± 0.09
$\bar{D}^0\pi^+ \to [K^+\pi^-\pi^0\pi^0]_{\bar{D}^0}\pi^+$	49.95 ± 2.68	99.81 ± 0.07
$\bar{D}^0\pi^+ \to [K^+\pi^-\pi^-\pi^+]_{\bar{D}^0}\pi^+$	72.63 ± 6.90	99.73 ± 0.27
$D_s^+\bar{D}^0 \to [K^+K^-\pi^+]_{D_s^+}[K^+\pi^-]_{\bar{D}^0}$	78.57 ± 22.39	100.00
$J/\psi K^+ \to [\ell^+\ell^-]_{J/\psi}K^+$	85.87 ± 4.13	99.90 ± 0.24

all cut efficiencies, namely the cut on the flight distance, cuts on invariant masses of intermediate particles, and the final B^+-meson energy. This section closes the motivation, description and evaluation of a new b-hemisphere tagger for the application at the Tera-Z programme at FCC-ee. Its validity and feasibility have been shown and the principle has been demonstrated with the exclusive reconstruction of the $B^+ \to [K^+\pi^-\pi^0]_{\bar{D}^0}\pi^+$ decay. The next section presents the application of the reconstructed b-hadrons for the measurement of R_b and A_{FB}^b.

4.4 Application to the measurement of R_b

The following section details the use of the exclusive hemisphere flavour and charge tagger individually for R_b and A_{FB}^b. It covers the specifics of each measurement and, crucially, the remaining systematic uncertainties.

For R_b, only the flavour tag of the hemisphere is of interest; therefore, information about the direction or about the charge of the hemisphere is not necessary. This specificity allows to significantly increase the tagger efficiency $\varepsilon_{b_{1,2}}$ from the targeted 1 % by including also partially reconstructed candidates as hemisphere taggers. This approach is mainly driven by the absence of *udsc* contributions outside the signal-peak region. The possibility of releasing the mass-peak constraint and its impact on the purity and tagging efficiency is discussed below. All studies regarding the increase of the tagging efficiency have been carried out using the generated dataset (1), while systematic uncertainties have been investigated from dataset (2).

The left panel of Fig. 4.6 illustrates $\varepsilon_{b_{1,2}}$ as a function of the invariant B^+-mass cut, where $\varepsilon_{b_{1,2}}$ is determined by

$$\varepsilon_{b_{1,2}} = \frac{N_{\text{S}}^{\text{all}}}{N_{\text{gen}}}\,. \tag{4.17}$$

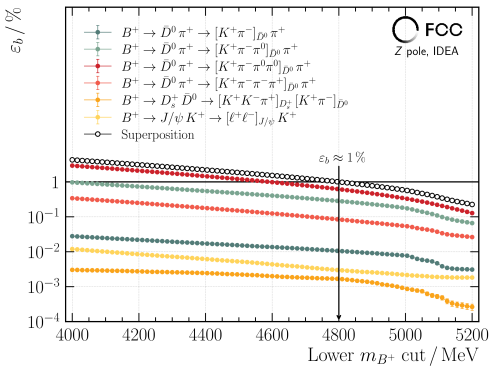

(a) Lower invariant-mass cuts highly increase the efficiency of the tagger. The sum of the different modes is shown in black dots and is labelled *Superposition*.

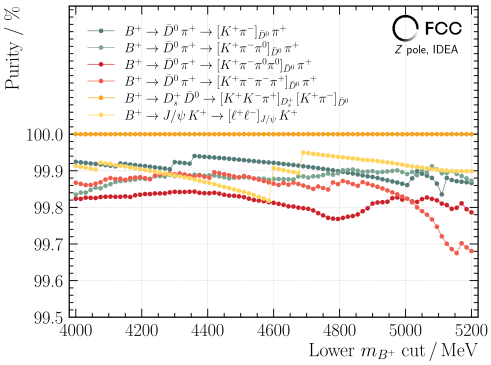

(b) The purity as function of the lower invariant mass cut. All of the values converge to purities above 99.8 %. The more neutral pions are included in the final state, the lower the purity of the mode.

Figure 4.6: Already with the six representative decay modes and a cut at $m_{B^+} \geq 4800\,\text{MeV}$, the targeted 1 % tagging efficiency is reached without loss in purity.

In Eq. (4.17), $N_{\text{gen}} = 9.5 \cdot 10^6$ represents the number of generated events and $N_{\text{S}}^{\text{all}}$ is the number of all candidates originating from the $Z \to b\bar{b}$ decay, respectively. As anticipated, the efficiency for all decay modes increases significantly with decreasing mass threshold, even reaching the 1 % threshold for the modes with neutral pions within the mass window studied. In addition, the combined efficiencies of the decay modes studied are highlighted in black and are referred to as *Superposition*. The plot indicates that the six representative decay modes with a lower invariant-mass cut of $m_{B^+} > 4800\,\text{MeV}$ are sufficient to achieve a tagging efficiency of $\varepsilon_{b_{1,2}} \approx 1\,\%$.

Consequently, the purity at the same invariant-mass cuts, as calculated in Eq. (4.16), is displayed in the right panel of Fig. 4.6. A convergence towards purities exceeding 99.8 % can be observed for all decay modes. Even tighter cuts on the B^+ energy can be applied when the mass window constraint is released, which would further reduce the impact from gluon radiation and would lead to even higher purities. However, this would require a dedicated investigation into the impact on the systematic uncertainties for R_b, which is beyond the scope of this thesis. The impact of systematic uncertainties has only been examined assuming the candidates in the signal-peak region. Their sources and handling are discussed in the following sections.

Sources and impact of systematic uncertainty Systematic uncertainties arise from two main origins:

1. Gluon radiation from a light quark and subsequent splitting into a $b\bar{b}$ pair through $q \to q\left[b\bar{b}\right]_g$ for $q \in [u, d, s, c]$. These enter the signal region when the b

quark hadronises and decays into the channel under study. The probability of gluon splitting is given by $g_{b\bar{b}}$ and its precision and impact on $\sigma_{\text{syst.}}(R_b)$ are examined.

2. Correlation of single- and double-tagging efficiencies between the two hemispheres, C_b. The sources of this correlation and the appropriate methods for addressing it in the measurement of R_b are discussed.

The impact of both sources of systematic uncertainties on $\sigma_{\text{syst.}}(R_b)$ is first worked out, assuming that each contribution adds in quadrature to the total systematic uncertainty

$$\sigma_{\text{syst.}}(R_b) = \sqrt{\left(\sigma_{\text{syst.}}^{\text{from } g_{b\bar{b}}}(R_b)\right)^2 + \left(\sigma_{\text{syst.}}^{\text{from } C_b}(R_b)\right)^2} \tag{4.18}$$

For this analysis, the most precise measurements for $g_{b\bar{b}}$ (where the average value has been calculated from all LEP and SLD measurements [144–148] as described in Ref. [149]) and the hemisphere-correlation coefficient C_b obtained by the ALEPH Collaboration [140] are used as reference values

$$g_{b\bar{b}} = 0.002\,47 \pm 0.000\,56\,, \tag{4.19}$$

$$\Delta C_b^{\text{ALEPH}} = 0.0376 \pm 0.0025(\text{stat.}) \pm 0.0027(\text{syst.}) = 0.0376 \pm 0.0037\,. \tag{4.20}$$

Because in most measurements of R_b, the difference to unity, $\Delta C_b = 1 - C_b$, is stated, it will also be used in the following. A value of $\Delta C_b = 0$ would refer to no bias in the tagging of the hemispheres.

Both values have been used to compute the systematic uncertainty on R_b. To individually study the effect of gluon splitting on R_b, Eq.(4.3) is adjusted as follows

$$N_b = 2N_Z \cdot (R_b \varepsilon_{b_{1,2}}^{Z\to b\bar{b}} \varepsilon_E^{Z\to b\bar{b}} + (1 - R_b) g_{b\bar{b}} \varepsilon_{b_{1,2}}^{g\to b\bar{b}} \varepsilon_E^{g\to b\bar{b}})\,, \tag{4.21}$$

with the efficiency of the energy cut on the B-meson candidates, individually for the signal and background events, $\varepsilon_E^{Z\to b\bar{b}} = 88\,\%$ and $\varepsilon_E^{g\to b\bar{b}} = 8\,\%$, respectively. Furthermore, $\varepsilon_{b_{1,2}}^{g\to b\bar{b}} \approx \varepsilon_{b_{1,2}}^{Z\to b\bar{b}} = 1\,\%$ neglects any kinematic difference for signal and background events. Rearranging Eq. (4.21) gives the following for R_b

$$R_b = \frac{N_b - 2N_Z \varepsilon_{b_{1,2}}^{g\to b\bar{b}} \varepsilon_E^{g\to b\bar{b}}}{2N_Z \left(\varepsilon_{b_{1,2}}^{Z\to b\bar{b}} \varepsilon_E^{Z\to b\bar{b}} - g_{b\bar{b}} \varepsilon_{b_{1,2}}^{g\to b\bar{b}} \varepsilon_E^{g\to b\bar{b}}\right)}\,. \tag{4.22}$$

The left panel of Fig. 4.7 illustrates the systematic uncertainty of R_b as a function of the relative uncertainties due to $g_{b\bar{b}}$ and ΔC_b, depicted in orange and blue, respectively, arising from the central values from Eqs. (4.19) and (4.20). The figure indicates that the bias from the gluon-splitting uncertainty is suppressed by more than two orders of magnitude compared to the effect of the hemisphere correlation. Furthermore, the

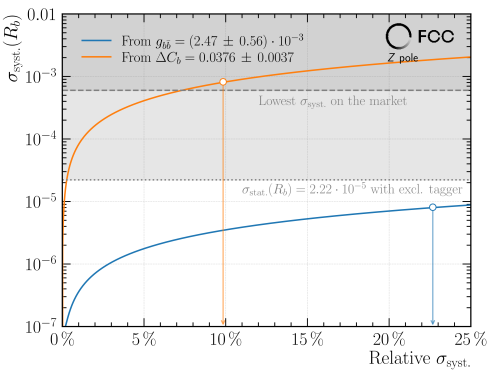

(a) Impact of relative systematic uncertainties (expressed as a percentage) on the precision of R_b values derived from two sources: the hemisphere correlation ΔC_b in orange and the gluon-splitting rate $g_{b\bar{b}}$ in blue. The dominating uncertainty in $\sigma_{\text{syst.}}(R_b)$ originates from the hemisphere correlation.

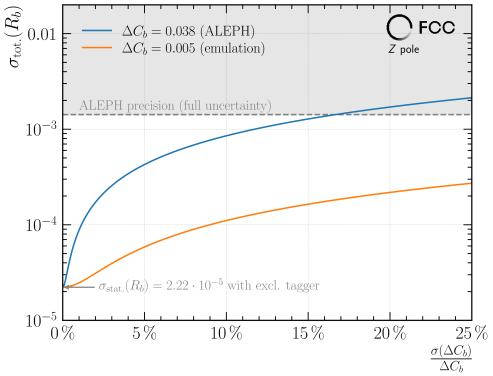

(b) The total precision on R_b as function of the relative uncertainty on ΔC_b for two cases: the value from the ALEPH measurement [140] and emulated ΔC_b value of 0.005. The nominal value of ΔC_b has a strong impact on the uncertainty of R_b, as well as the precision in the determination of ΔC_b.

Figure 4.7: The importance of the hemisphere correlation on the measurement precision of R_b. Other sources such as the gluon splitting rate (contamination of the background in the signal region) become negligible.

systematic uncertainty on R_b is highly dependent on the precision of the respective inputs $g_{b\bar{b}}$ and ΔC_b. Although measured with a higher accuracy at FCC-ee, the current precision on $g_{b\bar{b}}$ is sufficient such that it does not limit the measurement of R_b, where the statistical limit at $\sigma_{\text{stat.}}(R_b) = 2.22 \cdot 10^{-5}$ is indicated by the lighter grey colour. Therefore, the systematic uncertainty on R_b simply reduces to

$$\frac{\sigma_{\text{syst.}}(R_b)}{R_b} = \frac{\sigma(\Delta C_b)}{\Delta C_b} \,. \tag{4.23}$$

In conclusion, the primary influencing factor arises from the hemisphere correlation, whose effect on the measurement is described in the following discussion.

4.4.1 Hemisphere correlation

The hemisphere correlation ΔC_b measures the bias introduced in the probed hemisphere by the tagged one. The precision of ΔC_b has been shown to be a handle to reduce $\sigma_{\text{syst.}}(R_b)$. Furthermore, its nominal value is another crucial factor in minimising its effect on the systematic uncertainty of R_b. This is shown in the right graph of Fig. 4.7, which shows the total uncertainty $\sigma_{\text{tot.}}(R_b) = \sqrt{\sigma^2_{\text{syst.}}(R_b) + \sigma^2_{\text{stat.}}(R_b)}$ as a function of the relative uncertainty on ΔC_b for two different cases: the first

case represents the best current determination from the measurement of the ALEPH Collaboration [140]. The second case emulates a reduced hemisphere correlation by approximately a factor of ten, resulting in $\Delta C_b = 0.005$. It can be seen that the reduction of the nominal value of ΔC_b directly impacts the measurement uncertainty of R_b, reducing it by about a factor of ten.

Therefore, the primary causes of ΔC_b deviating from zero are examined in the next paragraph, starting with the findings from Ref. [140]. Four sources of hemisphere correlations have been identified:

Detector-acceptance effects Due to the back-to-back configuration of the two b quarks initially, if one enters a region with lower detector acceptance, such as the very forward or backward region, the other hemisphere is likely to present a similar lower acceptance.

Hard gluon radiation In events where a high energetic gluon in the initial state has been radiated ($Z \to b\bar{b}g$), the momenta of the b hadrons in each hemisphere will decrease, making the reconstruction of the other b hadron less probable.

Shared PV When both hemispheres share a single PV, increased measurement uncertainty of the PV affects the probability of tagging both b hadrons; a bias of the PV measurement towards one hemisphere increases the likelihood of tagging the b hadron in the opposite hemisphere.

Unequal flight distances A longer flight distance of one b hadron caused by a higher b-hadron momentum reduces the fragmentation tracks that form the PV, decreasing its measurement precision. As a consequence, the reconstruction of the second b hadron is less likely.

The first two effects have been identified as less significant, whereas the third and fourth factors are particularly influential in determining the hemisphere correlations. The latter two share a similar origin, which can be attributed to the reconstruction of a common and shared PV in the event, as outlined in Sec. 3.4. Consequently, measurements at LEP have reconstructed two PVs (one in each hemisphere) to mitigate the bias caused by a single PV per event. Although this method has proven effective, a simpler alternative approach based on a different track-selection procedure has been pursued to address the limitations imposed by the measurement uncertainty of the PV. Nevertheless, all results are compared to the method of using a shared PV. To thoroughly investigate the impacts of detector imperfections, the following studies have been outlined using the fully-simulated dataset (2) described in Sec. 3.3 in Tab. 3.4, which use the CLD concept as detector. The alternative track selection is described below.

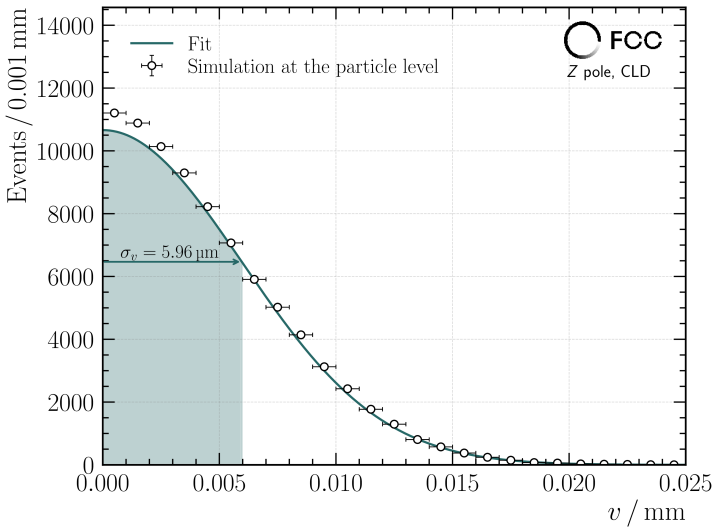

Figure 4.8: Distribution of v as defined in Eq. (4.24) with a fit of a truncated Gaussian function, from which the size of the LR of $\sigma_v = 5.96\,\mu\text{m}$ is extracted.

Tracks outside the luminous region The accurate knowledge of the beam-spot region (luminous region (LR)) as well as its smallness is used to select tracks issued from the primary and secondary vertices. The LR refers to the area where the two beams intersect, also referred to as the PV at the truth level. Given the finite sizes of the beams, their intersection point has specific dimensions in the $(x, y, z)^\top$ plane. In order to define variables that measure the agreement of track origins with the IP, the IP region in the $(x, y)^\top$ plane has been translated into a single transverse variable, v, defined as

$$v = \sqrt{\left(\text{PV}_x^{\text{Particle-level}}\right)^2 + \left(\text{PV}_y^{\text{Particle-level}}\right)^2}, \tag{4.24}$$

where the size of the transverse beam-spot region is given by the width of the distribution of v, σ_v, and is taken as the LR. The resulting distribution of v is presented in Fig. 4.8 and has been derived from the exclusive dataset (2). The superscript *Particle-level* indicates that the true collision point of the electron and positron beam has been used. In order to identify whether the tracks are consistent with the beam-spot region, track-wise variables $v_{1,2}$ have been introduced

$$v_1 = \frac{d_0}{\sqrt{\sigma_{d_0}^2 + \sigma_v^2}}, \quad v_2 = \frac{z_0}{\sqrt{\sigma_{z_0}^2 + \sigma_v^2}}, \tag{4.25}$$

where σ_{d_0} and σ_{z_0} are the respective uncertainties of the impact parameters. Although v_2 uses the longitudinal impact parameter z_0 and quantifies its agreement with the transverse extension of the beam spot, at this stage of the analysis it has served its

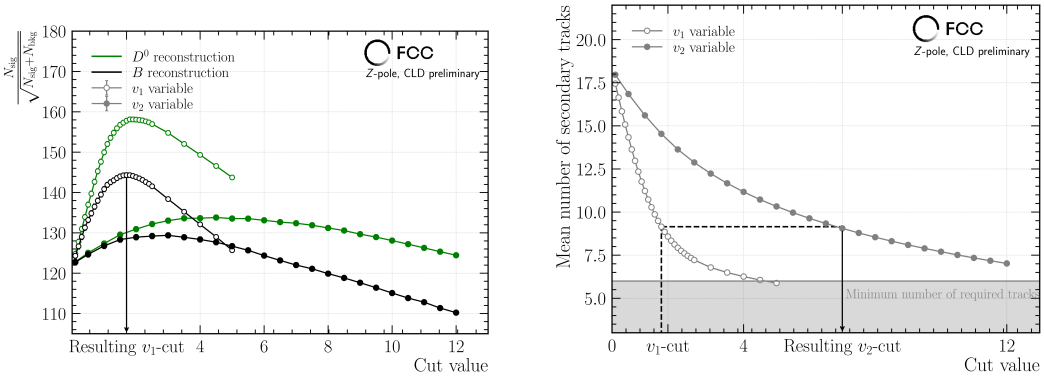

(a) Signal significance S as function of the $v_{1,2}$ variable thresholds. The resulting v_1 cut is extracted from the maximum of the B^+-reconstruction significance.

(b) The cut on v_2 extracted from the mean number of secondary tracks slope where the same number is reached as for the given v_1 cut.

Figure 4.9: Optimised parameters for the determination of the LR and to select tracks that are inconsistent with the LR. They have been further used to perform the reconstruction of $\bar{D}^0$ and B^+ mesons.

purpose to find thresholds up to which tracks are taken as consistent or inconsistent with the beam-spot region. These thresholds have been determined by independently varying the cuts of v_1 and v_2 and maximising the significance S of the $\bar{D}^0$- and B^+-meson reconstruction, along with the number of remaining tracks after selection. The significance is defined as

$$S = \frac{N_{\text{sig}}}{\sqrt{N_{\text{sig}} + N_{\text{bkg}}}}\,, \tag{4.26}$$

where N_{sig} represents the number of truth-matched meson candidates and N_{bkg} denotes the number of background events (where background refers to partially reconstructed and combinatorial background events, since only $Z \to b\bar{b}$ events have been used) in the region of interest. Here, in the considered mass region, the background rate is approximated to be uniform. The dependence of S as a function of the $v_{1,2}$ thresholds and the mean number of tracks inconsistent with the LR are shown in Fig. 4.9. The significance of the B^+ meson shows a maximum around 1.7 for v_1, which has been chosen as the optimal cut. In contrast, v_2 shows only a slight dependence on the significance, so its threshold has been determined based on the mean number of tracks that are inconsistent with the LR. This threshold, where a similar number of tracks is observed as with the given v_1 cut, has been set at eight. Given that the v_1 and v_2 distributions are symmetric around zero, the absolute value is used to decide whether tracks have been used in the B^+-meson reconstruction process.

Particle reconstruction The evaluation of ΔC_b requires a full reconstruction of the charged B^+ mesons in both hemispheres. In contrast to the exemplary reconstruction in Sec. 4.2, the decay $B^+ \to [K^+\pi^-]_{\bar{D}^0}\,\pi^+$ has been simulated in the hemispheres (plus the charge-conjugate decay). In contrast to the reconstruction method described in Sec. 4.2, the vertexing features of the `DELPHES` package were fully applicable and have been used [143]. During this phase of the analysis, the neutral vertexing capabilities have been made available for the reconstruction of neutral intermediate $\bar{D}^0$ tracks. As in the reconstruction method detailed in Sec. 4.2, a pair of oppositely charged kaon and pion tracks has been combined to a common vertex, constraining their mass to the $\bar{D}^0$ pole-mass. The fit provides updated momenta for the tracks, which then have been used to form $\bar{D}^0$ candidates. Candidates with $(1800 \leq m_{\bar{D}^0} \leq 1930)\,\text{MeV}$ have been further vertexed with another pion track, resulting in B^+ candidates that fall within $(5150 \leq m_{B^+} < 5400)\,\text{MeV}$ and have a vertex quality of $\chi^2_{B^+} < 25$.

Subsequently, the single- and double-tag efficiencies $\varepsilon_{b_{1,2}}$ and $\varepsilon_{b_1}\varepsilon_{b_2}$ have been calculated and then differentially assessed in distributions that are sensitive to deviations of ΔC_b from zero.

4.4.2 Integrated and differential hemisphere-correlation

The integrated ΔC_b value has been determined for both the shared PV and the LR, taking into account detector-acceptance effects by excluding events where the absolute value of the thrust-axis polar angle $|\cos(\theta_{\text{Thrust}})|$ exceeds 0.9. They result to

$$\begin{aligned} \Delta C_b^{\text{shared PV}} &= \quad 0.035 \pm 0.003\,, \\ \Delta C_b^{\text{LR}} &= -0.001 \pm 0.003\,, \end{aligned} \tag{4.27}$$

where ΔC_b^{LR} is statistically consistent with zero, unlike the shared PV approach. Therefore, eliminating dependencies caused by intrinsic biases from the PV by choosing tracks independently of the PV already reduces the hemispheric correlation to the required level for an accurate measurement of R_b. Nevertheless, the potential causes of a non-zero ΔC_b value are examined in the following, with an emphasis on detector-acceptance effects and displacement from the IP.

Dependence on detector acceptances The influence of detector acceptance has been analysed in bins of the maximum allowed $|\cos(\theta_{\text{Thrust}})|$. A finer binning has been chosen for the extreme forward/backward region where $|\cos(\theta_{\text{Thrust}})| > 0.9$. The results are illustrated in Fig. 4.10, indicating that for $|\cos(\theta_{\text{Thrust}})| > 0.9$, ΔC_b decreases for both methods and converges for $|\cos(\theta_{\text{Thrust}})| < 0.9$, which also sets the cut value. The dependence and inclusive value of ΔC_b have been validated using the high-statistics fast simulation dataset (3) within the IDEA detector, also

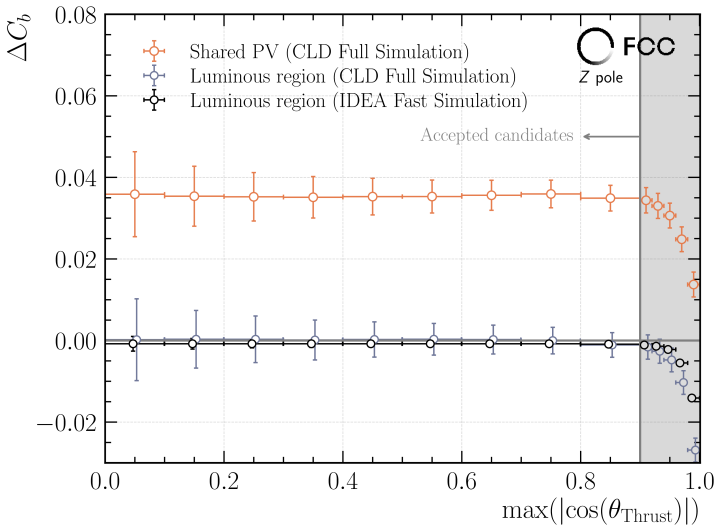

Figure 4.10: ΔC_b as function of the maximally allowed $|\cos(\theta_{\text{Thrust}})|$, comparing the shared PV and the LR approach. Although both drop towards higher values in the very forward/backward region, ΔC_b becomes compatible with zero within the statistical precision when $|\cos(\theta_{\text{Thrust}})| < 0.9$ for the LR approach. The value of ΔC_b has been confirmed from the fast simulation dataset.

depicted in Fig. 4.10 with black dots. Similar to the reconstruction applied on the dataset (2), the vertexing capabilities have been applied to form B^+ mesons. It shows a less pronounced drop in the extreme forward/backward region due to the larger acceptance area of the IDEA detector compared to CLD. Therefore, a precise measurement of R_b also requires a detector with a wide acceptance range, which would increase the fraction of accepted events while reducing the hemisphere correlation at the same time.

Displacement from the PV The deviation of the PV at the object level from the true collision point (PV at the particle level), defined as

$$d_{\text{PV}} = \sqrt{\sum_{i\in[x,y,z]} \left(\text{PV}_i^{\text{Object-level}} - \text{PV}_i^{\text{Particle-level}}\right)^2} \tag{4.28}$$

encapsulates two metrics simultaneously. Firstly, d_{PV} introduces a bias in one hemisphere, increasing the likelihood of tagging the b-hadron in that hemisphere, while decreasing the reconstruction probability for the b-hadron in the opposite hemisphere. Secondly, d_{PV} serves as an indicator of the PV reconstruction quality, which diminishes with increasing d_{PV}. Fig. 4.11a shows ΔC_b in bins of d_{PV}, separately for the shared PV and the LR approach. In addition, a χ^2 test has been used to

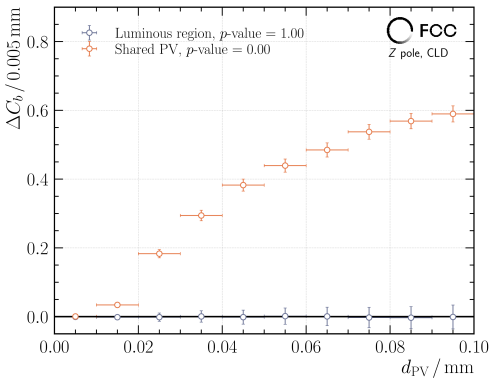

(a) ΔC_b as function of the displacement of the reconstructed PV from the true collision point. When the displacement is zero (most precise determination), there is no correlation for both methods. For further displaced PVs, the correlation increases for the shared PV, while staying zero for the LR approach.

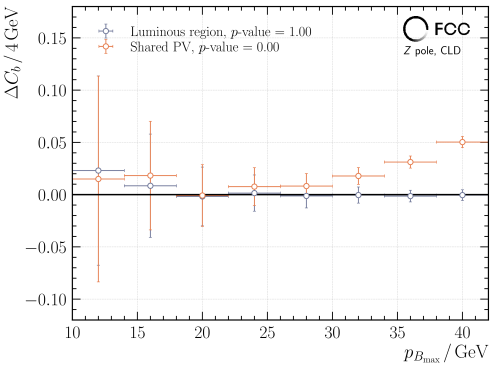

(b) ΔC_b in bins of the B-meson momentum. Higher momenta mesons induce a correlation when a shared PV is used, due to the bias in the other hemisphere coming from the PV which is shifted towards the tagged hemisphere.

Figure 4.11: The displacement of the PV has strong impact on the hemisphere correlation. When the PV has been reconstructed preferring one hemisphere, the b-hadron reconstruction probability decreases for the other hemisphere. All dependencies have been removed when using tracks for the reconstruction which have been selected due to their inconsistency with the LR.

evaluate the agreement of the points with zero, with the result presented in the legend as p-value. Values near one indicate support for the hypothesis that there is no deviation from zero, whereas p-values less than 0.05 generally lead to the rejection of this hypothesis.

It can be seen that there is a strong dependence of ΔC_b for the shared PV approach, already for PV displacements above 0.01 mm, for which ALEPH-like correlations are reached. As already discussed in Fig. 4.7b, the overall uncertainty in R_b would be significantly affected. In contrast, no dependence within the statistical precision can be observed for the LR ansatz.

Flight distance / Momentum The flight distance is directly related to the momentum, as shown in Eq. (4.5). Therefore, the momentum has been used as a proxy for the flight distance, which resolves any ambiguities with respect to the reference point for the flight distance (either $(0,0,0)^\top$ or the PV) in the two methods. Concerning ΔC_b, the higher momentum B-meson introduces a bias, reducing the likelihood of reconstructing the oppositely-charged B meson in the opposite hemisphere. Fig. 4.11b displays ΔC_b in different B^+-meson momentum bins. Both methods show good

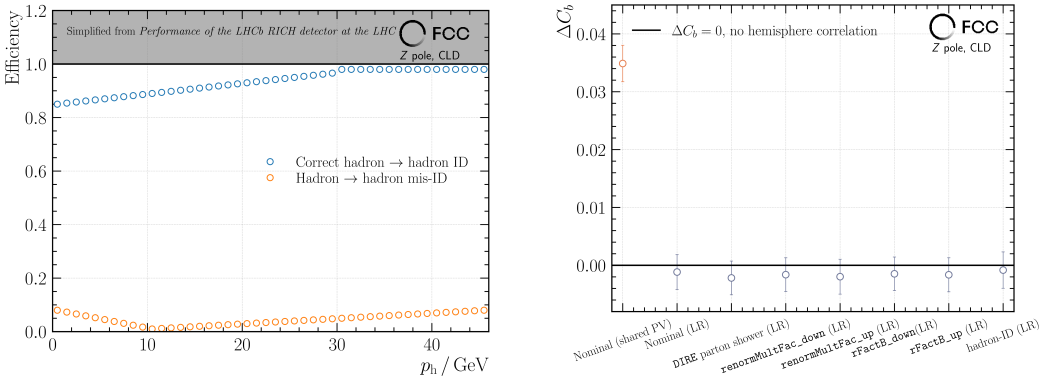

(a) Adapted, simplified version of a more realistic scenario of the particle-ID performance from the RICH detector at LHCb. The interpolations are defined in Eq. (4.29).

(b) Variation of the renormalisation scale, the b fragmentation, the parton shower and the variation in the particle-ID probabilities. No significant excess above the statistical uncertainty can be seen.

Figure 4.12: The assumption of a more realistic, momentum-dependent particle-ID does not lead to an excess of ΔC_b, which would not be covered by the statistical uncertainty.

agreement within the statistical uncertainty in the low-momentum range, but the correlation increases at higher momenta for the shared-PV method. This also leads to the rejection of the hypothesis that ΔC_b is consistent with zero for the shared PV.

Especially considering a minimal energy cut on the B-meson candidates to remove background contamination in the signal region, which would cause a significant increase in systematic uncertainty from ΔC_b, although further removing the impact from $udsc$-physics events. However, this dilemma can be overcome with the LR approach.

4.4.3 First assessment to systematic uncertainties for ΔC_b

In addition to the inherent statistical precision of ΔC_b related to the finite size of the simulated samples, the determination is affected by systematic uncertainties arising primarily from the modelling of b-hadron fragmentation, lifetimes, and the multiplicities of mesons in both production and decay [140]. As highlighted in Ref. [140], the most significant influence originates from the multiplicity of B decays and the possibility that both b quarks may end up in the same hemisphere, a result of high-energetic gluons that have been radiated. However, the latter will be drastically reduced in the presence of B^+-meson energy cuts, as presented in Sec. 4.5 in the context of A_{FB}^b. For the sake of this study, the different inputs described in Sec. 3.3

have been varied within the given ranges. Furthermore, the assumption of a 100 % accurate particle-ID has been relaxed and substituted with a more realistic scenario based on the LHCb Collaboration's findings [150]. For better comparability with the other variations of the input parameters, the fully simulated dataset has been used for this study. In addition, no significant impact on ΔC_b is expected due to symmetric effects in both hemispheres. The RICH detector at LHCb has demonstrated a momentum-dependent hadron (mis-)ID, which has been adapted and simplified for the momentum range p_h of interest from $(0-45)\,\mathrm{GeV}$

$$\begin{aligned} \text{Correct-ID}(p_\mathrm{h}) &= \begin{cases} 0.004 \cdot p_\mathrm{h} + 0.85, & \text{if } p_\mathrm{h} < 30\,\mathrm{GeV}\,, \\ 0.98, & \text{else.} \end{cases} \\ \text{mis-ID}(p_\mathrm{h}) &= \begin{cases} -0.007 \cdot p_\mathrm{h} + 0.08, & \text{if } p_\mathrm{h} < 10\,\mathrm{GeV}\,, \\ 0.002 \cdot p_\mathrm{h} - 0.01, & \text{else.} \end{cases} \end{aligned} \tag{4.29}$$

Here, hadron refers to either pions or kaons, which are the relevant ones for this analysis and have been treated equally in the calculation. The implemented correct hadron-to-hadron ID efficiency and mis-ID efficiency are presented in the left panel of Fig. 4.12. Nonetheless, this method is quite conservative, as recent updates from the LHCb Collaboration indicate that the RICH detector's performance with 2023 data achieves nearly 100 % correct-ID efficiency for hadrons [151].
The right panel of Fig. 4.12 provides an overview of the various scenarios and concludes that, given the statistical accuracy of the samples, no deviation from the nominal value is detected.

4.4.4 Conclusions for R_b

In summary, the use of exclusively reconstructed b-hadrons as b-hemisphere taggers enables unprecedented purity levels during the Z-pole run at FCC-ee. For six representative decay modes and a target efficiency of 1 %, purities exceeding 99.8 % are achievable, leaving ΔC_b as the sole unknown in the set of equations (refer to Eqs. (4.10)) due to the minimal impact of gluon radiation on the systematic uncertainty. From fully-simulated events, ΔC_b has been found to be consistent with zero by eliminating dependencies from a shared PV and selecting tracks outside the LR. With the current dataset, ΔC_b has been found to be

$$\Delta C_b = -0.001 \pm 0.003(\mathrm{stat.})\,. \tag{4.30}$$

Given the nominal value of ΔC_b from Eq. (4.30) and assuming that the precision of R_b only depends on the precision of ΔC_b, achieving a relative precision of 10 % on ΔC_b is necessary to determine R_b with exclusive b-hadron decays such that $\sigma_\mathrm{stat.}(R_b) \approx \sigma_\mathrm{syst.}(R_b)$. Consequently, ΔC_b must be derived from a simulation dataset of at least $N_Z \approx 10^9$ events to reduce $\sigma(\Delta C_b)$ by about a factor of 30 to reach

$\sigma(\Delta C_b)/\Delta C_b = 10\,\%$, where in both hemispheres the b-hadron decays according to a list of approximately 200 decay modes. Based on this, R_b results in

$$\begin{aligned} R_b &= \mu(R_b) \pm 2.22 \cdot 10^{-5}(\text{stat.}) \pm 2.16 \cdot 10^{-5}(\text{syst.})\,, \\ &= \mu(R_b) \pm 3.10 \cdot 10^{-5}(\text{tot.})\,. \end{aligned}$$

The simultaneous use of both, a novel ultra-pure tagger and a selection of the secondary tracks based on the inconsistency with the LR, which have been presented in this dissertation, enables the precision on R_b to be improved by about a factor of 60 [28] with respect to the state-of-the-art while keeping a measurement dominated by statistics of the sample.

4.5 Application to the measurement of A_{FB}^{b}

The forward-backward asymmetry of the b quark is of particular interest for the hemisphere tagger based on the exclusive b-hadron reconstruction. To date, it still has the highest tension [1] among all EWPOs with the SM prediction of

$$A_{\text{FB}}^{b,\text{SM}} = 0.1037 \pm 0.0008\,, \tag{4.31}$$

which is in $2.9\,\sigma$ tension with the average of the LEP measurements

$$A_{\text{FB}}^{b} = 0.0992 \pm 0.0016\,. \tag{4.32}$$

Similarly to R_b, the primary challenge of the measurement is the effective reduction of the systematic uncertainty given the raw statistical precision available at FCC-ee. However, in addition to the hemisphere flavour tag, which is sufficient to measure R_b, an estimation of the charge and direction of the initial b-quark is necessary. This leads to two consequences:

1. The criteria for the decay modes to be considered are more stringent. To mitigate one source of systematic uncertainty that comes from the charge confusion of neutral B-meson mixing, only the modes of the B^+ meson and the Λ_b^0 baryon can be used as taggers.

2. Various estimators of the b-quark direction can be employed, such as jets, the thrust axis, or the flight direction of the b hadron. In the latter, only fully reconstructed b-hadrons can be used, restricting the selection of candidates to those from the mass-peak region.

Nevertheless, the exclusive b-hadron reconstruction provides all tools in order to overcome limitations induced by the main source of systematic uncertainties, which is the accounting for the correction of the direction estimation from high-energetic gluon radiations, the QCD corrections. Therefore, the application is described in this section. However, the principle of the A_{FB}^{b} measurement is discussed first, before going into detail about the remaining systematic uncertainty.

4.5.1 Measurement principle

The forward-backward asymmetry can be calculated by counting the number of *forward* and *backward* events (see Eq. (4.14)) or by extracting the value from a fit to the differential cross-section distribution. To begin with, it is demonstrated that both methods lead to the same result. Therefore, the proportionality in Eq. (2.6) is explicitly written as

$$\frac{\mathrm{d}\sigma}{\mathrm{d}\cos(\theta_b)} = \frac{1}{1+f_\mathrm{L}}\left(\frac{3}{8}(1+\cos^2(\theta_b)) + \frac{3}{4}f_\mathrm{L}(1-\cos^2(\theta_b))\right) + A_\mathrm{FB}^b\cos(\theta_b)\,. \quad (4.33)$$

The parameter f_L represents the fraction of longitudinally polarised Z bosons along the quark's flight path and has been set to zero in the fit[3]. The b-quark polar-angle distribution before gluon radiations, shown in the left panel of Fig. 4.13, has been taken to extract $A_\mathrm{FB}^{b,0}$. Although at this stage the kinematic properties of the b quark are not affected by radiation effects in the final state, ISR from the colliding beams can reduce the energy of the b quarks. In order to account for effects from ISR, a minimal energy-cut on the b quarks has been set to 45 GeV. In addition, the correction factor to account for γ exchange and Z/γ propagator interference even at $\sqrt{s} = m_Z$ has not been considered here, since it introduces a constant bias.
The result of the fit and the counting leads to

$$\begin{aligned} \text{Fit:} \quad & A_\mathrm{FB}^{b,0} = 0.1009 \pm 0.0001\,, \\ \text{Counting:} \quad & A_\mathrm{FB}^{b,0} = 0.1010 \pm 0.0001\,, \end{aligned} \quad (4.34)$$

where the fit result is shown as green line in Fig. 4.13a. Both results are in precise agreement with each other. However, since the fitting procedure is insensitive to angular acceptance and/or efficiency effects and provides a generally smaller statistical uncertainty, it has been used as default method to compute A_FB^b from angular distributions. Furthermore, the impact of a restricted fit range in $\cos(\theta_b)$ on the uncertainty of is investigated in App. A.2. Yet, since the b-quark polar angle is experimentally inaccessible, different estimators have been used to approximate the initial quark direction $\cos(\theta_b)$ in Eq. (4.33). They are presented below.

Experimental access to the quark direction

In the following paragraphs, different quark-direction estimators are presented, before their accuracy to model the b-quark direction is examined.
First, the thrust axis is considered, which has been the conventional event-shape variable to assess the b-quark direction at LEP [134–137]. Second, a revision of A_FB^b at FCC-ee [152] has explored the possibility of utilising the reconstructed b-tagged

[3] In a first approach, f_L is expected to be zero without considering effects that might distort the b-quark's direction of flight from the radiation of gluons.

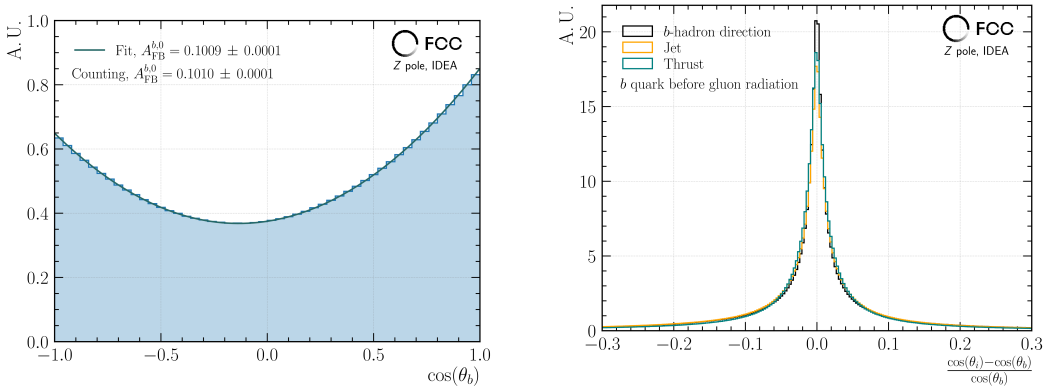

(a) The polar-angle distribution of the b quark before gluon radiation. The fit to Eq. (4.33) results within the statistical uncertainty in the same value as counting the forward and backward hemispheres.

(b) Relative difference of the polar angle of different estimators to the b-quark polar angle before gluon radiation, with the b-hadron direction being the precise approximation.

Figure 4.13: Proof of concept, that extracting $A_{FB}^{b,0}$ from the fit and counting leads to the same result in Fig. (a). In Fig. (b), different approximations of the b-quark direction have been examined.

jet direction, also to reduce the impact of QCD corrections. A recapitulation of this approach is discussed in Sec. 4.5.2. Finally, the list is extended by incorporating the reconstructed b-hadron, which, when fully reconstructed, also approximates the original b-quark direction. The basic principle of this method is described in Sec. 4.2. All of the aforementioned direction estimators are discussed in the following.

Thrust The thrust has been calculated from all particles at the object level as per Eq. (4.2), with the thrust direction identified from the polar angle, where the sign of the z component is extracted from the hemisphere with the higher energy.

Jets Jets at both the particle and object levels have been reconstructed using the anti-k_t jet-clustering algorithm with a cone-radius parameter of $R = 0.4$. More information on the jet-clustering algorithm can be found in Sec. 3.4. To account for additional jets from radiated gluons, the jets have been clustered inclusively with a minimum transverse momentum of 5 GeV. For this analysis, the flavour and charge of the jet have been determined from a matching procedure with the nearest b hadron. However, dedicated algorithms must be installed for a more realistic analysis. Details of the matching are provided in the following paragraph. Furthermore, the jet polar-angle distribution at the object level has been corrected for acceptance effects in the very forward and backward region of the detector using the polar-angle distribution from the jets at the particle level.

B^+ meson Similar to the b-hadron reconstruction described in Sec. 4.4.1, B^+ candidates have been reconstructed by vertexing $\bar{D}^0$ candidates in a first stage from the fast-simulation dataset (3). They have been furthermore combined with a charged-pion track. The final B^+ candidates must have a reconstructed vertex-quality $\chi^2 < 25$ and must meet the mass criteria $(5150 \leq m_{B^+} \leq 5400)\,\text{MeV}$. In the following, it is generally referred to as the b hadron.

An important aspect arises from the reconstructed b-hadron: usually, the b-jet flavour tagging achieves efficiencies of the order $(10 - 90)\,\%$ depending on the background-rejection rate. This is at least an order of magnitude larger compared to the presence of a reconstructed b-hadron from the list of possible decay modes to consider with efficiencies of the order $0.5\,\%$. However, in the case of a reconstructed b-hadron in the event, valuable information can be obtained from it to identify the jet flavour and charge. This can be achieved by matching the b hadron with the jet that is closest to it to minimise the effect from jet-charge confusion using traditional methods discussed in Sec. 4.1.1 and the misidentification of the jet flavour. In addition, the same procedure can be applied to tag the hemisphere charge and flavour when using the thrust axis as a direction estimator. The matching criterion is based on a distance measure ΔR, defined via

$$\Delta R = \sqrt{(\eta_k - \eta_B)^2 + (\phi_k - \phi_B)^2}\,, \quad \text{where} \quad k \in [\text{Jet}_n, \text{Thrust}]\,, \tag{4.35}$$

considering the pseudorapidity η_i and the azimuth ϕ_i. In case of at least two jets per event, the index n considers all of them. Given that the sample used is biased and has been produced so that each hemisphere contains a b hadron, the jet or thrust-hadron pair with the smallest opening angle has been selected to act as the charge and flavour tagger for the hemisphere. This choice has been determined by finding the smallest angle ω between the b hadron, represented as $\boldsymbol{B} = (B_x, B_y, B_z)^\top$, and either a jet or the thrust vector, $\boldsymbol{q} = (q_x, q_y, q_z)^\top$ using the known formula

$$\omega = \sin^{-1}\left(\frac{|\boldsymbol{B} \times \boldsymbol{q}|}{|\boldsymbol{B}| \cdot |\boldsymbol{q}|}\right) \tag{4.36}$$

This method ensures that the pairing reduces the impact of hemisphere confusion caused by high-energy gluon radiation that might change the b-hadron direction. Experimentally, with typically only one b hadron per hemisphere, minimising ΔR from Eq. (4.35) is usually sufficient. The result, shown as the relative difference in the polar-angle distribution in the right panel of Fig. 4.13, compares the different estimators to the b-quark direction before gluon radiation, from which $A_{\text{FB}}^{b,0}$ has been extracted. A narrow, zero-centred distribution is obtained for all estimators; however, the novel approach based on the b-hadron reconstruction method serves as the most precise approximation of the b-quark direction. The jet and thrust axes produce similar results in terms of precision.

Nevertheless, as pointed out earlier, the direction of flight can be distorted by the radiation of gluons, referred to as QCD corrections. An introduction is given in the following, with a focus on experimental handles to minimise their effects.

4.5.2 Angular distortions: QCD corrections

In the determination of A_{FB}^{b} at LEP [134–137] and their combined analysis [1], QCD corrections have contributed to about 50 % of the systematic uncertainty budget and are the leading uncertainty after excluding contamination from *udsc*-physics events. These QCD corrections are mainly due to the emission of high-energy gluons from the b quark before it hadronises, causing the quark's initial direction to change, potentially even reversing it. The degree of this distortion depends on the energy of the emitted gluon(s) and the chosen method for estimating the b-quark's direction, since the quark direction cannot be directly measured in experiments. Consequently, a correction factor must be applied later to account for the distortion, which is further detailed below.

Typically, the uncorrected b-quark forward-backward asymmetry $A_{\mathrm{FB}}^{b,0}$ without gluon radiation is adjusted using a scaling factor $C_{\mathrm{QCD}}(\mu)$ to derive the experimentally measurable A_{FB}^{b}

$$A_{\mathrm{FB}}^{b} = \left(1 - \frac{\alpha_{\mathrm{S}}}{\pi} C_{\mathrm{QCD}}(\mu)\right) A_{\mathrm{FB}}^{b,0}\,, \tag{4.37}$$

where $\mu = {}^{2m_q}\!/_{\sqrt{s}}$ is the quark-specific energy-scale parameter of a quark with mass m_q. In the following, μ is set to 0.107 for b quarks with $m_b = 4.8\,\mathrm{GeV}$ and has been neglected in notations. The main challenge is to reduce the impact of C_{QCD}, making sure that its uncertainty does not increase the total uncertainty of the measurement by using experimental methods that are sensitive to C_{QCD}.

A sensitive parameter identified is the acollinearity between the two b quarks. This method has been explored in earlier studies (see, for example, Ref. [153]), but has been first implemented in an experimental FCC-ee setting in Ref. [152]. Mathematically, the acollinearity angle $\cos(\zeta(x,\bar{x}))$, defined as

$$\cos(\zeta(x,\bar{x})) = \frac{x\bar{x} + \mu^2 + 2(1-x-\bar{x})}{\sqrt{x^2-\mu^2}\sqrt{\bar{x}^2-\mu^2}}\,, \tag{4.38}$$

is a measure for the angle between the two b quarks when projected onto the plane orthogonal to the initial beam-direction. It solely depends on the energy of the b and $\bar{b}$ quark, $x = {}^{2E_b}\!/_{\sqrt{s}}$ and $\bar{x} = {}^{2E_{\bar{b}}}\!/_{\sqrt{s}}$. Furthermore, the analytical expression of C_{QCD} is written in App. A.2.2. However, to illustrate the main conclusions of the formula, the differential correction $I(x,\bar{x})$ in the integral of C_{QCD}, expressed via

$$I(x,\bar{x}) = \frac{(x^2+\bar{x}^2)\cdot(1-\cos(\zeta(x,\bar{x})))}{3(1-x)(1-\bar{x})}\,, \tag{4.39}$$

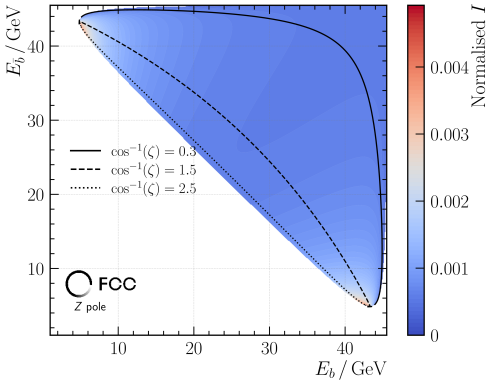

(a) The normalised value of the integrand I on the z axis as function of the b- and $\bar{b}$-quark energy on the x- and y-axis, respectively. The lowest values are achieved for the highest-energetic quarks.

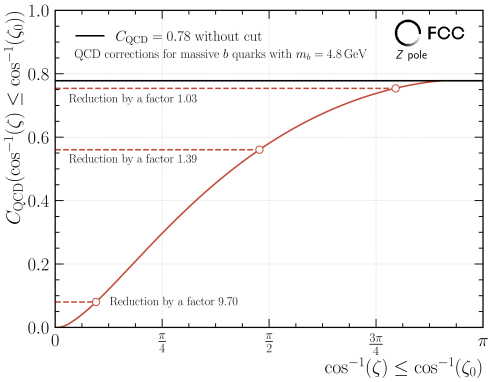

(b) Cuts on the maximally allowed angle effectively reduce the impact of the QCD corrections by about an order of magnitude for $\cos^{-1}(\zeta) \leq 0.3$.

Figure 4.14: Since the QCD corrections C_{QCD} affect the precision of A_{FB}^b, regions in the phase space are found, in which their impact is minimised.

is presented in the left panel of Fig. 4.14 as a function of E_b and $E_{\bar{b}}$ on the x- and y-axis, respectively. It represents a measure for the amount of QCD corrections, where higher values of I correspond to larger values of C_{QCD}. The possibility of radiating gluons from either the b and/or $\bar{b}$ quark is accounted for by symmetrising I accordingly to the expression in Eq. (A.1).

It can be seen that the QCD corrections are largest for the lowest energies possible for the b quarks. The reason for this is the reduction of the b-quark energy when gluons have been radiated beforehand. In the figure, constant acollinearity angles at $\cos^{-1}(\zeta) = [0.3, 1.5, 2.5]$ are shown as black lines and indicate the cut in the phase space when the acollinearity of the b quarks is required to have a certain value.
The effect on the actual QCD corrections C_{QCD} as a function of the upper limit on the acollinearity angle is shown on the right side of Fig. 4.14. Without cuts, $C_{\mathrm{QCD}} = 0.78$, indicated as a horizontal black line. For tighter cuts applied, C_{QCD} reduces significantly by about an order of magnitude for $\cos^{-1}(\zeta) \leq 0.3$, therefore mitigating its impact on the systematic uncertainty of A_{FB}^b. However, a direct approach to reduce I would be to select the highest energetic b-quarks, which requires, in addition to the direction estimation of the b quark, an estimation of E_b and/or $E_{\bar{b}}$. The potential of the reconstructed b-hadron as an energy estimator is discussed in the second part of the following analysis. Furthermore, f_{L} also influences the measurement of A_{FB}^b, and becomes nonzero when including QCD corrections. The impact of f_{L} has been examined in Refs. [152, 154] and is expected to have a minimal effect on A_{FB}^b when kinematic cuts are applied with the aim of reducing the effect of

QCD corrections.

Two strategies have been followed, which are described in detail in the following:

1. A recapitulation of the analysis in Ref. [152] is performed using acollinearity cuts on reconstructed jets as direction estimators. Since cuts on the jet acollinearity require the reconstruction of at least two objects in the event that approximate the b-quark direction, limits on the b-hadron acollinearity are not directly applicable because typically only one b hadron per event is reconstructed. However, the b hadron has been used to extend the study by serving as an unambiguous charge identifier for the hemisphere in the unlikely case of a reconstructed b-hadron in the event (details are given in Sec. 4.5.1). Furthermore, the impact of incorrect pairing of the b hadron with a jet is greatly reduced when acollinearity cuts on the jets are applied, as these cuts are designed to lower the probability for scenarios with three or more jets originating from gluons.
2. A more straightforward and novel approach is presented to experimentally reduce the effects of QCD corrections, which involves leveraging the kinematic properties of the reconstructed b-hadron. This approach is based on also estimating the $b(\bar{b})$-quark energy $E_b(E_{\bar{b}})$ from the energy of the b hadron.

For both, the proof of principle is demonstrated at the parton level first, before applying the concept at the object level.

4.5.3 Acollinearity cuts

In the following section, a recapitulation of the analysis in Ref. [152] is performed using the events in the dataset (3). As a further development of the presented method in Ref. [152], the assumption of a perfect flavour tag in an inclusive $Z \to b\bar{b}$ sample can be adapted by using the exclusively reconstructed b-hadron of the event. However, since only one b hadron is expected to be reconstructed for the measurement of A_{FB}^{b}, an inclusive tag of the other hemisphere jet would be needed to apply acollinearity cuts. In the following, the method is presented first at the parton level.

Parton level The impact of acollinearity cuts is first studied at the parton level, considering the b quarks after gluon radiation. According to Ref. [152], the quark acollinearity cuts have been chosen to

$$\max\left(\cos^{-1}(\zeta)\right) = \{\pi, 1.5, 1.0, 0.5, 0.3, 0.2, 0.1\}\,. \tag{4.40}$$

The size of QCD corrections has then been estimated from Eq. (4.37) to

$$C_{\mathrm{QCD}} = \frac{\pi}{\alpha_{\mathrm{S}}} \frac{A_{\mathrm{FB}}^{b,0} - A_{\mathrm{FB}}^{b}}{A_{\mathrm{FB}}^{b,0}}\,. \tag{4.41}$$

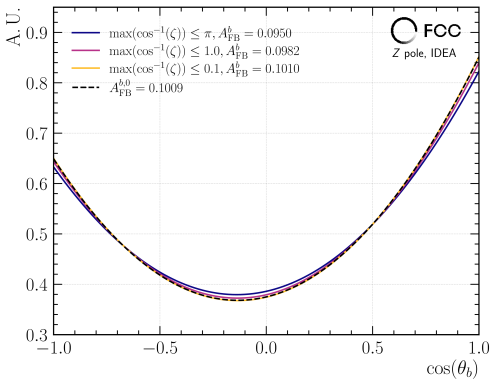

Figure 4.15: The fit result for different cuts on the b-quark acollinearity. The b-quark forward-backward asymmetry without gluon radiation is shown as a dashed line. For tighter cuts, the results converge.

Cut	A_{FB}^{b}	$\alpha_{\mathrm{S}}/\pi \cdot C_{\mathrm{QCD}}$
π	0.0950 ± 0.0001	0.0585
1.5	0.0975 ± 0.0001	0.0337
1.0	0.0982 ± 0.0001	0.0268
0.5	0.0990 ± 0.0002	0.0188
0.3	0.0997 ± 0.0002	0.0119
0.2	0.1003 ± 0.0002	0.0059
0.1	0.1010 ± 0.0004	-0.0009

Table 4.2: A_{FB}^{b} and C_{QCD} computed from the b quarks after gluon radiation for different cuts on the acollinearity. A convergence of A_{FB}^{b} towards $A_{\mathrm{FB}}^{b,0} = 0.1009$ can be observed due to a significant reduction of C_{QCD}.

Given that $A_{\mathrm{FB}}^{b,0}$ and A_{FB}^{b} have been derived from the same dataset, there is no statistical uncertainty associated with C_{QCD}. The numerical values for A_{FB}^{b} and C_{QCD} are shown in Tab. 4.2. The decrease in C_{QCD} due to acollinearity cuts results in A_{FB}^{b} approaching $A_{\mathrm{FB}}^{b,0}$. Consequently, this reduces the influence of C_{QCD} on the overall uncertainty of $A_{\mathrm{FB}}^{b,0}$, which is derived from the propagation of the uncertainty and is considered as the only systematic uncertainty

$$\sigma_{\mathrm{syst.}}(A_{\mathrm{FB}}^{b,0}) = \frac{\sigma(C_{\mathrm{QCD}})A_{\mathrm{FB}}^{b}}{\left(1 - \frac{\alpha_{\mathrm{S}}}{\pi}C_{\mathrm{QCD}}\right)^{2}}\,, \tag{4.42}$$

with the uncertainty on C_{QCD}, $\sigma(C_{\mathrm{QCD}})$. The impact of acollinearity cuts is visualised in Fig. 4.15, which presents the interpolation result for cuts at $\max(\cos^{-1}(\zeta)) = [\pi, 1.0, 0.1]$ together with the result from $A_{\mathrm{FB}}^{b,0}$ in the dashed line. It can be seen that towards tighter cuts, the effect of QCD radiations becomes negligible.

Consequently, cuts on the b-quark acollinearity impact the longitudinal fraction f_{L} as shown in the left panel of Fig. 4.16, while f_{L} has been determined from the simultaneous fit at the parton level to Eq. (4.33). The errorbars represent the uncertainty of the fit. Again, a significant decrease towards $f_{\mathrm{L}} = 0$ can be seen for tighter acollinearity cuts. With the result obtained at the parton level, the study has been extended to use the experimentally accessible jet acollinearity in the following.

Object level At the object level, acollinearity cuts have been implemented between the two jets identified as b jets. In an analysis with actual data from an FCC-ee

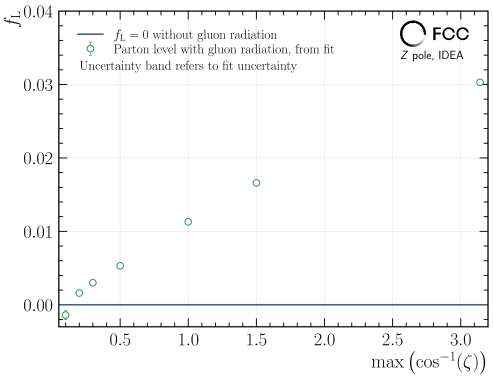

(a) The f_L parameter as function of the maximally allowed b-quark acollinearity.

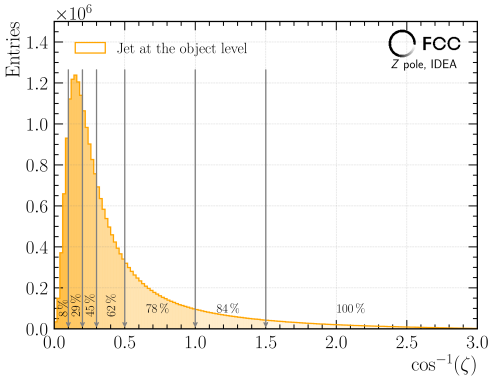

(b) The jet-acollinearity distribution, highlighting also the fraction of events after the application of the cut. About 30 % of the events remain for $\max(\cos^{-1}(\zeta)) \leq 0.2$, for which the effect of QCD corrections is reduced by about one order of magnitude.

Figure 4.16: The longitudinal component f_L as function of the acollinearity cuts at the parton level for the b quarks after gluon radiation. Experimentally, cuts on the jet acollinearity reduce the number of events. The remaining fraction of events is presented in the one-dimensional distribution of the jet acollinearity in Fig. (b).

experiment, specialised tools are required to identify the flavour of both b jets. Additionally, employing a jet-flavour tagging algorithm requires careful handling and consideration of factors such as detector-acceptance effects, since the performance of these algorithms typically depends on the polar angle of the jet.

Compared to the acollinearity cuts applied at the quark level, the acollinearity between two reconstructed jets derived from the jet angles can be greater than one due to inaccuracies in the jet-energy estimation. Consequently, imposing $0 \leq \cos^{-1}(\zeta) \leq \pi$ inherently results in an event cut, which has been determined to be insignificant. The jet-acollinearity distribution for the b jets at the object level is shown in the right panel of Fig. 4.16. This distribution indicates that a substantial portion of events has jet acollinearities below 0.2, thereby reducing C_{QCD} by about an order of magnitude at this working point (refer to Tab. 4.2).

In a manner similar to the parton-level studies, cuts on the jet acollinearity have been applied and A_{FB}^{b} has been determined from the fit. Due to the lack of experimental sensitivity to the longitudinal fraction, the values of f_L have been fixed to those obtained at the parton level. The fit has been performed on the polar-angle distribution of the jet that has been assigned the negative charge in the event.

To establish a threshold where the systematic uncertainty matches the statistical uncertainty, two scenarios have been considered for the systematic uncertainty due

to C_{QCD}. For clarity, the QCD-corrected result from

$$A_{\mathrm{FB}}^{b,0} = \frac{1}{1 - \frac{\alpha_{\mathrm{S}}}{\pi} C_{\mathrm{QCD}}} A_{\mathrm{FB}}^{b}\,, \tag{4.43}$$

has been evaluated below, and the uncertainty from Eq. (4.42) has been computed. The first scenario considers a relative uncertainty on C_{QCD} from Tab. 4.2 to be 1 %, while the second, more conservative scenario, assumes an uncertainty of 5 %. The reduction of the statistical precision $\sigma_{\mathrm{stat.}}(A_{\mathrm{FB}}^{b}) = 1.56 \cdot 10^{-5}$ from Eq. 4.15 is derived from the remaining fraction of events given the jet-acollinearity distribution.

Fig. 4.17 illustrates the results as a function of jet acollinearity, employing a finer binning for the maximum allowed acollinearity cuts compared to previous analyses. The left panel displays A_{FB}^{b} without any QCD corrections at both the object and parton levels following gluon radiation in black and green, respectively. Both results converge towards the horizontal line, which indicates the parton-level value prior to gluon radiation and includes the expected statistical precision as an uncertainty band. It is evident that the statistical uncertainty grows considerably with very stringent acollinearity cuts. The discrepancy between the object-level and parton-level results stems from selection criteria and the impact of jet acollinearity, such as the requirement for at least two b-tagged jets. Further factors include the detector-acceptance effects of additional gluon jets. However, this effect reduces with tighter acollinearity cuts, thus reducing the discrepancy, since the general event topology of the jets becomes more *back-to-back*. For acollinearity cuts below 0.8, the difference becomes almost negligible.

In contrast, the QCD-corrected value $A_{\mathrm{FB}}^{b,0}$ from Eq. (4.43) is illustrated on the right side of Fig. 4.17. In this context, A_{FB}^{b} has been derived from the object-level distribution to overcome the discrepancies between the object- and parton-level quantities, as previously discussed, since the aim of this study is to determine an appropriate cut on the jet acollinearity, where the systematic precision matches the statistical precision. The systematic uncertainty is shown for the two scenarios $\sigma(C_{\mathrm{QCD}})/C_{\mathrm{QCD}} = [1, 5]\,\%$ in darker and lighter orange, respectively. The result shows that in both cases the systematic uncertainty reduces with tighter jet-acollinearity cuts. From the intersection $\sigma_{\mathrm{stat.}}(A_{\mathrm{FB}}^{b,0}) = \sigma_{\mathrm{syst.}}(A_{\mathrm{FB}}^{b,0})$, the optimal thresholds have been determined to be $\max(\cos^{-1}(\zeta)) \leq 0.66$ and $\max(\cos^{-1}(\zeta)) \leq 0.24$ and the uncertainties on $A_{\mathrm{FB}}^{b,0}$ result to

$$\begin{aligned}
\frac{\sigma(C_{\mathrm{QCD}})}{C_{\mathrm{QCD}}} = 5\,\% \;&\Rightarrow\; A_{\mathrm{FB}}^{b,0} = \mu(A_{\mathrm{FB}}^{b,0}) \,\pm\, 4.5 \cdot 10^{-5}(\mathrm{stat.}) \,\pm\, 4.5 \cdot 10^{-5}(\mathrm{syst.}) \\
\frac{\sigma(C_{\mathrm{QCD}})}{C_{\mathrm{QCD}}} = 1\,\% \;&\Rightarrow\; A_{\mathrm{FB}}^{b,0} = \mu(A_{\mathrm{FB}}^{b,0}) \,\pm\, 2.2 \cdot 10^{-5}(\mathrm{stat.}) \,\pm\, 2.2 \cdot 10^{-5}(\mathrm{syst.})\,.
\end{aligned} \tag{4.44}$$

Here, it is assumed that in a more realistic scenario the statistical uncertainty behaves similarly when only one hemisphere has been exclusively reconstructed and the other

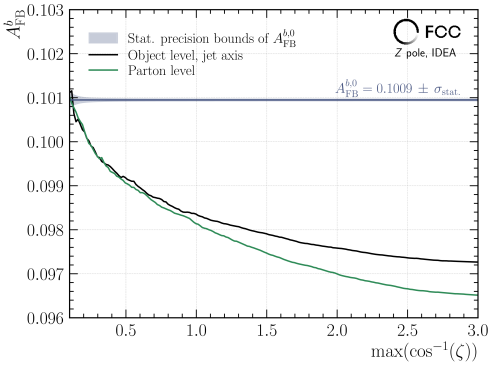

(a) The non-QCD-corrected A_{FB}^{b} as function of the jet-acollinearity, comparing the jet direction at the object level and the b-quark direction at the parton level. Differences become negligible for jet acollinearities below 0.8.

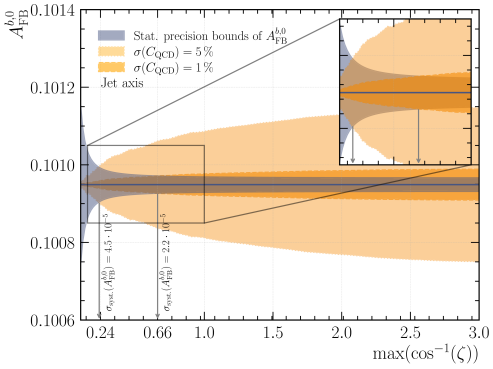

(b) The QCD-corrected A_{FB}^{b} from the jet-axis direction. The decrease and increase of the systematic and statistical uncertainty are shown as orange and blue bands, respectively. The intersection defines the threshold value for two scenarios of the QCD corrections uncertainty.

Figure 4.17: Jet-acollinearity cuts are valid estimators for the amount of direction distortion of the b quark and the jet direction. For tighter cuts, both converge towards $A_{\mathrm{FB}}^{b,0}$. By applying the QCD corrections, optimal thresholds at $\max(\cos^{-1}(\zeta)) \leq 0.66$ and $\max(\cos^{-1}(\zeta)) \leq 0.24$ have been found for two scenarios of the uncertainty on the QCD corrections, for which $\sigma_{\mathrm{stat.}}(A_{\mathrm{FB}}^{b}) = \sigma_{\mathrm{syst.}}(A_{\mathrm{FB}}^{b})$.

one decays inclusively. With this result, the analysis of jet-acollinearity cuts as a means to reduce the QCD corrections is concluded. Nevertheless, the effects of the jet-clustering algorithm, b-jet tagging, and the transverse-momentum cut still require further investigation. To inherently address the aforementioned issues, the next section studies the potential of minimising the QCD correction through kinematic cuts on the b hadron, eliminating the necessity of clustering and tagging b jets in the event.

4.5.4 *b*-hadron energy cuts

In order to minimise the QCD corrections, the kinematic characteristics of the reconstructed b-hadron in the event can be used. Analogously to the investigation of acollinearity cuts, the feasibility has initially been confirmed at the parton level with energy cuts on the b quarks after gluon radiation. It is mentioned that, because both hemispheres are compelled to contain two b hadrons, there are events with one or two reconstructed b hadrons in the event. If both b hadrons have been reconstructed, one has been chosen randomly to avoid biases in the determination of A_{FB}^{b}. To comply with this strategy at the parton level, only one of the b quarks is randomly required to meet the energy criterion.

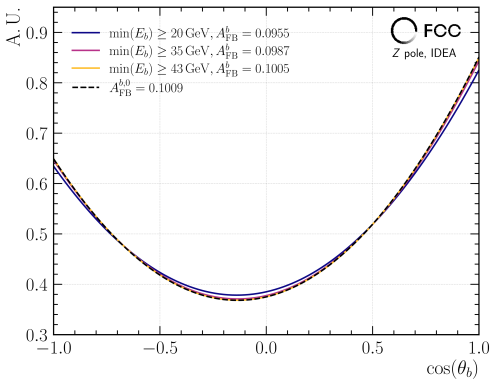

Figure 4.18: The fit result for different cuts on the b-quark energy. The b-quark forward-backward asymmetry without gluon radiation is shown as a dashed line. For tighter cuts, the results converge.

Cut	A_{FB}^b	$\alpha_{\text{S}}/\pi \cdot C_{\text{QCD}}$
10	0.0955 ± 0.0001	0.0535
20	0.0968 ± 0.0001	0.0406
30	0.0980 ± 0.0001	0.0287
35	0.0987 ± 0.0002	0.0218
40	0.0994 ± 0.0002	0.0156
41	0.0996 ± 0.0002	0.0129
42	0.0998 ± 0.0002	0.0109
43	0.1005 ± 0.0003	0.0040
44	0.1009 ± 0.0004	0.0000

Table 4.3: A_{FB}^b and C_{QCD} computed from the b quarks for different cuts on the b-quark energy. A convergence of A_{FB}^b towards $A_{\text{FB}}^{b,0}$ can be observed due to a significant reduction of C_{QCD}.

Parton level As first step, suitable energy cuts have been chosen to be

$$\min(E) \geq \{10, 20, 30, 35, 40, 41, 42, 43, 44\}\,, \tag{4.45}$$

with an emphasis on the higher energies, since it is expected that the reduction of the QCD corrections is driven by the highest-energetic b quarks or hadrons.

The parton-level result is illustrated in Fig. 4.18 and is numerically detailed in Tab. 4.3. As expected, the magnitude of the QCD corrections is significantly reduced for higher b-quark energies following gluon radiation. Consequently, the QCD corrections are reduced by approximately an order of magnitude for b-quark energies above 43 GeV.

The impact on f_{L} is presented on the left side of Fig. 4.19, which shows a similar trend towards zero compared to the acollinearity cuts for higher-energy cuts on the b quark. This result motivates the use of an effective reduction of the QCD corrections by applying cuts on the b-hadron energy in the paragraph below.

Object level Since the cuts on the b-hadron energy aim to improve the direction estimation of the initial b-quark prior to gluon radiation, a differential analysis of the relative polar-angle difference has been carried out, showing the mean of the relative difference in bins of the b-hadron energy in the left panel of Fig. 4.20. For clarity, the standard error of the mean has been increased by a factor of ten and is shown as an error bar on the points. The bias in the distribution, expressed by the difference of the points to the zero line, reduces to zero for the highest-energetic b hadrons. Accordingly, the 68 % and 90 % smallest intervals of the relative polar-angle

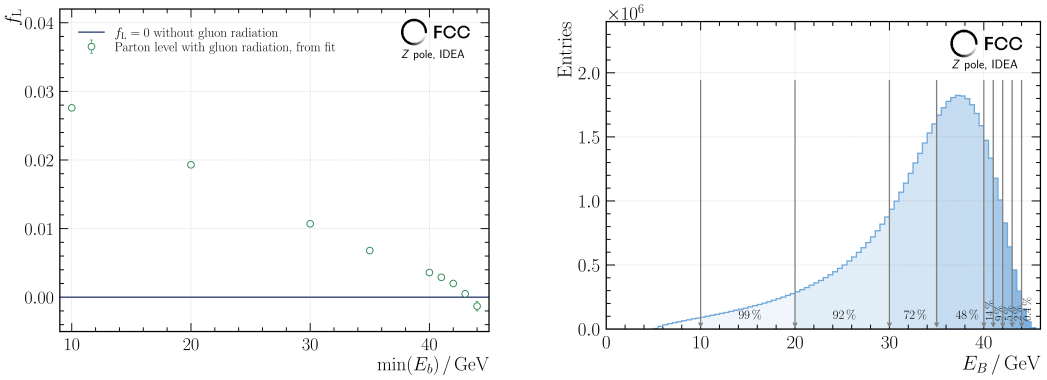

(a) The f_L parameter as function of the maximally allowed b-quark energy.

(b) The energy distribution of the b hadron, indicating also the fraction of events when applying the different energy cuts.

Figure 4.19: The longitudinal component f_L as function of the energy cuts at the parton level for the b quarks after gluon radiation. Experimentally, cuts on the b-hadron energy reduce the number of events, where the remaining fraction of events is presented in the one-dimensional distribution in Fig. (b).

resolution are shown in the right panel of Fig. 4.20, which decrease significantly with increasing energy. The remaining ranges of the order 0.03 and 0.1 for the smallest 68 % and 90 % intervals at energies above 44 GeV are due to hadronisation effects.

Although a notable reduction in bias and a gain in direction-estimation precision can be achieved for the highest-energetic candidates, the loss in statistical precision is significant. This is evident when examining the b-hadron's energy distribution in the right panel of Fig. 4.19, where only a small fraction of candidates of the order 10 % remains after placing cuts on the b-hadrons energy above 40 GeV.

Nevertheless and similarly to the study of the jet-acollinearity cuts, the primary focus is on the threshold value that reduces the impact of C_{QCD} on A_{FB}^b to a level such that the systematic uncertainty on A_{FB}^b becomes competitive with the statistical precision. Following this, A_{FB}^b has been derived from the polar-angle distribution of the negatively charged b-hadron.

In analogy to the studies in Sec. 4.5.3, a finer binning of the energy cuts has been chosen to properly identify the threshold, at which $\sigma_{\mathrm{stat.}}(A_{\mathrm{FB}}^b) = \sigma_{\mathrm{syst.}}(A_{\mathrm{FB}}^b)$ for the two scenarios of the relative QCD-correction uncertainty $\sigma(C_{\mathrm{QCD}})/C_{\mathrm{QCD}} = [1, 5]\,\%$. The left panel of Fig. 4.21 presents the result normalised to the object level as a function of the reconstructed b-hadron energy, similar to Fig. 4.17b. The statistical precision is again shown in the grey uncertainty band, while the systematic uncertainty for $A_{\mathrm{FB}}^{b,0}$ for the more conservative and optimistic estimations for $\sigma(C_{\mathrm{QCD}})/C_{\mathrm{QCD}}$ are presented in lighter and darker orange, respectively. The threshold values have been

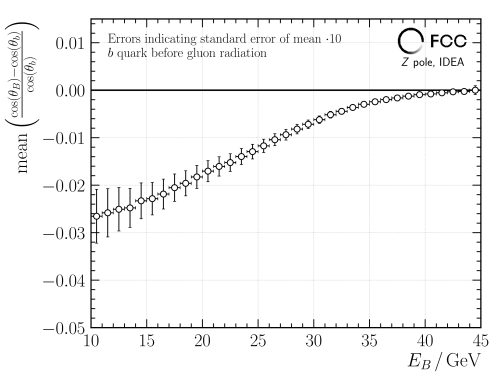

(a) The mean of the relative difference of the b-quark polar-angle before gluon radiation and the reconstructed B meson. The uncertainties shown refer to the standard error of the mean and have been scaled by a factor of ten for visibility.

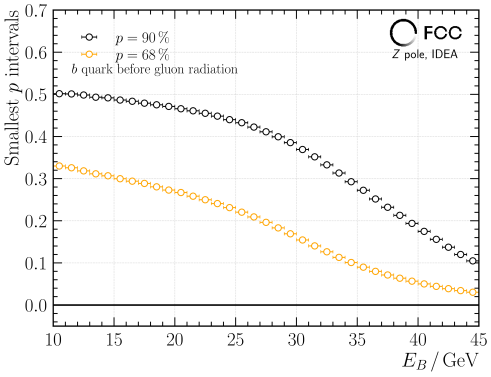

(b) The 68 % and 90 % smallest intervals of the relative polar-angle resolution.

Figure 4.20: The impact of energy cuts applied on the reconstructed b hadrons on the accuracy of the b-quark direction estimation.

found to be $\min(E_B) \geq 32\,\text{GeV}$ and $\min(E_B) \geq 38.1\,\text{GeV}$ for $^{\sigma(C_{\text{QCD}})}/_{C_{\text{QCD}}} = 1\,\%$ and 5 %, respectively. This results in the final uncertainties for $A_{\text{FB}}^{b,0}$

$$\begin{aligned} \frac{\sigma(C_{\text{QCD}})}{C_{\text{QCD}}} = 5\,\% \;&\Rightarrow\; A_{\text{FB}}^{b,0} = \mu(A_{\text{FB}}^{b,0}) \pm 5.6 \cdot 10^{-5}\,(\text{stat.}) \pm 5.6 \cdot 10^{-5}\,(\text{syst.})\,, \\ \frac{\sigma(C_{\text{QCD}})}{C_{\text{QCD}}} = 1\,\% \;&\Rightarrow\; A_{\text{FB}}^{b,0} = \mu(A_{\text{FB}}^{b,0}) \pm 2.3 \cdot 10^{-5}\,(\text{stat.}) \pm 2.3 \cdot 10^{-5}\,(\text{syst.})\,. \end{aligned} \tag{4.46}$$

The total uncertainty on $A_{\text{FB}}^{b,0}$ in the conservative and optimistic scenario results to $7.9 \cdot 10^{-5}$ and $3.3 \cdot 10^{-5}$, respectively. Consequently, this would improve the measurement uncertainty from the LEP average in Eq. (4.32) by about a factor of 20 and 50.

4.5.5 Impact on SM parameters

Fundamental SM parameters directly depend on the measurement of A_{FB}^{b}, as pointed out in Sec. 2.2.1. Especially the constraints on $\sin^2(\theta_{\text{W}})$ are expected to be competitive with those in reach from the muon forward-backward asymmetry, A_{FB}^{μ}, with a notable improvement in the measurement of A_{FB}^{b}. The impact on $\sin^2(\theta_{\text{W}})$ is discussed in the following. Furthermore, indirect constraints on the top-quark mass can be obtained from virtual top-quarks in loops that contribute to the $Zb\bar{b}$ vertex corrections. These indirect constraints are presented at the end of this section.

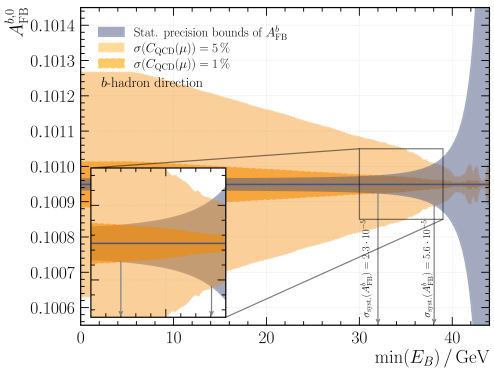

(a) Similar to Fig. 4.17b, but for the b-hadron energy instead of the jet-acollinearity on the x axis, since E_B does not require to reconstruct and tag the flavour of the jets, which introduce another source of systematic uncertainty.

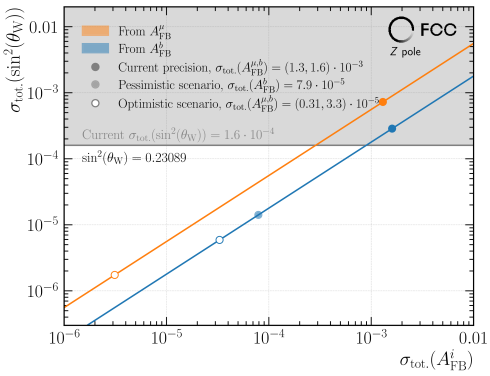

(b) The total uncertainty on $\sin^2(\theta_W)$ as function of the total uncertainty on A_{FB}^i for $i \in [\mu, b]$, assuming that $\sigma_{tot.}(\sin^2(\theta_W))$ only arises from variations in A_{FB}^i. With the exclusively reconstructed b hadrons as hemisphere tagger, a competitive method has been developed to challenge the precision on $\sin^2(\theta_W)$ from A_{FB}^{μ}.

Figure 4.21: The energy of the b hadron directly serves as estimator for the amount of gluon radiation, which distort the initial b-quark direction. With a cut of $\min(E_B) \geq 32\,\text{GeV}$ and a knowledge of the QCD corrections of 1 %, $\sin^2(\theta_W)$ can be derived with similar precision compared to A_{FB}^{μ}.

Constraints on the weak mixing angle From the b-quark forward-backward asymmetry, the weak mixing angle $\sin^2(\theta_W)$ can be extracted using Eq. (2.7) and the explicit formulations of v_f and a_f. Although the standard method for extracting $\sin^2(\theta_W)$ is through A_{FB}^{μ}, A_{FB}^{b} can provide a competitive method for comparing both methods to probe departures. This is because the sensitivity of A_{FB}^{b} is approximately three times higher than that of A_{FB}^{μ}. Consequently, the uncertainty on $\sin^2(\theta_W)$ derived from A_{FB}^{b} is about three times lower than that derived from A_{FB}^{μ}, given the same total uncertainty.

Therefore, it is worthwhile to calculate $\sigma_{tot.}(\sin^2(\theta_W))$ using the latest estimation [39] for the precision of A_{FB}^{μ} expected at FCC-ee

$$\sigma_{tot.}(A_{FB}^{\mu}) = \sqrt{(2 \cdot 10^{-6}(\text{stat.}))^2 + (2.4 \cdot 10^{-6}(\text{syst.}))^2} \tag{4.47}$$

and $\sigma_{tot.}(A_{FB}^{b})$ (see Eq. (4.46)). In $\sigma_{tot.}(A_{FB}^{\mu})$, the systematic uncertainty mainly arises from the knowledge of the COM energy. Numerical methods from the `scipy` library have been used to calculate

$$\begin{aligned} \sin^2(\theta_W) &= f(A_{FB}^i)\,, \\ \sigma_{tot.}(\sin^2(\theta_W)) &= \left(\frac{\partial f(A_{FB}^i)}{\partial A_{FB}^i}\right) \cdot \sigma_{tot.}(A_{FB}^i)\,, \end{aligned} \tag{4.48}$$

for $\sin^2(\theta_{\mathrm{W}}) = 0.23089$. The result is presented in the right panel of Fig. 4.21 for the muon and b quark in orange and blue, respectively. The grey-shaded area indicates the most precise uncertainty of $\sin^2(\theta_{\mathrm{W}})$ to date. The filled points represent the currently most accurate measurements of $A_{\mathrm{FB}}^{\mu,b}$ [28]. The shaded and white blue dot show the pessimistic and optimistic scenario, where the pessimistic scenario assumes $\sigma(C_{\mathrm{QCD}})/C_{\mathrm{QCD}} = 5\,\%$ and the optimistic scenario assumes $\sigma(C_{\mathrm{QCD}})/C_{\mathrm{QCD}} = 1\,\%$.

The figure reveals a bias between both representations, which originates from the higher sensitivity of A_{FB}^{b} to $\sin^2(\theta_{\mathrm{W}})$. In the pessimistic case, an improvement in the precision of $\sin^2(\theta_{\mathrm{W}})$ of about one order of magnitude is within reach. In contrast, the result becomes comparable to the one obtainable with A_{FB}^{μ} in the optimistic scenario, where the precision from A_{FB}^{b} compared to A_{FB}^{μ} is worse by about a factor of three.

Indirect top-quark mass constraint From the relation in Eqs. (2.8) and (2.9), indirect constraints on the top-quark mass can be derived, as done at LEP with an uncertainty of the order of 10 GeV before the discovery of the top quark at Tevatron [155]. Here, this has been carried out for A_{FB}^{b}, while probing the top-quark mass in vertex corrections from R_b brings additional precision. For A_{FB}^{b}, radiative and vertex corrections are assumed to originate solely from top-quark loops. The remaining definitions are provided in App. A.2. Again, a numerical minimisation has been performed to calculate the uncertainty on the top-quark mass, $\sigma_{\mathrm{tot.}}(m_t)$ as a function of the uncertainty of A_{FB}^{b}. The result has been computed for both the pessimistic and optimistic scenarios and is presented graphically in Fig. A.7 in App. A.2. The numerical results are $\mathcal{O}(\sigma_{\mathrm{tot.}}(m_t)) = 200\,\mathrm{MeV}$ and $\mathcal{O}(\sigma_{\mathrm{tot.}}(m_t)) = 100\,\mathrm{MeV}$ in the pessimistic and optimistic scenarios of $\sigma_{\mathrm{syst.}}(A_{\mathrm{FB}}^{b})$, respectively.

4.6 Conclusions

Although a powerful collider concept like FCC-ee unlocks unprecedented statistical precision with an enormous amount of $\mathcal{O}(10^{12})$ Z-boson decays, it requires careful consideration of controlling systematic uncertainties, which do not shrink by default when collecting more data. To substantially improve on fundamental SM parameters and to provide a competing method for their validation, new approaches to measuring the quantities of interest are needed. This has been demonstrated in the field of b-quark EWPOs by tagging the hemisphere flavour with exclusively reconstructed b-hadrons, eliminating over 75 % of the systematic uncertainty in the measurement of R_b and A_{FB}^{b}. Historically, both observables have suffered from contamination by lighter quarks. It could be shown through six representative decay modes that purities above 99.8 % are achievable using exclusively reconstructed b-hadrons as hemisphere-flavour tagger. Further studies have addressed subleading systematic

uncertainties, specifically the hemisphere correlation and the QCD correction for R_b and A_{FB}^b, respectively. The sources of these uncertainties have been identified and mitigated by removing the PV dependence and using the energy of the b hadron to estimate the angular distortion from radiated gluons prior to hadronisation. For A_{FB}^b, QCD corrections must be known with a relative precision of 1 %, while it is sufficient to estimate the hemisphere correlation with 10 % precision. With these assumptions, R_b, A_{FB}^b and $\sin^2(\theta_{\mathrm{W}})$ can be measured with the following precisions

$$\begin{aligned} R_b &= \mu(R_b) && \pm\, 2.22 \cdot 10^{-5}\,(\text{stat.}) \pm\, 2.16 \cdot 10^{-5}\,(\text{syst.})\,, \\ A_{\mathrm{FB}}^b &= \mu(A_{\mathrm{FB}}^b) && \pm\, 2.30 \cdot 10^{-5}\,(\text{stat.}) \pm\, 2.30 \cdot 10^{-5}\,(\text{syst.})\,, \\ \Rightarrow \sin^2(\theta_{\mathrm{W}}) &= \mu(\sin^2(\theta_{\mathrm{W}})) && \pm\, 5.55 \cdot 10^{-6}\,. \end{aligned}$$

Furthermore, indirect top-quark mass constraints of the order $\mathcal{O}(100\,\mathrm{MeV})$ are in reach.

4.7 Outlook

Disclaimer: Parts of the following results have been achieved and were kindly provided by the master student A. Garcia Gonzalez under the author's supervision. All studies are outlined at the object level.

The successful application of exclusively reconstructed b-hadrons as hemisphere-flavour taggers has motivated the extension of the technique to measure R_c and potentially A_{FB}^c using exclusively reconstructed c-hadrons. The possible decay modes include both neutral and charged c-mesons, as well as cs mesons and c baryons, as detailed in App. A.3.1. The sum of these modes results in a significantly increased tagging efficiency of approximately 22 %, considering only 15 decay modes in total. Unlike b-hadron decays, contamination in the signal region is expected not only from gluon-splitting events but also from b-meson decays via $X_b \to X_c$. Therefore, in contrast to R_b, the double-tag equations are extended in case for R_c

$$\begin{aligned} \text{Single } c\text{-tag:} \quad & N_{\mathrm{ST}}^c = 2N_Z \cdot (R_c\varepsilon_c^c + R_b\varepsilon_b^c + R_{uds}\varepsilon_{uds}^c) \\ \text{Double } c\text{-tag:} \quad & N_{\mathrm{DT}}^c = N_Z \cdot (R_c(\varepsilon_c^c)^2 C_c + R_b(\varepsilon_b^c)^2 C_b + R_{uds}(\varepsilon_{uds}^c)^2 C_{uds}) \\ \text{Double } c\text{- and } b\text{-tag:} \quad & N_{\mathrm{DT}}^{cb} = N_Z \cdot (R_c\varepsilon_c^c\varepsilon_c^b C_{cb} + R_b\varepsilon_b^b\varepsilon_b^c C_{bc} + R_{uds}\varepsilon_{uds}^{uds}\varepsilon_{uds}^c C_{udsc}) \end{aligned} \tag{4.49}$$

Again, N_Z corresponds to the total hadronic fraction of Z-boson decays and ε_i^j are the efficiencies to tag a flavour j of a quark flavour i. This set of equations allows to simultaneously measure R_c, ε_c^c and ε_b^c, while the remaining inputs have to be determined either from MC simulation or directly from data in the case of R_b and ε_b^b via, for example, the exclusive b-hadron reconstruction presented earlier in this thesis. Furthermore, the efficiency correlation of the hemispheres, quantified by $C_{i(j)}$,

requires a precise control at unity. Since the effect of gluon splitting is negligible compared to the impact of misidentification, ε_c^b and ε_{uds}^c are assumed to be zero.

Since the background contamination from ε_i^c is itself a source of systematic uncertainty, a balanced trade-off must be found between the loss in statistical precision and reduction in systematic uncertainty from high-purity charm tags. For the sake of the feasibility study of this approach, the $\bar{D}^0 \to K^+\pi^-$ mode has been chosen to be exclusively reconstructed from a sample of $8 \cdot 10^7$ $Z \to q\bar{q}$ in the IDEA detector concept. The following kinematic and topological cuts have been applied to the signal candidates in order to reduce the contamination from background events

- $p(\bar{D}^0) \geq 16\,\text{GeV}$
- $\log(1-\Omega) \leq -9.2$
- $\bar{D}^0$ flight-distance $\leq 3\,\text{mm}$
- No leptons in the same hemisphere
- $|d_0(K^+)| \leq 1\,\text{mm}$

Furthermore, the scaled pointing angle $\log(1-\Omega)$ is defined as

$$\Omega = \frac{\boldsymbol{d} \cdot \boldsymbol{p}(\bar{D}^0)}{|\boldsymbol{d}| \cdot |\boldsymbol{p}(\bar{D}^0)|}\,, \tag{4.50}$$

with the vector $\boldsymbol{d}$ defined between the PV and the $\bar{D}^0$ decay-vertex and its flight direction $\boldsymbol{p}(\bar{D}^0)$ to account for angular distortions from previous b-meson decays. Its distribution is shown in the left panel of Fig. 4.22. The resulting tagging efficiencies are summarised to be

$$\begin{aligned}
\varepsilon_c^c &= 0.006\,35 \pm 0.000\,03\,, \\
\varepsilon_b^c &= 0.000\,35 \pm 0.000\,01\,, \\
\varepsilon_{uds}^c &= (1.42 \pm 0.06) \cdot 10^{-6}\,.
\end{aligned}$$

The invariant-mass distribution of the $\bar{D}^0$ candidates is shown in the right panel of Fig. 4.22. With the stated efficiencies the statistical precision of R_c has been calculated to

$$\sigma_{\text{stat.}}(R_c) = 3.4 \cdot 10^{-5}\,, \tag{4.51}$$

which translates in an improvement of about a factor 100 compared to the statistically most precise measurement from the SLD Collaboration [156]. The inclusion of more decay modes will improve on the statistical precision, however, the control of the systematic uncertainty already at this level becomes challenging.

Controlling the background contamination From the set of equations (4.49) the impact of ε_b^c and its uncertainty on the uncertainty of R_c can be calculated. In order to meet the statistical precision of R_c in Eq. (4.51), ε_b^c must be known with a total uncertainty of $\sigma(\varepsilon_b^c) \approx 1.1 \cdot 10^{-7}$, which corresponds to a relative uncertainty of

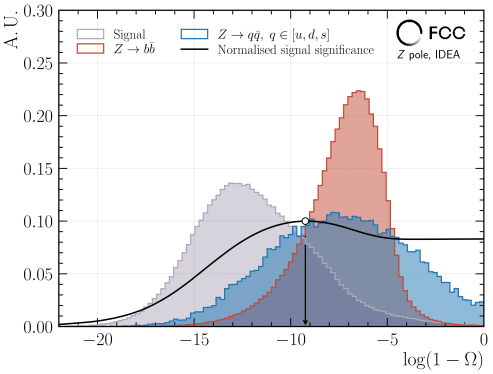

(a) Distribution of the scaled pointing angle $\log(1 - \Omega)$, which shows good separation power, especially against background events originating from b-hadron decays.

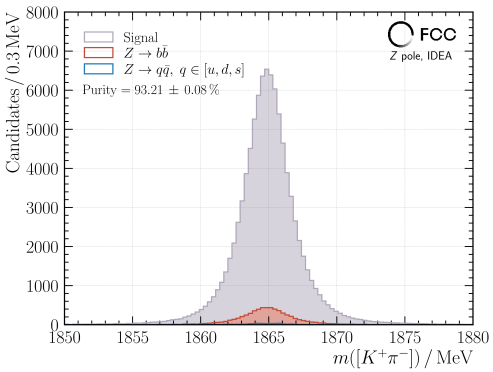

(b) Invariant-mass distribution of $\bar{D}^0$ candidates. Simple kinematic and topological cuts have been applied to suppress the background contamination. A purity of the preliminary selection of about 93 % is in reach.

Figure 4.22: The distribution of the scaled pointing angle as defined in Eq. (4.50) in Fig. (a) and the invariant-mass distribution in Fig. (b) after the cuts summarised above.

$\frac{\sigma(\varepsilon_b^c)}{\varepsilon_b^c} = 0.0003$. However, from the counting rate N_{DT}^{cb} and the precision on R_b and ε_b^b in reach ($\sigma(R_b) = 3.1 \cdot 10^{-5}$ and $\sigma(\varepsilon_b^b) = 1.5 \cdot 10^{-6}$), the precision on ε_b^c from these inputs is calculated to

$$\sigma(\varepsilon_b^c) = 2.1 \cdot 10^{-7}\,, \tag{4.52}$$

which would still result in a systematically dominated measurement with

$$\sigma_{\mathrm{syst.}}(R_c, \text{ from } \varepsilon_b^c) = 6.6 \cdot 10^{-5}\,. \tag{4.53}$$

Therefore, more sophisticated methods to further reduce ε_b^c need to be employed such as multivariate analyses techniques, which are, however, beyond the scope of this thesis.

Going further down in the quark-mass hierarchy, a preliminary approach to assess R_s, R_{us} and eventually A_{FB}^s using strange hadrons is presented in App. A.4.

5 Sensitive top-quark measurements

Complementary to the high-precision measurements of EWPOs from the run at the Z-pole energy at and around $\sqrt{s} = m_Z$, at FCC-ee the properties of the top quark and its couplings will be studied from the threshold scan at $\sqrt{s} = (340-350)\,\text{GeV}$ and the subsequent run at $\sqrt{s} = 365\,\text{GeV}$. The following chapter covers the exploration of top-quark-related observables that show sensitivity to modifications due to effective dimension-six operators.

The chapter is organised as follows: at the beginning in Sec. 5.1, methods for assessing how observables are affected by the modifications from dimension-six operators are described, followed by a detailed study of the $t\bar{t}$-system reconstruction in a FCC-ee environment in the semi and dileptonic final-state in Sec. 5.3. In Sec. 5.4, statistical uncertainties and a first assessment of systematic uncertainties are presented.

5.1 Sensitive observables

Starting point for the exploration of possible observables has been the former analysis presented in Ref. [65], which has considered the total production cross-section and the top-quark forward-backward asymmetry at the CLIC [88] as a proxy for a future Higgs factory. Ref. [65] also considers the interplay between current LHC measurements from the ATLAS, CMS, and LHCb Collaborations in the top- and beauty-quark sector by including recent B anomalies [157, 158] through a common set of SMEFT operators.

The exploration of top-quark observables at a future lepton collider is motivated by recent measurements at the LHC, where also anomalous couplings have been tested [43, 45]. In contrast to the primary production process via gluon-gluon fusion in pp collisions, at an e^+e^- collider, top-quark pair production predominantly occurs through the s-channel Feynman diagram with an intermediate Z-boson or photon. As indicated in Fig. 5.1, modification of the $t\bar{t}$ production and decay vertices can include gauge bosons or point-like interactions in the case of four-fermion operators. Their effect can be probed in different observables[1]. This difference in the production

[1] Here, only the observables relevant for the following analysis are mentioned.

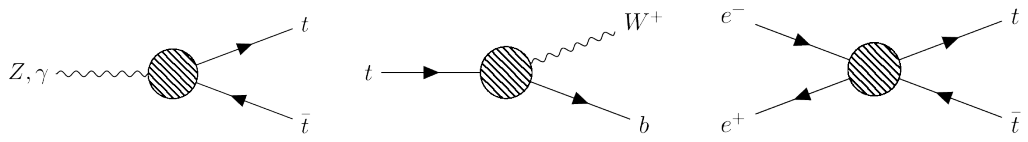

(a) Modification of the $t\bar{t}$ production.

(b) Modification of the $t\bar{t}$ decay at the Wtb vertex.

(c) Point-like interaction of four fermions.

Figure 5.1: Vertex modifications from dimension-six operators indicated as circle.

mechanism allows for the consideration of additional observables, such as the top-quark forward-backward asymmetry, which can be experimentally accessed at a lepton collider due to the coupling of the top quark to the Z boson. Furthermore, the semi and dileptonic production cross-sections $\sigma_{t\bar{t}}^{1\ell}$ and $\sigma_{t\bar{t}}^{2\ell}$ can be influenced by the presence of BSM physics. The unique capability of an energy threshold scan around the top-quark pair production threshold, in the range of $\sqrt{s} = (340 - 350)\,\text{GeV}$, offers the opportunity to measure the top-quark decay width Γ_t with a statistical precision of 45 MeV.

The near-instantaneous decay of the top quark before hadronisation preserves its spin information in the decay products. The helicity states of the W boson, particularly the left-handed and longitudinal helicity fractions F_L and F_0, may contain signatures of BSM physics. Similarly, angular relations of the two leptons from the W-boson decays contain sensitive information about the top-quark polarisation states $B_i^\pm$ and their spin correlations C_{ii} and $C_{ij} + C_{ji}$. In addition, the asymmetry of the opening-angle distribution of the two leptons $A_{\ell\ell}$ with excellent experimental resolution has been used.

In order to examine the observable's potential to discover deviations from the SM prediction, sensitivity studies have been outlined, which are described in detail in the following section.

5.2 Exploration of the BSM phase-space

The following section describes the exploration of the Wilson coefficient parameter-space corresponding to dimension-six operators in the top-quark sector at FCC-ee with relevant observables that are sensitive to modifications of the SM Lagrangian. For this, the MG event generator in version `2.7.0` has been used, and the effective operators have been provided by the `dim6top_LO` UFO model. This setup has been used to generate MC events at LO at the parton level with a beam energy of 182.5 GeV for the electron and positron beams, respectively. The default top-quark mass has been set to 172 GeV and the BSM energy-scale to $\Lambda = 1\,\text{TeV}$. Semi and dileptonic $t\bar{t}$ events have been generated by varying only one Wilson coefficient at a

time within $-1.0 \leq \tilde{C}_i \leq 1.0$ while setting all other coefficients to zero. For better comparability with the selection applied during the reconstruction as outlined in detail in Sec. 5.3, a minimal energy cut on the final-state leptons[2] of 10 GeV has been applied. Subsequently, the sensitivity of the observable as a function of the Wilson coefficient value has been evaluated. While this approach requires measuring the observables from the fully reconstructed $t\bar{t}$ system, an alternative approach is briefly presented below, solely based on the kinematic properties of final-state objects. It is referred to as *optimal-observable* approach [159].

Excursion: optimal observables An important study that has already been performed to investigate BSM modifications of the top-quark coupling to the photon and the Z boson in production processes is an optimal-observable analysis [160]. It has investigated the potential sensitivity to independently access the (anomalous) $t\bar{t}\gamma$ and $t\bar{t}Z$ couplings. With this analysis, it could be shown that no longitudinally polarised incoming electron and positron beams in addition to COM energies well above the $t\bar{t}$ threshold are needed to disentangle the two bosonic couplings, for which the final-state polarisation of the top quarks compensates. Other use cases have been presented in Ref. [161] which explores the sensitivity of top-quark cross sections and the forward-backward asymmetry for different future lepton collider concepts.

The conceptual principles of an optimal-observable analysis are described in the following.
The idea of using optimal observables was born in studies at LEP, inferring the polarisation of the τ lepton from the total $Z \to \tau^+\tau^-$ rate [159]. It is known to maximise the sensitivity to linear modifications of a nominal quantity taking into account the fully differential cross-section $\mathrm{d}\sigma/\mathrm{d}\Phi$ of a phase-space element $\mathrm{d}\Phi$. In the case of dimension-six operator modifications and their strength in terms of Wilson coefficients C_i, the squared SM matrix-element S_{SM} is modified in linear order via

$$\frac{\mathrm{d}\sigma}{\mathrm{d}\Phi} = S_{\mathrm{SM}}(\Phi) + \sum_i C_i S_i(\Phi)\,. \tag{5.1}$$

In Eq. (5.1), Φ is a set of kinematic variables that characterise the final state (for example momenta or polar angles of leptons) and $S_i(\Phi)$ are the interference EFT matrix-elements. The sum ranges over all the included EFT operators. Then the optimal observables $O^{\mathrm{opt}}_{n,i}$ are defined for each event $n = 1, \ldots, n_{\mathrm{events}}$ and for each set of final-state variables

$$O^{\mathrm{opt.}}_{n,i} = \frac{S_i(\Phi_n)}{S_{\mathrm{SM}}(\Phi_n)}\,. \tag{5.2}$$

[2]Here, only electrons and muons have been considered as final-state leptons. Muons originating from tau decays have not been included.

The mean value is finally calculated by averaging over the number of events

$$\bar{O}_i^{\text{opt.}} = \frac{1}{n_{\text{events}}} \sum_{n=1}^{n_{\text{events}}} \frac{S_i(\Phi_n)}{S_{\text{SM}}(\Phi_n)} \,. \tag{5.3}$$

Although the concept of optimal observables fully explores the sensitivity arising from anomalous couplings, at this juncture of the thesis, it was not immediately clear whether S from Eq. (5.1) necessitated the use of an analytical form. Therefore, higher-level observables described in Sec. 5.1 have been used to explore the potential sensitivity of anomalous top-quark couplings in production and decay processes. The methodology and procedure for deriving the sensitivity are described below.

5.2.1 Interpolation setup

For a first assessment of the different top-quark observables and an estimation of their sensitivity to dimension-six operator modifications, the simulated observables from the one-dimensional Wilson-coefficient scan have been used. A polynomial function has then been interpolated to the observables to evaluate the sensitivity from the gradient of the interpolation function. The details are described in the following using the forward-backward asymmetry of the top quark A_{FB}^t as an example.

Starting from the definition of A_{FB}^t it follows that

$$A_{\text{FB}}^t = \frac{\sigma_{\text{F}} - \sigma_{\text{B}}}{\sigma_{\text{F}} + \sigma_{\text{B}}} \,, \text{ with } \sigma_{\text{F}} = \int_0^1 \mathrm{d}\sigma_\theta \, \mathrm{d}\cos(\theta_t) \,, \; \sigma_{\text{B}} = \int_{-1}^0 \mathrm{d}\sigma_\theta \, \mathrm{d}\cos(\theta_t) \,, \tag{5.4}$$

and $\mathrm{d}\sigma_\theta = {}^{\mathrm{d}\sigma}/_{\mathrm{d}\cos(\theta_t)}$. In Eq. (5.4), $\cos(\theta_t)$ is the top-quark polar angle, which is defined in its laboratory frame via

$$\cos(\theta_t) = \frac{p_{t,z}}{|\boldsymbol{p}_t|} \,. \tag{5.5}$$

According to Eq. (2.13), the cross sections σ_{F} and σ_{B} depend quadratically on the Wilson coefficients via

$$\sigma_{\text{F,B}} = \sigma_{\text{F,B}}^{\text{SM}} + \tilde{C}_i \sigma_{\text{F,B}}^{\text{int.}} + \tilde{C}_i^2 \sigma_{\text{F,B}}^{\text{BSM}} \,, \tag{5.6}$$

with the interference part between SM and BSM $\sigma_{\text{F,B}}^{\text{int.}}$ and the pure BSM contribution $\sigma_{\text{F,B}}^{\text{BSM}}$. Together with $\sigma_{\text{F,B}}^{\text{SM}}$ they are taken as free parameters in the interpolation. In the end, a ratio of two polynomial functions has been used to parameterise BSM effects in A_{FB}^t. However, this approach can be used similarly to describe other observables considered, which depend on a differential cross-section. For example, the top-quark polarisation parameter $B_i^{\pm}$ consists of a differential cross-section part ${}^{\mathrm{d}\sigma}/_{\mathrm{d}\cos(\theta)}$ together with a normalisation ${}^1/_\sigma$. Both follow a quadratic expansion for the

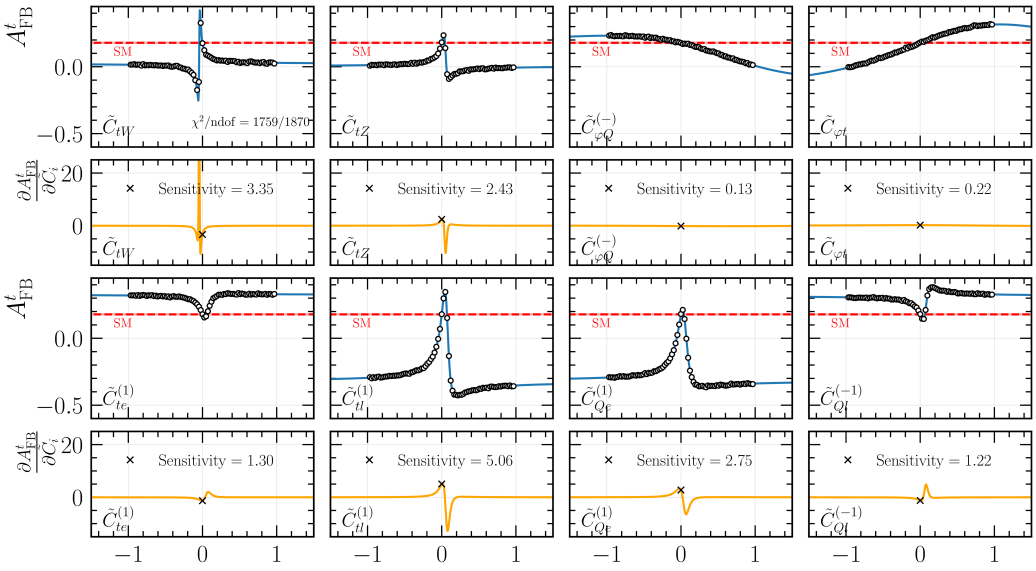

Figure 5.2: Top-quark forward-backward asymmetry at the parton level, simulated with MG and `dim6top_LO` in the first and third row, while the second and fourth row show the first derivative of the interpolation function. The absolute sensitivity has been extracted at the SM point at $\tilde{C}_i = 0$.

interference and pure BSM part according to Eq. (5.6), which allows to parameterise the spin-correlation observables with a ratio of two polynomial functions.

Subsequently, a χ^2 minimisation has been used to estimate the free parameters of the interpolation function using the package `iminuit` [162]. The sensitivity has been evaluated from the gradient of the interpolation at the SM point $\tilde{C}_i = 0$ according to

$$\text{Sensitivity} = \left| \left[\frac{\partial A_{\mathrm{FB}}^t}{\partial \tilde{C}_i} \right]_{\tilde{C}_i = 0} \right| . \tag{5.7}$$

Numerically, the `gradient` method from the `numpy` package [163] has been utilised to calculate the gradient.

For A_{FB}^t, the results of the interpolation are shown in Fig. 5.2 for all the operators considered in this analysis. The simulated observables from MG are shown as black points, and the interpolation is coloured blue. Below each graph, the gradient is presented in orange, where the black cross gives the absolute value of the sensitivity at the SM value.

The top-quark forward-backward asymmetry shows significant dependence to especially the bosonic operators O_{tW} and O_{tZ} and the four-fermion operators $O_{te}^{(1)}$, $O_{tl}^{(1)}$, $O_{Qe}^{(1)}$ and $O_{Ql}^{(-)}$. Modifications from the operators $O_{\varphi t}$ and $O_{\varphi Q}^{(-1)}$ only slightly

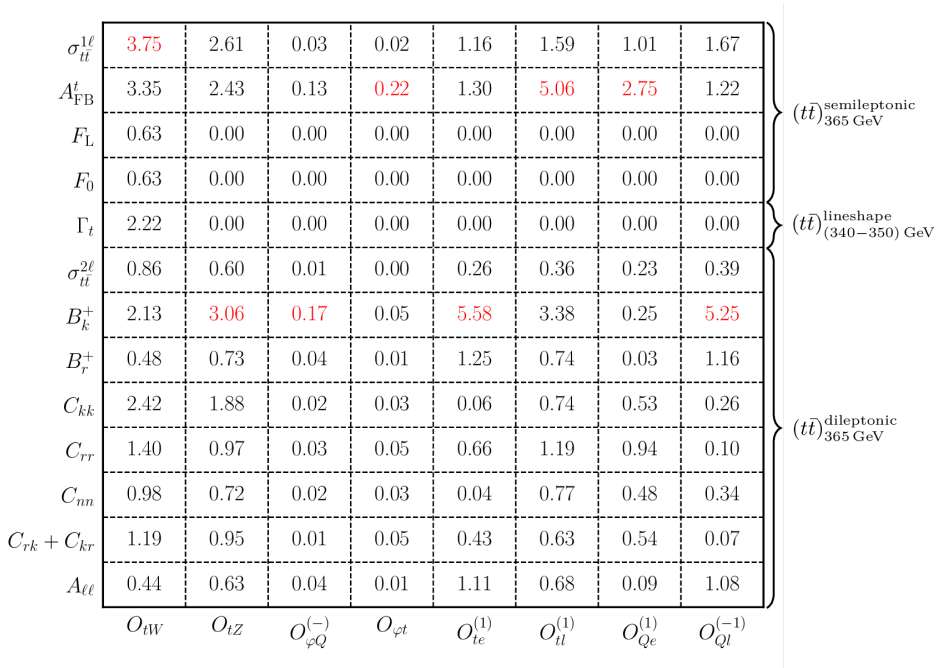

Figure 5.3: Summary of all extracted sensitivities of top-quark observables to the different dimension-six operators on the x axis. The most sensitive observable per operator is highlighted in red. The respective decay channel, in which each observable has been calculated, is indicated on the right side.

impact A_{FB}^{t} through interaction changes of the top quark and the Higgs field. These also reflect in changes in the interaction of the top quark and the gauge bosons, primarily the Z boson and the photon in the $t\bar{t}$ production. Following the strategy outlined for A_{FB}^{t}, all observables have been examined and the results are summarised below.

Except for the W-helicity fractions $F_{\mathrm{L},0}$ and the top-quark decay width Γ_t, where analytical expressions exist at NLO in Ref. [164], the procedure has been performed on simulated events at the parton level. The sensitivities have been further collected and ordered in a sensitivity matrix, shown in Fig. 5.3. The different decay channels and energy stages in a FCC-ee operation in which each observable can be measured are also indicated on the right side. For each operator on the x axis, the most sensitive observable is highlighted in red. Additional observables that do not show any sensitivity to one of the operators are not shown here. It can be seen that especially A_{FB}^{t} and the longitudinal top-quark polarisation B_k^+ are the most sensitive observables for most of the operators. In contrast, for example, B_r^+, which quantifies the transverse polarisation of the top quark, is predominantly influenced by the top-quark decay process and remains largely unaffected by the majority of the operators. Conversely, observables exclusively influenced by alterations from operators at the

top-quark decay, specifically F_{L}, F_0, and Γ_t, exhibit sensitivity solely to O_{tW}, which makes up the predominant contribution. Higher-order corrections arising from gluon radiation would additionally induce sensitivities to the O_{tG} operator; however, these effects have been ignored in the present analysis.

The set of sensitive observables defines the guideline for the following chapter, in which the reconstruction of $t\bar{t}$ and the evaluation of the expected measurement uncertainties have been performed in a FCC-ee environment.

5.3 Top-quark reconstruction

Simulated samples, centrally produced and provided by the FCC community, have been used to perform the reconstruction of the $t\bar{t}$ system in the semi and dileptonic decay channels. Since the top-quark reconstruction procedure differs in some aspects from the one usually followed at LHC, this section first guides through the different ingredients needed to reconstruct top quarks in Sec. 5.3.1 and the particularities of those in a lepton-collider environment. The specific aspects of the individual decay channels are described in Secs. 5.3.2 and 5.3.3 for the semi and dileptonic channels, respectively.

5.3.1 Ingredients

Reconstructing the $t\bar{t}$ system requires identifying and reconstructing its decay products, which can be accessed experimentally. The quantity of final-state objects varies for each decay channel of interest but typically adheres to the same sequence. Initially, one or two leptons must be identified as likely originating from the W-boson decay; subsequently, jet clustering is performed, and the undetected particles of the events, which are termed *missing momentum*, are further studied. This sequence is used as a framework for the following paragraphs.

Leptons Although the lepton reconstruction and identification have been simulated using `DELPHES` [118], it is necessary to identify the lepton originating from the decay of W bosons (also known as the *prompt lepton*). Given the short lifetimes of the top quark and the W boson, the source of prompt leptons is expected to be near the IP of the colliding beams. In contrast, leptons from semileptonic heavy-quark decays of b and c mesons exhibit a significant displacement from the IP due to their relatively longer lifetimes. These distinct characteristics are directly reflected in the PV fitting procedure. Once one (two) lepton track(s) is (are) identified in the list of tracks remaining after the PV fit, they are considered to be prompt. Furthermore, the energy of these leptons is expected to be significantly higher than that of non-prompt leptons.

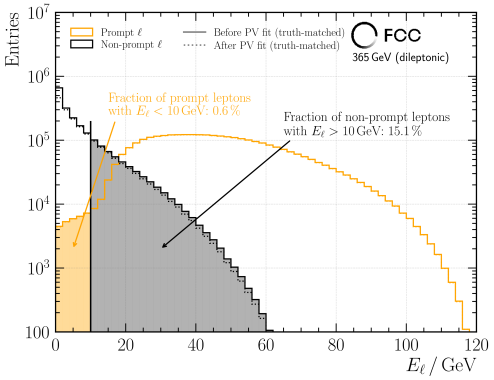

(a) The energy distribution for prompt leptons (originating from the W decay) and non-prompt leptons, identified from the truth information before and after the PV fit in the solid and dashed lines, respectively. Good agreement between the distributions before and after the PV fit can be observed over the entire energy range.

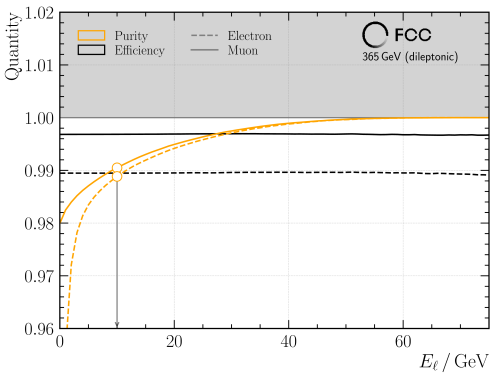

(b) The purity and efficiency of prompt leptons as defined in Eqs. (5.8) as function of the electron and muon energy in the dashed and solid lines, respectively. At an energy of 10 GeV, prompt leptons are identified with a purity of about 99 %.

Figure 5.4: Prompt leptons have a much harder energy spectrum and the identification with the PV fit results, together with an energy cut of 10 GeV, to high purities and efficiencies around and above 99 %.

Therefore, the use of the PV vertex fit with a combined energy cut is evaluated in th following on a sample of dileptonic events, where the actual origin of the leptons has been confirmed through their decay history, hereafter referred to as truth-matched. To validate the application of the PV fitting tool, the energy distribution of prompt and non-prompt leptons, depicted in orange and black, respectively, is illustrated in the left panel of Fig. 5.4. It differentiates between the truth-matched distributions before and after the PV fit, shown with solid lines and dotted lines, respectively.

Two primary conclusions can be drawn: first, merely applying a cut on the lepton energy to distinguish prompt leptons is insufficient, as a significant number of non-prompt leptons has energies exceeding $(10 - 20)$ GeV. Secondly, the good agreement of both distributions validates the use of using the PV fit to identify the prompt lepton(s) in the event. This is reflected in the very high purities of around 99 % for an energy cut at 10 GeV, as illustrated in the graph on the right of Fig. 5.4. The purity and efficiency metric are defined by means of

$$\begin{aligned} \text{Purity} &= \frac{\text{Prompt as prompt}}{\text{Prompt as prompt} + \text{Non-prompt as prompt}}\,, \\ \text{Efficiency} &= \frac{\text{Prompt as prompt}}{\text{Prompt as prompt} + \text{Prompt as non-prompt}}\,. \end{aligned} \tag{5.8}$$

No notable variation in purity between electrons and muons is detected, and the efficiency remains consistent across both lepton types, as expected. To achieve a balanced trade-off between the number of remaining events and purity, an energy threshold of $E_\ell \geq 10\,\text{GeV}$ has been applied, which must be independently met by all prompt leptons of the event.

Furthermore, the identification of the $t\bar{t}$ decay-channel based on the selection of leptons per event has been validated from an inclusive $t\bar{t}$ sample containing equally sized proportions of fully hadronic, semileptonic and dileptonic events. Furthermore, the energy cut of 10 GeV has been applied. The result as migration matrix is presented in Tab. 5.1 taking into account the respective branching fractions of 4 %, 30 % and 46 % for the dileptonic, semileptonic, and fully hadronic channels, respectively. The truth class is presented in the row, while the class selected after the PV fit from only the cut on the number of leptons N_ℓ is shown in the columns. The fully hadronic and

Table 5.1: Migration probabilities from an inclusive $t\bar{t}$ sample with a cut on the number of isolated leptons from the PV fit. Probabilities after an upper energy-cut on the highest-energtic jet are shown in parentheses. The matrix has been normalised per column.

		Cut on N_ℓ		
		$= 0\ell$	$= 1\ell$	$= 2\ell$
True	Fully hadronic	0.978 (0.979)	0.034 (0.034)	0.033 (0.005)
	Semileptonic	0.020 (0.020)	0.920 (0.920)	0.389 (0.071)
	Dileptonic	0.001 (0.001)	0.046 (0.046)	0.578 (0.924)

semileptonic channels are selected with a high purity of 98 %, while the contamination in the $N_{2\ell}$ channel is the largest from semileptonic $t\bar{t}$ events. This effect is reinforced by the smallness of the dileptonic Br compared to the semileptonic. Migration can be reduced with an upper energy cut on the highest-energetic jet when exactly two jets are clustered in the $N_{2\ell}$ channel by approximately a factor of five. For this, the cut is set to $\max(E_{\text{jet}}) \leq 100\,\text{GeV}$. The distribution of the jet energy in the $N_{2\ell}$ channel for the semileptonic and dileptonic events is presented in App. A.5 in the left panel of Fig. A.15. The migration probabilities after the jet-energy cut are presented in parentheses in Tab. 5.1. A graphical representation of Tab. 5.1 is shown in the right panel of Fig. A.15. Further investigations like a removal of overlapping leptons with the jets of the event are beyond the scope of this thesis. In the following, exclusive $t\bar{t}$ samples have been used with only the energy cut applied to the isolated leptons.

Jets Jets and their reconstruction are generally discussed in Sec. 3.4. In the context of $t\bar{t}$ decays, the Durham algorithm has been applied in its exclusive mode, which means that all reconstructed objects, excluding leptons to prevent double counting, have been grouped into exactly two or four jets for the dileptonic and semileptonic

channels, respectively. The energy recombination scheme has been utilised to sum the four-momentum vectors of the particles during the clustering process. Given that top-quark analyses are highly dependent on correctly identifying jets originating from b quarks, known as b jets, multivariate techniques are employed to leverage the distinctive features of b jets, such as significant secondary vertex masses or displaced secondary vertices within the jet [165]. As previously discussed in Sec. 3.4, this necessitates specialised tools for tagging, which have been simplified and replaced here by randomly assigning the b flavour in 80 % of cases based on the decay history of the jet constituents. Jets that do not come from b quarks are referred to as *light jets*.

However, the performance of the jet clustering has been examined in Fig. 5.5, requiring the association of jets derived from stable particle-level tracks with those at the object level. This association is achieved using a geometric matching criterion ΔR, defined as

$$\Delta R = \sqrt{\left(\eta_{\text{Object-level}} - \eta_{\text{Particle-level}}\right)^2 + \left(\phi_{\text{Object-level}} - \phi_{\text{Particle-level}}\right)^2} \,. \tag{5.9}$$

In Eq. (5.9), η and ϕ denote the pseudorapidity and the azimuth, respectively. The matching process is carried out iteratively by initially pairing the object- and particle-level jets with the minimum ΔR until every jet at the object level is matched with a jet at the particle level.

The jet-energy response (JER), a key metric to assess jet clustering performance [166], is mathematically defined via

$$\text{JER} = \frac{E_{\text{jet}}^{\text{Object-level}} - E_{\text{jet}}^{\text{Particle-level}}}{E_{\text{jet}}^{\text{Particle-level}}} \,. \tag{5.10}$$

It measures the accuracy of the reconstructed jet-energy, which is essential for accurately reconstructing the top-quark kinematics. As a result, the JER is shown in the left panel of Fig. 5.5 in the semileptonic decay channel. No further selection cuts have been applied. The figure also illustrates the contributions from both light and b jets, with a double-sided Crystal-Ball function fitting both types. The double-sided approach has been employed to address the asymmetry in the distribution, caused by a slight underestimation of jets at the object level because of acceptance effects in the extreme forward and backward regions of the detector. However, the distribution is predominantly centred around zero with a standard deviation of approximately 1.7 %, and about 90 % of the jets are reconstructed with an error less than 5 %.

To further investigate acceptance effects, the right panel of Fig. 5.5 displays a differential analysis of the JER, categorised by bins of the absolute polar-angle of the jet $\cos(\theta_{\text{jet}})$. The left y-axis represents the average JER. It is observed that the bias towards underestimating the jet energy increases up to 8 % for jets reconstructed in the extreme forward or backward regions of the detector. Furthermore, the smallest

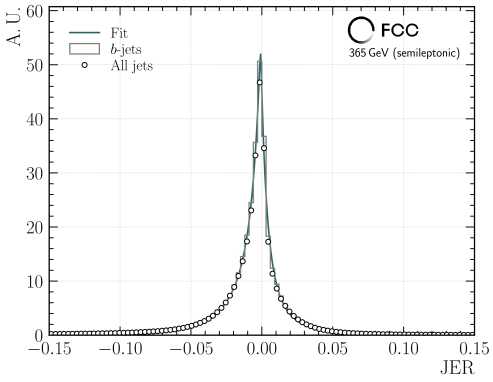

(a) Inclusive JER-distribution.

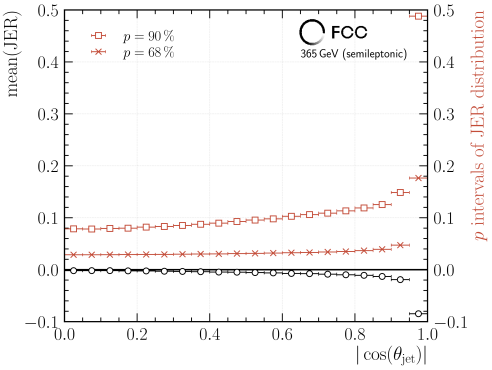

(b) Mean and the smallest p intervals of the JER distribution on the left and right y-axis, respectively, in bins of the absolute jet polar-angle.

Figure 5.5: No significant difference in the JER resolution can be observed between b- and light jets in Fig. (a). The asymmetry is due to acceptance effects of the detector, which increase significantly when the jet is reconstructed closer to the beam pipe (see Fig. (b)). However, the precision within the smallest 68 % interval, shown in Fig. (b), remains fairly constant up to $|\cos(\theta_{\text{jet}})| < 0.9$.

68 % and 90 % intervals of the distribution are shown on the right y-axis in Fig. 5.5b as crosses and squares, respectively. The trend of these intervals indicates that, despite a more significant bias from the mean of the JER distribution, the accuracy of the jet-energy estimation remains constant for the majority of jets (68 %).

Missing momentum Missing momentum corresponds to the momentum that is not detected by the detector. In $t\bar{t}$ decays, this occurs because particles escape detection, specifically neutrinos in the SM arising from leptonic $W \to \ell\nu$ decays, as they interact only via the weak interaction[3]. Consequently, the momentum taken by one or more neutrinos does not add to the measured total momentum. Given that the total momentum is conserved in the collision and matches the initial state's momentum, which is zero in the e^+e^- COM frame, the missing momentum is characterised as the negative sum of all observed momenta in this frame

$$\boldsymbol{p}_{\text{miss}} = -\boldsymbol{p}_{\text{detected}} \,. \tag{5.11}$$

In the semileptonic decay-channel, it is expected that a single neutrino will carry all the missing momentum. Therefore, it follows that $\boldsymbol{p}_{\text{miss}} = \boldsymbol{p}_{\nu}$, where ν could also represent an antineutrino depending on the charge of the charged lepton and

[3]Momentum from the collision may also be missed due to detector acceptance effects, which have not been considered here.

assuming that all other particles are detected. In the case of two neutrinos in the final state as in the dileptonic decay channel, it follows

$$|\boldsymbol{p}_{\text{miss}}| = \sqrt{(p_{\nu,x} + p_{\bar{\nu},x})^2 + (p_{\nu,y} + p_{\bar{\nu},y})^2 + (p_{\nu,z} + p_{\bar{\nu},z})^2}\,. \tag{5.12}$$

Thus, specialised methods are required to determine the complete momentum vectors $\boldsymbol{p}_\nu = (p_{\nu,x}, p_{\nu,y}, p_{\nu,z})^\top$ and $\boldsymbol{p}_{\bar{\nu}} = (p_{\bar{\nu},x}, p_{\bar{\nu},y}, p_{\bar{\nu},z})^\top$ within the $t\bar{t}$ system, utilising the well-defined initial conditions of the e^+e^- collision. More information on the reconstruction process can be found in Sec. 5.3.3.

In the subsequent section, the combination of the components is shown, distinguishing between the semi and dileptonic decay-channels to emphasise the unique aspects of each channel separately. Nevertheless, for both decay modes, only events in which two b jets have been identified have been considered. Any misidentification of the b-quark flavour has been ignored. In addition to the energy cut on the lepton of 10 GeV, no additional cuts on final-state objects have been applied.

5.3.2 Semileptonic $t\bar{t}$ decay

This section explains the process of reconstructing W bosons and top quarks in both the leptonic and hadronic decay channels of the W boson. Additionally, it emphasises the primary difficulty in the semileptonic channel, which is to accurately match one of the b jets with either the leptonic or hadronic W-boson.

***W* bosons** The leptonic W-boson has been reconstructed by combining the lepton and the missing-momentum vector, whereas hadronic W-boson candidates have been formed from the two light jets in the event. The charge of both W bosons is deduced from the charge of the prompt lepton, which will be measured with high precision. The invariant mass at the parton, particle, and object levels is shown in Fig. 5.6. Both

Table 5.2: Fit parameters and their statistical uncertainty from a double-sided Crystal-Ball function to the distributions at the object level in Fig. 5.6.

Parameters	Leptonic W	Hadronic W
μ / GeV	80.264 ± 0.010	79.831 ± 0.007
σ / GeV	1.643 ± 0.030	2.201 ± 0.015
α_{L}	0.458 ± 0.009	0.965 ± 0.008
n_{L}	3.553 ± 0.045	1.329 ± 0.012
α_{R}	0.630 ± 0.011	0.994 ± 0.008
n_{R}	2.743 ± 0.028	1.645 ± 0.016

distributions show the expected peak at the W-boson mass, where reconstruction,

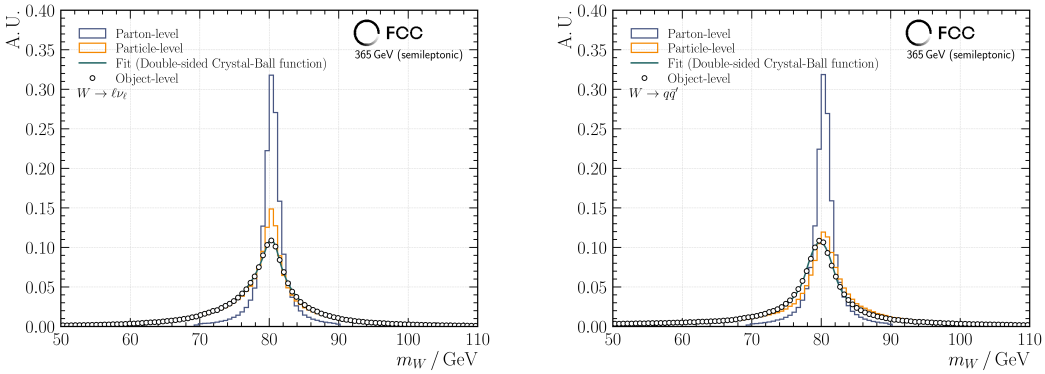

(a) Leptonic $W \to \ell\nu_\ell$.

(b) Hadronic $W \to q\bar{q}'$.

Figure 5.6: Leptonic and hadronic W-boson candidates in Fig. (a) and (b), respectively. Both mass distributions at the object level have been interpolated with a double-sided Crystal-Ball function, where the fit parameters are presented in Tab. 5.2. As expected, the leptonic W-boson distribution has a slightly smaller width.

radiation, and acceptance effects widen the distribution at the object level. The shift, particularly in the hadronic W-boson reconstruction, arises from the underestimation of the jet energy at the object level, as illustrated in Fig. 5.5a. The size of the effect of the underestimation of the W-boson mass is comparable to that of the jet energies. A double-sided Crystal-Ball function, as specified in Eq. (3.7), has been used to interpolate the object-level distribution, taking into account the asymmetry in the tails below and above the W pole-mass. The fit parameters, summarised in Tab. 5.2, indicate a broader tail for the leptonic W-boson, characterised by the exponent of the power law n_i, due to photon-radiation effects from the final-state lepton. However, for both the leptonic and hadronic W-boson, comparable results have been achieved in terms of width and reconstruction precision.

Top quarks As previously stated, the top-quark reconstruction accuracy is based on the proper matching of the b jets with the W bosons. The method employed here builds upon the approach from the research detailed in Ref. [88] and utilises the variables d_0 and d_1, which measure the b-jet pairing similar to a χ^2

$$d_0^2 = \left(\frac{m(W_{q\bar{q}'} + b_0) - \hat{m}_t}{\hat{\sigma}_{m_t}}\right)^2 + \left(\frac{E(W_{q\bar{q}'} + b_0) - \hat{E}_t}{\hat{\sigma}_{E_t}}\right)^2 + \left(\frac{m(W_{\ell\nu} + b_1) - \hat{m}_t}{\hat{\sigma}_{m_t}}\right)^2 + \left(\frac{E(W_{\ell\nu} + b_1) - \hat{E}_t}{\hat{\sigma}_{E_t}}\right)^2, \tag{5.13}$$

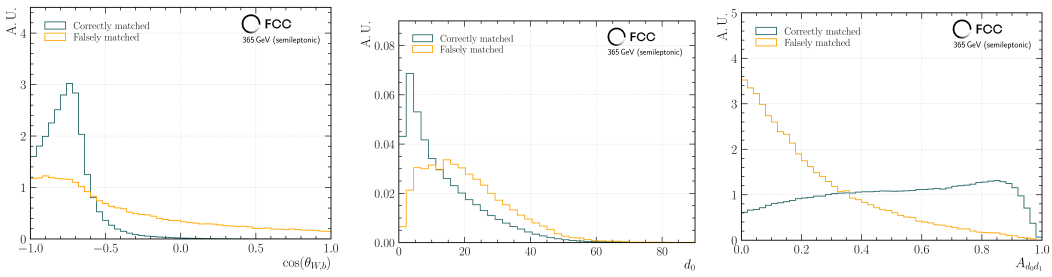

(a) $\cos(\theta_{W,b})$ distribution. **(b)** d_0 variable. **(c)** The asymmetry $A_{d_0d_1}$.

Figure 5.7: Different measures to quantify the b-jet pairing. The separation of correctly and falsely paired candidates significantly improves for the asymmetry $A_{d_0d_1}$. The more separated both distributions are, the easier it is to perform cuts on the measures to improve the top-quark reconstruction. For clarity, the distributions are normalised.

with d_1^2 defined with the opposite pairing of the two b-jets b_0 and b_1. In the given equation, $m(i+j)$ and $E(i+j)$ represent the invariant mass and energy of the objects i and j, respectively. The mean $\hat{x}$ and the standard deviations $\sigma_{\hat{x}}$ have been derived from the respective distributions at the parton level. Although Ref. [88] has also considered the opening angle between the W boson and the b jet, $\cos(\theta_{W,b})$, examining its distribution on the left side of Fig. 5.7 has revealed that it is a non-Gaussian, truncated at minus one, asymmetric distribution, where the mean value does not coincide with the most probable value. However, applying a cut at $\cos(\theta_{W,b}) \leq 0$ effectively eliminates incorrectly paired events, reducing the total number of events by approximately 4 %.

The distribution for d_0 is depicted in the central panel of Fig. 5.7, and due to the combinatorical methods used, the d_1 distribution appears similar. The d_0 distribution indicates that correctly matched W bosons and b jets tend to have values closer to zero compared to incorrectly matched pairs.

To enhance the distinction between correctly and incorrectly paired W-bosons and b jets, the absolute value of the asymmetry of d_0 and d_1, denoted as $A_{d_0d_1}$, is used. It is defined as

$$A_{d_0d_1} = \frac{|d_0 - d_1|}{d_0 + d_1} \tag{5.14}$$

and has been shown to provide a significant separation between correctly and falsely paired configurations, since it takes into account both possible combinations. One more benefit of $A_{d_0d_1}$ is that it is constrained within the range $0 \leq A_{d_0d_1} \leq 1$. The distribution is illustrated in the right panel of Fig. 5.7.

In order to quantify the performance of the variables under study, traditional classification metrics have been used. A visual approach involves analysing the ROC

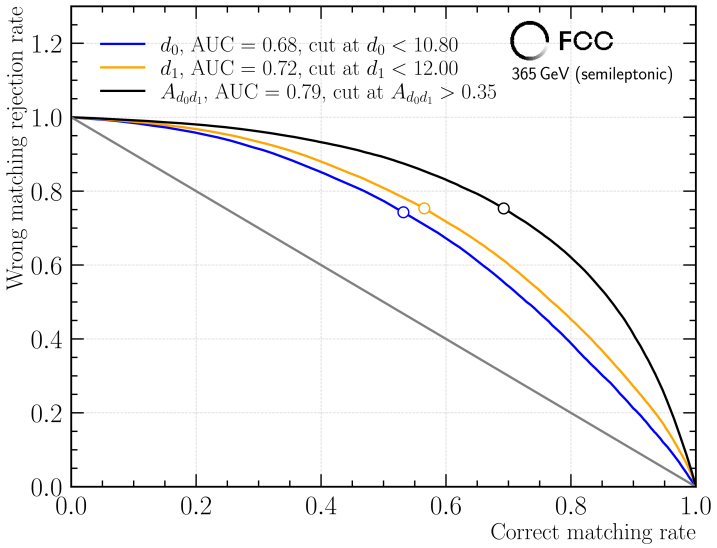

Figure 5.8: The wrong pairing-rejection rate as a function of the correct pairing-rate of b jets to the W bosons. The point farthest away from the diagonal is taken as the cut value of the variable. The best performance has been achieved with $A_{d_0d_1}$, where the AUC is the highest with 0.79. As expected, d_0 and d_1 achieve similar performance results.

curve to measure the pairing performance as the discrimination threshold changes. Fig. 5.8 illustrates the true positive rate (correct pairing-rate) versus the false positive rate (wrong pairing-rejection rate), and the optimal cut in the distribution has been determined from the point farthest away from the diagonal line. The AUC score summarises all potential threshold values, with values closer to one signifying superior performance. The highest performance according to the AUC has been achieved with $A_{d_0d_1}$, as already suspected from the distributions in Fig. 5.7.

Ultimately, top-quark candidates are selected when $\cos(\theta_{W,b}) < 0$ and $A_{d_0d_1} > 0.35$. In this case, the combination with the lower d_i-value has been chosen. Both cuts remove approximately 38 % of all events. Nevertheless, this improves the correct matching rate from around 85 % (simply by selecting the combination with the lower d_0 or d_1) to up to 96 % with the specified cuts. The leptonic and hadronic top-quark candidates are shown in Fig. 5.9. The parameters of a double-sided Crystal-Ball function, obtained from an unbinned maximum likelihood fit with an additional Gaussian that shares the same mean value, are detailed in Tab. 5.3. The shift in the mean value of the hadronic top-quark is due to the underestimation of the jet energy. By interpolating the invariant-mass spectrum of fully reconstructed top-quarks, it can be inferred from Tab. 5.3 that a direct measurement of top-quark mass with a statistical precision at the order of 10 MeV is achievable.

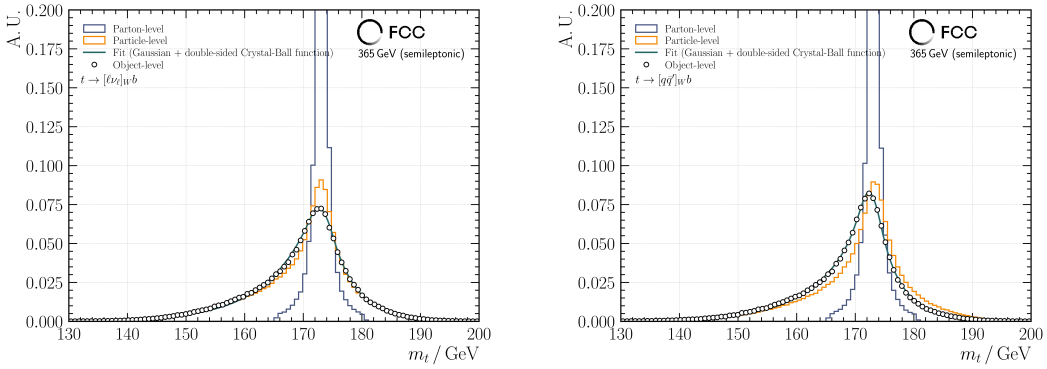

(a) Leptonic top-quark. **(b)** Hadronic top-quark.

Figure 5.9: Leptonic and hadronic top-quark candidates in Fig. (a) and (b), respectively. Both object-level distributions have been interpolated with a double-sided Crystal-Ball function and an additional Gaussian distribution sharing one mean value. Both channels lead to very comparable mass-resolution results.

Table 5.3: Fit parameters and their statistical uncertainty from a double-sided Crystal-Ball function to the distributions at the object level in Fig. 5.9.

Parameters	Leptonic top	Hadronic top
μ_{shared} / GeV	172.952 ± 0.009	172.313 ± 0.034
σ_{Gauss} / GeV	4.000	1.816 ± 0.091
$\sigma_{\text{DS CB}}$ / GeV	2.368 ± 0.006	2.871 ± 0.014
α_{L}	0.305 ± 0.001	0.385 ± 0.019
n_{L}	96.9370 ± 0.0013	79.691 ± 5.100
α_{R}	0.554 ± 0.003	0.719 ± 0.037
n_{R}	83.4530 ± 0.0025	98.384 ± 8.100

5.3.3 Dileptonic $t\bar{t}$ decay

When both W bosons decay leptonically, there is a significant fraction of missing momentum of the event energy due to the two undetected neutrinos. To accurately reconstruct the $t\bar{t}$ system, specialised algorithms are required due to the relation $\boldsymbol{p}_{\text{miss}} = \boldsymbol{p}_{\nu} + \boldsymbol{p}_{\bar{\nu}}$ (see Sec. 5.3.1). However, the known initial state of e^+e^- collisions, hence knowing the COM energy, provides new possibilities to fully reconstruct the dileptonic $t\bar{t}$ system [167–169]. The decay process can be mathematically expressed on the basis of the conservation of energy and momentum via

$$\boldsymbol{P}_{\ell_1} + \boldsymbol{P}_{\ell_2} + \boldsymbol{P}_{\nu} + \boldsymbol{P}_{\bar{\nu}} + \boldsymbol{P}_{j_1} + \boldsymbol{P}_{j_2} = (\sqrt{s}, 0, 0, 0)^{\top}\,, \tag{5.15}$$

where $\boldsymbol{P}_{\ell_1}$ and $\boldsymbol{P}_{\ell_2}$ denote the four-momenta of the leptons, $\boldsymbol{P}_{\nu}$ and $\boldsymbol{P}_{\bar{\nu}}$ the four-momenta of the neutrinos, and $\boldsymbol{P}_{j_1}$ and $\boldsymbol{P}_{j_2}$ the four-momenta of the two b jets. The

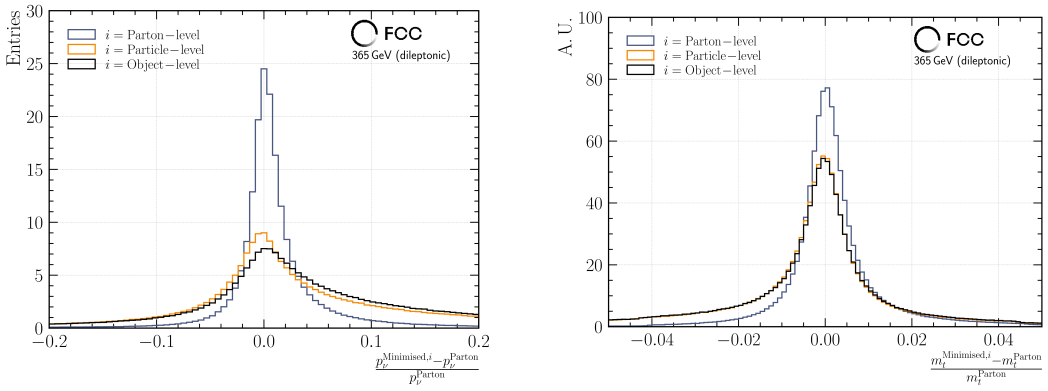

(a) Neutrino momentum. **(b)** Top-quark mass.

Figure 5.10: The resolution plots at different levels: parton, particle, and object level are shown. Asymmetries in the distributions arise through ISR and BS effects, which could only be mitigated through an event-wise determination of the effective COM energy after radiation effects prior to the collision.

COM energy $\sqrt{s}$ is set to 365 GeV. The most advanced technique for numerically solving the set of equations, while considering the mass constraints of the W bosons and the top quarks, has been developed in Ref. [170]. It accounts for the off-shell production of W bosons and top quarks by introducing a weight function proportional to the propagators of the top quark and the W boson. The algorithm also requires the pole masses of the W boson and the top quark, along with their decay widths. These parameters will be determined with exceptional precision from experiments at the WW threshold and the top-quark threshold scan. In this context, the pole masses and decay widths used are taken from the simulation inputs:

$$m_W = 80.42\,\text{GeV}\,, \quad \Gamma_W = 2.04\,\text{GeV}\,, \quad m_t = 173.1\,\text{GeV}\,, \quad \Gamma_t = 1.51\,\text{GeV}\,.$$

The analysis detailed in Ref. [170] is conducted exclusively at the parton level, disregarding the impacts of hadronisation, reconstruction efficiencies, and other experimental distortions. As an initial demonstration, the reconstruction is initially carried out using the quantities from Eq. (5.15) at the parton level, prior to implementing the reconstruction at the object level with emulated experimental conditions. The parton-level results have been found to be similar to those in Ref. [170]: the neutrino momentum can be reconstructed with an error of less than 2 % in 60 % of the cases. At the object level, the resolution worsens, achieving an error of less than 2 % in only about 20 % of the events.

Subsequently, the W bosons and top quarks have been reconstructed from all final-state objects. Fig. 5.10 displays the relative neutrino-momentum in the left panel, along with the top-quark mass resolutions in the right panel. As anticipated, the resolutions degrade at the object level, yet maintain a consistent pattern at both the

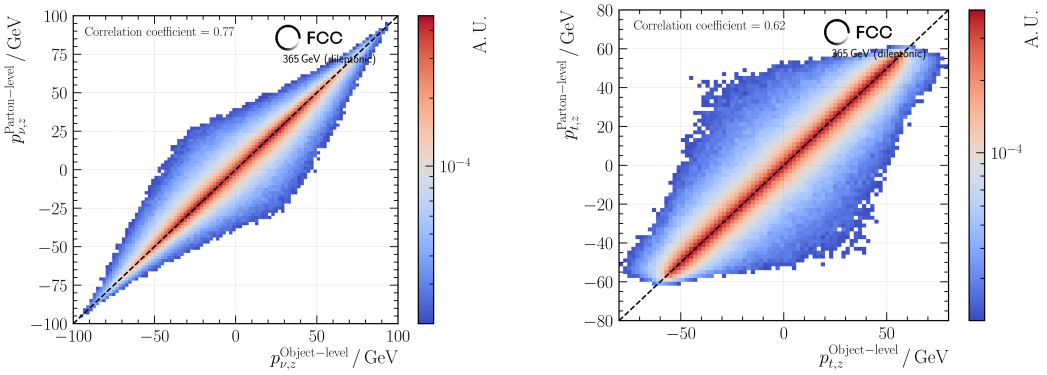

(a) Neutrino p_z component.

(b) Top-quark p_z component.

Figure 5.11: Two dimensional representation of the neutrino and top-quark z-momentum component. Overall, good agreement has been found and the minimisation algorithm works well for quantities at the object level, including effects from hadronisation and reconstruction.

particle and object levels. An asymmetry is evident in the top-quark mass resolution shown in Fig. 5.10b, and its origin has been examined and discussed below.

In addition to the one-dimensional representations, Fig. 5.11 illustrates the two-dimensional correlation between the z-momentum components of the neutrino and the top quark. The y-axis displays the parton-level quantity as a function of the object-level quantity on the x-axis. Here, object level refers to the quantity after solving Eq. (5.15). The linear correlation coefficient is presented in the upper left corner of each figure. It can be seen that the correlation coefficient is lower for the top-quark distribution compared to that of the neutrino [171]. This reduction is also attributed to the ambiguities arising from the additional matching of the b quark to either of the W bosons.

Sources for the mass-resolution asymmetry Given that the asymmetry in the top-quark mass is of a comparable order of magnitude at the particle and object level, the effects of the JER are found to be less significant than the influence of the COM energy, which is used as input for the minimisation algorithm in Eq. (5.15). Consequently, any changes in $\sqrt{s}$ affect the accuracy of the $t\bar{t}$ reconstruction.

A crucial factor affecting $\sqrt{s}$ is the presence of ISR and BS, where photon emissions reduce the effective collision-energy, causing an overestimation of $\sqrt{s}$ when it is assumed that it is exactly 365 GeV. The influence of ISR on the precision of the reconstruction is depicted in Fig. 5.12, which shows the median resolutions of the W-boson and top-quark masses in different bins of the ISR photon energy $E_{\gamma_{\text{ISR}}}$. It becomes evident that high-energy photon emissions from the e^+ and/or e^- beams

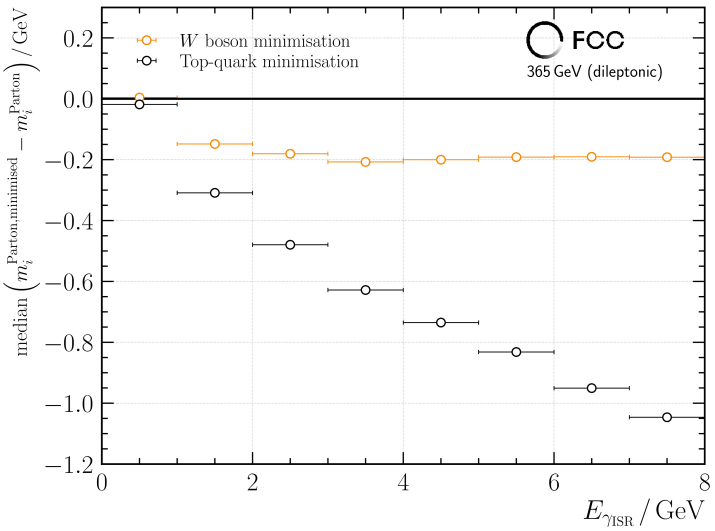

Figure 5.12: The median of the absolute difference of the minimised object mass to the true one, separately for W bosons and top quarks in orange and black, respectively, as function of the ISR photon-energy on the x axis. A clear trend, especially for the top quarks, towards zero for lower energetic photon-emission from the beams can be observed.

significantly affect the $t\bar{t}$ reconstruction. The lower the energy of the emitted photons, the more central the median value.

In conclusion, the method proposed in Ref. [170] is applicable to events in more realistic FCC-ee settings. The limiting factors of the methodology have been addressed, particularly the need for an event-specific estimation of the energy loss due to ISR and BS, which reduce the effective COM energy.

5.4 Expected experimental precision

This section outlines the methods and techniques used to determine the experimental precision of the observables that are influenced by dimension-six operators, as discussed in Sec. 5.1. Generally, this involves establishing a functional relationship between the measurement and the true underlying value, which may depend on various external parameters. The accuracy of the translation enters the precision of the observable as an additional systematic uncertainty, and several approaches are common in high-energy physics to perform the translation. In the end, the goal is to find the most accurate measurement of the theoretical parameter under study.

The first and conceptually most straightforward method involves the derivation of an analytical expression that directly returns the true value from the measured one. This task becomes highly complex when several convoluted effects starting from the event generation, over the parton showering, up to detector effects have to be considered.

The second and often used method is to run the simulation n times with n different parameter settings that could influence the result, for example, assuming different values of the particle masses within their current precision. Although computationally intensive, this approach allows one to bypass the need for an analytical functional dependence. In some cases, it might be difficult or even impossible to run the n simulations. In the end, the effects can be emulated by reweighting the events at the parton level to assess their effect at the object level.

The third method is known as unfolding, which corrects for the smearing effects of the detector through matrix inversion. In its simplest form, the true distribution matrix $\boldsymbol{T}$ is altered by detector effects, which are composed into a response matrix $\boldsymbol{R}$, resulting in the observed distribution $\boldsymbol{M}$ through $\boldsymbol{M} = \boldsymbol{R} \cdot \boldsymbol{T}$. Thus, the true distribution can be obtained by

$$\boldsymbol{T} = \boldsymbol{R}^{-1} \cdot \boldsymbol{M}. \tag{5.16}$$

5.4.1 Semileptonic observables

In this analysis, systematic uncertainties in semileptonic $t\bar{t}$ observables have been considered through a variety of simulation inputs for the top-quark forward-backward asymmetry and the W-helicity fractions, which have been translated further to the parton level with a reweighting procedure. Their reconstruction and uncertainty assessment procedure are described below.

Top-quark forward-backward asymmetry

The forward-backward asymmetry of the top quark, denoted as A_{FB}^{t}, has been investigated using two different methods. Initially, fully reconstructed top quarks have been employed to determine A_{FB}^{t} from its polar-angle distribution $\cos(\theta_t)$. This method is influenced by the reconstruction technique and the analysis chain, necessitating the conversion of the measured value to the true value with a calibration curve or a reweighting procedure, which introduces additional systematic uncertainties. In the second approach, the sign of the top-quark polar-angle is inferred from the lepton arising from the W-boson decay, which are assumed to be correlated. Given that the lepton momentum is measured with high precision, cuts affecting the top-quark reconstruction, such as $\cos(\theta_{W,b})$ and $A_{d_0 d_1}$ from Sec. 5.3.2, are no longer required, thereby enhancing the statistical precision. As can be seen in the following,

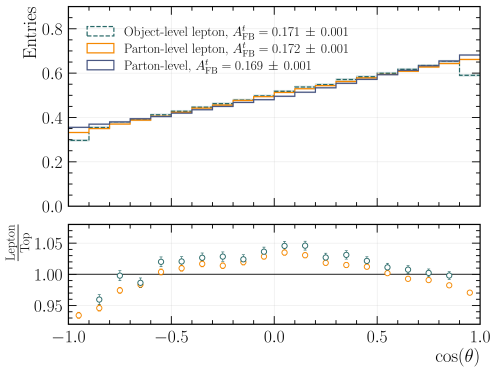

(a) The polar-angle distribution of the top quark and lepton at the parton level as well as the lepton at the object level. The effects of limited acceptances of the detector at the object level in the very forward and backward directions are visible.

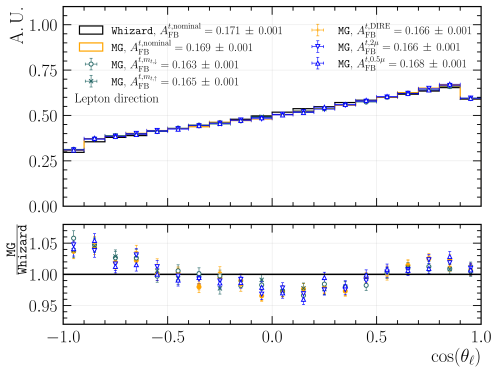

(b) The lepton polar-angle distribution at the object level, separately for the nominal sample and the variate samples.

Figure 5.13: Within statistical uncertainties, A_{FB}^{t} is in agreement across all different direction estimators in Fig. (a). The lepton polar-angle is used to estimate A_{FB}^{t} and a variety of samples is used to extract systematic uncertainties.

using the leptonic forward-backward asymmetry allows to directly measure A_{FB}^{t} at the parton level.

The validation of the lepton hypothesis to deduce A_{FB}^{t} is illustrated in Fig. 5.13a, which shows the $\cos(\theta)$ distribution of the top quark at the parton level in addition to the $\cos(\theta)$ distribution of the lepton, both at the parton and object levels. No cuts have been applied, except for the lepton-energy cut. The ratio is also displayed and indicates agreement within 5 % relative to the top-quark $\cos(\theta_t)$ distribution. However, detector-acceptance effects can be observed for $|\cos(\theta)| > 0.9$ at the object level. The uncertainty presented in the legend is statistical, resulting in a precision of about 0.6 %. As indicated above, the leptonic forward-backward asymmetry at the object level agrees well with A_{FB}^{t} at the parton level, within the statistical precision.

An initial evaluation of the systematic uncertainty has been performed using a variety of samples as outlined in Sec. 3.3. The result is shown in Fig. 5.13b, which presents the lepton polar-angle distribution, while the ratio compares the varied samples to the nominal one. Again, the variations remain within 5 %. For the systematic uncertainty estimate, the maximum variation which comes from the alternative parton-shower model is considered, resulting in

$$A_{FB}^{t} = 0.171 \pm 0.001(\text{stat.}) \pm 0.003(\text{syst.}) = 0.171 \pm 0.003(\text{tot.})\,. \tag{5.17}$$

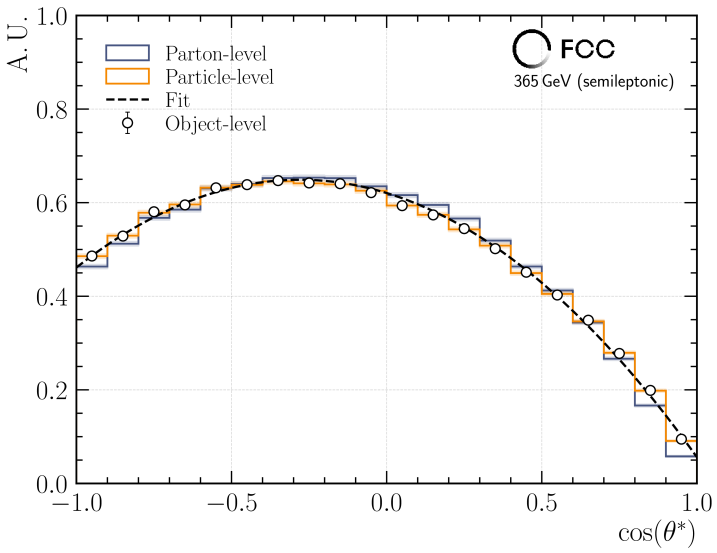

Figure 5.14: The $\cos(\theta^*)$ distribution at the different levels. From an unbinned maximum likelihood fit to Eq. (5.19) the individual fractions $F_{0,\mathrm{L,R}}$ are extracted. All reconstruction cuts have been applied at the particle and object level. Shaded areas indicate the statistical uncertainty.

W-helicity fractions

The nearly exclusive and direct decay of the top quark into a W boson and a b quark allows to transfer the top quark's characteristics to its decay products. This information would otherwise be smeared through the hadronisation process. In turn, three potential polarisation states for the W boson exist in the SM: left-handed, right-handed, or longitudinal. The specific fractions are known as helicity fractions and are defined as the ratio to the total decay width of the top quark

$$F_\mathrm{L} = \frac{\Gamma_\mathrm{L}}{\Gamma_t}\,, \quad F_\mathrm{R} = \frac{\Gamma_\mathrm{R}}{\Gamma_t}\,, \quad F_0 = \frac{\Gamma_0}{\Gamma_t}\,. \tag{5.18}$$

The most accurate SM predictions at NNLO in QCD are $F_\mathrm{L}^\mathrm{SM} = 0.311 \pm 0.005$, $F_\mathrm{R}^\mathrm{SM} = 0.0017 \pm 0.0001$, and $F_0^\mathrm{SM} = 0.687 \pm 0.005$ [47]. Any new-physics contribution would modify these values.

Experimentally, the angular distribution of the charged lepton from the leptonically decaying W-boson shows the highest sensitivity to the polarisation of the W boson. The helicity angle θ^* is defined as the angle between the charged lepton and the opposite direction of the b quark, both measured in the rest frame of the W boson. The differential cross-section as a function of the helicity fractions is given by [45]

$$\frac{1}{\sigma}\frac{\mathrm{d}\sigma}{\mathrm{d}\cos(\theta^*)} = \frac{3}{4}\left(1-\cos^2(\theta^*)\right)F_0 + \frac{3}{8}\left(1-\cos(\theta^*)\right)^2 F_\mathrm{L} + \frac{3}{8}\left(1+\cos(\theta^*)\right)^2 F_\mathrm{R}\,. \tag{5.19}$$

In contrast to A_{FB}^{t}, fully reconstructed top-quarks have been used to compute $F_{\mathrm{L,R,0}}$ at the parton, particle, and object level. The respective distributions for the leptonic $\cos(\theta^{*})$ are depicted in Fig. 5.14. In this analysis, only the leptonic helicity-angle has been used, since the hadronically decaying W-boson, while using the down-type quark as an analyser with the same weak isospin, suffers from lower reconstruction efficiency and resolution of jets. Additionally, the hadronic decay products are experimentally more difficult to separate, making the leptonic decay a more precise choice for the analysis.

The W-helicity fractions $F_{\mathrm{L,0}}$ are derived from an unbinned maximum likelihood fit to Eq. (5.19). The right-handed fraction is extracted from the unitary condition $1 = \sum_{i\in[\mathrm{L,R,0}]} F_i$. The fit results at the object level are also shown in Fig. 5.14 as a dashed black line and correspond to

$$F_0 = 0.308 \pm 0.002\,, \quad F_{\mathrm{L}} = 0.655 \pm 0.002\,, \quad F_{\mathrm{R}} = 0.037 \pm 0.003\,. \tag{5.20}$$

The uncertainties stated refer to the fit uncertainty and are taken as statistical uncertainty in the following.

Owing to the discrepancies between the distributions at the parton and object levels, a reweighting and subsequent interpolation method has been adopted from Ref. [45] to infer the parton level W-helicity fractions from a set of measured (F_0, F_{L}) at the object level. For this, an event weight w via

$$w = \frac{\frac{3}{4}\left(1-\cos^2(\theta^{*}_{\mathrm{PL}})\right) F_0^{\mathrm{var}} + \frac{3}{8}\left(1-\cos(\theta^{*}_{\mathrm{PL}})\right)^2 F_{\mathrm{L}}^{\mathrm{var}} + \frac{3}{8}\left(1+\cos(\theta^{*}_{\mathrm{PL}})\right)^2 F_{\mathrm{R}}^{\mathrm{var}}}{\frac{3}{4}\left(1-\cos^2(\theta^{*}_{\mathrm{PL}})\right) F_0^{\mathrm{SM}} + \frac{3}{8}\left(1-\cos(\theta^{*}_{\mathrm{PL}})\right)^2 F_{\mathrm{L}}^{\mathrm{SM}} + \frac{3}{8}\left(1+\cos(\theta^{*}_{\mathrm{PL}})\right)^2 F_{\mathrm{R}}^{\mathrm{SM}}} \tag{5.21}$$

has been defined. In Eq. (5.21), the subscript PL denotes *parton level*, and $F_{\mathrm{L,0}}^{\mathrm{var}}$ has been adjusted in 20 evenly spaced increments around their respective SM values F_i^{SM}. The event weight w has then been applied to the object-level distribution, and the fit has been repeated, resulting in pairs of $(F_{\mathrm{L}}^{\mathrm{OL}}, F_0^{\mathrm{OL}})$.

The true helicity fractions at the parton level have been determined from a two-dimensional interpolation method, employed from the `scipy` library [172]. This method utilises a piecewise linear interpolation to map $(F_{\mathrm{L}}^{\mathrm{OL}}, F_0^{\mathrm{OL}})$ to $(F_{\mathrm{L}}^{\mathrm{var}}, F_0^{\mathrm{var}})$. The results of this interpolation for a set of test pairs $(F_{\mathrm{L}}^{\mathrm{OL}}, F_0^{\mathrm{OL}})$ on the (x, y) axis are shown in Fig. 5.15, while the uncertainties arising from the interpolation have been neglected here. The figure shows both F_0^{var} and $F_{\mathrm{L}}^{\mathrm{var}}$ in the left and right panels at the parton level on the z axis, respectively. The contours presented in the graphs refer to the regions in which the SM values including their uncertainties are reached. The interpolation result for the right-handed polarisation state is presented in App. A.5.2 in Fig. A.16.

Similarly to the method applied for A_{FB}^{t}, an initial evaluation of the systematic uncertainty arising from changes in the simulation input has been performed. This

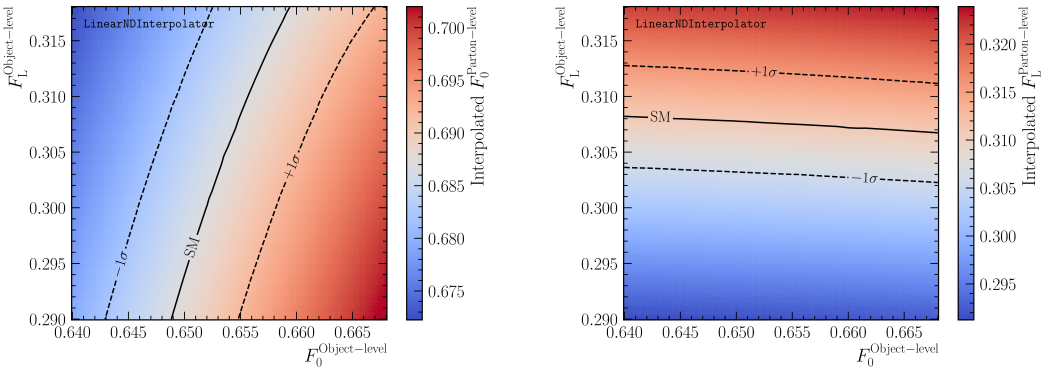

(a) $F_0^{\text{Parton-level}}$. **(b)** $F_L^{\text{Parton-level}}$.

Figure 5.15: The individual, interpolated W-helicity fractions in the two-dimensional plane of $(F_0^{\text{OL}}, F_L^{\text{OL}})$. The lines correspond to regions, where the SM value within uncertainties is reached.

evaluation involves to initially adjust the W-helicity fractions of the varied samples to match the values of the nominal samples generated with `Whizard` through a weighting process

$$v = \frac{\frac{3}{4}\left(1-\cos^2(\theta_{\text{PL}}^{*,\text{var}})\right)F_0^{\text{nom}} + \frac{3}{8}\left(1-\cos(\theta_{\text{PL}}^{*,\text{var}})\right)^2 F_L^{\text{nom}} + \frac{3}{8}\left(1+\cos(\theta_{\text{PL}}^{*,\text{var}})\right)^2 F_R^{\text{nom}}}{\frac{3}{4}\left(1-\cos^2(\theta_{\text{PL}}^{*,\text{var}})\right)F_0^{\text{var}} + \frac{3}{8}\left(1-\cos(\theta_{\text{PL}}^{*,\text{var}})\right)^2 F_L^{\text{var}} + \frac{3}{8}\left(1+\cos(\theta_{\text{PL}}^{*,\text{var}})\right)^2 F_R^{\text{var}}}\,.$$

Subsequently, the event weight v has been applied to the $\cos\left(\theta_{\text{OL}}^{*,\text{var}}\right)$ distribution to determine F_0^{var} and F_L^{var} at the object level. Finally, the interpolation setup from the nominal sample has been used to infer the true W-helicity fractions at the parton level. The results are summarised in Tab. 5.4. Given that the samples generated

Table 5.4: Interpolated W-helicity fractions to the parton level. From the variate samples, systematic uncertainties can be assessed.

Sample	F_0^{PL}	F_L^{PL}	F_R^{PL}
Reference	0.311	0.687	0.0017
`MG`, default	0.302	0.694	0.004
`MG`, $m_{t,\downarrow}$	0.303	0.692	0.005
`MG`, $m_{t,\uparrow}$	0.302	0.693	0.005
`MG`, 0.5μ	0.301	0.697	0.003
`MG`, 2μ	0.302	0.694	0.004
`MG`, `DIRE` PS	0.290	0.700	0.010

with `MadGraph` are at LO and have been adjusted to align with the NLO calculations from the reference sample, the variations observed in Tab. 5.4 can be attributed

solely to the kinematic differences of the entities involved in the calculation of $\cos(\theta^*)$. Consequently, a systematic uncertainty on the W-helicity fractions from Eq. (5.22) is derived from the variations in the LO samples. At the object level, it follows

$$\begin{aligned} F_0 &= 0.311 \pm 0.002(\text{stat.}) \pm 0.006(\text{syst.}) \,, \\ F_\text{L} &= 0.687 \pm 0.002(\text{stat.}) \pm 0.006(\text{syst.}) \,, \\ F_\text{R} &= 0.0017 \pm 0.003(\text{stat.}) \pm 0.006(\text{syst.}) \,. \end{aligned} \tag{5.22}$$

The statistical precision in Eq. (5.22) is of the same order of magnitude compared to the most precise measurement performed with the ATLAS experiment [46]. However, the systematic uncertainty in Ref. [46] is about one order of magnitude larger than the statistical uncertainty, primarily due to uncertainties in jet reconstruction and signal modelling. Both sources are expected to be better understood at the FCC-ee to bring the systematic uncertainty to the level of the statistical uncertainty.

In the following, the results of the spin-correlation observable studies in the dileptonic $t\bar{t}$ system are presented. For this, a brief introduction is provided first.

5.4.2 Dileptonic observables

The spin configurations of the W boson have been inferred in the semileptonic channel by measuring the W-helicity fractions. Given that leptons provide excellent spin information analysis, recent measurements at the LHC [43, 44] have focused on spin correlations in $t\bar{t}$ production. Therefore, this section describes the measurement of the spin-correlation coefficients in the dileptonic decay-channel. Since this measurement requires to fully reconstruct the $t\bar{t}$ system, an indirect probe from the angular distribution of the two leptons in their laboratory frame provides a good proxy for the top-quark spins. In addition, they are experimentally precisely measurable.

The objective is to measure the $t\bar{t}$ production spin-density matrix $\boldsymbol{R}$, which is a $n \times n$ matrix with $n = 2 \cdot 3 = 6$ (two top quarks and three spatial projections). It is proportional to the squared matrix element and contains the top- and antitop-quark polarisations $\tilde{\boldsymbol{B}}^{\pm}$ on the main diagonal with entries $B_i^{\pm}$. The correlations between the two top-quark spins on the main diagonal are collected in a matrix $\tilde{\boldsymbol{C}}$. Therefore, the correlation coefficients are a set of $n \cdot (n-1)/2 = 15$ entries, which are labelled as C_{ij}.

Experimentally, an orthonormal basis is usually chosen to extract information about the top-quark spin(s). The choice of basis is illustrated in Fig. 5.16, where the so-called helicity axis $\boldsymbol{k}$ is defined by the direction of the top quark. Together with the direction of the incoming electron $\boldsymbol{e}^-$, the direction $\boldsymbol{n}$ is defined perpendicular to $\boldsymbol{e}^-$ and $\boldsymbol{k}$

$$\boldsymbol{n} = \frac{\boldsymbol{e}^- \times \boldsymbol{k}}{\sin(\theta)} \,, \tag{5.23}$$

Figure 5.16: The axes $\boldsymbol{r}$ and $\boldsymbol{n}$ defined with respect to the incoming electron direction and the direction of the top quark $\boldsymbol{k}$. The left figure shows the case for $\theta > \pi/2$, the right for $\theta < \pi/2$.

with the top-quark polar angle θ. Finally, the axis $\boldsymbol{r}$ is given by

$$\boldsymbol{r} = \frac{\boldsymbol{e}^- - \boldsymbol{k} \cdot \cos(\theta)}{\sin(\theta)} \,. \tag{5.24}$$

The polarisation and spin-correlation coefficients $B_i^{\pm}$ and C_{ij} are derived from the differential cross-sections with respect to $\cos(\theta_i^{\pm})$, where θ_i^+ and θ_i^- represent the angles of the positively and negatively charged leptons relative to the axis i, respectively. These angles are measured in the rest frames of their respective parent top- and antitop-quarks. Finally, the coefficients can be extracted from the normalised differential cross-section

$$\frac{1}{\sigma}\frac{\mathrm{d}\sigma}{\mathrm{d}\cos(\theta_i^{\pm})} = \frac{1}{2}\left(1 + B_i^{\pm}\cos(\theta_i^{\pm})\right) \,, \tag{5.25}$$

$$\frac{1}{\sigma}\frac{\mathrm{d}\sigma}{\mathrm{d}\cos(\theta_i^+)\cos(\theta_j^-)} = \frac{1}{2}\left(1 - C_{ij}\cos(\theta_i^+)\cos(\theta_j^-)\right) \cdot \ln\left(|\cos(\theta_i^+)\cos(\theta_j^-)|^{-1}\right) \,, \tag{5.26}$$

$$\frac{1}{\sigma}\frac{\mathrm{d}\sigma}{\mathrm{d}y_{\pm}} = \frac{1}{2}\left(1 - \frac{C_{ij} \pm C_{ji}}{2} y_{\pm}\right) \arccos(|y_{\pm}|) \,, \tag{5.27}$$

with $y_{\pm} = \cos(\theta_i^+)\cos(\theta_j^-) \pm \cos(\theta_j^+)\cos(\theta_i^-)$. Furthermore and following the analysis from Ref. [43], the opening angle between the two leptons $\cos(\theta_{\ell\ell})$ can be measured with high precision in their laboratory frame to determine the asymmetry

$$A_{\ell\ell} = \frac{N(\cos(\theta_{\ell\ell}) > 0) - N(\cos(\theta_{\ell\ell}) < 0)}{N(\cos(\theta_{\ell\ell}) > 0) + N(\cos(\theta_{\ell\ell}) < 0)} \,. \tag{5.28}$$

Fig. 5.17 illustrates the $\cos(\theta_i^{\pm})$ distribution across the parton, particle, and object levels. At the parton level, no cuts have been implemented, whereas the other two distributions have been normalised to the number of dileptonic events observed at $\sqrt{s} = 365\,\mathrm{GeV}$, with both leptons required to have energies greater than $10\,\mathrm{GeV}$. Furthermore, both reconstructed top-quarks must lie within a mass window of $\pm 5\,\mathrm{GeV}$ around the pole mass of the top quark of $173.1\,\mathrm{GeV}$.

The values of the polarisation coefficients $B_i^{\pm}$ have been extracted from an unbinned maximum likelihood fit to Eq. (5.25). For clarity, only the fit at the object level is displayed in Fig. 5.17 and the uncertainties shown in the legend correspond to the fit uncertainty. In general, a good agreement of the distributions and of the extracted polarisations is observed. It can be confirmed that due to the $\mathcal{CP}$ invariance of the SM, the top- and antitop-quark polarisation are expected to be the same, which results in $B_i^+ = B_i^-$. An alternative method to determine the polarisation parameters $B_i^{\pm}$ is by using the average value of the $\cos(\theta_i^{\pm})$ distribution, given by $B_i^{\pm} = 3 \cdot \langle \cos(\theta_i^{\pm}) \rangle$ [173]. It has been confirmed that the two approaches, the fit and the mean, are consistent within 1 %.

The distributions of $\cos(\theta_i^+)\cos(\theta_i^-)$ for the main diagonal elements of the spin-density matrix $\tilde{\boldsymbol{C}}$ are illustrated in Fig. 5.18 for each of the three distinct reference axes i. The event selection criteria used are identical to those applied for the $\cos(\theta_i^{\pm})$ distributions.

Due to the γ and Z-boson exchange in the $t\bar{t}$ production at a lepton collider, only the P- and $\mathcal{CP}$-even spin-correlation coefficients are allowed to have non-vanishing values, which are the main diagonal elements C_{ii}, as well as $C_{rk} + C_{kr}$, which has been extracted from the $\cos(\theta_r^+)\cos(\theta_k^-) + \cos(\theta_k^+)\cos(\theta_r^-)$ distribution. Again, the spin-correlation parameters have been determined from an unbinned maximum likelihood fit to Eqs. (5.26) and (5.27). The discrepancy between the coefficients at the particle and object levels can be addressed through a calibration and reweighting method, similar to the one used for the W-helicity fractions. However, this is beyond the scope of this thesis. Similarly to $B_i^{\pm}$, it has been confirmed that extracting the correlation coefficient from the mean value using $C_{ii} = -9 \cdot \langle \cos(\theta_i^+)\cos(\theta_i^-) \rangle$ is consistent within 1 % with the fit result [173].

The off-diagonal element, derived from fitting Eq. (5.27), is shown along with the distribution of the angle between the two leptons, $\cos(\theta_{\ell\ell})$, in Fig. 5.19. For the latter, the constraint on the reconstructed top-quark mass has been lifted.
For all polarisation and spin-correlation coefficients, the fit uncertainty is stated. However, the intrinsic statistical precision of 0.008 and 0.01 for $B_i^{\pm}$ and C_{ii} has been used for the EFT fit in the following chapter. Although these uncertainties are about twice and 100 times as large as the fit uncertainties for the polarisation and spin-correlation coefficients, respectively, it is assumed to be a more realistic assumption in terms of systematic uncertainty, which has not been considered here. In the case of $C_{rk} + C_{kr}$, the uncertainty has been set to 0.02. In conclusion, all values are summarised in Tab. 5.5.

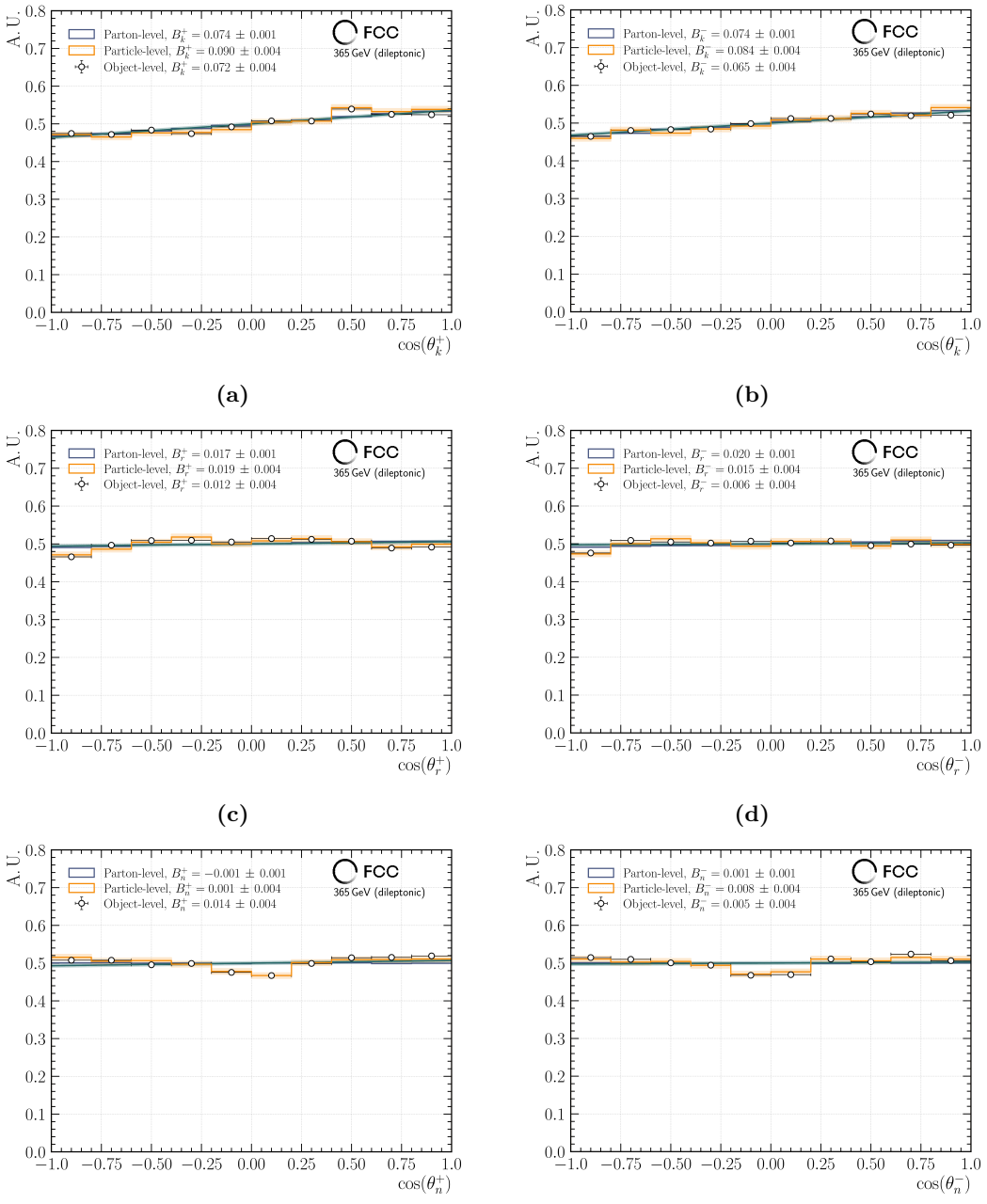

Figure 5.17: The top- and antitop-quark polarisations in the left (Figs. (a), (c), (e)) and right column (Figs. (b), (d), (f)), respectively. The $\mathcal{CP}$ invariance of the SM requires $B_i^+ = B_i^-$.

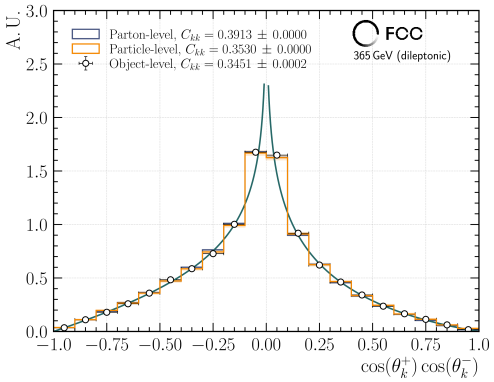

(a) Distribution to extract C_{kk}.

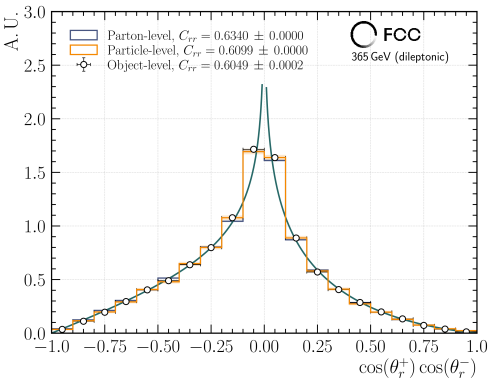

(b) Distribution to extract C_{rr}.

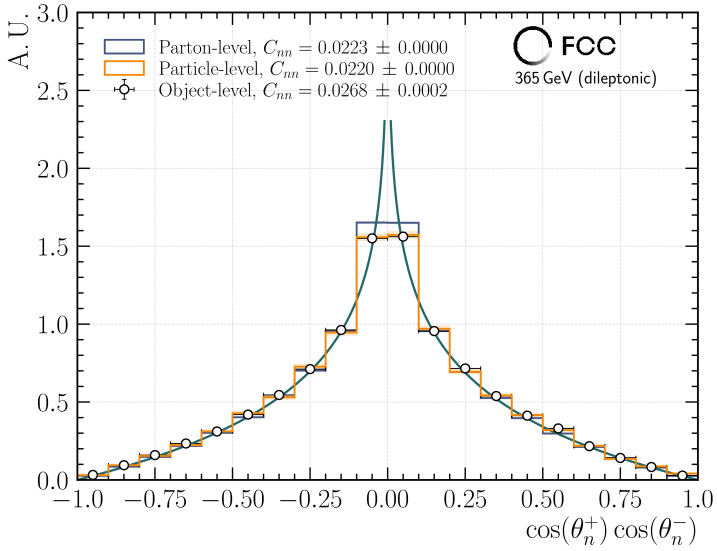

(c) Distribution to extract C_{nn}.

Figure 5.18: Main diagonal elements C_{ii} with $i \in [k, r, n]$ of the top-quark spin correlation matrix $\tilde{\boldsymbol{C}}$. All coefficient values have been derived from an unbinned maximum likelihood fit, whereby only the one to the object-level distribution is shown in the figures.

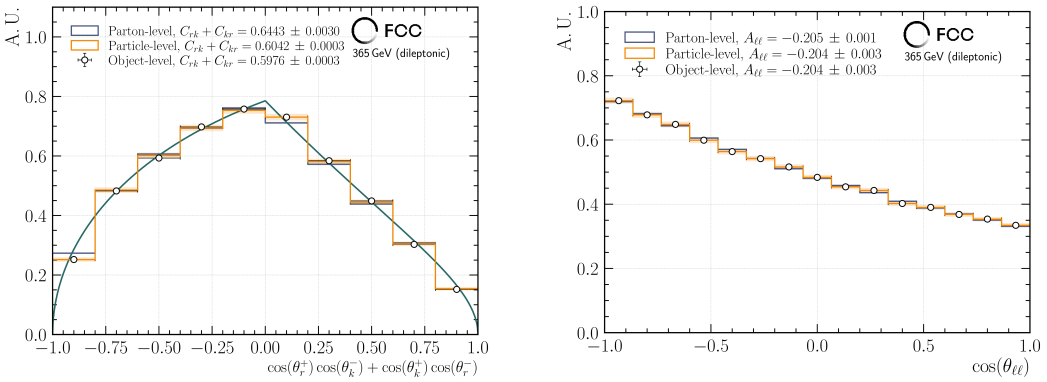

(a) **(b)**

Figure 5.19: The only off-diagonal element $C_{rk} + C_{kr}$, that shows sensitivity to modifications from dimension-six operators in Fig. (a). The distribution of the opening angle between the two leptons in their laboratory frames, which are experimentally precisely measurable in Fig. (b).

Table 5.5: The $t\bar{t}$ spin-correlation coefficients and the lepton-angle asymmetry at the parton and object level. Uncertainties refer to the fit uncertainty.

Coefficient	Parton level	Object level
B_k^+, B_k^-	0.0740 ± 0.0001, 0.0740 ± 0.0001	0.072 ± 0.004, 0.065 ± 0.004
B_r^+, B_r^-	0.0170 ± 0.0010, 0.0200 ± 0.0010	0.012 ± 0.004, 0.006 ± 0.004
B_n^+, B_n^-	-0.0010 ± 0.0010, 0.0010 ± 0.0010	0.014 ± 0.004, 0.005 ± 0.004
C_{kk}	0.3913	0.3451 ± 0.0002
C_{rr}	0.6340	0.6049 ± 0.0002
C_{nn}	0.0223	0.0268 ± 0.0002
$C_{rk} + C_{kr}$	0.6443 ± 0.0030	0.5976 ± 0.0003
$C_{rk} - C_{kr}$	-0.0027 ± 0.0031	-0.0151 ± 0.0003
$C_{nr} + C_{rn}$	0.0048 ± 0.0031	0.0031 ± 0.0003
$C_{nr} - C_{rn}$	0.0020 ± 0.0031	-0.0125 ± 0.0003
$C_{nk} + C_{kn}$	-0.0017 ± 0.0031	0.0019 ± 0.0003
$C_{nk} - C_{kn}$	0.0032 ± 0.0031	0.0086 ± 0.0003
$A_{\ell\ell}$	-0.205 ± 0.001	-0.204 ± 0.003

5.4.3 Cross-section measurements

The chapter on sensitive top-quark observables concludes with the total production cross-sections in the semi and dileptonic channels, denoted $\sigma_{t\bar{t}}^{1\ell}$ and $\sigma_{t\bar{t}}^{2\ell}$, respectively. They have been determined from the expected number of events N_{kl} and the integrated luminosity $\int \mathcal{L}\,\mathrm{d}t = 2.32\,\mathrm{ab}^{-1}$ according to

$$\sigma_{t\bar{t}}^{k\ell} = \frac{N_{kl}}{\int \mathcal{L}\,\mathrm{d}t}\,, \quad \text{with} \quad k \in [1,2]\,. \tag{5.29}$$

From the approximated $1.9 \cdot 10^6$ $t\bar{t}$ pairs at $\sqrt{s} = 365\,\mathrm{GeV}$, N_{kl} has been estimated to

$$\begin{aligned} N_{1\ell} &= 540\,000 \pm 5130\,, \\ N_{2\ell} &= 65\,835 \pm 627\,. \end{aligned} \tag{5.30}$$

The calculation is based on the semi and dileptonic branching-fraction $\varepsilon_{k\ell}$ and a combined efficiency $\varepsilon_{\mathrm{comb}}$, which includes the two b-tagging efficiencies of 80 %, as well as the identification efficiency of prompt leptons from the PV, which has been taken to be 99 % (refer to Fig. 5.4b). An overall uncertainty on $\varepsilon_{\mathrm{comb}}$ of 1 % has been assumed, leading to $\varepsilon_{\mathrm{comb}}^{k\ell} \approx (63.0 \pm 0.6)\,\%$ for both decay channels. Consequently, the cross section has been calculated to

$$\sigma_{t\bar{t}}^{1\ell} = (232 \pm 2)\,\mathrm{fb}\,, \tag{5.31}$$

$$\sigma_{t\bar{t}}^{2\ell} = (28.4 \pm 0.3)\,\mathrm{fb}\,. \tag{5.32}$$

5.5 Conclusions and Outlook

In this chapter, top-quark observables have been identified that show sensitivity to modifications from dimension-six operators in $t\bar{t}$ production- and decay-processes. In particular, the bosonic W and Z, as well as the four-fermion operators, show high sensitivity to the top-quark forward-backward asymmetry A_{FB}^{t} and the polarisation along its flight direction. Following the selection of observables, the $t\bar{t}$-system reconstruction within a more realistic FCC-ee environment has been presented, using lepton-collider unique characteristics like the presence of one PV to identify prompt leptons with purities around 99 %. Furthermore, novel neutrino-reconstruction approaches have been explored, which use the precise knowledge of the initial state to compute the full neutrino momentum-vectors. In the dileptonic decay-channel, the main source of reconstruction uncertainties arises from the knowledge of the COM energy, which is effectively reduced by the presence of ISR and BS.

In both the semi and the dileptonic $t\bar{t}$ decay-channels, the expected statistical precision for the sensitive observables has been computed. In case of A_{FB}^{t} and the

W-helicity fractions, a first assessment of systematic uncertainties has been performed by considering variations of the simulation input parameters. For all observables under study, a relative uncertainty of the order $\mathcal{O}(1\,\%)$ could be achieved.

However, future works in this sector should also consider more realistic jet-flavour tagging, since multivariate techniques for hadronic Higgs-decay processes at the ZH threshold show promising performance. In addition, further sources of systematic uncertainties should be considered, as well as techniques to estimate the effective COM energy to improve the neutrino reconstruction in the dileptonic decay channel from, for example, undetected photons along the beam pipe or the use of a kinematic fitting procedure within in the minimisation algorithm proposed in Ref. [170].

6 Combining top-quark measurements in SMEFT

This chapter describes the exploration of the Wilson coefficient parameter-space given the expected precision of the top-quark measurements outlined in Chap. 5. Synergies from EWPOs as shown in Ref. [65] would further imply tighter constraints on the Wilson coefficients, especially on O_{tW} and O_{tZ}. However, since contributions from top quarks in the measurement of R_b and A_{FB}^b only arise at loop level, as shown in Fig. 2.2 and theoretical calculations of that process are not available to date, only constraints from the top-quark measurements are considered in the following chapter.

The chapter is organised as follows: First, the interpolation method that takes into account the correlation of different operators on one observable is described in Sec. 6.1, followed by an introduction to Bayesian inference and its application to derive limits on the Wilson coefficients in Sec. 6.2. In Sec. 6.4, the results of the limit calculation utilising the `EFTfitter.jl` [174] package are presented before concluding in Sec. 6.5.

6.1 Interpolating with correlations

As already briefly described in Sec. 5.2, for the fast calculation of an observable given a configuration of Wilson coefficients, interpolations have been derived to continuously describe the observables as functions of them. An example of the one-dimensional interpolation of A_{FB}^t as a function of $\tilde{C}_i$ and only varying one coefficient with all other coefficients fixed to zero is presented in Sec. 5.2.1.

In order to take into account the correlation between the different operators, Eq. (2.13) has been used to simulate the observables, again with the MG event generator and the `dim6top_LO` model. In this case, the phase space has been evaluated for different configurations of the Wilson coefficients, which have been chosen from a Sobol sequence [175]. The Sobol sequence is assumed to cover the phase space in the most equal way. In total about 2000 different Wilson-coefficient configurations have been used, and the functionalities of the `iminuit` package have been applied to find the optimal interpolation parameters. The validity of the fit has been evaluated with

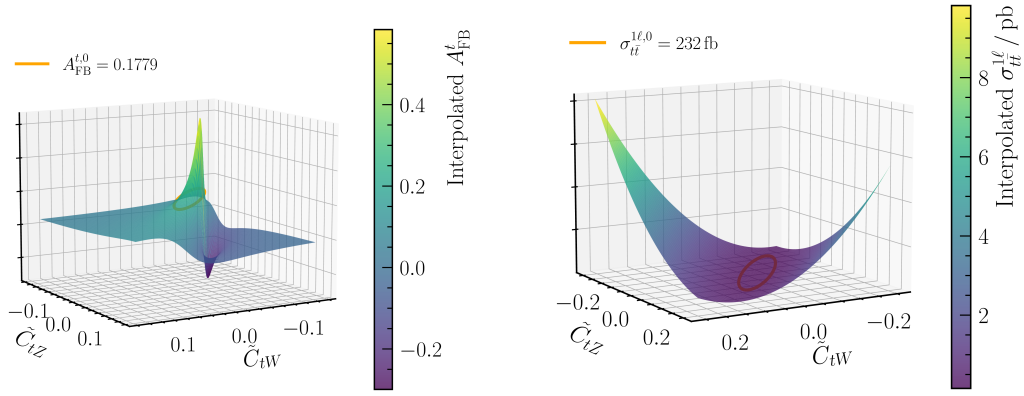

(a) Top-quark forward-backward asymmetry.

(b) Semileptonic cross-section $\sigma_{t\bar{t}}^{1\ell}$.

Figure 6.1: Three-dimensional representation of the top-quark forward-backward asymmetry and the semileptonic cross-section in Figs. (a) and (b), respectively. The SM values at $C_i = 0$, $A_{\mathrm{FB}}^{t,0}$ and $\sigma_{t\bar{t}}^{1\ell,0}$, are indicated as orange lines.

the χ^2/ndof value, which is indicated in the top left corner of each parameterisation figure (see, for example, Fig. 5.2). The values have all been found to be approximately one, and therefore the interpolation is assumed to describe well the simulated points in the region between $-1 \leq \tilde{C}_i \leq 1$.

Semileptonic observable interpolations The effect of correlations between the different operators is shown in the three-dimensional representation of the top-quark forward-backward asymmetry and the semileptonic cross-section $\sigma_{t\bar{t}}^{1\ell}$ in the $(\tilde{C}_{tW}$–$\tilde{C}_{tZ})$ plane in Fig. 6.1. They present the profiled interpolation on the z axis for the two active operators on the x and y axis, while setting the other Wilson coefficients to zero. The region, where the SM values[1] $A_{\mathrm{FB}}^{t,0} = 0.1779$ and $\sigma_{t\bar{t}}^{1\ell,0} = 232\,\mathrm{fb}$, respectively, are reached is shown as a orange band in the figures. Here, the SM value corresponds to the value of the interpolation at $\tilde{C}_i = 0$. Especially for A_{FB}^{t}, a strong correlation between the two bosonic operators can be seen, whereas the correlation is rather mild for the cross section. However, including all correlations is a crucial part in calculating the limits on the Wilson coefficients.

A special case are the top-quark decay width Γ_t and the W-helicity fractions $F_{\mathrm{L},0}$, for which analytical expressions from Ref. [164] have been used, whereby only the dependence on $\tilde{C}_{tW}$ has been included here. Again, the SM value has been taken

[1]This value differs slightly from the one obtained from the nominal FCC-ee sample, which has been generated with `Whizard`. Reasons might be a different set of input parameters such as the top-quark mass and the LO calculation from MG compared to the NLO calculation of `Whizard`. In addition, the imperfect interpolation is another source of the difference.

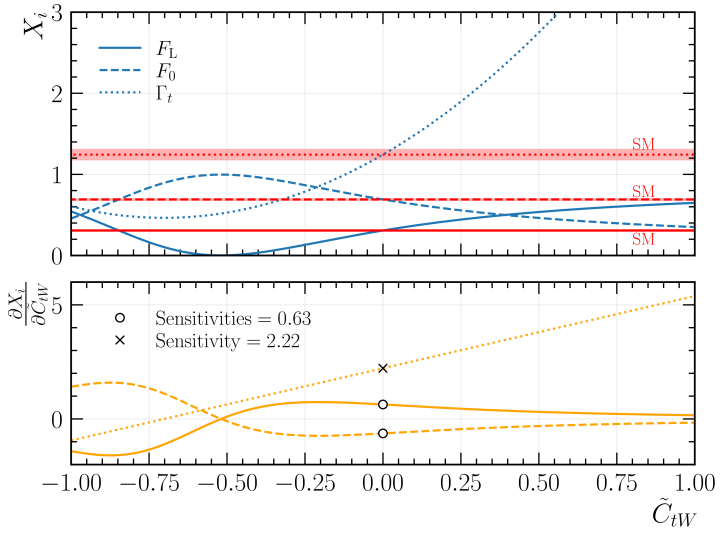

Figure 6.2: The top-quark decay observables Γ_t and the W-helicity fractions F_L and F_0, respectively. Only the dependence on $\tilde{C}_{tW}$ has been considered. Although the expected uncertainty of the W-helicity fractions is smaller, the sensitivity of Γ_t is about three times larger.

as the value evaluated at $\tilde{C}_i = 0$ and is presented in all representations as a red line that includes the total uncertainty $\sigma_{\text{tot.}}$. It is the expected value based on the results from Chap. 5 or the predictions from Ref. [10]. If both statistical and systematic uncertainties for an observable have been calculated, they have been added in quadrature via $\sigma_{\text{tot.}} = \sqrt{\sigma^2_{\text{stat.}} + \sigma^2_{\text{syst.}}}$.

The dependencies for Γ_t and $F_{L,0}$ are presented together in Fig. 6.2. For Γ_t the expected statistical uncertainty of $\sigma_{\text{stat.}}(\Gamma_t) = 45\,\text{MeV}$ has been used and the systematic uncertainty has been assumed to be of the same size [10]. It can be seen that especially the top-quark decay width shows a high sensitivity to $\tilde{C}_{tW}$, while the sensitivity of the W-helicity fractions is mild. However, F_0 and F_L benefit from a precise measurement in the semileptonic $t\bar{t}$ decay-channel. The interpolation of the semileptonic cross-section $\sigma^{1\ell}_{t\bar{t}}$ is presented in App. A.6.1 in Fig. A.17.

Dileptonic observable interpolations The dileptonic observables, which have shown sensitivity to modifications due to dimension-six operators, are $\sigma^{2\ell}_{t\bar{t}}$, $B^+_{k,r}$, C_{ii} with $i \in [r,k,n]$, $C_{rk} + C_{kr}$ and $A_{\ell\ell}$. As an example, the profiled interpolation for the top-quark polarisation parameter B^+_k is presented in Fig. 6.3 for each Wilson coefficient $\tilde{C}_i$ individually while setting $\tilde{C}_j = 0$ for $j \neq i$. Again, a good agreement of the interpolation and the simulated observables has been found, which is reflected in the χ^2/ndof value of around one. As indicated with the gradient in orange, the sensitivity

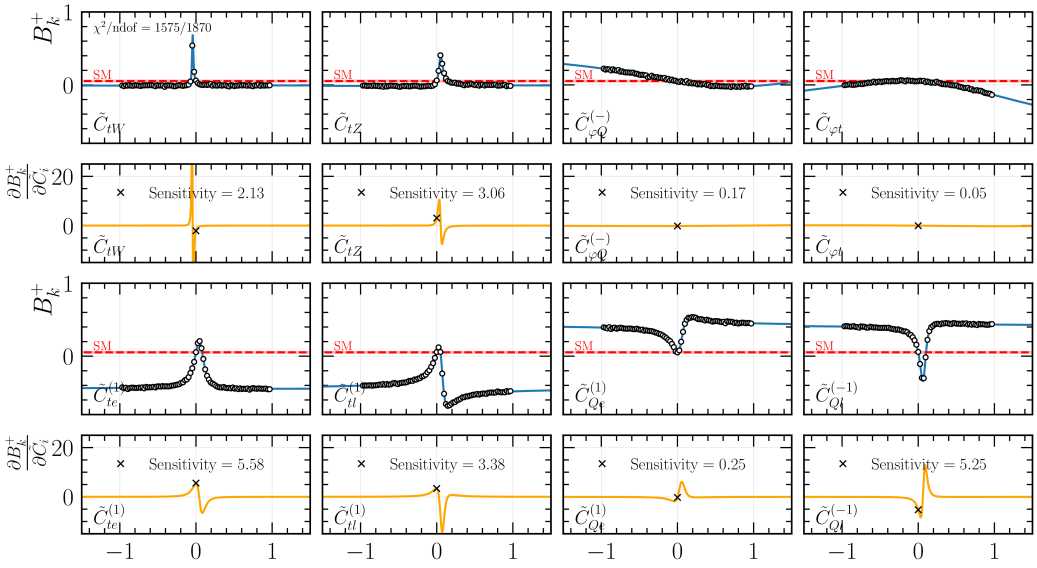

Figure 6.3: The top-quark polarisation B_k^+ as a function of the different Wilson coefficients with the interpolations in blue and the gradient in orange. The SM prediction at $\tilde{C}_i = 0$ is shown as a red line.

is especially high for the four-fermion operators $O_{te}^{(1)}$, $O_{tl}^{(1)}$ and $O_{Ql}^{(-1)}$, followed by the effective W- and Z-boson operators. Similarly to A_{FB}^t in Fig. 5.2, only a modest sensitivity can be observed for operators that involve interactions with the Higgs field $O_{\varphi t}$ and $O_{\varphi Q}^{(-)}$.
The interpolations for the remaining dileptonic $t\bar{t}$ observables are presented in App. A.6.1 from Fig. A.18 up to Fig. A.24.

In addition to the expected precision of the semi and dileptonic observables, the interpolations have been used in the next step to derive limits on the Wilson coefficients using Bayesian inference. Its basic principle and the implementation in `EFTfitter.jl` [174] are described below.

6.2 Bayesian inference

The Bayesian method provides a framework for interpreting probabilities in data analysis across various scientific disciplines. This approach uses the update of prior knowledge about the parameters of a model by integrating new data. It is fundamentally grounded on Bayes' theorem, which describes the conditional probability for an event B to occur, given that a condition A is true. In its simplest

form, Bayes' theorem can be expressed via

$$p(B|A) = \frac{p(A|B)p(B)}{p(A)}\,. \tag{6.1}$$

Since A has already occurred, $p(B|A)$ is called the *posterior probability density*. Within Bayesian inference, $p(B)$ is termed the *prior probability density*[2], representing the initial probability of event B. The *likelihood* $p(A|B)$ denotes the probability of observing event A under the condition that B is true. Expressing Bayes' theorem in a model-based manner, B becomes a set of free parameters $\boldsymbol{\theta}$ of, for instance, a physical model, given that some quantity A, in the following referred to as data D, has been observed

$$p(\boldsymbol{\theta}|D) = \frac{p(D|\boldsymbol{\theta})p(\boldsymbol{\theta})}{p(D)}\,. \tag{6.2}$$

The denominator of Eq. (6.2) is referred to as the *evidence* and provides a normalisation over all possible states

$$p(D) = \int p(D|\boldsymbol{\theta})p(\boldsymbol{\theta})\,\mathrm{d}\boldsymbol{\theta}\,. \tag{6.3}$$

In the case of a set of parameters of a model, knowledge about a single parameter θ_i can be obtained by marginalising the posterior distribution accordingly

$$p(\theta_i|D) = \int p(\boldsymbol{\theta}|D) \prod_{i\neq j} \mathrm{d}\theta_j\,. \tag{6.4}$$

In BSM searches, the Bayesian approach allows to refine the knowledge about the Wilson coefficients $\tilde{C}_i$, which are the free parameters in the effective Lagrangian. This refinement is based on the data gathered from experiments, such as those from particle colliders. Since the parameter space of the model is often high dimensional and Eqs. (6.3) and (6.4) require for solving complex integrals, numerical methods are utilised. A variety of tools for the sampling of high-dimensional parameter spaces, integration and mode estimation are provided by the Bayesian Analysis Toolkit in `julia` (`BAT.jl`) toolkit [176, 177]. An interface of the functionalities of `BAT.jl` for constraining parameters of a physics model and allowing for the combination of different measurements is provided by `EFTfitter.jl`, which is particularly suited for EFT interpretations [178, 179].

The following section briefly describes the basics of `EFTfitter.jl` software, the concept of combining different measurements, and its application for the interpretation of measurements in the EFT framework.

[2]In the following, the notation *probability density* is neglected.

6.3 Combining measurements in SMEFT

In the current implementation of `EFTfitter.jl`[3] in version `0.2.0`, the likelihood $p(D|\boldsymbol{\theta})$ of Eq. (6.2) is a function of a set of measurements $\boldsymbol{D}$ and parameters $\boldsymbol{\theta}$, which are assumed to depend on the respective observable $\boldsymbol{y} = \boldsymbol{y}(\boldsymbol{\theta})$. Then the likelihood can be expressed as

$$\ln(p(\boldsymbol{D}|\boldsymbol{\theta})) = -\frac{1}{2}\sum_i \sum_j \left(\boldsymbol{D} - \boldsymbol{U}\boldsymbol{y}(\boldsymbol{\theta})\right)_i M_{ij}^{-1} \left(\boldsymbol{D} - \boldsymbol{U}\boldsymbol{y}(\boldsymbol{\theta})\right)_j , \tag{6.5}$$

with the covariance matrix $\boldsymbol{M}$. The matrix $\boldsymbol{U}$ describes the linking from the set of measurements $\boldsymbol{D}$ to either of the observables $\boldsymbol{y}(\boldsymbol{\theta})$, via

$$U_{ij} = \begin{cases} 1\,, & \text{if } D_i \text{ is a measurement of the observable } y_j\,, \\ 0\,, & \text{else.} \end{cases} \tag{6.6}$$

Eq. (6.5) assumes that all measurements follow a Gaussian distribution for simplicity, which, in reality, is not always the case. The parameterisations $\boldsymbol{y}(\boldsymbol{\theta})$ with the set of Wilson coefficients $\boldsymbol{\theta}$ are those derived in Sec. 6.1. Furthermore, $\boldsymbol{y}$ is the set of semi and dileptonic top-quark observables. Together with the measurements and their expected uncertainties, which have been worked out in Sec. 5, the posterior probability can be explored with suitable methods for sampling the parameter space. `BAT.jl` is optimised for such use cases and provides numerous sampling algorithms to effectively explore the high-dimensional parameter space. Here, the *Robust adaptive Metropolis algorithm* [180] is used to draw samples from the posterior distribution.

6.4 Resulting Wilson coefficients constraints

The results of the posterior-distribution sampling are presented in Fig. 6.5, with the Wilson coefficient indicated in the top left corner of each one-dimensional distribution. Here, the prior distribution has been chosen to be uniform in the range from $-1 \leq \tilde{C}_i \leq 1$, where it has been confirmed that the interpolations describe the observables well. For every posterior-coefficient distribution, it has been ensured that no significant secondary peak has been neglected in the analysis, with only the region of interest displayed. The marginalised, one- and two-dimensional posterior distributions are presented on the main diagonals and the side diagonals, respectively. The two-dimensional heatmaps of the different configurations are shown in the upper side-diagonal. In case of the contour plots on the main diagonal and lower side-diagonal, the smallest 68.3 %, 95.5 % and 99.7 % intervals are displayed in different shades of blue. The SM value at $\tilde{C}_i = 0$ and $(\tilde{C}_i = 0, \tilde{C}_j = 0)$ for $i \neq j$ is indicated with a black line and a white star, respectively.

[3] `https://github.com/tudo-physik-e4/EFTfitter.jl/tree/main`

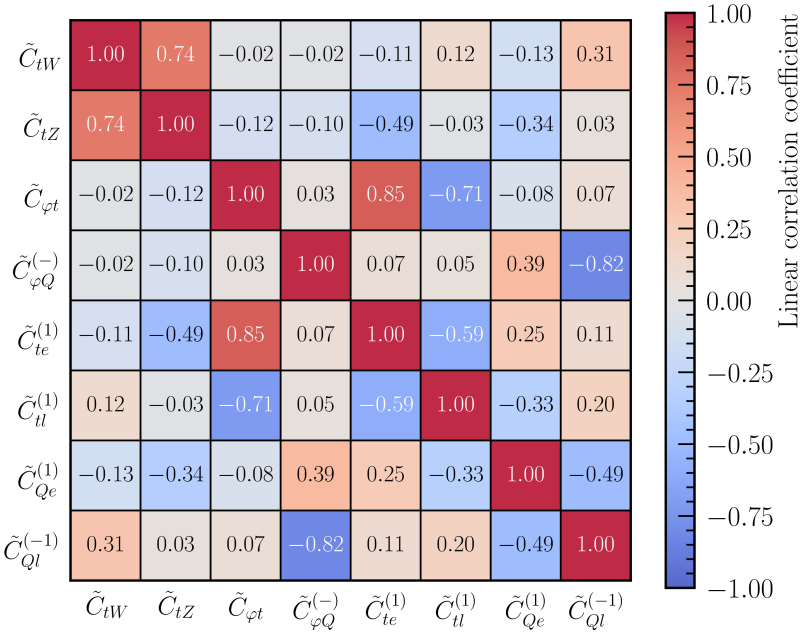

Figure 6.4: Correlations between the different Wilson coefficients from the fit to the top-quark sector at FCC-ee. Values closer to +1 and −1 correspond to a strong positive and negative correlation, respectively.

In general, all distributions are centred around zero. This is expected because the SM hypothesis has been assumed in the interpolations for each observable. Except for the heavy operators that include interactions with the Higgs field, $O^{(-)}_{\varphi Q}$ and $O_{\varphi t}$, the distributions have similar widths. This results from the generally reduced sensitivity of these operators to the included measurements, which is of the order $\mathcal{O}(10^{-2} - 10^{-1})$, while all other operators show a similar sensitivity of the order $\mathcal{O}(10^{-1} - 1)$ (see Fig. 5.3).

Although the lower and upper side-diagonals of Fig. 6.5 already qualitatively show the correlation between different Wilson coefficients, a quantitative analysis has been performed with the samples from the posterior distribution. The correlation matrix is presented in Fig. 6.4, with values below and above zero indicating negative and positive linear correlation, respectively. Higher-order correlations have not been considered here. The closer the values are to zero, the lower the correlation between the operators. The strong positive correlation of 0.74 between O_{tW} and O_{tZ} verifies the linked effect in the gauge-boson sector, which is theoretically described in Eq. (2.15) and expresses the linear dependence between O_{tZ} and O_{tW} with an additional term from the $\mathrm{SU}(2)_\mathrm{L}$ field-strength tensor $B_{\mu\nu}$. In general, strong positive and negative correlations, such as 0.85 between $O^{(1)}_{te}$ and $O_{\varphi t}$, imply that effects on

one observable cannot be directly translated to originate from one specific operator. The presence of such strong correlations highlights the importance of considering a broader set of observables and measurements, which can help to disentangle the contributions of different operators.

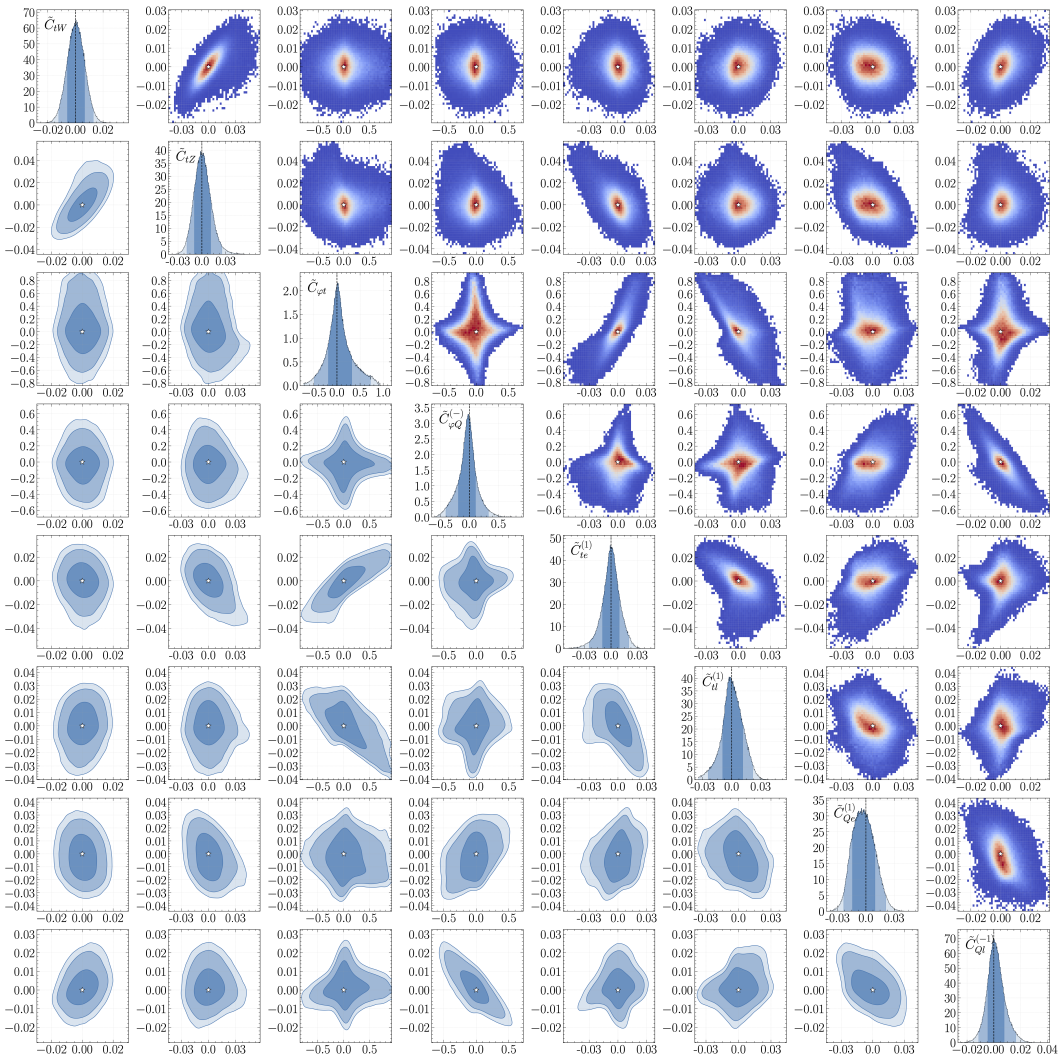

Figure 6.5: Marginalised, one- and two-dimensional distributions of the Wilson coefficients on the main and side diagonal. The colour coding represents the smallest 68.3 %, 95.5 %, and 99.7 % intervals for the contour and one-dimensional plots. Heatmaps are presented on the upper side-diagonal. Similar constraints are obtained for O_{tW} and O_{tZ}, as well as for the four-fermion operators. The constraints on $O_{\varphi t}$ and $O_{\varphi Q}^{(-)}$ are about an order of magnitude looser.

Limits on Wilson coefficients with FCC-ee precision From the marginalised distributions, the one-dimensional widths and ranges of the smallest 68.3 % and 95.5 % intervals have been calculated. They are presented in the left and right panels of Fig. 6.6 in solid and dotted blue for the 68.3 % and 95.5 % intervals, respectively. The tightest constraints have been obtained for O_{tW} with a width of its smallest 95.5 % interval of approximately $2 \cdot 10^{-2}$. The constraints on $O_{Ql}^{(-1)}$ are similar in size. These tight constraints are a consequence of a high sensitivity of $O_{Ql}^{(-1)}$ to, for example, the polarisation of the top quark B_k^+. On the other hand, O_{tW} shows high sensitivities to all observables under study with the highest to the semileptonic cross section $\sigma_{t\bar{t}}^{1\ell}$, which is assumed to be measured with one of the highest precision of $\mathcal{O}(1\,\%)$ among all observables considered in this analysis. By far the loosest constraints are achieved for $O_{\varphi t}$ and $O_{\varphi Q}^{(-)}$, showing the lowest sensitivity to all observables.

Comparison to current LHC constraints Fig. 6.6 also includes the reproduced result from Ref. [65] in orange as comparison to current constraints from top-quark measurements. The result has been obtained from a fit to present LHC data from the ATLAS and CMS Collaborations. The measurements considered in the analysis are summarised in Tab. 6.1, which has been taken from Ref. [65]. In the table, *fiducial*

Table 6.1: Summary of top-quark measurements included in the fit. Fiducial and inclusive cross-section measurements as well as the top-quark decay observables F_0, F_L and Γ_t are considered. The table is adapted from Ref. [65].

Observable	COM energy	$\int \mathcal{L}\,\mathrm{d}t$	Experiment	Reference
Fiducial $\sigma_{t\bar{t}\gamma}^{1\ell}, \sigma_{t\bar{t}\gamma}^{2\ell}$	13 TeV	$36.1\,\mathrm{fb}^{-1}$	ATLAS	[181]
Inclusive $\sigma_{t\bar{t}Z}$	13 TeV	$77.5\,\mathrm{fb}^{-1}$	CMS	[182]
Inclusive $\sigma_{t\bar{t}}^{2\ell}$	13 TeV	$36.1\,\mathrm{fb}^{-1}$	ATLAS	[183]
F_0, F_L, Γ_t	8 TeV	$20.2\,\mathrm{fb}^{-1}$	ATLAS	[184, 185]

means that only a certain kinematic and/or detector phase-space has been considered in the analysis. This is in contrast to *inclusive*, where such cuts have not been set.

The limits on the Wilson coefficients from the measurements have also been derived from a fit using `EFTfitter.jl`. Since the limits in Ref. [65] are provided for the common subset of operators

$$\{O_{uB}, O_{uW}, O_{\varphi q}^{(1)}, O_{\varphi Q}^{(3)}, O_{\varphi u}\}\,, \tag{6.7}$$

the following relations [66] have been used to achieve comparabilit with the ones used for the top-quark measurements at FCC-ee

$$\begin{aligned} C_{\varphi Q}^{(-)} &= C_{\varphi q}^{(1)} - C_{\varphi q}^{(3)}\,, \\ C_{tZ} &= \cos(\theta_\mathrm{W}) C_{uW} - \sin(\theta_\mathrm{W}) C_{uB}\,. \end{aligned} \tag{6.8}$$

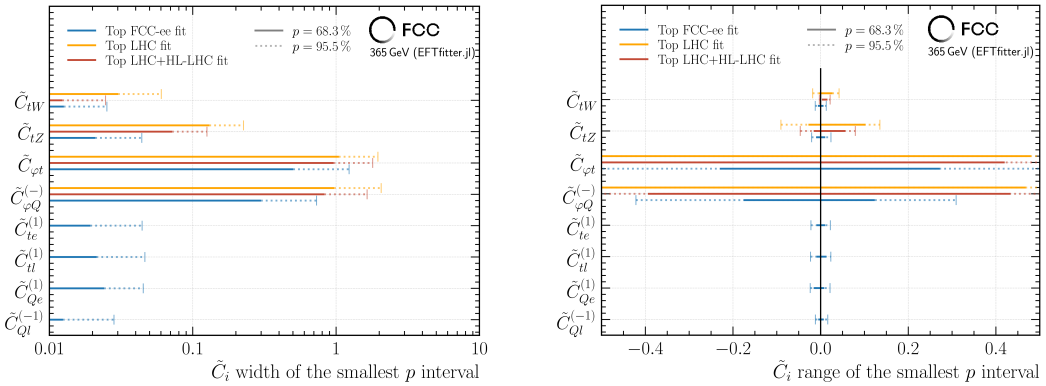

(a) Total width of the smallest intervals of the marginalised Wilson-coefficient distribution.

(b) Range of the smallest intervals of the marginalised Wilson-coefficient distribution.

Figure 6.6: Smallest 68.3 % and 95.5 % interval widths and ranges in Figs. (a) and (b), respectively, for the fit in the top-quark sector. The limits are shown separately for the projected FCC-ee precision in blue and the current LHC measurements orange. In dark red, a combination of top-quark measurements from LHC and HL-LHC are presented.

Since the modifications affect interactions with top quarks, the index u in Eqs. (6.7) and (6.8) refers to the up-type top quark. Modifications due to four-fermion operators with charged leptons in the initial state cannot be constrained with data collected in a pp collider.

The comparison of the limits derived from the projected FCC-ee precision and the top-quark LHC measurements shows an improvement in the constraints of O_{tW} of about a factor two, while for O_{tZ} the improvement is about a factor five. This is due to the direct probe of modifications at the $Zt\bar{t}$ vertex in $t\bar{t}$ production at a lepton collider. Only mild improvements have been achieved for the operators that modify the interaction with the Higgs field.

Comparison to HL-LHC projections In Ref. [65], limits on the Wilson coefficients including both, measurements at the LHC and its upgrade phase, the HL-LHC have been derived. The projected measurements that have been included in the Bayesian fit are summarised in Tab. 6.2. In these projections, improvements have been assumed not only in the statistical uncertainty arising from a larger amount of data, but also on the theoretical uncertainties by a factor of two and further improvements on the systematic uncertainty. Again, the transformations as shown in Eq. (6.8) have been applied and the results are presented in dark red in the left and right panels of Fig. 6.6. In conclusion, tighter limits can be observed in comparison to the LHC-only fit, especially in O_{tW}, achieving constraints that are now competitive

Table 6.2: Summary of top-quark measurements included in the fit from projections at the HL-LHC. The table has been adapted from Ref. [65].

Observable	COM energy	$\int \mathcal{L}\,\mathrm{d}t$	Experiment	Reference
Fiducial $\sigma^{1\ell}_{t\bar{t}\gamma}, \sigma^{2\ell}_{t\bar{t}\gamma}$	14 TeV	$3000\,\mathrm{fb}^{-1}$	ATLAS	[186, 187]
Inclusive $\sigma_{t\bar{t}Z}$	14 TeV	$3000\,\mathrm{fb}^{-1}$	CMS	[186, 188]
Inclusive $\sigma^{2\ell}_{t\bar{t}}$	14 TeV	$3000\,\mathrm{fb}^{-1}$	ATLAS	[186, 189]
F_0, F_L, Γ_t	———	———	———	[190, 191]

with those obtained from the bare FCC-ee fit. Moreover, the improvement factor of approximately five in O_{tZ} is reduced, yielding an enhancement of roughly a factor of three. The limits on $O_{\varphi t}$ and $O^{-}_{\varphi Q}$ have not improved significantly, remaining the least constrained operators in the fit.

The marginalised posterior distributions for both, the LHC measurements and the combined one of the LHC measurements including the HL-LHC projections, are provided in the App. A.6 in Fig. A.25 and A.26, respectively.

6.5 Conclusions and Outlook

In this chapter, constraints on the Wilson coefficients have been derived, whose operators have shown sensitivity to affect at least one top-quark observable. For this, the concept of Bayesian inference and the implementation of the likelihood in the `EFTfitter.jl` package have been presented, which allow the combination of different measurements. In order to take into account the correlation between different Wilson coefficients, semi and dileptonic observables have been simulated by varying all Wilson coefficients at the same time. In this multidimensional phase-space of Wilson coefficients, observable interpolations have been found to allow for a fast and efficient evaluation of the observable value given a set of Wilson coefficients. Numerical methods for sampling and integration from the `BAT.jl` software toolkit have been used to explore the full posterior phase-space and derive limits from the marginalised one-dimensional posterior distributions. Particularly for the effective W- and Z-boson operators O_{tW} and O_{tZ}, as well as the four-fermion operators, tight constraints of the order of $\mathcal{O}(10^{-2})$ have been obtained. The operators affecting the interaction with the Higgs field are only moderately constrained at the order one. These results are consistent with the limits and hierarchy from current LHC measurements in the top-quark sector, which have been improved by about a factor of five in the case of O_{tZ} given the smallest 95.5 % intervals. When also projected measurement uncertainties from the HL-LHC are considered, the difference with

respect to the limits from FCC-ee reduces to the same order for O_{tW}, while still improving by about a factor three for O_{tZ}.

In recent analyses that have explored the potential synergy of top-quark measurements with EWPO[4] and B-physics observables, the combination of top-quark and $Zb\bar{b}$ observables has enabled the disentanglement of the contributions from $O_{\varphi Q}^{(1)}$ and $O_{\varphi Q}^{(3)}$ [65, 192]. Both, $O_{\varphi Q}^{+} = O_{\varphi Q}^{(1)} + O_{\varphi Q}^{(3)}$ and $O_{\varphi Q}^{-} = O_{\varphi Q}^{(1)} - O_{\varphi Q}^{(3)}$, have constrained $\tilde{C}_{\varphi Q}^{(-)}$ in the case of top-quark observables and $\tilde{C}_{\varphi Q}^{(+)}$ with EWPO from the process $Z \to b\bar{b}$ individually. In the combination, constraints on the individual operators $O_{\varphi Q}^{+}$ and $O_{\varphi Q}^{-}$ can be obtained.

However, these operators act at the tree-level $Zb\bar{b}$ vertex. The effects of top-quark-induced loops at the production vertex could become significant for R_b and A_{FB}^{b} with the precision in reach with FCC-ee. This ultimately requires calculating the effect of O_{tW} and O_{tZ} acting in vertex corrections, as shown in Fig. 2.2.

[4]Here, EWPO refers only to those including b quarks, namely R_b and A_{FB}^{b}.

7 Conclusions

The discovery of the Higgs boson in 2012 at CERN was a milestone in particle physics, completing the Standard Model of Particle Physics (SM) as the most successful theory known today. Over decades, the SM demonstrated its exceptional ability to predict the dynamics of elementary particles, particularly in particle-collider experiments. Although no significant deviations have been observed yet, measurements may eventually reveal tiny discrepancies between theory and experiment, especially concerning the heaviest, third-generation fermions and their coupling structure to gauge bosons. This thesis has presented a novel approach to unlocking the physics potential of a possible future circular electron-positron collider at CERN, the FCC-ee, which is part of the FCC project and has been introduced in Chap. 3. This project also includes a hadron-hadron collider programme aimed at achieving the highest possible energies by the end of the century.

Building upon the legacy of the Z-physics programme at the Large Electron-Positron Collider (LEP), the FCC-ee will collect about a million times more Z-boson decays. This substantial increase in data poses a major challenge: achieving raw statistical precision while maintaining rigorous control over external influences, particularly contamination from light quarks in precision measurements of the beauty-quark coupling. In Chap. 4, the use of exclusively reconstructed b-hadrons for measuring the partial decay-width ratio R_b and the beauty-quark forward-backward asymmetry A_{FB}^b has demonstrated the capability to identify the beauty quark with a purity consistent with 100 %. The remaining systematic uncertainties have been identified and addressed, effectively mitigating external factors such as the dependence on the collision position and distortions of the flight direction from radiative effects, thereby enabling competition with the statistical precision at the 0.01 % level. Consequently, this allows for the measurement of the weak mixing angle with a precision comparable to that derived from the more experimentally clean muon measurements. A brief outlook on the use of exclusive charm-hadron reconstruction to measure R_c has validated the principle under simplified assumptions so far and concluded the chapter.

This potential gain in accuracy has significant implications for measurements of the heaviest particle in the SM, the top quark, particularly if SM deviations at the Z pole manifest. The almost exclusive decay to a W boson and a beauty quark combined with its lifetime shorter than the hadronisation timescale make the top quark an exquisite laboratory to search for Beyond the Standard Model (BSM) physics effects.

A consistent approach to test BSM effects within an Effective Field Theory (EFT) at energy scales higher than those currently accessible in collider experiments is the Standard Model Effective Field Theory (SMEFT), extending the SM Lagrangian with higher-dimensional operators. In Chap. 5, the sensitivity of top-quark observables at FCC-ee modified by effective dimension-six operators has been examined, revealing significant modifications from effective W- and Z-boson operators, as well as point-like interactions. The expected experimental precision of these top-quark observables that affect both the production and decay has been studied using simulated events in a more realistic FCC-ee environment in Chap. 5. Lepton-collider unique techniques for reconstructing the system of two top quarks and an initial assessment of systematic uncertainties for selected observables have been examined. In combination, limits on the coupling strength of SMEFT operators, the *Wilson coefficients*, have been derived from a Bayesian fit using the `EFTfitter.jl` functionalities, an interface of the Bayesian Analysis Toolkit in `julia` (`BAT.jl`) toolkit. It allows to derive constraints on the Wilson-coefficient parameter space by combining top-quark measurements. The fit setup and numerical methods have been presented in Chap. 6, which has also shown the marginalised distributions of the Wilson-coefficient parameter space allowed by the measurement uncertainties. The tightest constraints could be achieved for operators that affect the Wtb and $Zt\bar{t}$ vertex, improving their current limits from LHC measurements by approximately a factor of five. However, both operators may affect beauty-quark EWPOs through top-quark induced loops and would allow for highly improved constraints from indirect measurements at the Z pole; unique opportunities for a future circular e^+e^- collider. Nevertheless, theoretical calculations are needed to accurately model the effect of dimension-six operators in top-quark loops in $Z \to b\bar{b}$ processes.

New large-scale collider experiments need motivation for a physics programme that outperforms former and competing machines. The FCC-ee achieves this, and the novel strategy developed in this thesis to measure beauty-quark EWPOs from $6 \cdot 10^{12}$ Z-boson decays with outstanding precision is a unique highlight. Particularly through the combination of precision measurements in the third generation of quarks, a new era of SMEFT interpretations is opening.

A Appendices

A.1 R_b analysis

The following sections provide additional material for the R_b analysis.

A.1.1 List of *b*-hadron decay modes

In this section of the appendix, the list of all b-hadron decay modes to be included to reach a tagging efficiency of $\approx 1\,\%$ is first presented before the results of the remaining representative decay modes are presented.

The following tables present the b-hadron decay modes, separately for the different b hadrons: $B^{\pm}$ in Tab. A.1, B^0 in Tab. A.2, B_s^0 in Tab. A.3 and for the Λ_b^0 baryon in Tab. A.4. If available, the subsequent decay of, for example, heavy c-hadrons and baryons is indicated in the third column. The sum of Brs in percentage values, which quantifies the overall tagging efficiency, is given in the last column. Heavy c-hadron decays in the $B_{(s)}^0$ and Λ_b^0 decays are expected to be the ones of Tab. A.1.

Table A.1: List of possible B^+ decay-modes. The decay modes in bold indicate the first decay stage of the B^+ meson followed by the subsequent decays in the third column. The hadronisation fraction of a b quark to a B^+ is 40.7 % and is not included in the branching fraction calculations.

Mode	$\mathrm{Br}(B^+ \to XY)$ / %	$\mathrm{Br}(X \to \text{final state})$ / %	$\sum \mathrm{Br}$ / %
$\boldsymbol{J/\psi\, K^+}$	0.102 ± 0.002	$J/\psi \to e^+e^-$ 5.971 ± 0.032	**0.012**
		$J/\psi \to \mu^+\mu^-$ 5.961 ± 0.033	
$\boldsymbol{\bar{D}^0\, \rho^+}$	1.340 ± 0.180	$\bar{D}^0 \to K^+\pi^-\pi^0$ 14.400 ± 0.500	**0.545**
$\boldsymbol{\bar{D}^0\, \pi^+\pi^-\pi^+}$	0.560 ± 0.210	$\bar{D}^0 \to K^+\pi^-2\pi^0$ 8.860 ± 0.230	**0.723**
$\boldsymbol{\bar{D}^0\, \pi^+}$	0.468 ± 0.013	$\bar{D}^0 \to K^+2\pi^-\pi^+$ 8.220 ± 0.140	**0.909**
$\boldsymbol{[\bar{D}^0\pi^+]_{D^*(2010)^+}\, \pi^-\pi^-\pi^0}$	10.160 ± 4.740	$\bar{D}^0 \to K^+2\pi^-\pi^+\pi^0$ 4.300 ± 0.400	**0.950**
		$\bar{D}^0 \to K^+\pi^-$ 3.947 ± 0.030	
$\boldsymbol{D^-\, \pi^+\pi^-}$	0.107 ± 0.005	$D^+ \to K^-2\pi^+$ 9.380 ± 0.160	**0.966**
		$D^+ \to K^-2\pi^+\pi^0$ 6.250 ± 0.180	
$\boldsymbol{D_s^+\, \bar{D}^0}$	0.900 ± 0.090	$D_s^+ \to [\pi^+\pi^-\pi^0]_\eta\, \pi^+\pi^0$ 9.500 ± 0.500	**1.081**
		$D_s^+ \to [\pi^+\pi^-\pi^0]_\eta [\pi^+\pi^0]_{\rho^+}$ 8.900 ± 0.800	
		$D_s^+ \to K^+K^-\pi^+\pi^0$ 5.500 ± 0.240	
		$D_s^+ \to K^+K^-\pi^+$ 5.380 ± 0.100	
		$D_s^+ \to 2\pi^+\pi^-$ 1.080 ± 0.040	
		$D_s^+ \to K^+K^-2\pi^+\pi^-$ 0.860 ± 0.150	
		$D_s^+ \to 3\pi^+2\pi^-$ 0.790 ± 0.080	

Table A.2: List of possible B^0 decay-modes. The subsequent decays of the J/ψ and c mesons are not shown as they can be found in Table A.1. The hadronisation fraction of a b quark to a B^0 is 40.7 % and is not included in the branching fraction calculations.

Mode	Br($B^0 \to$ final state) / %	$\sum$ Br / %
$\boldsymbol{J/\psi\, K^+\pi^-}$	0.014	**0.014**
$\boldsymbol{D^*(2010)^-\, \pi^+\pi^+\pi^-\pi^0}$	0.473	**0.487**
$\boldsymbol{D^*(2010)^-\, \pi^+\pi^0}$	0.403	**0.891**
$\boldsymbol{D^*(2010)^-\, \pi^+\pi^+\pi^-}$	0.194	**1.084**
$\boldsymbol{D^-\, \pi^+\pi^+\pi^-}$	0.094	**1.178**
$\boldsymbol{D^*(2010)^-\, \pi^+}$	0.074	**1.252**
$\boldsymbol{D^*(2010)^-\, D_s^+}$	0.069	**1.321**
$\boldsymbol{D^-\, \pi^+}$	0.039	**1.360**
$\boldsymbol{D^-\, D_s^+}$	0.036	**1.396**
$\boldsymbol{D^*(2010)^-\, D^0\, K^+}$	0.026	**1.422**
$\boldsymbol{D^-\, D^0\, K^+}$	0.007	**1.429**

Table A.3: List of possible B_s^0 decay-modes. The subsequent decays of the c mesons are not shown as they can be found in Tab. A.1. The hadronisation fraction of a b quark to a B_s^0 is 10.1 % and is not included in the branching fraction calculations.

Mode	Br($B_s^0 \to$ final state) / %	$\sum$ Br / %
$\boldsymbol{D_s^-\, [\pi^+\pi^0]_{\rho^+}}$	0.218	**0.218**
$\boldsymbol{D_s^-\, \pi^+\pi^+\pi^-}$	0.195	**0.413**
$\boldsymbol{D^*(2010)^-\, \pi^+\pi^+\pi^-}$	0.194	**0.607**
$\boldsymbol{D_s^-\, \pi^+}$	0.095	**0.702**
$\boldsymbol{D_s^+\, D_s^-}$	0.045	**0.747**
$\boldsymbol{D^0\, K^-\pi^+}$	0.041	**0.789**

Table A.4: List of possible Λ_b^0 decay-modes. The hadronisation fraction of a b quark to a Λ_b^0 is 8.4 % and is not included in the branching fraction calculations.

Mode	Br($\Lambda_b^0 \to XY$) / %	Br($X \to$ final state) / %		$\sum$ Br / %
$\boldsymbol{\Lambda_b^0 \to \Lambda_c^+\pi^+\pi^-\pi^-}$	0.760 ± 0.110	$\Lambda_c^+ \to pK^-\pi^+$	6.280 ± 0.320	**0.082**
		$\Lambda_c^+ \to pK^-\pi^+\pi^0$	4.460 ± 0.300	

A.1.2 Reconstruction of the remaining *b*-hadron decay modes

The characteristics of the decay modes in the aforementioned tables are represented in the listing of six decay modes in Sec. 4.2.1. As an example, the decay $B^+ \to [K^+\pi^-\pi^0]_{\bar{D}^0}\pi^+$ has been reconstructed. In the following, the results of the remaining five decay modes are shown. In general, the assumptions made for the vertex-resolution emulation and for kinematic cuts on intermediate particles have been applied similarly.

Fully charged D^0 decay The invariant-mass distribution of the B^+ meson from $B^+ \to [K^+\pi^-]_{\bar{D}^0}\pi^+$ is shown on the right side of Fig. A.1 after an energy cut on the B^+ candidates of 20 GeV has been applied. The distribution of the energy is presented on the left side of Fig. A.1. With an energy cut of $E_{B^+} \geq 20\,\text{GeV}$, a purity of $(99.93 \pm 0.11)\,\%$ has been achieved, where the uncertainty originates only from the size of the available sample.

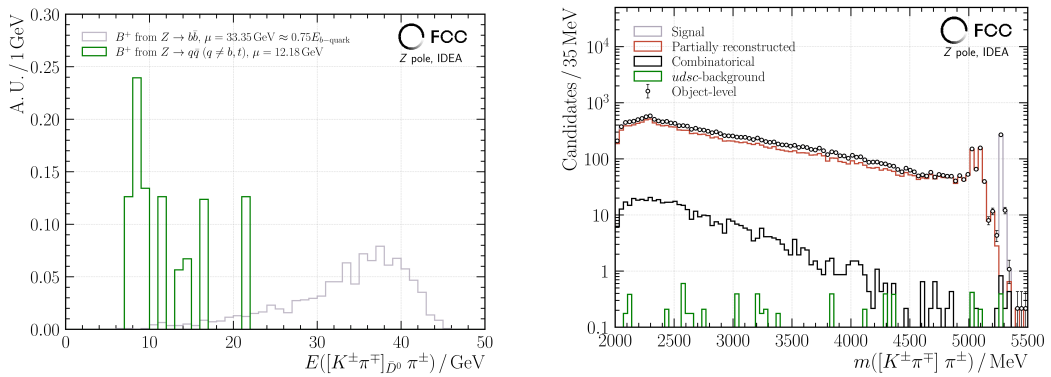

(a) **(b)**

Figure A.1: Energy and invariant-mass distribution of the signal and background candidates in Figs. (a) and (b), respectively. The energy cut has been set to 20 GeV.

D^0 decay with two π^0 The invariant-mass distribution of the B^+ meson from $B^+ \to [K^+\pi^-\pi^0\pi^0]_{\bar{D}^0}\pi^+$ is shown on the right side of Fig. A.2 after an energy cut on the B^+ candidates of 20 GeV has been applied. The distribution of the energy is presented on the left side of Fig. A.2. With an energy cut of $E_{B^+} \geq 20\,\text{GeV}$, a purity of $(99.81 \pm 0.07)\,\%$ has been achieved, where the uncertainty originates only from the size of the available sample.

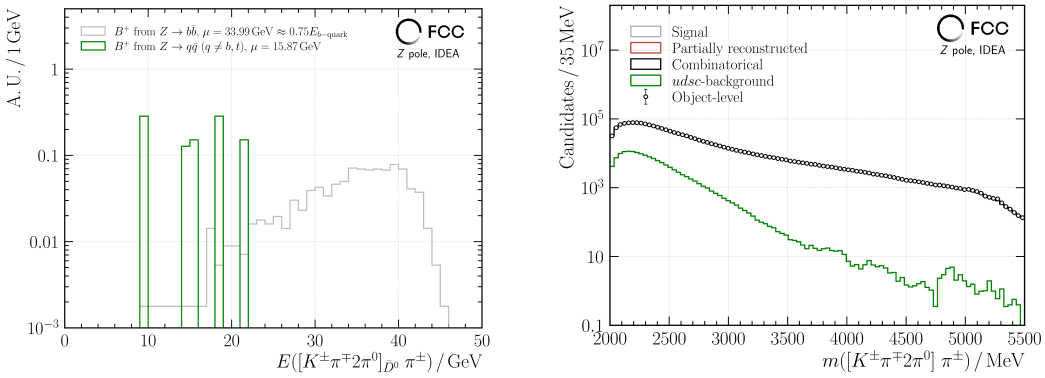

(a) **(b)**

Figure A.2: Energy and invariant-mass distribution of the signal and background candidates in Figs. (a) and (b), respectively. The energy cut has been set to 20 GeV.

Four charged tracks at the D^0 decay-vertex The invariant-mass distribution of the B^+ meson from $B^+ \to [K^+\pi^-\pi^-\pi^+]_{\bar{D}^0}\pi^+$ is shown on the right side of Fig. A.3 after an energy cut on the B^+ candidates of 20 GeV has been applied. The distribution of the energy is presented on the left side of Fig. A.3. With an energy cut of $E_{B^+} \geq 20\,\text{GeV}$, a purity of $(99.73 \pm 0.27)\,\%$ has been achieved, where the uncertainty originates only from the size of the available sample.

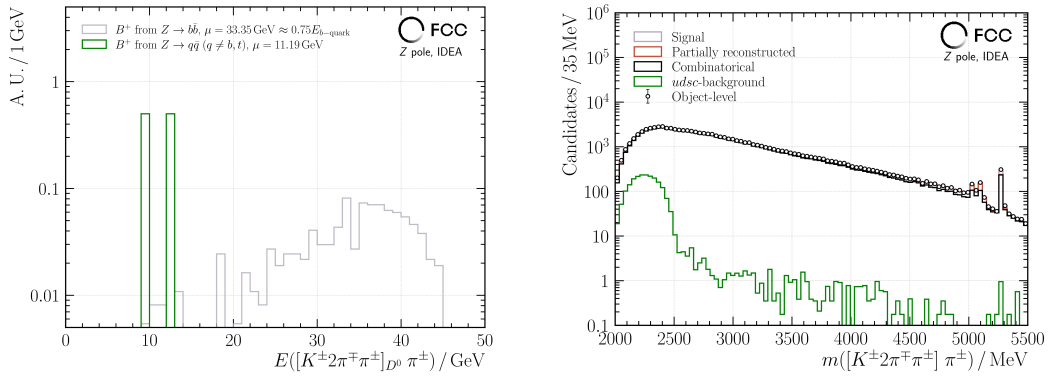

(a) **(b)**

Figure A.3: Energy and invariant-mass distribution of the signal and background candidates in Figs. (a) and (b), respectively. The energy cut has been set to 20 GeV.

Including two *c* mesons The invariant-mass distribution of the B^+ meson from $B^+ \to \bar{D}^0 D_s^+$ with the subsequent decays $\bar{D}^0 \to K^+\pi^-$ and $D_s^+ \to K^+K^-\pi^+$ is shown in Fig. A.4 without any energy cut on the B^+ candidates, since with the limited amount of simulated events, no *udsc* events have been found in the signal mass window. Therefore, a purity of 100.00 % has been achieved, which is expected to be slightly lowered with more events available.

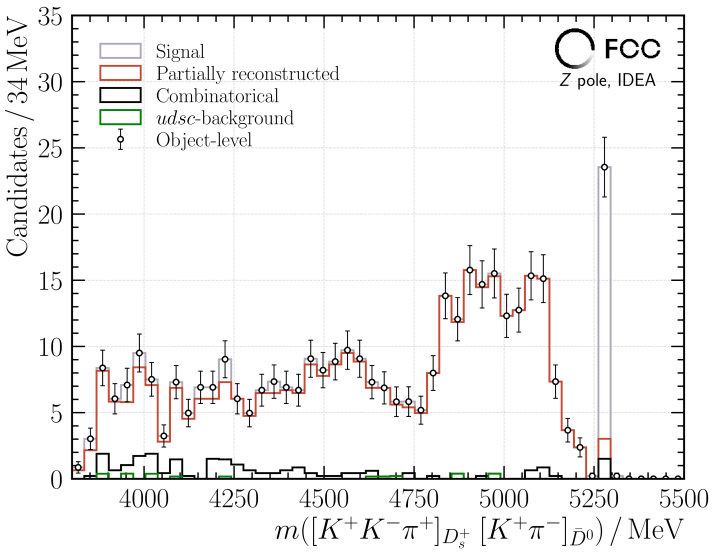

Figure A.4: The invariant-mass distribution without any energy cut. However, it is expected to have some light-quark contamination when considering the full event statistics.

Including a $c\bar{c}$ meson The invariant-mass distribution of the B^+ meson from $B^+ \to [\ell^+\ell^-]_{J/\psi} K^+$ with $\ell \in [e, \mu]$ is shown on the right side of Fig. A.5 after an energy cut on the B^+ candidates of 20 GeV has been applied. The distribution of the energy is presented on the left side of Fig. A.5. With an energy cut of $E_{B^+} \geq 20\,\text{GeV}$, a purity of $(99.90 \pm 0.24)\,\%$ has been achieved, where the uncertainty originates only from the size of the available sample.

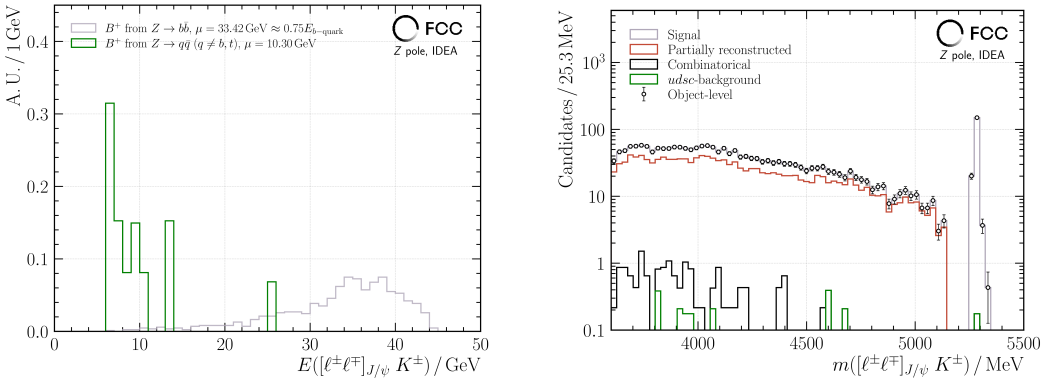

(a) **(b)**

Figure A.5: Energy and invariant-mass distribution of the signal and background candidates in Figs. (a) and (b), respectively. The energy cut has been set to 20 GeV.

A.2 A_{FB}^{b} analysis

The following sections provide additional information for the analysis of A_{FB}^{b}.

A.2.1 Polar-angle range impact on the fit uncertainty

In order to study the impact of the very forward and backward regions on the fit uncertainty to extract A_{FB}^{b}, upper limits on $\cos(\theta_b)$ have been placed and the fitting procedure has been repeated at the parton level. However, the reduction of actual detector effects at the object level is beyond the scope of this study. For the intrinsic reduction of the dataset when placing cuts has been accounted for. The result is presented in Fig. A.6 and shows a slight relative decrease of the fit uncertainty up to 5 % when restricting the range within $\max(\cos(\theta_b)) \approx 0.8$.

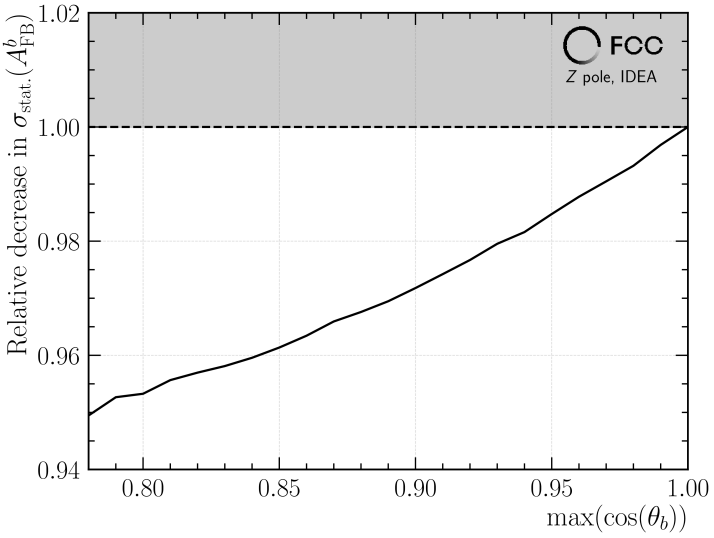

Figure A.6: Relative decrease of the fit uncertainty corrected for the reduction of the intrinsic size of the dataset as a function of the maximally allowed polar angle of the b quark.

A.2.2 Theory of QCD correction and longitudinal boson-polarisation

In the following, the theoretical basis is provided, mainly motivated and adapted by the studies in Ref. [152]. The analytical expressions for C_{QCD} are provided as follows

$$C_{\mathrm{QCD}}(\mu) \approx \int_{x_{\min}}^{x_{\max}} \int_{\bar{x}_{\min}(x)}^{\bar{x}_{\max}(x)} \frac{2\bar{x}^2(1-\cos(\zeta(x,\bar{x},\mu)))}{3(1-x)(1-\bar{x})}\,\mathrm{d}\bar{x}\,\mathrm{d}x\,, \tag{A.1}$$

with the energy fractions of the b and $\bar{b}$ quark $x = {}^{2E_b}/_{\sqrt{s}}$ and $\bar{x} = {}^{2E_{\bar{b}}}/_{\sqrt{s}}$, respectively. The acollinearity here is written explicitly as a function of $(x, \bar{x}, \mu)$ and the definition is given according to Ref. [153] as

$$\cos(\zeta(x,\bar{x},\mu)) = \frac{x\bar{x}+\mu^2+2(1-x-\bar{x})}{\sqrt{x^2-\mu^2}\sqrt{\bar{x}^2-\mu^2}}\,. \tag{A.2}$$

The integral limits in Eq. (A.1) are derived from the possible configurations for the b and $\bar{b}$ quarks. This means $x_{\min} = \mu$, $x_{\max} = 1$ (either carrying no momentum or the full momentum of ${}^{\sqrt{s}}/_2$), such that

$$\bar{x}_{\min}(x) = 1 - \frac{x+\sqrt{x^2-\mu^2}}{2} + \frac{\mu^2}{2-x-\sqrt{x^2-\mu^2}}\,, \tag{A.3}$$

$$\bar{x}_{\max}(x) = 1 - \frac{x-\sqrt{x^2-\mu^2}}{2} + \frac{\mu^2}{2-x+\sqrt{x^2-\mu^2}}\,. \tag{A.4}$$

The analytical expression for f_{L} is given as

$$f_{\mathrm{L}}(\mu) \approx \int_{x_{\min}}^{x_{\max}} \int_{\bar{x}_{\min}(x)}^{\bar{x}_{\max}(x)} \frac{4\alpha_{\mathrm{S}}\sqrt{\bar{x}^2-\mu^2}(1-\cos^2(\zeta(x,\bar{x},\mu)))}{3\pi(1-x)(1-\bar{x})}\mathrm{d}x\,\mathrm{d}\bar{x}\,. \tag{A.5}$$

A.2.3 Derivation of indirect limits on the top-quark mass

The following description has been taken from Ref. [38].

Starting from the definition in Eq. (2.8), the factor ξ has been introduced to account for radiative corrections of the Z-boson propagator, with the leading contribution originating from virtual top-quarks as provided by $\Delta\rho$ in Eq. (2.9). In order to also account for vertex corrections, a correction factor $\Delta\tau$ is introduced

$$\Delta\tau = -2x_t - \frac{G_{\mathrm{F}}m_Z^2}{6\sqrt{2}\pi^2}\cdot(1+\cos(\theta_{\mathrm{W}}))\ln\left(\frac{m_t}{m_W}\right) - 2x_t^2\cdot\left(9-\frac{\pi^2}{3}\right)\,. \tag{A.6}$$

This allows to modify the quark vector and axial-vector coupling according to

$$
\begin{aligned}
v_f \to \bar{v}_f &= \sqrt{\rho_f}\left(T_f - \frac{2Q_f \sin^2(\theta_{\mathrm{W}}^{\mathrm{eff}})}{1+\Delta\tau}\right), \\
a_f \to \bar{a}_f &= \sqrt{\rho_f} T_f, \\
\text{with} \quad \rho_f &= \frac{(1+\Delta\tau)^2}{1-\Delta\rho}.
\end{aligned}
$$

Fig. A.7 shows the uncertainty on the top-quark mass indirectly derived from radiative and loop corrections in the process $Z \to b\bar{b}$ as a function of the uncertainty on A_{FB}^b. The following parameters have been used to derive the result:

$$
\sin^2(\theta_{\mathrm{W}}) = 0.23089\,, \quad m_t = 173.1\,\mathrm{GeV}\,, \quad G_{\mathrm{F}} = 1.166\,378\,7 \cdot 10^{-5}\,\mathrm{GeV}^{-2}\,.
$$

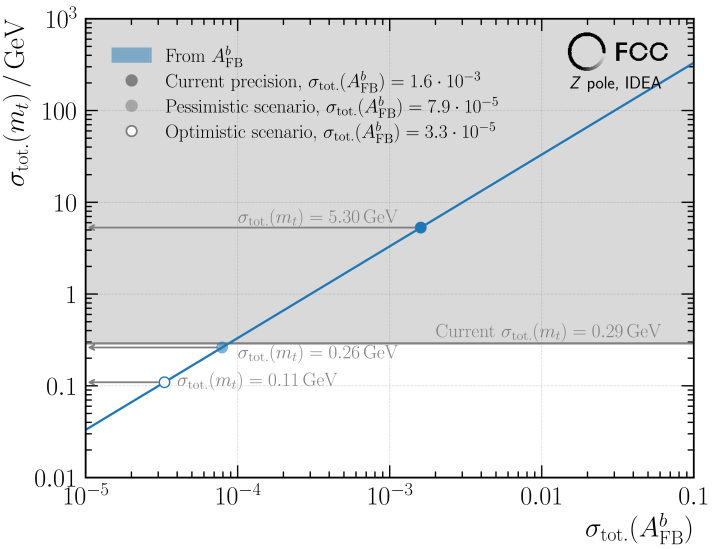

Figure A.7: The uncertainty of the top-quark mass in dependence of the b-quark forward-backward asymmetry. Eqs. (2.8) and (2.9) have been used with the input parameters listed above.

A.3 R_c analysis

The following sections provide additional material for the R_c analysis.

A.3.1 List of *c*-hadron decay modes

Table A.5: List of possible $\bar{D}^0$ decay modes for the measurement of R_c.

Mode	Br($\bar{D}^0 \to$ final state) / %	$\sum$ Br / %
$\boldsymbol{\bar{D}^0 \to K^+\pi^-}$	3.947	**3.947**
$\boldsymbol{\bar{D}^0 \to K^+2\pi^-\pi^+}$	8.220	**12.167**
$\boldsymbol{\bar{D}^0 \to K^+\pi^-\pi^0}$	14.400	**26.567**
$\boldsymbol{\bar{D}^0 \to K_S\pi^+\pi^-}$	2.800	**29.367**

Table A.6: List of possible D^+ decay modes for the measurement of R_c.

Mode	Br($D^+ \to$ final state) / %	$\sum$ Br / %
$\boldsymbol{D^+ \to K^-2\pi^+}$	9.380	**3.947**
$\boldsymbol{D^+ \to K^-2\pi^+\pi^0}$	6.250	**15.63**
$\boldsymbol{D^+ \to K_S2\pi^+\pi^-}$	3.100	**18.71**

Table A.7: List of possible D_s^+ decay modes for the measurement of R_c.

Mode	Br($D_s^+ \to$ final state) / %	$\sum$ Br / %
$\boldsymbol{D_s^+ \to K^+K^-\pi^+}$	5.370	**5.370**
$\boldsymbol{D_s^+ \to K^+K^-\pi^+\pi^0}$	5.500	**10.87**
$\boldsymbol{D_s^+ \to K_SK^-2\pi^+}$	1.530	**12.40**

For Λ_c^+ decay-modes, please consider the third column of Tab. A.4. In addition, $\Lambda_c^+ \to pK_S$ (Br = 1.59 %) and $\Lambda_c^+ \to pK_S\pi^+\pi^-$ (Br = 1.59 %) can be included. The respective fragmentation functions have been taken from Ref. [193].

A.3.2 Kinematic distributions

In the following figures, the additional kinematic distributions are presented. Cuts in these distributions have been used to purify the event selection and reduce the contamination from $Z \to b\bar{b}$ events.

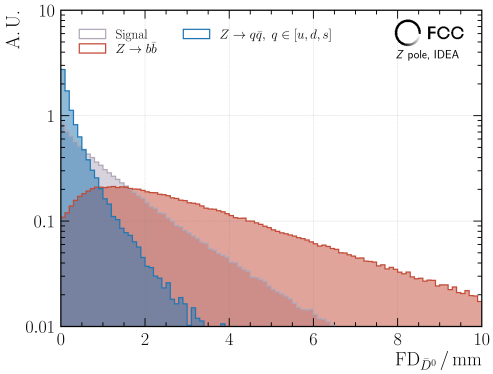

(a) $\bar{D}^0$ flight-distance.

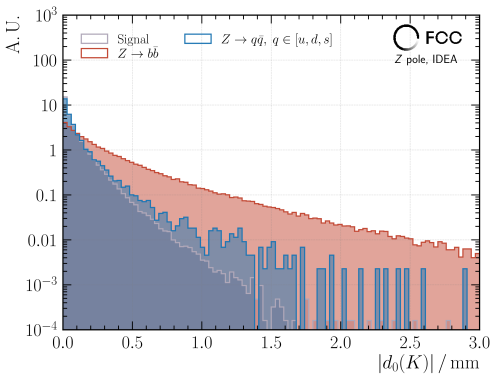

(b) The transverse impact-parameter d_0 of the kaon.

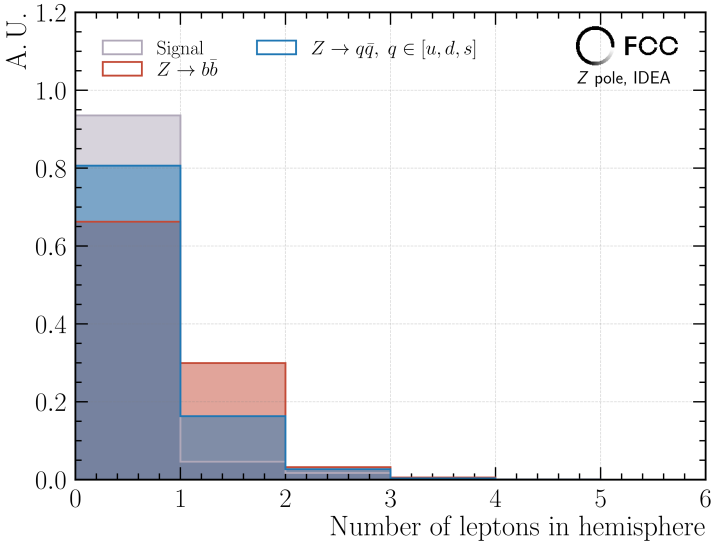

(c) The number of aligned, secondary leptons.

Figure A.8: Further kinematic and discriminative variables to reduce the contamination of $\bar{D}^0$ candidates from $Z \to b\bar{b}$ events.

A.4 R_s analysis–the concept

Disclaimer: Parts of the following results have been achieved and were kindly provided by the student J. Dutta under the author's supervision.

This section briefly introduces the application of exclusive strange-hadron reconstruction for the measurement of R_s, R_{us}, and A_{FB}^s. Since tagging of light quarks from hadron Z-boson decays is experimentally challenging, a former measurement at LEP has measured the partial decay-width ratios of the combination of the d and s quarks with respect to all light-flavour decay-width ratios from energetic $K^{\pm}$, $\pi^{\pm}$, $p(\bar{p})$, K_{S}^0 and $\Lambda(\bar{\Lambda})$ particles. However, with the large dataset available at a possible FCC-ee, exclusive reconstruction of strange mesons and baryons can allow to measure solely R_s. For this analysis, the $\phi(1020)$ meson, a $s\bar{s}$ vector-meson, and the Ξ^- baryon, a $s\bar{s}d$ baryon, have been used as hemisphere-flavour tagger. The latter might also serve as charge and direction tagger of the initial s-quark, allowing to assess A_{FB}^s.

A.4.1 Proof of principle

Inclusive $Z \to q\bar{q}$ samples with a total amount of approximately $4 \cdot 10^9$ events have been used, while the reconstruction of $\phi(1020) \to K^+K^-$ with a Br of 50 % has been seeded with truth information. However, `DELPHES` has been used to vertex the two kaon tracks to the $\phi(1020)$ meson. On the other hand, only charged Ξ baryons that decay to $\Lambda\pi^-$ at the particle level, again seeded with truth information, have been used. Similarly to the analysis for R_c, cuts in kinematic distributions have been used to purify the sample in $s\bar{s}$ (signal) events. The event selection is discussed in the following, separately for the two decay modes. Nevertheless, for both decay modes, the main background contribution has been found to originate from $Z \to c\bar{c}$ events, motivating the use of variables that aim to reduce heavy-flavour background events in general. In both cases, the energy distribution of the candidates serves as a measure of purity.

$\phi(1020)$ meson Four main discriminative variables have been chosen to separate events originating from $Z \to s\bar{s}$ events from other flavours: the flight distance $\mathrm{FD}_{\phi(1020)}$, where candidates from heavy-meson decays are expected to be significantly further displaced from the PV. This can be seen in the left panel of Fig. A.9 with a peak at lower flight distances for light-quark contributions and a broad tail for both heavy-quark contributions. Closely related to the displacement from the PV, the scaled pointing angle $\log(1-\Omega)$ as defined in Eq. (4.50) shows a high level of discrimination between the light- and heavy-quark contributions. The distribution is presented on the right side of Fig. A.9. The cuts have been placed at $\mathrm{FD}_{\phi(1020)} \leq 1.5\,\mathrm{mm}$ and $\log(1-\Omega) \geq -3$. Furthermore, the aligned non-primary

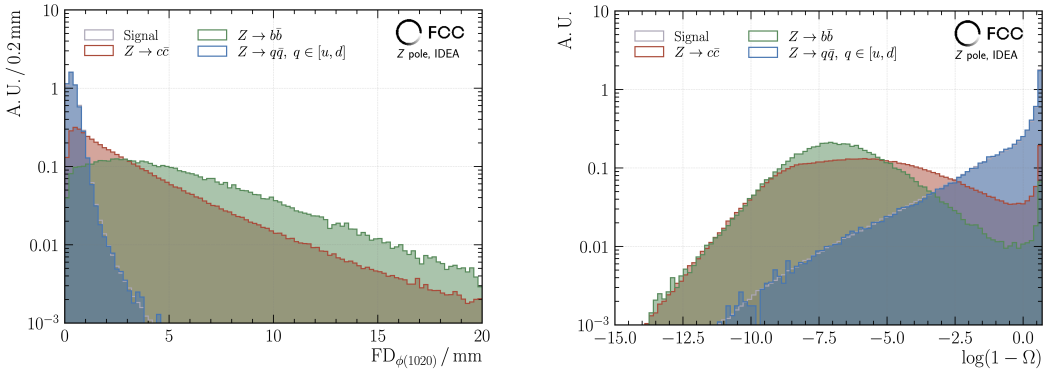

(a) $\phi(1020)$ flight-distance distribution. **(b)** Scaled pointing angle $\log(1 - \Omega)$.

Figure A.9: The flight-distance distribution shows large tails for background contamination originating from heavy quarks in Fig. (a). Further discriminating power is provided by the scaled directional opening angle $\log(1 - \Omega)$ in Fig. (b).

track and lepton multiplicity have been used to account for the generally higher number of tracks in heavy-quark decays. The distributions are presented in the left and right panels of Fig. A.10 for the track and lepton multiplicities, respectively. For the evaluation of the purity, no secondary lepton as well as a maximum number of two non-primary tracks are allowed.

Ξ^- baryon While there are obvious kinematic variables to enhance the purity of the $\phi(1020)$ selection, less obvious ones exist in case of the Ξ^- baryon (the charge conjugated is included if not stated otherwise). This is due to the relatively long lifetime of the baryon with $1.639 \cdot 10^{-10}$ s, which smears the effect of even further displaced candidates from heavy-meson and baryon decays. Therefore, cuts have only been applied to the number of non-primary aligned tracks and leptons, which have been set to six and zero, respectively. The distributions of both are presented in Fig. A.11.

In conclusion, the results are presented in Fig. A.12 for the $\phi(1020)$ and Ξ^- in the left and right panel, respectively. They show the corresponding energy distribution before and after applying the aforementioned cuts in the solid and dashed lines. The purities are indicated in the legend and have been evaluated before and after the cuts for $\phi(1020)$ and Ξ^- candidates exceeding 35 GeV and 40 GeV, respectively. They result in 98.4 % and 97.3 %.

After confirmation of the high purity of the selection, the statistical precision in reach with these stringent cuts has been examined, and limits on the precision of the background efficiencies have been derived.

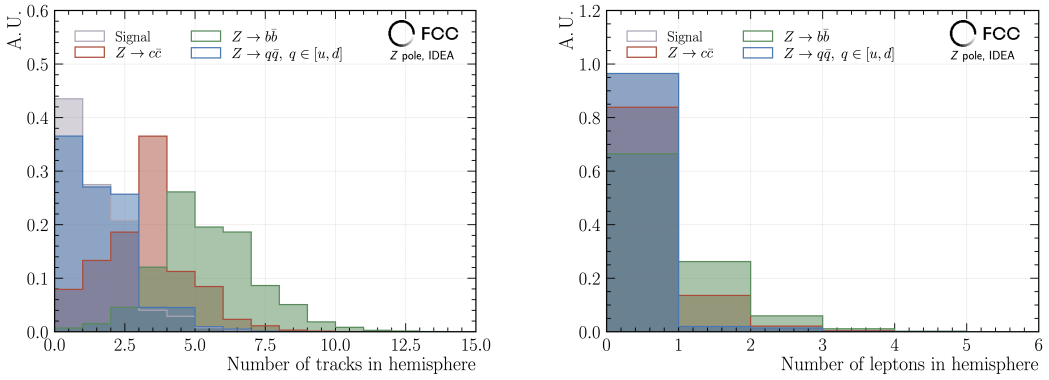

(a) **(b)**

Figure A.10: The number of secondary tracks and leptons in the same hemisphere in Figs. (a) and (b).

A.4.2 Statistical precision and knowledge of background efficiencies

The statistical precision has been derived from the known equation for the number of single- and double-tagged events

$$\begin{aligned} N_s &= 2N_Z \cdot (R_s\varepsilon_s^s + R_c\varepsilon_s^c + R_{ud}\varepsilon_{ud})\,, \\ N_{s\bar{s}} &= N_Z \cdot (R_s(\varepsilon_s^s)^2 C_s^s + R_c(\varepsilon_s^c)^2 C_s^c + R_{ud}(\varepsilon_s^{ud})^2 C_s^{ud})\,. \end{aligned} \tag{A.7}$$

In the following, the hemisphere correlations C_i^j have been assumed to be unity. Furthermore, the tagging efficiencies ε_i^j are composed of the production probability $(\varepsilon_i^j)_{\text{prod.}}$ and the reconstruction efficiency $(\varepsilon_i^j)_{\text{reco.}}$ via

$$\varepsilon_i^j = (\varepsilon_i^j)_{\text{prod.}} \cdot (\varepsilon_i^j)_{\text{reco.}}\,, \tag{A.8}$$

where the reconstruction efficiency also includes the reduction due to kinematic cuts in the phase space. Here, $(\varepsilon_i^j)_{\text{prod.}}$ has been calculated from the number of candidates found, $N_{s\text{-hadron}}$, and the number of events produced in the sample, $N_{\text{prod.}}$, via $(\varepsilon_i^j)_{\text{prod.}} = {}^{N_{s\text{-hadron}}}\!/_{N_{\text{prod.}}}$. The appearance of two or more hadrons per event following the specified decay chain has been considered. Using Eq. (4.11), the statistical precision is of the order $\mathcal{O}(\sigma_{\text{stat.}}(R_s)) = 10^{-4}$.

Since the goal is to find a balance between the statistical precision and the control of systematic uncertainties arising from the quantities that must be determined from MC simulation, the impact of ε_s^c, ε_s^{ud} and C_s^s on $\sigma_{\text{syst.}}(R_s)$ has been examined. For the sake of the studies, C_s^s has been assumed to unity and the impact of C_s^c and C_s^{ud} has been neglected due to the small values of ε_s^c and ε_s^{ud}. The relative precision to which the background efficiencies and the hemisphere correlation must be known has been found to be of the order $(5 - 10)\,\%$ and $0.1\,\%$, respectively.

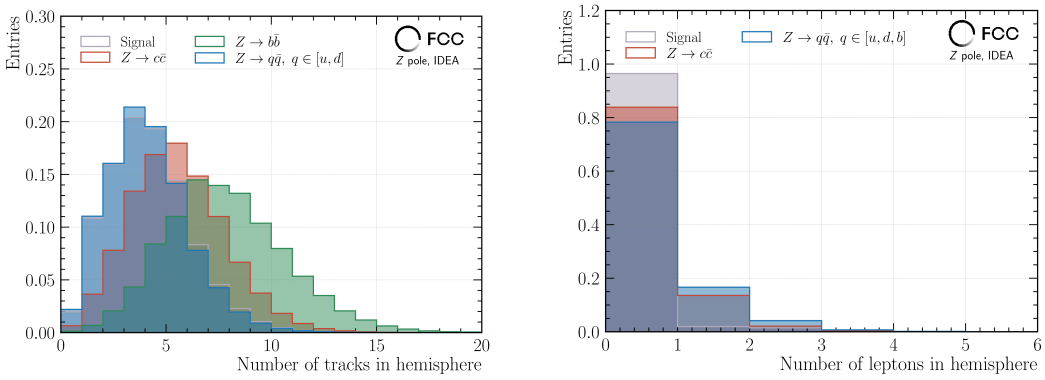

(a) **(b)**

Figure A.11: The number of secondary tracks and leptons in the same hemisphere in Figs. (a) and (b).

A.4.3 The next steps: first assessment of A_{FB}^{s}

Similarly to A_{FB}^{b}, A_{FB}^{s} can be experimentally accessed from the charged taggers used for R_s. In the presented case, the polar angle of the Ξ^- baryon is used to unambiguously identify the charge and flavour of the hemisphere with a potential purity of $> 98\,\%$. The energy applied to purify the selection at the same time reduces the impact from QCD corrections. A detailed study in the case of A_{FB}^{b} is outlined in Sec. 4.5. However, at an energy cut above 40 GeV, the QCD corrections are expected to be reduced by at least one order of magnitude. A preliminary assessment of A_{FB}^{s} from the Ξ^- baryon is presented in Fig. A.13, which shows the parton-level polar angle in the histogram for the different contributions of signal and background with the kinematic and topological cuts applied for candidates with an energy above 40 GeV. The value $A_{\mathrm{FB}}^{s,0}$ has been extracted from uncut s-quark events, where only the energy of the initial s-quarks has been set above 45.5 GeV to reduce the effect of ISR. The polar-angle distribution for the Ξ^- baryon is presented in black dots after all cuts have been applied. Furthermore, the fit of Eq. 4.33 to the $\cos(\theta_{\Xi^-})$ distribution is shown as a black line, again fixing the longitudinal polarisation-fraction f_{L} to the parton-level value. The uncertainties refer to the statistical uncertainties and do not represent the one obtainable at FCC-ee. However, the results agree well within the uncertainties and provide a consistent proof of the concept.

Furthermore, preliminary results have indicated that a measurement precision of the order $\mathcal{O}(\sigma_{\mathrm{stat.}}(A_{\mathrm{FB}}^{s})) = \mathcal{O}(\sigma_{\mathrm{syst.}}(A_{\mathrm{FB}}^{s})) \approx 10^{-4}$ is in reach with a knowledge of the QCD corrections at the 5 % level.

However, studies using the reconstruction capabilities of `DELPHES` must be installed to further explore the possibility of measuring the displaced track of the Ξ^- baryon in

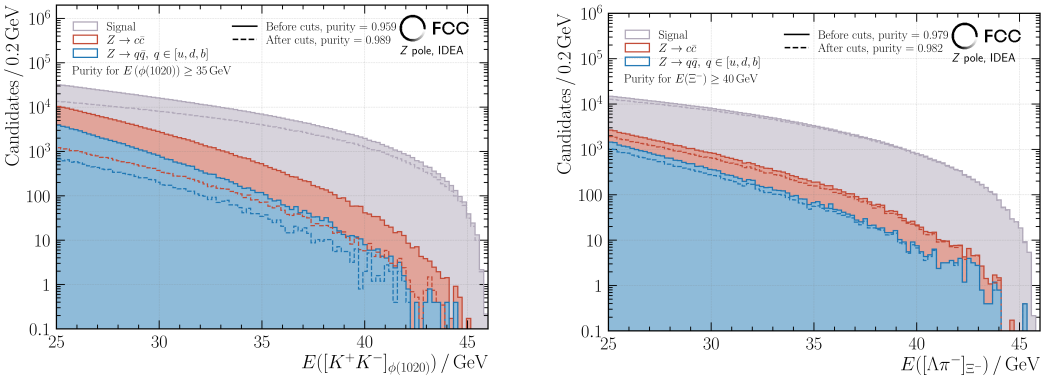

(a) Energy distribution of the $\phi(1020)$ meson.

(b) Energy distribution of the Ξ^- baryon.

Figure A.12: Energy distributions as measure for the background rejection. Especially for beam-like hadrons, purities above 98 % can be achieved.

the tracking system. This leads to detector requirements that explore the feasibility of further separate the signal from background events with a cut on the scaled pointing angle $\log(1 - \Omega)$.

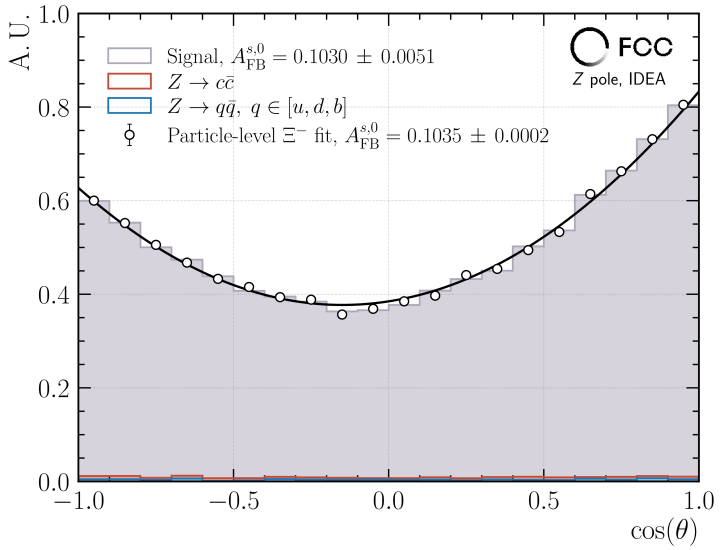

Figure A.13: The polar-angle distribution of the quarks and the Ξ^- baryons in the histogram and black dots, respectively. Both agree well within the statistical uncertainty stated, which does not represent the actual one from FCC-ee.

A.4.4 Last but not least: R_{us}

In this last section, the possibility of accessing R_{us}, defined as

$$R_{us} = \frac{\Gamma_{s\bar{s}} + \Gamma_{u\bar{u}}}{\Gamma_{Z\to\mathrm{had.}}}\,, \tag{A.9}$$

has been examined by tagging beam-like kaons from the beam-spot region. Similarly to the LR ansatz described in Sec. 4.4.1, kaon tracks have been selected for $|v_1| \leq 3$ and $|v_2| \leq 25$ assuming 100 % particle-ID. At a working point of $E_{K^+} \geq 42.5\,\mathrm{GeV}$, candidates have been extracted with a purity above 99 %. With this purity, $\varepsilon_{s,u}^{b,c,d}$ become negligible, assuming that $\varepsilon_s^u \approx 0.1\varepsilon_s^s$. From a preliminary estimation, the order of the statistical precision in this energy regime is of the order 10^{-5}. The energy distribution of the charged kaons is presented in Fig. A.14.

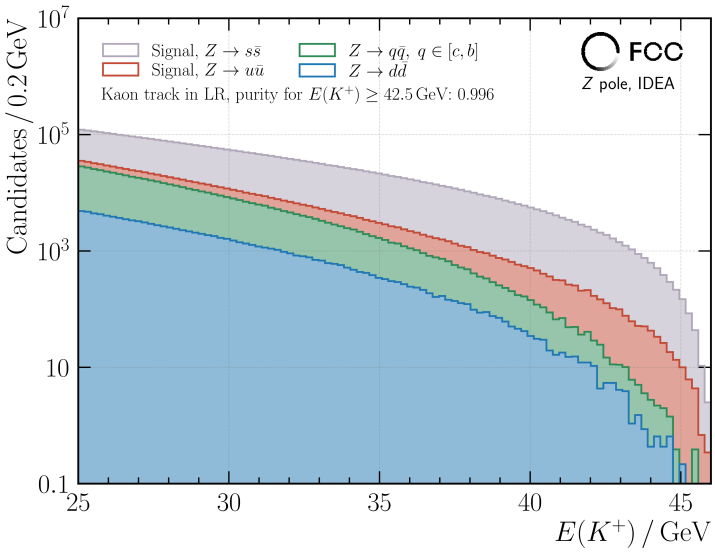

Figure A.14: The energy spectrum of charged kaons, selected from the beam-spot region. Here, the origins $Z \to s\bar{s}$ and $Z \to u\bar{u}$ are treated as signal, since $K^{\pm}$ is a composition of an up- and strange quark.

A.5 Top-quark reconstruction

The following sections provide additional material for the top-quark reconstruction analysis.

A.5.1 Decay-channel identification

In the right panel of Fig. A.15, the distribution of the number of isolated leptons extracted from the PV fit is shown for different origins: the fully hadronic, semileptonic and dileptonic $t\bar{t}$ decays. Significant migration from semileptonic events in the $N_{2\ell}$ channel can be observed. However, when targeting the $N_{2\ell}$ channel, the total number of jets per event in the clustering process is equal to two. This in turn implies that the energy of the highest-energetic jet arising in the semileptonic channel with more hadronic activity from the hadronically decaying W-boson has on average a higher energy compared to the dileptonic channel. Therefore, the left panel of Fig. A.15 shows the energy distribution of the highest-energetic jet, comparing the semi and dileptonic samples in orange and dark red, respectively. When considering a maximum energy cut $\max(E_{\text{jet}})$ of 100 GeV the contamination in the $N_\ell = 2\ell$ region is reduced by about a factor of five. The result after applying the jet-energy cut is shown as a dashed line in the plot on the left side.

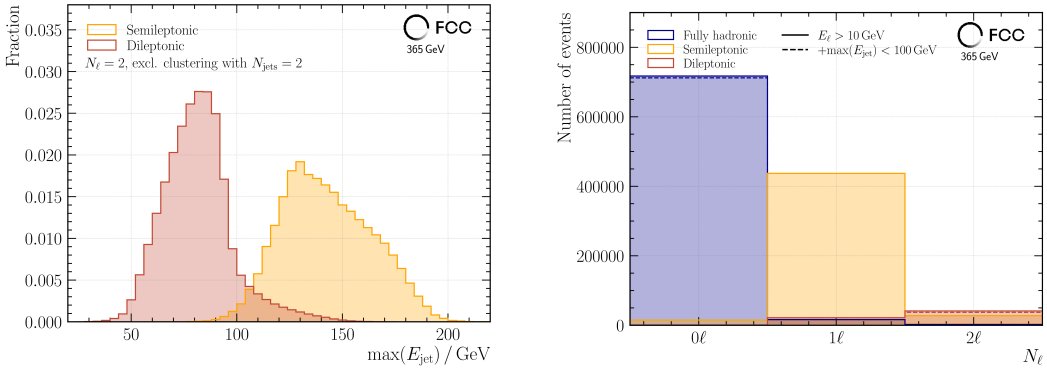

Figure A.15: Energy distributions in the $N_\ell = 2\ell$ channel for the highest energetic jet on the left side, separately for the semileptonic and dileptonic sample in orange and dark red, respectively. The right plot shows the distribution of events in the $N_\ell = [0\ell, 1\ell, 2\ell]$ category.

A.5.2 Interpolation result for F_{R}

In Fig. A.16, the interpolation result for F_{R} as a function of F_0 and F_{L} at the object level is presented.

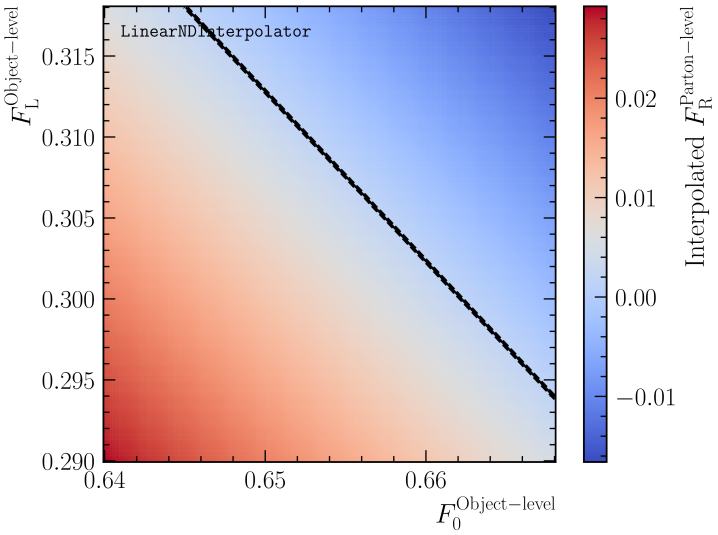

Figure A.16: $F_{\mathrm{R}}^{\text{Parton-level}}$.

A.6 EFT fit results

The following section provides additional material for the EFT interpretation of selected top-quark processes.

A.6.1 Interpolation results

Here, the remaining interpolations are presented for the semi and dileptonic $t\bar{t}$ observables.

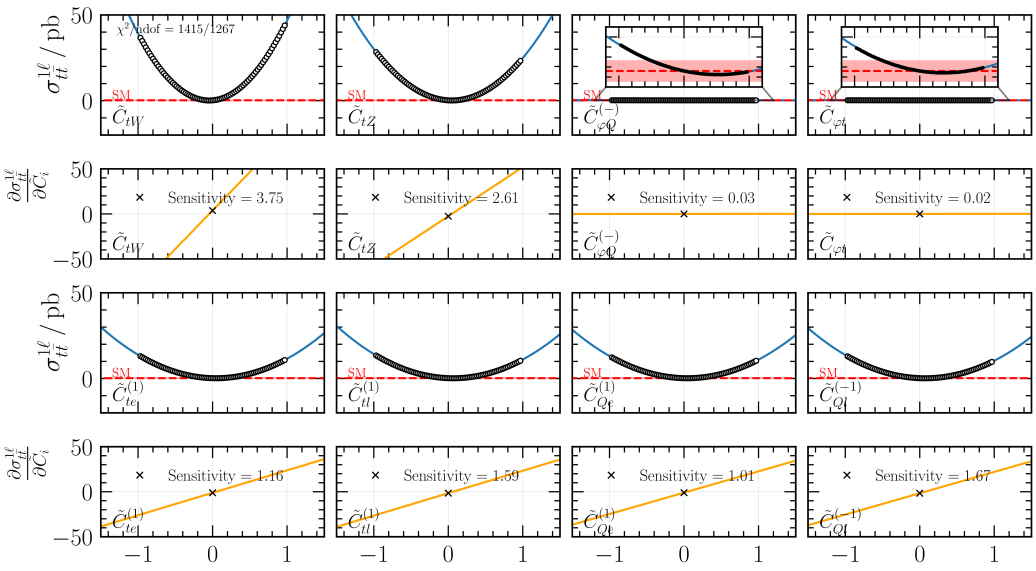

Figure A.17: Semileptonic cross-section $\sigma_{t\bar{t}}^{1\ell}$.

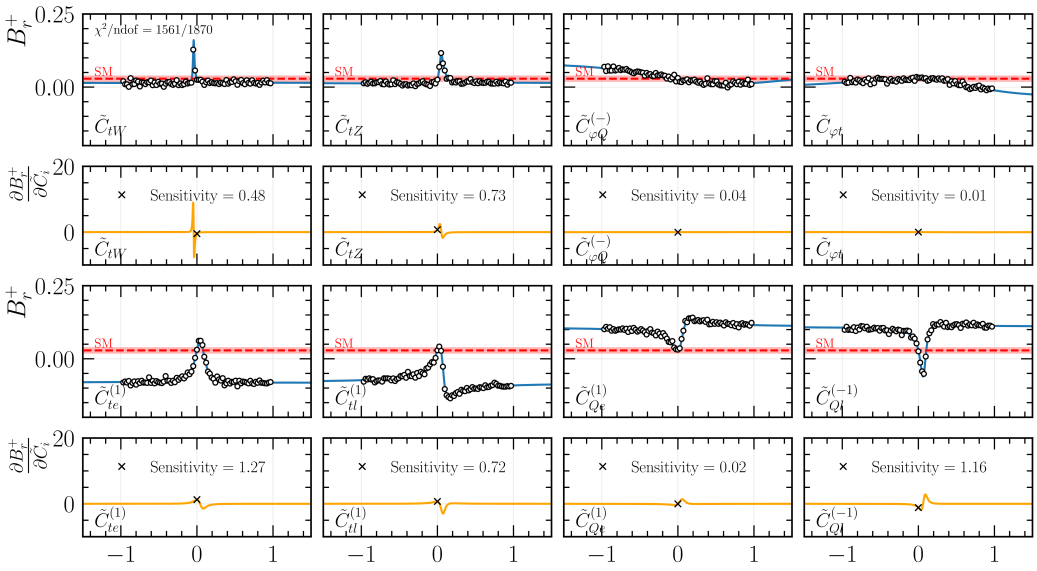

Figure A.18: Top-quark polarisation parameter B_r^+.

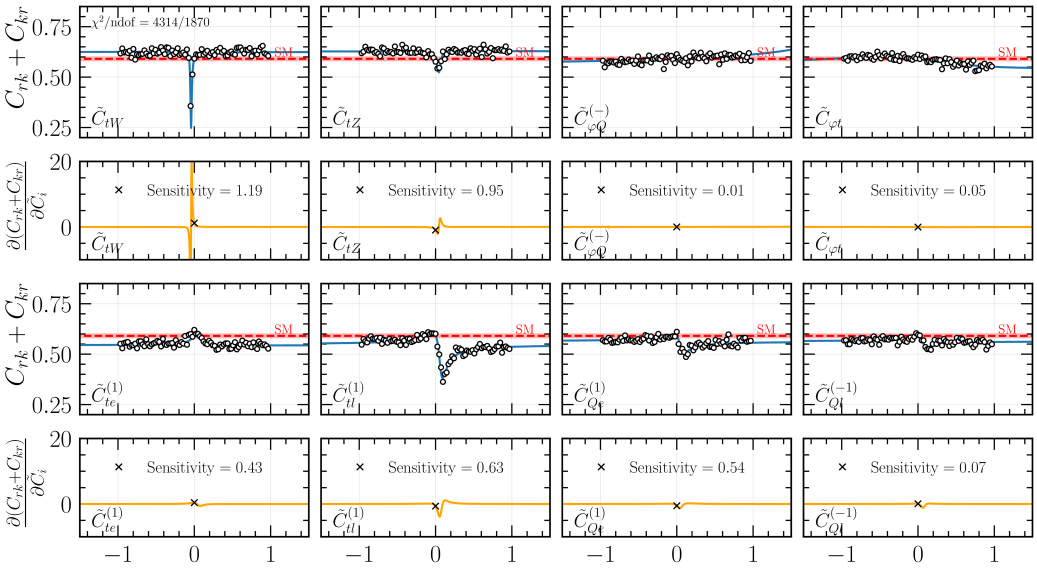

Figure A.19: $t\bar{t}$ spin-correlation matrix element $C_{rk} + C_{kr}$.

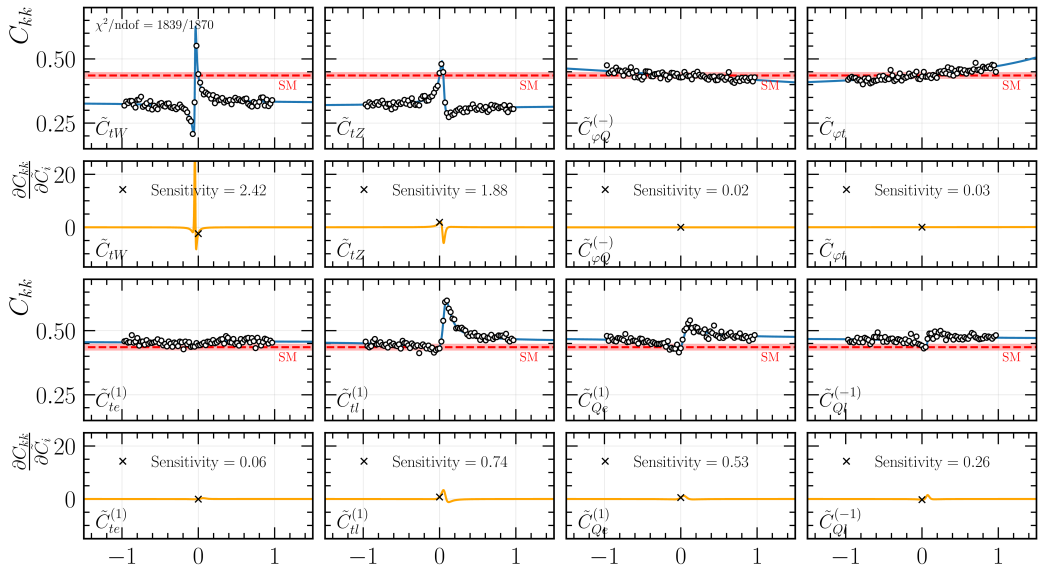

Figure A.20: Main diagonal element C_{kk} of the spin-correlation matrix.

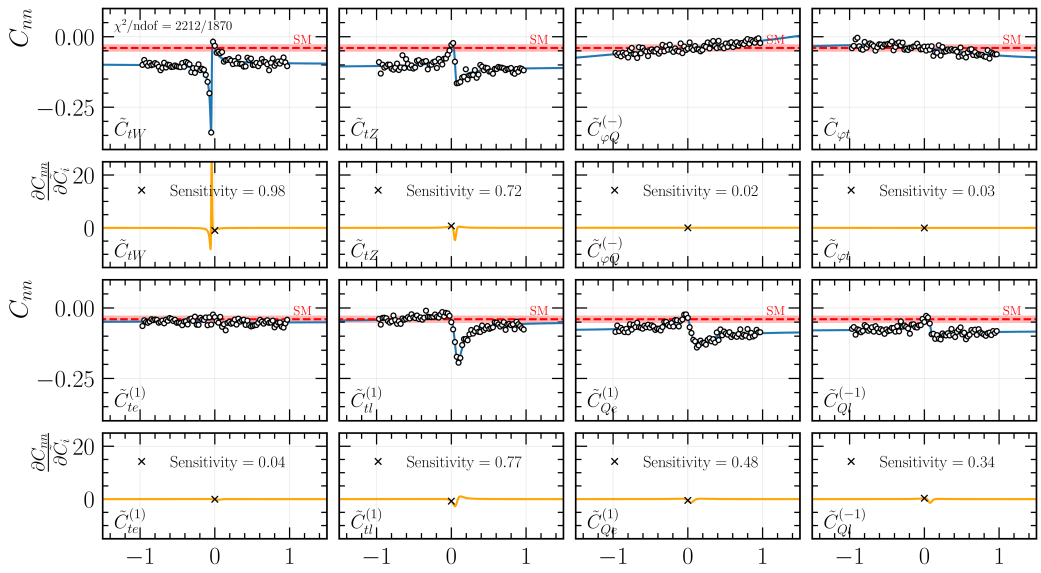

Figure A.21: Main diagonal element C_{nn} of the spin-correlation matrix.

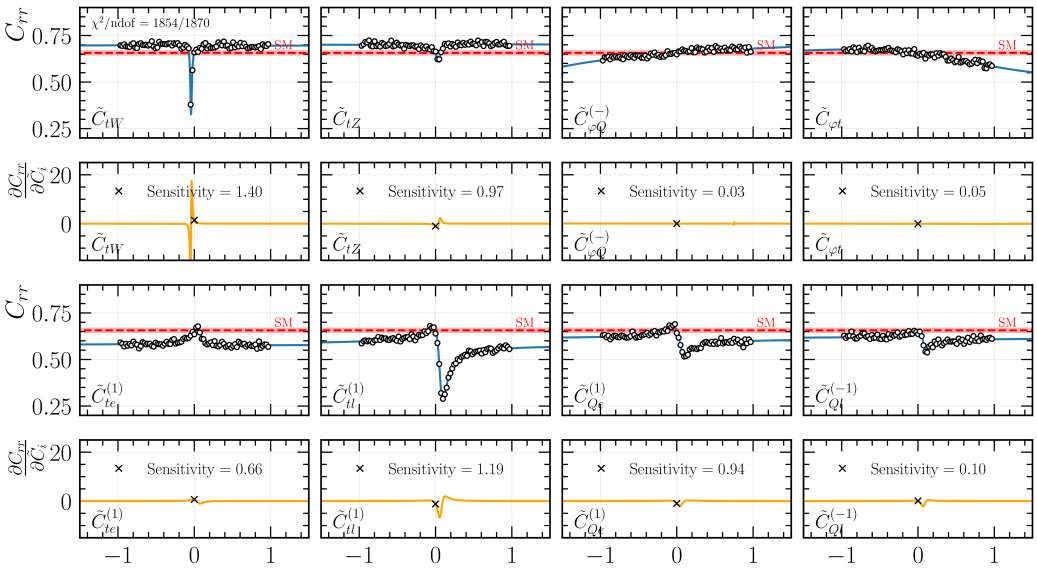

Figure A.22: Main diagonal element C_{rr} of the spin-correlation matrix.

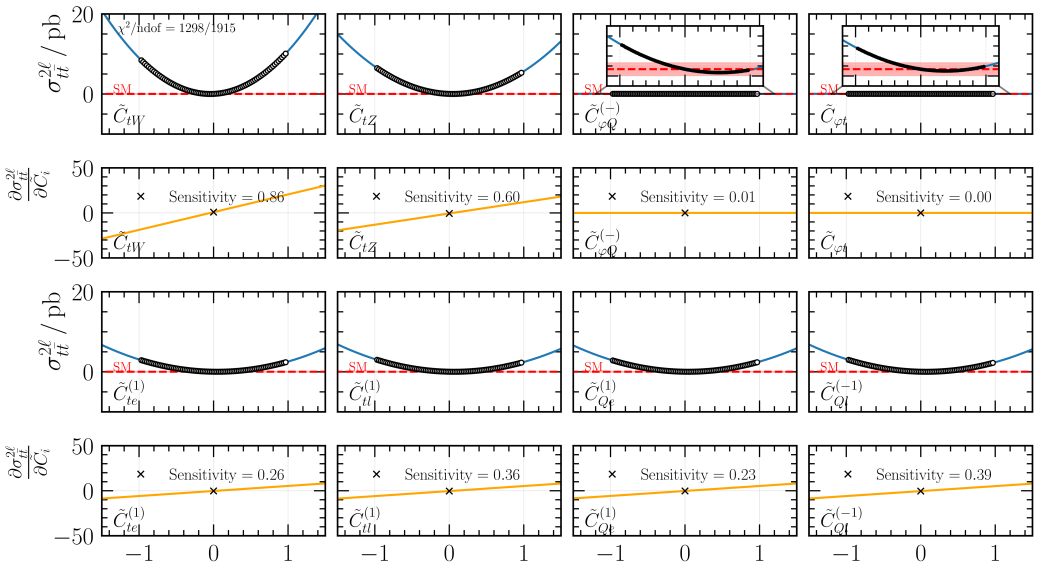

Figure A.23: Dileptonic cross-section $\sigma^{2\ell}_{t\bar{t}}$.

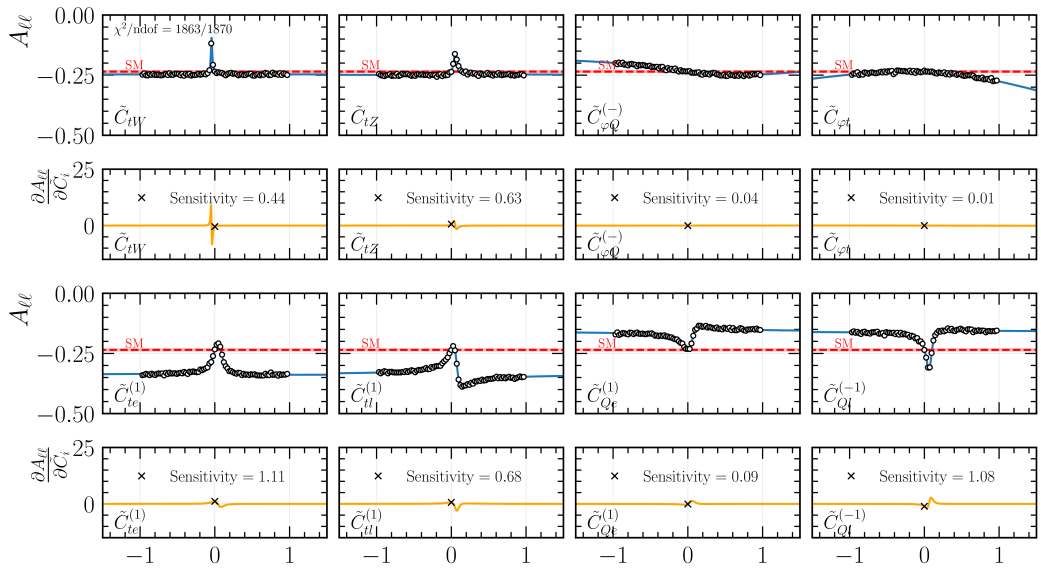

Figure A.24: Lepton-angle asymmetry $A_{\ell\ell}$.

A.6.2 Marginalised posterior distributions

In the following section, the marginalised posterior distributions of the EFT fit are presented, derived from a fit of current LHC top-quark measurements in Fig. A.25. In Fig. A.26, the result of the combination of the current LHC-measurements and the projected HL-LHC-precision is shown.

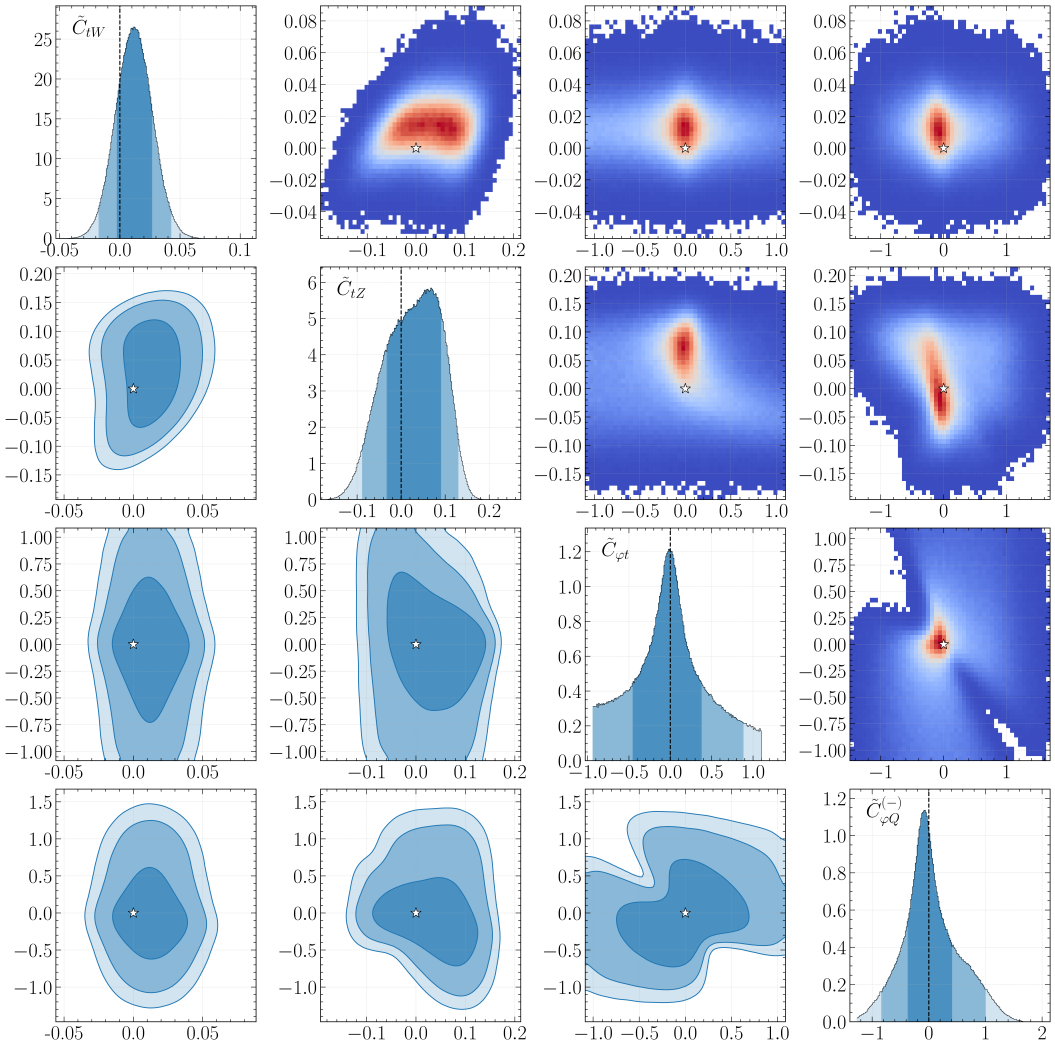

Figure A.25: Marginalised distributions of the Wilson coefficients from the fit to LHC measurements in the top-quark sector.

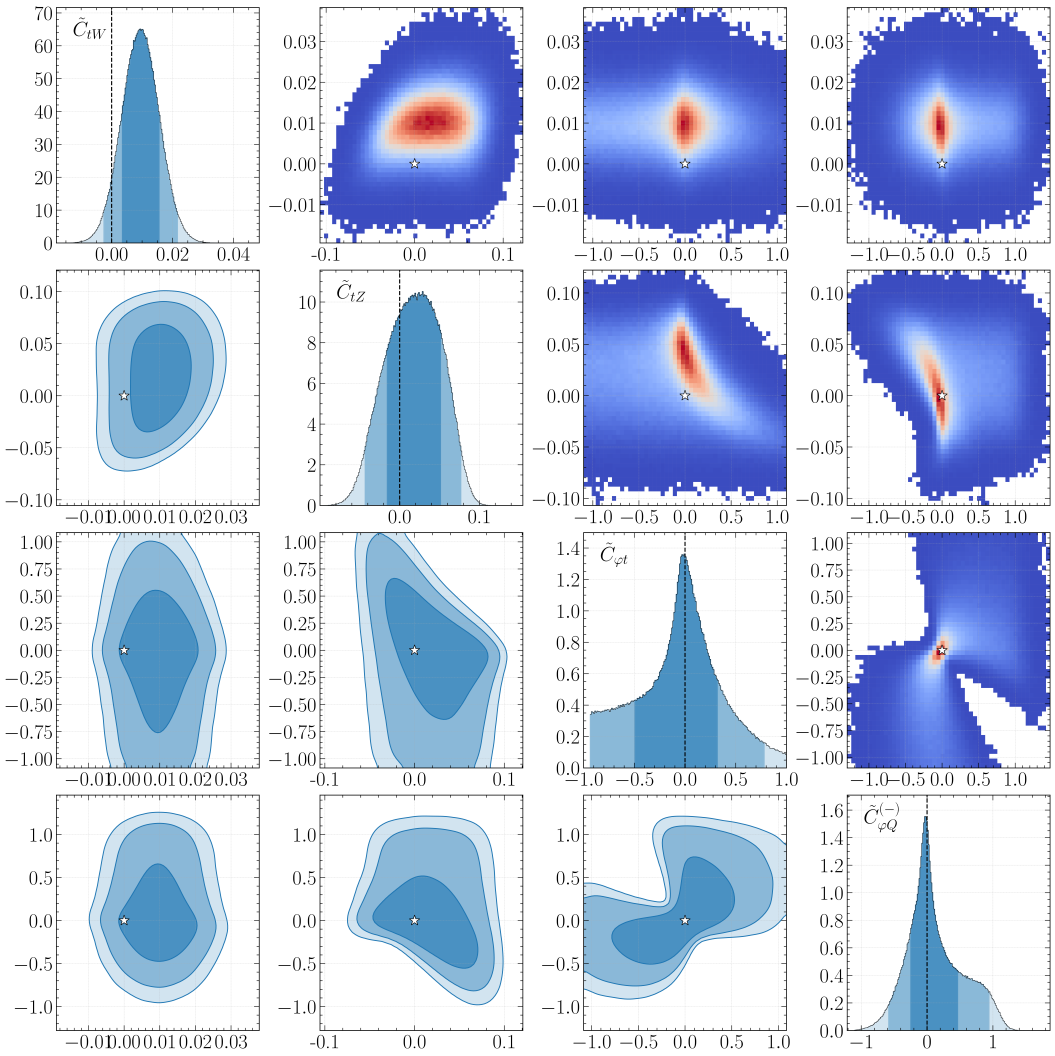

Figure A.26: Marginalised distributions of the Wilson coefficients from the fit to LHC measurements including the projected precision gains from the HL-LHC in the top-quark sector.

Bibliography

[1] ALEPH Collaboration, DELPHI Collaboration, L3 Collaboration, OPAL Collaboration, SLD Collaboration, *Precision electroweak measurements on the Z resonance*, Physics Reports **427** (2006) 257.

[2] ATLAS Collaboration, *Observation of a new particle in the search for the Standard Model Higgs boson with the ATLAS detector at the LHC*, Physics Letters B **716** (2012) 1.

[3] CMS Collaboration, *Observation of a new boson at a mass of 125 GeV with the CMS experiment at the LHC*, Physics Letters B **716** (2012) 30.

[4] ATLAS Collaboration, *Search for electroweak production of supersymmetric particles in final states with two τ-leptons in $\sqrt{s}$ =13 TeV pp collisions with the ATLAS detector*, Journal of High Energy Physics **2024** (2024) 150.

[5] ATLAS Collaboration, *Search for pair production of higgsinos in events with two Higgs bosons and missing transverse momentum in $\sqrt{s}$ =13 TeV pp collisions at the ATLAS experiment*, Phys. Rev. D **109** (11 2024) 112011.

[6] ATLAS Collaboration, *Search for direct production of electroweakinos in final states with one lepton, jets and missing transverse momentum in pp collisions at $\sqrt{s}$ =13 TeV with the ATLAS detector*, Journal of High Energy Physics **2023** (2023) 167.

[7] J. Kretzschmar, ATLAS and CMS Collaborations, *Searches for extra dimensions with the ATLAS and CMS detectors*, Nuclear and Particle Physics Proceedings **273-275** (2016) 541, 37th International Conference on High Energy Physics (ICHEP).

[8] CMS Collaboration, *Search for Extra Dimensions in Dimuon Events in pp Collisions at $\sqrt{s}$ =8 TeV*, tech. rep., CERN, 2013.

[9] ATLAS Collaboration, *Search for boosted low-mass resonances decaying into hadrons produced in association with a photon in pp collisions at $\sqrt{s}$ =13 TeV with the ATLAS detector*, (2024).

[10] A. Abada et al., *FCC-ee: The Lepton Collider*, The European Physical Journal Special Topics **228** (2019) 261.

[11] A. Abada et al., *FCC-hh: The Hadron Collider*, The European Physical Journal Special Topics **228** (2019) 755.

[12] SLD, LEP, Tevatron Electroweak Working Group, Heavy Flavour Groups, D0, *Precision Electroweak Measurements and Constraints on the Standard Model*, (2010).

[13] J. J. Thomson, *XL. Cathode Rays*, The London, Edinburgh, and Dublin Philosophical Magazine and Journal of Science **44** (1897) 293.

[14] E. Rutherford, *LIV. Collision of α particles with light atoms. IV. An anomalous effect in nitrogen*, The London, Edinburgh, and Dublin Philosophical Magazine and Journal of Science **37** (1919) 581.

[15] J. S. Chadwick, *The existence of a neutron*, Proceedings of The Royal Society A: Mathematical, Physical and Engineering Sciences **136** (1932) 692.

[16] S. Tomonaga, *On a relativistically invariant formulation of the quantum theory of wave fields*, Prog. Theor. Phys. **1** (1946) 27.

[17] J. S. Schwinger, *On Quantum electrodynamics and the magnetic moment of the electron*, Phys. Rev. **73** (1948) 416.

[18] R. P. Feynman, *Space-time approach to quantum electrodynamics*, Phys. Rev. **76** (1949) 769, ed. by L. M. Brown.

[19] S. L. Glashow, *Partial Symmetries of Weak Interactions*, Nuclear Physics **22** (1961) 579.

[20] A. Salam, *Weak and Electromagnetic Interactions*, Conf. Proc. C **680519** (1968) 367.

[21] S. Weinberg, *A Model of Leptons*, Phys. Rev. Lett. **19** (1967) 1264.

[22] H. Fritzsch, M. Gell-Mann, and H. Leutwyler, *Advantages of the Color Octet Gluon Picture*, Phys. Lett. B **47** (1973) 365.

[23] H. D. Politzer, *Reliable Perturbative Results for Strong Interactions?* Phys. Rev. Lett. **30** (1973) 1346, ed. by J. C. Taylor.

[24] D. J. Gross and F. Wilczek, *Ultraviolet Behavior of Nonabelian Gauge Theories*, Phys. Rev. Lett. **30** (1973) 1343, ed. by J. C. Taylor.

[25] P. W. Higgs, *Broken Symmetries and the Masses of Gauge Bosons*, Phys. Rev. Lett. **13** (1964) 508, ed. by J. C. Taylor.

[26] P. W. Higgs, *Broken symmetries, massless particles and gauge fields*, Phys. Lett. **12** (1964) 132.

[27] F. Englert and R. Brout, *Broken Symmetry and the Mass of Gauge Vector Mesons*, Phys. Rev. Lett. **13** (1964) 321, ed. by J. C. Taylor.

[28] R. L. Workman et al., *Review of Particle Physics*, PTEP **2022** (2022) 083C01.

[29] UA1 Collaboration, *Intermediate-Vector-Boson Properties at the CERN Super Proton Synchrotron Collider*, Europhysics Letters **1** (1986) 327.

[30] UA2 Collaboration, *Observation of single isolated electrons of high transverse momentum in events with missing transverse energy at the CERN pp collider*, Physics Letters B **122** (1983) 476.

[31] UA1 Collaboration, *Experimental observation of lepton pairs of invariant mass around 95 GeV/c^2 at the CERN SPS collider*, Physics Letters B **126** (1983) 398.

[32] UA2 Collaboration, *Evidence for $Z^0 \to e^+e^-$ at the CERN pp collider*, Physics Letters B **129** (1983) 130.

[33] C. Burgard, 2016, URL: `https://texample.net/tikz/examples/model-physics/` (visited on 04/28/2021).

[34] N. Cabibbo, *Unitary Symmetry and Leptonic Decays*, Phys. Rev. Lett. **10** (1963) 531.

[35] M. Kobayashi and T. Maskawa, *CP Violation in the Renormalizable Theory of Weak Interaction*, Prog. Theor. Phys. **49** (1973) 652.

[36] *LHC Top Working Group Summary Plots*, 2023, URL: `https://twiki.cern.ch/twiki/bin/view/LHCPhysics/LHCTopWGSummaryPlots`.

[37] J. Swain and L. Taylor, *First determination of the quark mixing matrix element V_{tb} from electroweak corrections to Z decays*, Phys. Rev. D **58** (9 1998) 093006.

[38] S. Monteil, *Mesures de précision électrofaibles*, 2009.

[39] A. Blondel et al., *Polarization and Centre-of-mass Energy Calibration at FCC-ee*, 2019.

[40] M. Jeżabek and J. Kühn, *QCD corrections to semileptonic decays of heavy quarks*, Nuclear Physics B **314** (1989) 1.

[41] A. H. Hoang, *What Is the Top Quark Mass?* Annual Review of Nuclear and Particle Science **70** (2020) 225.

[42] CDF and D0 Collaboration, *Combined Forward-Backward Asymmetry Measurements in Top-Antitop Quark Production at the Tevatron*, Phys. Rev. Lett. **120** (4 2018) 042001.

[43] CMS Collaboration, *Measurement of the top quark polarization and $t\bar{t}$ spin correlations using dilepton final states in proton-proton collisions at $\sqrt{s} = 13$ TeV*, Phys. Rev. D **100** (7 2019) 072002.

[44] ATLAS Collaboration, *Measurements of top-quark pair spin correlations in the $e\mu$ channel at $\sqrt{s} = 13$ TeV using pp collisions in the ATLAS detector*, The European Physical Journal C **80** (2020) 754.

[45] CMS Collaboration, *Measurement of the W boson helicity fractions in the decays of top quark pairs to lepton+jets final states produced in pp collisions at $\sqrt{s} = 8$ TeV*, Physics Letters B **762** (2016) 512.

[46] ATLAS Collaboration, *Measurement of the polarisation of W bosons produced in top-quark decays using dilepton events at $\sqrt{s}$ = 13 TeV with the ATLAS experiment*, Physics Letters B **843** (2023) 137829.

[47] A. Czarnecki, J. G. Körner, and J. H. Piclum, *Helicity fractions of W bosons from top quark decays at next-to-next-to-leading order in QCD*, Phys. Rev. D **81** (11 2010) 111503.

[48] D. Clowe et al., *A Direct Empirical Proof of the Existence of Dark Matter**, The Astrophysical Journal **648** (2006) L109.

[49] G. Bertone, D. Hooper, and J. Silk, *Particle dark matter: evidence, candidates and constraints*, Physics Reports **405** (2005) 279.

[50] G. R. Farrar and M. E. Shaposhnikov, *Baryon asymmetry of the universe in the standard electroweak theory*, Phys. Rev. D **50** (1994) 774.

[51] Super-Kamiokande Collaboration, *Evidence for Oscillation of Atmospheric Neutrinos*, Phys. Rev. Lett. **81** (8 1998) 1562.

[52] SNO Collaboration, *Direct Evidence for Neutrino Flavor Transformation from Neutral-Current Interactions in the Sudbury Neutrino Observatory*, Phys. Rev. Lett. **89** (1 2002) 011301.

[53] KamLAND Collaboration, *First Results from KamLAND: Evidence for Reactor Antineutrino Disappearance*, Phys. Rev. Lett. **90** (2 2003) 021802.

[54] K2K Collaboration, *Measurement of neutrino oscillation by the K2K experiment*, Phys. Rev. D **74** (7 2006) 072003.

[55] ATLAS Collaboration, *Search for dark matter produced in association with a dark Higgs boson in the $b\bar{b}$ final state using pp collisions at $\sqrt{s}$ =13 TeV with the ATLAS detector*, (2024).

[56] ATLAS Collaboration, *Search for Dark Photons in Rare Z Boson Decays with the ATLAS Detector*, Phys. Rev. Lett. **131** (25 2023) 251801.

[57] ATLAS Collaboration, *Search for the decay of the Higgs boson to a Z boson and a light pseudoscalar particle decaying to two photons*, Physics Letters B **850** (2024) 138536.

[58] ATLAS Collaboration, *Search for high-mass resonances in final states with a τ-lepton and missing transverse momentum with the ATLAS detector*, Phys. Rev. D **109** (11 2024) 112008.

[59] CMS Collaboration, *Search for high-mass resonances in dilepton final states in proton-proton collisions at $\sqrt{s}$ =13 TeV*, Journal of High Energy Physics **2018** (2018) 120.

[60] E. Fermi, *Tentativo di una Teoria Dei Raggi β*, Il Nuovo Cimento (1924-1942) **11** (1934) 1.

[61] B. Grzadkowski, M. Iskrzyński, M. Misiak, and J. Rosiek, *Dimension-six terms in the Standard Model Lagrangian*, Journal of High Energy Physics **2010** (2010) 85.

[62] ATLAS Collaboration, *Measurements of differential cross-sections in top-quark pair events with a high transverse momentum top quark and limits on beyond the Standard Model contributions to top-quark pair production with the ATLAS detector at $\sqrt{s}$ =13 TeV*, Journal of High Energy Physics **2022** (2022) 63.

[63] ATLAS Collaboration, *Measurement of the energy asymmetry in $t\bar{t}j$ production at $\sqrt{s}$ =13 TeV with the ATLAS experiment and interpretation in the SMEFT framework*, The European Physical Journal C **82** (2022) 374.

[64] ATLAS Collaboration, *Measurement of the polarisation of single top quarks and antiquarks produced in the t-channel at $\sqrt{s}$ =13 TeV and bounds on the tWb dipole operator from the ATLAS experiment*, Journal of High Energy Physics **2022** (2022) 40.

[65] S. Bißmann, C. Grunwald, G. Hiller, and K. Kröninger, *Top and beauty synergies in SMEFT-fits at present and future colliders*, Journal of High Energy Physics **2021** (2021) 10.

[66] J. A. A. Saavedra et al., *Interpreting top-quark LHC measurements in the standard-model effective field theory*, 2018.

[67] M. Krammer, *The update of the European strategy for particle physics*, Physica Scripta **2013** (2013) 014019.

[68] E. Strategy Group, *2020 Update of the European Strategy for Particle Physics*, Geneva: CERN Council, 2020.

[69] T. Behnke et al., *The International Linear Collider Technical Design Report – Volume 1: Executive Summary*, 2013.

[70] H. Baer et al., *The International Linear Collider Technical Design Report – Volume 2: Physics*, 2013.

[71] C. Adolphsen et al., *The International Linear Collider Technical Design Report – Volume 3.I: Accelerator R&D in the Technical Design Phase*, 2013.

[72] C. Adolphsen et al., *The International Linear Collider Technical Design Report – Volume 3.II: Accelerator Baseline Design*, 2013.

[73] T. Behnke et al., *The International Linear Collider Technical Design Report – Volume 4: Detectors*, 2013.

[74] M. J. Boland et al., *Updated baseline for a staged Compact Linear Collider*, (2016), ed. by P. Lebrun et al.

[75] S. Dasu et al., *Strategy for Understanding the Higgs Physics: The Cool Copper Collider*, 2022.

[76] M. Bai et al., *C^3: A "Cool" Route to the Higgs Boson and Beyond*, 2021.

[77] T. C. S. Group, *CEPC Technical Design Report – Accelerator (v2)*, 2024.

[78] The TLEP Design Study Working Group, *First look at the physics case of TLEP*, Journal of High Energy Physics **2014** (2014) 164.

[79] A. Abada et al., *FCC Physics Opportunities*, The European Physical Journal C **79** (2019) 474.

[80] A. Blondel and E. Gianfelice, *The challenges of beam polarization and keV-scale centre-of-mass energy calibration at the FCC-ee*, The European Physical Journal Plus **136** (2021) 1103.

[81] D. d'Enterria, A. Poldaru, and G. Wojcik, *Measuring the electron Yukawa coupling via resonant s-channel Higgs production at FCC-ee*, The European Physical Journal Plus **137** (2022) 201.

[82] The LEP Energy Working Group, *Calibration of centre-of-mass energies at LEP1 for precise measurements of Z properties*, The European Physical Journal C - Particles and Fields **6** (1999) 187.

[83] A. A. Sokolov and I. M. Ternov, "On The Spin And Polarization Effects In The Theory Of Synchrotron Radiation," *4th International Conference on High-Energy Accelerators*, 1963 1271.

[84] J. Zhang et al., *Precise beam energy measurement using resonant spin depolarization in the SOLEIL storage ring*, Nuclear Instruments and Methods in Physics Research Section A: Accelerators, Spectrometers, Detectors and Associated Equipment **697** (2013) 1.

[85] FCC Collaboration, *FCC Feasibility Study Midterm Report*.

[86] S. Monteil and G. Wilkinson, *Heavy-quark opportunities and challenges at FCC-ee*, The European Physical Journal Plus **136** (2021) 837.

[87] P. Azzurri et al., *A special Higgs challenge: measuring the mass and production cross section with ultimate precision at FCC-ee*, The European Physical Journal Plus **137** (2021) 23.

[88] H. Abramowicz et al., *Top-quark physics at the CLIC electron-positron linear collider*, Journal of High Energy Physics **2019** (2019) 3.

[89] D. Asner et al., "Top quark precision physics at the International Linear Collider," *Snowmass 2013: Snowmass on the Mississippi*, 2013.

[90] T. Horiguchi et al., *Study of top quark pair production near threshold at the ILC*, (2013).

[91] M. S. Amjad, *Forward-Backward asymmetry in top pair production at the ILC*, Theses: Université Paris Sud - Paris XI, 2014.

[92] F. Bedeschi, L. Gouskos, and M. Selvaggi, *Jet flavour tagging for future colliders with fast simulation*, The European Physical Journal C **82** (2022) 646.

[93] C. B. Verhaaren et al., *Searches for long-lived particles at the future FCC-ee*, Frontiers in Physics **10** (2022).

[94] M. Beneke, A. Signer, and V. Smirnov, *Top quark production near threshold and the top quark mass*, Physics Letters B **454** (1999) 137.

[95] D. Buskulic et al., *Performance of the ALEPH detector at LEP*, Nuclear Instruments and Methods in Physics Research Section A: Accelerators, Spectrometers, Detectors and Associated Equipment **360** (1995) 481.

[96] A. Sirunyan et al., *Particle-flow reconstruction and global event description with the CMS detector*, Journal of Instrumentation **12** (2017) P10003.

[97] J. Marshall, A. Münnich, and M. Thomson, *Performance of Particle Flow Calorimetry at CLIC*, Nuclear Instruments and Methods in Physics Research Section A: Accelerators, Spectrometers, Detectors and Associated Equipment **700** (2013) 153.

[98] G. Wilkinson, *Particle identification at FCC-ee*, The European Physical Journal Plus **136** (2021) 835.

[99] P. Azzi and E. Perez, *Exploring requirements and detector solutions for FCC-ee*, The European Physical Journal Plus **136** (2021) 1195.

[100] R. Aleksan, L. Oliver, and E. Perez, *CP violation and determination of the bs flat unitarity triangle at an FCC-ee*, Phys. Rev. D **105** (5 2022) 053008.

[101] LHCb Collaboration, *LHCb RICH: Technical Design Report*, Technical design report. LHCb, Geneva: CERN, 2000.

[102] M. Cascella, F. Grancagnolo, and G. Tassielli, *Cluster Counting/Timing Techniques for Drift Chambers*, Nuclear Physics B - Proceedings Supplements **248-250** (2014) 127, 1st Conference on Charged Lepton Flavor Violation.

[103] M. Antonello, *IDEA: A detector concept for future leptonic colliders*, Nuovo Cim. C **43** (2020) 27, ed. by G. D'Ambrosio and G. De Nardo.

[104] N. Bacchetta et al., *CLD – A Detector Concept for the FCC-ee*, 2019.

[105] N. Morange, *The Allegro Concept*, 2024.

[106] A. D'Onofrio, *Simulation and tools for the IDEA detector concept*, Nuovo Cim. C **47** (2024) 96.

[107] T. Miralles and S. Monteil, *Study of the feasibility of the observation of* $B^0 \to K^*(892)\tau^+\tau^-$ *at FCC-ee and related vertex detector performance requirements*, 2023.

[108] G. Gaudio, *The IDEA detector concept for FCCee*, PoS **ICHEP2022** (2022) 337.

[109] S. Barsuk et al., *First characterization of a novel grain calorimeter: the GRAiNITA prototype*, Journal of Instrumentation **19** (2024) P04008.

[110] CLICdp Collaboration, *CLICdet: The post-CDR CLIC detector model*, (2017).

[111] CLICdp Collaboration, *A detector for CLIC: main parameters and performance*, (2018).

[112] CMS Collaboration, *Performance study of the CMS barrel resistive plate chambers with cosmic rays*, Journal of Instrumentation **5** (2010) T03017.

[113] W. Kilian, T. Ohl, and J. Reuter, *WHIZARD—simulating multi-particle processes at LHC and ILC*, The European Physical Journal C **71** (2011) 1742.

[114] T. Sjöstrand et al., *An introduction to PYTHIA 8.2*, Computer Physics Communications **191** (2015) 159.

[115] B. Andersson, *The Lund Model*, Cambridge Monographs on Particle Physics, Nuclear Physics and Cosmology, Cambridge University Press, 1998.

[116] L. Hartgring, E. Laenen, and P. Skands, *Antenna showers with one-loop matrix elements*, Journal of High Energy Physics **2013** (2013) 127.

[117] S. Höche and S. Prestel, *The midpoint between dipole and parton showers*, The European Physical Journal C **75** (2015) 461.

[118] The DELPHES 3 Collaboration, *DELPHES 3: a modular framework for fast simulation of a generic collider experiment*, Journal of High Energy Physics **2014** (2014) 57.

[119] S. Agostinelli et al., *Geant4—a simulation toolkit*, Nuclear Instruments and Methods in Physics Research Section A: Accelerators, Spectrometers, Detectors and Associated Equipment **506** (2003) 250.

[120] F. Gaede et al., *EDM4hep - a common event data model for HEP experiments*, PoS **ICHEP2022** (2022) 1237.

[121] R. Brun and F. Rademakers, *ROOT — An object oriented data analysis framework*, Nuclear Instruments and Methods in Physics Research Section A: Accelerators, Spectrometers, Detectors and Associated Equipment **389** (1997) 81.

[122] D. J. Lange, *The EvtGen particle decay simulation package*, Nuclear Instruments and Methods in Physics Research Section A: Accelerators, Spectrometers, Detectors and Associated Equipment **462** (2001) 152, BEAUTY2000, Proceedings of the 7th Int. Conf. on B-Physics at Hadron Machines.

[123] M. G. Bowler, e^+e^- *production of heavy quarks in the string model*, Zeitschrift für Physik C Particles and Fields **11** (1981) 169.

[124] J. Alwall et al., *The automated computation of tree-level and next-to-leading order differential cross sections, and their matching to parton shower simulations*, JHEP **07** (2014) 079.

[125] J. A. A. Saavedra et al., *Interpreting top-quark LHC measurements in the standard-model effective field theory*, 2018.

[126] C. Degrande et al., *UFO - The Universal FeynRules Output*, Comput. Phys. Commun. **183** (2012) 1201.

[127] M. Cacciari, G. P. Salam, and G. Soyez, *The anti-kt jet clustering algorithm*, Journal of High Energy Physics **2008** (2008) 063.

[128] *; 1991 ed.* Durham Univ., Durham, NC: Durham Univ., 1991.

[129] M. Cacciari, G. P. Salam, and G. Soyez, *FastJet User Manual*, Eur. Phys. J. C **72** (2012) 1896.

[130] M. Cacciari and G. P. Salam, *Dispelling the N^3 myth for the k_t jet-finder*, Phys. Lett. B **641** (2006) 57.

[131] J. Eschle, A. Puig Navarro, R. Silva Coutinho, and N. Serra, *zfit: scalable pythonic fitting*, (2019).

[132] M. Bauer, M. Heiles, M. Neubert, and A. Thamm, *Axion-like particles at future colliders*, The European Physical Journal C **79** (2019) 74.

[133] ALEPH Collaboration, *Measurement of the Z resonance parameters at LEP*, Eur. Phys. J. C **14** (2000) 1.

[134] ALEPH Collaboration, *Measurement of A^b_{FB} using inclusive b-hadron decays*, The European Physical Journal C - Particles and Fields **22** (2001) 201.

[135] DELPHI Collaboration, *Measurement of the forward backward asymmetries of $e^+e^- \to Z \to b\bar{b}$ and $e^+e^- \to Z \to c\bar{c}$ using prompt leptons*, Eur. Phys. J. C **34** (2004) 109.

[136] OPAL Collaboration, *Measurement of heavy quark forward backward asymmetries and average B mixing using leptons in hadronic Z decays*, Phys. Lett. B **577** (2003) 18.

[137] L3 Collaboration, *Measurement of the $e^+e^- \to Z \to b\bar{b}$ forward-backward asymmetry and the $B^0\bar{B}^0$ mixing parameter using prompt leptons*, Phys. Lett. B **448** (1999) 152.

[138] ALEPH Collaboration, *Measurement of the strong coupling constant α_S from global event-shape variables of hadronic Z decays*, Physics Letters B **255** (1991) 623.

[139] OPAL Collaboration, *A measurement of R_b using a double tagging method*, The European Physical Journal C - Particles and Fields **8** (1999) 217.

[140] ALEPH Collaboration, *A measurement of R_b using a lifetime-mass tag*, Physics Letters B **401** (1997) 150.

[141] J. Revels, M. Lubin, and T. Papamarkou, *Forward-Mode Automatic Differentiation in Julia*, arXiv:1607.07892 [cs.MS] (2016).

[142] DELPHI Collaboration, *A precise measurement of the partial decay width ratio $R^0_b = \frac{\Gamma_{b\bar{b}}}{\Gamma_{had}}$*, The European Physical Journal C - Particles and Fields **10** (1999) 415.

[143] F. Bedeschi, *A vertex fitting package*, (2024).

[144] ALEPH Collaboration, *A Measurement of the gluon splitting rate into $b\bar{b}$ pairs in hadronic Z decays*, Phys. Lett. B **434** (1998) 437.

[145] DELPHI Collaboration, *Measurement of the multiplicity of gluons splitting to bottom quark pairs in hadronic Z^0 decays*, Physics Letters B **405** (1997) 202.

[146] DELPHI Collaboration, *Measurement of the rate of $b\bar{b}b\bar{b}$ events in hadronic Z decays and the extraction of the gluon splitting into $b\bar{b}$*, Phys. Lett. B **462** (1999) 425.

[147] OPAL Collaboration, *Measurement of the production rate of $b\bar{b}$ quark pairs from gluons and $b\bar{b}b\bar{b}$ events in hadronic Z^0 decays*, tech. rep., CERN, 1999.

[148] SLD Collaboration, "A Preliminary measurement of the gluon splitting rate into $b\bar{b}$ pairs in hadronic Z^0 decays," *American Physical Society (APS) Meeting of the Division of Particles and Fields (DPF 99)*, 1999.

[149] S. Schmitt, *Gluon splitting to $c\bar{c}$ and $b\bar{b}$ in hadronic Z^0 decays: Experimental results.*

[150] The LHCb RICH Collaboration, *Performance of the LHCb RICH detector at the LHC*, The European Physical Journal C **73** (2013) 2431.

[151] LHCb Collaboration, *Hadron PID performance with 2023 data*, (2023).

[152] J. Alcaraz Maestre, *Revisiting QCD corrections to the forward-backward charge asymmetry of heavy quarks in electron-positron collisions at the Z pole: really a problem?* (2020).

[153] A. Djouadi, B. Lampe, and P. M. Zerwas, *A note on the QCD corrections to forward-backward asymmetries of heavy-quark jets in Z decays*, Zeitschrift für Physik C Particles and Fields **67** (1995) 123.

[154] J. Jersák, E. Laermann, and P. M. Zerwas, *Electroweak production of heavy quarks in e^+e^- annihilation*, Phys. Rev. D **25** (5 1982) 1218.

[155] Tevatron Electroweak Working Group, CDF, D0, *Combination of CDF and D0 Results on the Mass of the Top Quark*, (2008).

[156] SLD Collaboration, *Measurement of the branching ratio of the Z^0 into heavy quarks*, Phys. Rev. D **71** (2005) 112004.

[157] LHCb Collaboration, *Angular analysis of the $B^0 \to K^{*0}\mu^+\mu^-$ decay using $3\,fb^{-1}$ of integrated luminosity*, Journal of High Energy Physics **2016** (2016) 104.

[158] LHCb Collaboration, *Test of Lepton Universality Using $B^+ \to K^+\ell^+\ell^-$ Decays*, Phys. Rev. Lett. **113** (15 2014) 151601.

[159] M. Davier, L. Duflot, F. Le Diberder, and A. Rougé, *The optimal method for the measurement of tau polarization*, Physics Letters B **306** (1993) 411.

[160] P. Janot, *Top-quark electroweak couplings at the FCC-ee*, Journal of High Energy Physics **2015** (2015) 182.

[161] J. de Blas, G. Durieux, C. Grojean, J. Gu, and A. Paul, *On the future of Higgs, electroweak and diboson measurements at lepton colliders*, Journal of High Energy Physics **2019** (2019) 117.

[162] F. James and M. Roos, *Minuit - a system for function minimization and analysis of the parameter errors and correlations*, Computer Physics Communications **10** (1975) 343.

[163] C. R. Harris et al., *Array programming with NumPy*, Nature **585** (2020) 357.

[164] R. Boughezal, C.-Y. Chen, F. Petriello, and D. Wiegand, *Top quark decay at next-to-leading order in the standard model effective field theory*, Phys. Rev. D **100** (5 2019) 056023.

[165] ATLAS Collaboration, *ATLAS flavour-tagging algorithms for the LHC Run 2 pp collision dataset*, The European Physical Journal C **83** (2023) 681.

[166] M. Boronat, J. Fuster, I. García, E. Ros, and M. Vos, *A robust jet reconstruction algorithm for high-energy lepton colliders*, Physics Letters B **750** (2015) 95.

[167] L. Sonnenschein, *Analytical solution of $t\bar{t}$ dilepton equations*, Phys. Rev. D **73** (2006) 054015, [Erratum: Phys.Rev.D 78, 079902 (2008)].

[168] R. Dalitz and G. R. Goldstein, *Analysis of top-antitop production and dilepton decay events and the top quark mass*, Physics Letters B **287** (1992) 225.

[169] H. Casler, M. Manganel, M. C. N. Fiolhais, A. Ferroglia, and A. Onofre, *Reconstruction of top quark pair dilepton decays in electron-positron collisions*, Phys. Rev. D **99** (5 2019) 054011.

[170] P. Martín-Ramiro and J. M. Moreno, *Improving $t\bar{t}$ reconstruction in the dilepton channel at future lepton colliders*, (2020).

[171] K. Pearson, *Note on Regression and Inheritance in the Case of Two Parents*, Proceedings of the Royal Society of London **58** (1895) 240.

[172] P. Virtanen et al., *SciPy 1.0: Fundamental Algorithms for Scientific Computing in Python*, Nature Methods **17** (2020) 261.

[173] W. Bernreuther, D. Heisler, and Z.-G. Si, *A set of top quark spin correlation and polarization observables for the LHC: Standard Model predictions and new physics contributions*, Journal of High Energy Physics **2015** (2015) 1.

[174] N. Castro, J. Erdmann, C. Grunwald, K. Kröninger, and N.-A. Rosien, *EFTfitter—A tool for interpreting measurements in the context of effective field theories*, Eur. Phys. J. C **76** (2016) 432.

[175] I. M. Sobol, *On the distribution of points in a cube and the approximate evaluation of integrals*, USSR Computational Mathematics and Mathematical Physics **7** (1967) 86.

[176] O. Schulz et al., *BAT.jl: A Julia-Based Tool for Bayesian Inference*, SN Computer Science **2** (2021) 210.

[177] J. Bezanson, A. Edelman, S. Karpinski, and V. B. Shah, *Julia: A fresh approach to numerical computing*, SIAM Review **59** (2017) 65.

[178] S. Bißmann, J. Erdmann, C. Grunwald, G. Hiller, and K. Kröninger, *Constraining top-quark couplings combining top-quark and B decay observables*, The European Physical Journal C **80** (2020) 136.

[179] C. Grunwald, G. Hiller, K. Kröninger, and L. Nollen, *More synergies from beauty, top, Z and Drell-Yan measurements in SMEFT*, Journal of High Energy Physics **2023** (2023) 110.

[180] M. Vihola, *Robust adaptive Metropolis algorithm with coerced acceptance rate*, 2011.

[181] ATLAS Collaboration, *Measurements of inclusive and differential fiducial cross-sections of $t\bar{t}\gamma$ production in leptonic final states at $\sqrt{s} = 13$ TeV in ATLAS*, The European Physical Journal C **79** (2019) 382.

[182] CMS Collaboration, *Measurement of top quark pair production in association with a Z boson in proton-proton collisions at $\sqrt{s} = 13$ TeV*, Journal of High Energy Physics **2020** (2020) 56.

[183] ATLAS Collaboration, *Measurement of the $t\bar{t}$ production cross-section and lepton differential distributions in $e\mu$ dilepton events from pp collisions at $\sqrt{s} = 8$ TeV with the ATLAS detector*, The European Physical Journal C **80** (2020) 528.

[184] ATLAS Collaboration, *Measurement of the W boson polarisation in $t\bar{t}$ events from pp collisions at $\sqrt{s} = 8$ TeV in the lepton+jets channel with ATLAS*, The European Physical Journal C **77** (2017) 264.

[185] ATLAS Collaboration, *Direct top-quark decay width measurement in the $t\bar{t}$ lepton+jets channel at $\sqrt{s} = 8$ TeV with the ATLAS experiment*, The European Physical Journal C **78** (2018) 129.

[186] ATLAS and CMS Collaborations, *Addendum to the report on the physics at the HL-LHC, and perspectives for the HE-LHC: Collection of notes from ATLAS and CMS*, CERN Yellow Rep. Monogr. **7** (2019) Addendum.

[187] ATLAS Collaboration, *Prospects for the measurement of $t\bar{t}\gamma$ with the upgraded ATLAS detector at the High-Luminosity LHC*, (2018).

[188] CMS Collaboration, *Anomalous couplings in the tt+Z final state at the HL-LHC*, (2018).

[189] CMS Collaboration, *Projection of measurements of differential ttbar production cross sections in the e/μ+jets channels in pp collisions at the HL-LHC*, (2018).

[190] A. Czarnecki, J. G. Körner, and J. H. Piclum, *Helicity fractions of W bosons from top quark decays at next-to-next-to-leading order in QCD*, Phys. Rev. D **81** (11 2010) 111503.

[191] J. Gao, C. S. Li, and H. X. Zhu, *Top-Quark Decay at Next-to-Next-to-Leading Order in QCD*, Phys. Rev. Lett. **110** (4 2013) 042001.

[192] G. Durieux, M. Perelló, M. Vos, and C. Zhang, *Global and optimal probes for the top-quark effective field theory at future lepton colliders*, Journal of High Energy Physics **2018** (2018) 168.

[193] L. Gladilin, *Fragmentation fractions of c and b quarks into charmed hadrons at LEP*, The European Physical Journal C **75** (2015) 19.

[194] M. Vihola, *Robust adaptive Metropolis algorithm with coerced acceptance rate*, Statistics and Computing **22** (2012) 997.

Résumé en français

1 Introduction

La description la plus précise du monde microscopique au niveau des particules élémentaires est fournie par le Modèle Standard de la Physique des Particules (MS). Il a été (et est toujours) testé avec une grande précision dans des environnements expérimentaux différents. Aucune mesure individuelle ou test de cohérence n'a pour l'instant mis en défaut ses prédictions. L'observation en 2012 d'un boson scalaire étroit pour l'instant compatible avec le boson de Higgs au Grand Collisionneur de Hadrons (LHC) au Organisation européenne pour la recherche nucléaire (CERN) a marqué la découverte de la dernière particule manquante du spectre du MS. Cependant, son incomplétude est un fait largement accepté dans la communauté des physiciens des particules en raison de plusieurs observations que le MS ne décrit pas de façon satisfaisante, tels que les oscillations des neutrinos changeant de saveur ou l'existence d'un univers dominé par la matière par rapport à l'antimatière. Ces phénomènes, parmi d'autres, pourraient être décrits par des particules simplement trop lourdes pour être accessibles expérimentalement ou interagissant trop faiblement avec les expériences actuelles pour laisser des signatures mesurables. Les deux cas ont fait l'objet de recherches intensives dans plusieurs générations d'expériences de collisionneur de particules. Cependant, aucune déviation évidente par rapport aux attentes du MS n'a encore été observée. Cette thèse a exploré le potentiel d'identification de telles déviations dans des mesures impliquant les fermions les plus lourds de la troisième génération avec un éventuel collisionneur de particules de prochaine génération, le Futur Collisionneur Circulaire (FCC), situé dans un tunnel de 91 km au CERN dans la région de Genève [10, 11]. Le concept de FCC (ou plutôt l'organisation de son étude) est né en 2014 après la découverte du boson de Higgs pour étudier plus en détail sa nature et son couplage aux particules du MS, et potentiellement à de nouvelles particules. Dans son idée de base, il envisage un fonctionnement en deux phases, avec une période de précision en tant que collisionneur électron-positron (FCC-ee) à partir du début des années 2040, et une prise de données pendant 16 ans. Pendant ces 16 ans, différents niveaux d'énergie sont prévus :

***Z* pôle** À une énergie de collision autour de m_Z, environ $6 \cdot 10^{12}$ désintégrations de bosons Z sont attendues. Cela permet d'étudier les processus électrofaibles (EW) avec une précision inégalée, et fait également du FCC-ee une véritable usine à saveurs, collectant environ 15 fois plus de mésons $B^{0,+}$ que Belle II.

***WW* seuil** Au seuil de production de paires WW de 157 GeV à 163 GeV, les propriétés du boson W telles que sa masse et sa largeur seront mesurées à partir d'environ $2.4 \cdot 10^8$ désintégrations de bosons W avec une précision environ un ordre de grandeur supérieure à la valeur actuelle.

***ZH* seuil** Par le biais du Higgsstrahlung, un échantillon propre d'environ $1.5 \cdot 10^6$ désintégrations de bosons de Higgs permet de mesurer sa masse avec une précision de 2 MeV.

***$t\bar{t}$* seuil** Avec un balayage d'énergie de (340−350) GeV, la masse et la largeur du quark top peuvent être extraites de la forme de la section efficace avec une précision de l'ordre de 10 MeV. Une phase ultérieure à 365 GeV permettra d'explorer les effets au-delà du MS (BSM) dans les mesures précises des processus de production et de désintégration des quarks top.

La sensibilité aux signatures BSM est potentiellement la plus grande pour les fermions les plus lourds du MS, le quark beauté et le quark top dans leur couplage aux bosons de jauge et de Higgs. En particulier, les références des mesures EW du quark beauté sont toujours établies par la précédente génération de collisionneurs électron-positron, à savoir le Grand Collisionneur Électron-Positron (LEP) et le Collisionneur Linéaire de Stanfort (SLC). Dans les collisions e^+e^-, le couplage du quark beauté au boson Z a été exploré en mesurant le rapport de largeur partielle R_b et l'asymétrie avant-arrière A_{FB}^b, une conséquence de la violation de la parité dans les transitions par courant faible neutre. Il convient de noter que A_{FB}^b a montré la plus grande tension avec les attentes du MS à un niveau de $2.9\,\sigma$ dans un ajustement combiné des observables de précision EW (Electroweak Precision Observabless (EWPOs)). De plus, des contributions BSM dans R_b et A_{FB}^b peuvent apparaître dans l'interaction avec des corrections induites par le quark top sur le propagateur du boson Z et au niveau du sommet $Zb\bar{b}$. Si des déviations se manifestent, elles affecteront également les mesures directes des observables du quark top au seuil de production $t\bar{t}$ et au-delà.

2 Mesures de EWPOs au pôle *Z*

Les EWPOs dans le secteur de la beauté, R_b et A_{FB}^b, sont d'un intérêt particulier en raison du couplage presque exclusif du quark beauté avec le quark top. Déjà, par la simple quantité de données provenant du fonctionnement autour et au pôle Z, une précision statistique exceptionnelle est à portée de main. Cependant, et encore plus important, les incertitudes systématiques associées à la mesure doivent être du même ordre de grandeur pour améliorer efficacement la précision de la mesure. La plus grande partie du budget d'incertitudes systématiques est liée à la mauvaise identification des événements de physique des quarks légers comme étant des quarks beauté. Pour R_b, qui est basé sur une technique de double étiquetage pour mesurer

simultanément R_b et l'efficacité d'étiquetage de la beauté $\varepsilon_{b_{1,2}}$, les inefficacités de mauvais étiquetage $\varepsilon_{c_{1,2}}$ et $\varepsilon_{uds_{1,2}}$ diluent l'échantillon d'événements étiquetés simple et double N_b et $N_{b\bar{b}}$

$$\begin{aligned} N_b &= 2N_Z \cdot (R_b\varepsilon_{b_{1,2}} + R_c\varepsilon_{c_{1,2}} + (1 - R_b - R_c)\varepsilon_{uds_{1,2}}) , \\ N_{b\bar{b}} &= \ N_Z \cdot (R_b\varepsilon_{b_1}\varepsilon_{b_2}C_b + R_c\varepsilon_{c_1}\varepsilon_{c_2}C_c + (1 - R_b - R_c)\varepsilon_{uds_1}\varepsilon_{uds_2}C_{uds}) . \end{aligned} \tag{A.1}$$

Dans l'Éq. (A.1), C_i quantifie la corrélation des deux efficacités d'étiquetage des hémisphères et suit $C_i = \frac{\varepsilon_{i_1}\varepsilon_{i_2}}{\varepsilon^2_{i_{1,2}}}$. Afin de réduire de manière significative l'impact de $\varepsilon_{c_{1,2}}$ et $\varepsilon_{uds_{1,2}}$ sur l'incertitude systématique, leur taille doit être réduite en conséquence. Cela a été accompli en introduisant une nouvelle méthodologie d'identification des quarks beauté dans les désintégrations du boson Z en reconstruisant exclusivement des hadrons beauté à partir d'une liste de modes de désintégration. Pour une incertitude statistique encore suffisante de l'ordre de 10^{-5}, une efficacité d'étiquetage de $\varepsilon_{b_{1,2}} = 1\,\%$ a été jugée atteignable avec environ 200 modes de désintégration de B^+, B^0, B^0_s et Λ^0_b. Parmi six modes représentatifs qui considèrent diverses topologies de désintégration, telles qu'un nombre différent de particules chargées ou un nombre différent de pions neutres dans l'état final, la pureté a été trouvée supérieure à 99.8 %. Cette pureté élevée permet de fixer $\varepsilon_{c_{1,2}} = \varepsilon_{uds_{1,2}} = 0$ dans l'Éq. (A.1), ce qui fait de C_b la principale source d'incertitude systématique. Pour A^b_{FB}, qui est basée sur une mesure à étiquetage unique, il convient de connaître, en plus des informations de saveur, l'estimation de la charge et de la direction du quark beauté. L'identification sans bruits de fond à partir de hadrons beauté reconstruits exclusivement fait de la distorsion de la direction du quark beauté la principale source d'incertitude systématique. Ces distorsions sont appelées corrections de chromodynamiques quantiques (QCD) et proviennent de la modélisation des radiations de gluons à haute énergie par le quark avant l'hadronisation. Ces deux sources sont brièvement discutées ci-dessous, et des méthodes pour surmonter leurs limitations sur la mesure finale sont présentées.

2.1 Contrôle de la corrélation d'efficacité des hémisphères

La corrélation des hémisphères est une mesure du biais introduit dans le second hémisphère si le premier a été identifié comme provenant d'un quark beauté. Il a été constaté que la valeur nominale de $\Delta C_b = 1 - C_b$, déviant de zéro, est en elle-même une source d'incertitude systématique et nécessite une gestion minutieuse afin de ne pas augmenter l'incertitude globale. Par conséquent, l'origine principale de ΔC_b étant différente de zéro, comme indiqué dans la Ref. [140], réside dans la détermination d'un vertex primaire (PV) commun de l'événement, ce qui rend plus probable de ne pas reconstruire le second hadron b en cas de déplacement du PV vers l'autre hémisphère. Une sélection indépendante du PV des particules chargées secondaires

pour la reconstruction des hadrons a été développée. Elle repose sur la petitesse de la région de collision des deux faisceaux. Une coupe géométrique rectangulaire a été utilisée pour exclure les particules chargées selon leurs paramètre d'impact transversal et longitudinal pour la reconstruction ultérieure, garantissant ainsi leur accord avec la contrainte de la région lumineuse des collisions. En comparaison avec la détermination d'un PV commun C_b^{PV}, les résultats de la corrélation des hémisphères sont

$$\begin{aligned} \Delta C_b &= -0.001 \pm 0.003\,, \\ \Delta C_b^{\mathrm{PV}} &= 0.035 \pm 0.003\,. \end{aligned} \tag{A.2}$$

Dans l'Éq. (A.2), l'incertitude est d'origine statistique et montre un résultat compatible avec l'unité (absence de corrélation) pour la sélection alternative des particules chargées. Le même résultat ne s'applique pas pour le PV commun. À partir des échantillons d'événements disponibles, qui considèrent une variation de l'échelle de renormalisation, de l'échelle de fragmentation des quarks b, et du modèle de cascade de partons, aucune déviation significative dépassant la précision statistique n'a été trouvée. Cependant, pour atteindre $\sigma_{\mathrm{stat.}}(R_b) \approx \sigma_{\mathrm{syst.}}(R_b)$, une précision relative totale de 10 % sur ΔC_b est requise. Dans ces conditions, R_b peut être déterminé avec une précision de

$$R_b = \mu(R_b) \pm 2.22 \cdot 10^{-5}(\mathrm{stat.}) \pm 2.16 \cdot 10^{-5}(\mathrm{syst.})\,. \tag{A.3}$$

Ainsi, l'utilisation simultanée de modes de désintégration de hadrons b reconstruits exclusivement et la sélection de particules chargées secondaires n'appartenant pas à l'enveloppe de croisement des faisceaux permettent d'améliorer la mesure de R_b d'un facteur d'environ 60 par rapport au résultat actuel.

2.2 Contrôle des corrections QCD

Pour la mesure de A_{FB}^b, des informations sur la charge et la direction du quark beau sont requises en plus de la saveur. Pour surmonter la limitation due au mélange des mésons neutres B, seules les désintégrations de B^+ et de Λ_b^0 sont utilisées. Cependant, la direction des estimateurs de la direction des quarks b accessibles expérimentalement, tels que l'axe de poussée ou l'axe du jet, peut être déformée jusqu'à confondre la charge par les gluons à haute énergie émis avant l'hadronisation. Les incertitudes systématiques liées aux corrections QCD représentent environ la moitié du budget total d'incertitudes systématiques. Une méthodologie décrite dans la Ref. [152] utilise l'axe du jet comme estimateur de direction et l'acollinearité entre les deux jets comme mesure de la quantité de radiation de gluons et donc de la distorsion de la direction estimée du quark b. Cependant, cela introduit la nécessité d'algorithmes de regroupement et d'étiquetage des jets, et donc une autre source d'incertitude systématique. Afin d'éliminer la reconstruction des jets et les incertitudes qui y sont

associées, les propriétés cinématiques du hadron b reconstruit sont utilisées. Étant donné que l'énergie du hadron b correspond directement à l'énergie du quark b juste avant l'hadronisation, et donc après la radiation de gluons, elle sert d'estimateur de la quantité de radiation de gluons. Des énergies plus élevées des hadrons b réduisent de manière significative l'impact des corrections QCD sur l'incertitude finale de la mesure. Comme l'objectif de l'étude est à nouveau de trouver un seuil où $\sigma_{\text{stat.}}(A_{\text{FB}}^b) \approx \sigma_{\text{syst.}}(A_{\text{FB}}^b)$, deux scénarios d'incertitudes relatives sur les corrections QCD ont été évalués. Dans le premier, plus pessimiste, l'incertitude relative a été supposée être de 5 %, tandis qu'un scénario plus optimiste considère une incertitude de 1 %. Les incertitudes obtenues selmon les deux scenarii sont :

$$\begin{aligned} \text{Pessimiste :} \quad & A_{\text{FB}}^b = \mu(A_{\text{FB}}^b) \pm 5.6 \cdot 10^{-5}(\text{stat.}) \pm 5.6 \cdot 10^{-5}(\text{syst.})\,, \\ \text{Optimiste :} \quad & A_{\text{FB}}^b = \mu(A_{\text{FB}}^b) \pm 2.3 \cdot 10^{-5}(\text{stat.}) \pm 2.3 \cdot 10^{-5}(\text{syst.})\,. \end{aligned} \tag{A.4}$$

À partir de l'asymétrie avant-arrière des fermions, des paramètres fondamentaux du MS, tels que l'angle de mélange électrofaible $\sin^2(\theta_{\text{W}})$, peuvent être déterminés. Cet angle est sensible à la composante vectorielle du couplage du boson Z. Bien que la méthode standard consiste à extraire $\sin^2(\theta_{\text{W}})$ à partir de A_{FB}^{μ}, l'amélioration de la mesure de A_{FB}^b offre une alternative compétitive et peut fournir une confirmation utile d'une éventuelle déviation du MS. Il a été montré qu'une précision de 0.002 % est atteignable dans le scénario optimiste, ce qui représente une amélioration par un facteur 50 par rapport à la moyenne mondiale actuelle. De plus, la masse du quark top peut être mesurée indirectement avec une précision de l'ordre de 100 MeV.

Dans ce qui suit, des mesures complémentaires au seuil du quark top sont présentées, où des effets BSM dans les mesures de R_b et A_{FB}^b pourraient se manifester. Cela est théoriquement décrit à travers un ensemble commun d'opérateurs de dimension six utilisé dans la densité lagrangienne effective du MS.

3 Observables sensibles au quark top

Comme première étape, des observables du quark top ont été identifiées, qui montrent une sensibilité aux modifications des vertex des opérateurs effectifs de dimension six de la Théorie Effective du Modèle Standard (SMEFT), qui est écrite via

$$\mathcal{L}_{\text{SMEFT}} = \mathcal{L}_{\text{MS}} + \Lambda^{-2} \sum_i C_i O_i^{(6)} + \mathcal{O}(\Lambda^{-4})\,. \tag{A.5}$$

Dans l'Éq. (A.5), Λ est l'échelle d'énergie de la physique BSM et est généralement fixée à 1 TeV. La magnitude des opérateurs de dimension six $O_i^{(6)}$ est donnée par les coefficients de Wilson C_i. Les opérateurs d'ordre supérieur sont supprimés par Λ^{-4}. Les opérateurs peuvent affecter la production du quark top, ainsi que la topologie de désintégration, et pourraient se manifester comme une déviation observable, par

exemple, dans l'asymétrie avant-arrière du quark top, les coefficients de corrélation de spin, les fractions d'hélicité des bosons W, ou simplement la section efficace de production dans les canaux de désintégration semi- et dileptonique. Au total, 13 observables ont été identifiées comme sensibles aux modifications des couplages provenant de différents opérateurs de dimension six :

$$\{O_{tW}, O_{tZ}, O_{\varphi Q}^{(-)}, O_{\varphi t}, O_{te}^{(1)}, O_{tl}^{(1)}, O_{Qe}^{(1)}, O_{Ql}^{(-1)}\}\,. \tag{A.6}$$

En particulier, A_{FB}^{t} et le paramètre de polarisation du quark top le long de sa direction de vol ont montré la plus grande sensibilité. La sensibilité a été évaluée à partir de la dérivée première au point du MS $C_i = 0$ de la paramétrisation de l'observable en fonction de C_i dans l'intervalle $-1 \leq \frac{v^2 C_i}{\Lambda^2} \leq 1$, avec v étant la valeur d'attente du vide du Higgs d'environ 246 GeV. Afin de dériver des contraintes sur la plage autorisée des coefficients de Wilson, une estimation plus réaliste de la précision de l'observable à partir des paires de quarks top reconstruites a été effectuée. La reconstruction a été divisée en deux canaux : le canal semi-leptonique et le canal dileptonique.

3.1 Canal semileptonique

L'état final semi-leptonique est caractérisé par la présence d'un lepton isolé et de quatre jets hadroniques, qui ont été regroupés à partir de toutes les particules stables à l'aide de l'algorithme de Durham, après avoir retiré le lepton isolé de la liste des particules. De plus, la quantité de mouvement manquante, provenant de la fraction non détectée de l'événement, a été supposée être le neutrino. L'étiquetage des saveurs de jet a été simplifié en assignant correctement la saveur du jet b dans 80 % des cas. Le défi restant dans ce canal est l'appariement d'un jet b à l'un des bosons W, qui sont formés en combinant le lepton avec le neutrino et les deux jets légers. L'assignation correcte des jets b a été effectuée par une méthode de χ^2, en minimisant l'énergie combinée et la masse invariante des deux combinaisons.

3.2 Canal dileptonique

Le canal dileptonique est plus compliqué en raison de la présence de deux neutrinos, qui partagent la quantité de mouvement manquante. Des algorithmes dédiés, utilisant l'état initial connu dans les collisions e^+e^-, ont été utilisés pour démêler les six composantes de la quantité de mouvement des neutrinos selon une minimisation par rapport aux masses du boson W et du quark top. La méthodologie décrite dans la Ref. [170] a été étendue pour appliquer la minimisation au niveau des objets reconstruits, prenant ainsi en compte les effets d'acceptance et de radiation. Bien que la méthode ait généralement prouvé être une estimation fiable des composantes des neutrinos, la radiation de l'état initial peut avoir un impact significatif sur la

précision de la cinématique du quark top, puisque l'énergie du centre de masse sert d'entrée pour la minimisation.

Après la reconstruction du système de paires de quarks top dans un environnement simulé FCC-ee plus réaliste, la précision expérimentale des observables sensibles aux modifications des opérateurs de dimension six a été évaluée. Pour A_{FB}^{t} et les fractions d'hélicité du boson W, des échantillons d'événements avec une variation de l'échelle de renormalisation, de la masse du quark top et du modèle de cascade de partons ont été utilisés pour évaluer, en utilisant une approche simplifiée, l'ordre de grandeur des incertitudes systématiques. En général, des incertitudes de l'ordre de 2 % ont été calculées pour toutes les observables.

4 Limites sur les coefficients de Wilson

À la date de la thèse et du calcul des limites sur les coefficients de Wilson, aucun calcul théorique au niveau des boucles n'était disponible, ce qui aurait permis de contraindre un ensemble commun d'opérateurs avec des mesures très précises des EWPOs du quark beauté. Par conséquent, seules des limites incluant les mesures du quark top ont été dérivées. Pour cela, une approche bayésienne a été utilisée, numériquement réalisée dans le package `EFTfitter.jl` [174], une interface au Bayesian Analysis Toolkit in `julia` (`BAT.jl`) [176, 177], fournissant des outils pour l'échantillonnage, l'intégration et la marginalisation des distributions a posteriori. La distribution a posteriori est donnée par

$$p(\boldsymbol{\theta}|D) = \frac{p(D|\boldsymbol{\theta})p(\boldsymbol{\theta})}{p(D)}\,, \tag{A.7}$$

avec la vraisemblance $p(D|\boldsymbol{\theta})$ et la distribution a priori $p(\boldsymbol{\theta})$, supposée uniforme dans l'intervalle $-1 \leq \frac{v^2 C_i}{\Lambda^2} \leq 1$. La vraisemblance est une fonction d'un ensemble de mesures et de coefficients de Wilson, qui sont décrits par les paramétrisations corrélées mises en évidence ci-dessus. En échantillonnant la distribution a posteriori avec l'algorithme *Robust adaptive Metropolis algorithm* [194], des distributions marginalisées des coefficients de Wilson ont été utilisées pour évaluer les plus petits intervalles à 95.5 %. Des contraintes strictes de l'ordre de $2 \cdot 10^{-2}$ sont atteignables pour O_{tW} et O_{tZ}, tandis que les opérateurs à quatre fermions $O_{te}^{(1)}, O_{tl}^{(1)}, O_{Qe}^{(1)}, O_{Ql}^{(-1)}$ donnent des limites de l'ordre de $4 \cdot 10^{-2}$. Les deux opérateurs affectant le couplage du quark top avec le champ de Higgs $O_{\varphi Q}^{(-)}$ et $O_{\varphi t}$ sont uniquement faiblement contraints, de l'ordre de l'unité. En comparaison avec les résultats déjà publiés, qui considèrent des mesures de quarks top au LHC et incluent également des projections pour la phase à haute luminosité du LHC, les contraintes sur O_{tW} sont de taille très similaire, tandis que pour O_{tZ} les limites sont environ trois fois plus strictes. Cependant, avec des calculs théoriques disponibles à l'avenir, les limites sur les opérateurs du quark

top devraient être considérablement resserrées grâce aux mesures de précision EW dans le secteur de la beauté et à la présence de quarks top, ainsi qu'à de potentiels effets BSM dans les amplitudes à boucles du vertex $Zb\bar{b}$.

List of Abbreviations

ALLEGRO A Lepton Collider Experiment with Granular Calorimeter Read-Out

`BAT.jl` Bayesian Analysis Toolkit in `julia`

BES beam-energy spread

Br branching ratio

BS beamstrahlung

BSM Beyond the Standard Model

C^3 Cool Copper Collider

CDR Conceptual Design Report

CEPC Circular Electron-Positron Collider

CERN European Organisation for Nuclear Research

CKM Cabibbo-Kobayashi-Maskawa

CLD CLIC Like Detector

CLIC Compact Linear Collider

COM centre-of-mass

CP charge-parity

DIRE dipole resummation

EFT Effective Field Theory

EM electromagnetic

EW electroweak

EWPO Electroweak Precision Observables

FCC Future Circular Collider

FCC-ee Future Circular Collider as electron-positron collider

FCC-hh Future Circular Collider as proton-proton collider

FSR final-state radiation

HL-LHC High-luminosity LHC

ID identification

IDEA Innovative Detector for Electron-Positron Accelerators

ILC International Linear Collider

IP interaction point

ISR initial-state radiation

JER jet-energy response

LEP Large Electron-Positron Collider

LHC Large Hadron Collider

LO leading order

LR luminous region

MC Monte Carlo

MG `MadGraph5_aMC@NLO`

μ-RWELL micro-Resistive WELL

MS Modèle Standard de la Physique des Particules

NLO next-to-leading order

NNLL next-to-next-to-leading log

NNLO next-to-next-to-leading order

P parity

PFO particle-flow object

PID particle identification

PV primary vertex

QCD quantum chromodynamics

QED quantum electrodynamics

QFT quantum field theory

RD resonant depolarisation

RICH Ring Imaging Cherenkov

SLC Stanford Linear Collider

SLD SLAC Large Detector

SM Standard Model of Particle Physics

SMEFT Standard Model Effective Field Theory

TLEP Tera-LEP

UFO Universal FeynRules Output

vev vacuum expectation value

Acknowledgements

This work was a collaborative achievement, journey, and experience. It would not have been possible without the participation and commitment of many people. First, I would like to thank Kevin Kröninger for making my thesis happen in his working group. His constant support and engagement as a supervisor made it possible to accomplish this journey from the beginning on, thank you! Second, Stéphane Monteil, who welcomed me with open arms in Clermont-Ferrand, which was a life-changing experience, and I am thankful for every second in this beautiful place. Your fire for science also kept mine alive, even in difficult times. Together with you, Romain Madar, you made this stay unforgettable, and your support through all the ups and downs was instrumental in being able to write these last words here. Furthermore, I would like to thank my reviewers, Frank Simon and Emmanuel Perez for the critical reading of my thesis and for providing valuable feedback. In addition, I would like to acknowledge the financial support from the Franco-German University as well as from the Heinrich Hertz-Stiftung.

Throughout this journey, many people have made this an unforgettable experience in Germany, as well as in France. E4, where it all started, made the (intermediate) *goodbye* emotional. Nevertheless, the warm welcome from the *Laboratoire de Physique de Clermont* crew and special people from Clermont-Ferrand made it feel like a second home for me. In particular, you, Mike, and Tristan, from whom I learnt the French pub culture and with whom I explored great cities across Europe during multiple conferences. It was a pleasure to meet you, guys.

Special thanks to my friends in CP-03-139, Benedikt, Michael, and Salvatore. It was a real joy to join your office and you made my return like a coming-home. Furthermore, E4 is like a family and I am grateful for all of you lovely guys here. This opportunity allows me to especially thank you, Hendrik, for that we became friends and that you showed me what a real *euro training* looks like. Furthermore, I appreciate the help from Andrea and Chris for reading parts of my thesis and for providing valuable input. No acknowledgements section without a great thank you to Andrea, who helped me fight against and with all administrative obstacles.

Nothing would have worked out without the constant and heartwarming support from my closest and long-standing friends, Chris, Luisa, Pascal, Timo, it were you who cheered me up, even in hard times.

I would like to dedicate my last words to my family. I am deeply grateful and pleased for your everlasting and loving support.